

Herstellung von Hybrid-Nanomaterialien für biologische Anwendungen

Zur Erlangung des akademischen Grades eines

DOKTORS DER NATURWISSENSCHAFTEN

(Dr. rer. nat.)

Fakultät für Chemie und Biowissenschaften

Karlsruher Institut für Technologie (KIT) – Universitätbereich
genehmigte

DISSERTATION

von

Marko Miljevic

aus

Zagreb

Dekan: Prof. Dr. Peter Roesky

Referent: Prof. Dr. Peter Nick

Korreferent: Prof. Dr. Christof M. Niemeyer

Tag der mündlichen Prüfung: 15.04.2014

Contents

1. Abstract	5
2. Introduction.....	7
2.1. Nanoparticles (NPs).....	7
2.1.1. Metallic Nanoparticles.....	10
2.1.2. Metal Oxide Nanoparticles - Titanium dioxide - TiO ₂ NPs.....	29
2.1.3. Semiconductor Nanoparticles - Quantum Dots (QDs)	37
2.2. Hybrid Nanomaterials	41
2.3. Nanoparticle Functionalization	48
3. Goals/Aims	53
4. Results and Discussion	54
4.1. Lipoic Acid – Dopamine Bifunctional Linker (LA-DA).....	54
4.1.1. Synthesis of LA-DA Linker	54
4.1.2. Characterization of LA-DA Linker	54
4.2. Nanoparticles Synthesis and Characterization.....	55
4.2.1. Citrate Au NPs.....	55
4.2.2. LA-DA coated NPs.....	58
4.3. Functionalization of TiO ₂ nanomaterials.....	66
4.3.1. Functionalization of commercial TiO ₂ NPs	66
4.3.2. Functionalization of TiO ₂ Nanorods (NR)	75
4.4. Preparation and Study of Au/TiO ₂ Nanocomposite	77
4.4.1. Synthesis of Au/TiO ₂ Nanocomposite Using Bifunctional LA-DA Linker.....	77
4.4.2. Characterization of Synthesized Au/TiO ₂ Nanocomposites (Type A and Type B)	81
4.4.3. ROS Production of Au/TiO ₂ Nanocomposites.....	95
4.4.4. Switchability of the Enzymatic Activity in the Presence of Au/TiO ₂ Nanocomposites	100
4.4.5. Other TiO ₂ Nanocomposite Materials	103
4.5. Nanomaterial Light-induced (NALI) Cell Toxicity.....	110
4.5.1. <i>Nicotiana tabacum</i> cultivar Bright Yellow-2 (cv. BY-2) - Tobacco Cell Line.....	110
4.5.2. Nanoparticle Light Induced (NALI) Toxicity in plant cells	111
4.5.3. Cancer Cell Lines.....	114
4.5.4. Non-cancer cell line	115
4.5.5. Nanocomposite Light Induced Toxicity on mammalian cells	115
5. Conclusion	120

6.	Experimental Part.....	123
6.5.	Synthesis of nanomaterials	123
6.5.1.	Synthesis of Au NPs	123
6.5.2.	LA-DA coated NPs.....	123
6.5.3.	Synthesis of hybrids.....	125
6.6.	Functionalization of TiO ₂ nanomaterials.....	127
6.6.1.	Functionalization of commercial TiO ₂ NPs	127
6.6.2.	DA Functionalization of TiO ₂ NRs	128
6.7.	Chemicals.....	128
6.8.	Instrumentation used.....	128
6.8.1.	TEM and HAADF-STEM Microscopy / EDX Spectroscopy / Selected Area Electron Diffraction (SAED).....	128
6.8.2.	UV-Vis Absorbance Spectroscopy	129
6.8.3.	Fluorescence Spectroscopy	129
6.8.4.	ICP-MS/ICP-OES.....	129
6.8.5.	DLS / Zeta potential measurements.....	130
6.8.6.	Other instrumentation	130
6.9.	Techniques	130
6.9.1.	The enzyme based HRP/AR fluorescence assay for determination of ROS production 130	
6.9.2.	Light controlled activity of Horseradish Peroxidase (HRP).....	131
6.9.3.	Evans Blue Cell Death Assays of Cells Treated with Nanoparticles.....	131
6.9.4.	MTT Assay.....	136
7.	Literature.....	142
8.	List of Publications.....	154
9.	List of Abbreviations.....	155
10.	Acknowledgments	158
11.	<i>Curriculum Vitae</i>	159

1. Abstract

Work described in this dissertation is focused on preparation of photoactive, reactive oxygen species (ROS) producing titanium oxide (TiO₂) based nanomaterials to be used in either enzyme activation or induced cell death. TiO₂ is well investigated, abundant, non-toxic semiconducting material with excellent photocatalytic properties at nanometer range. Namely, when irradiated with light of appropriate wavelengths (depending on the band gap, ~3.2eV), the electrons and hole pairs (excitons) are formed in TiO₂ nanostructures, which subsequently, depending on surrounding medium, lead to the production of different reactive species. The ROS production depends strongly on the fate of these excitons with quenching occurring both through entrapments of the excitons in the surface defect sites or through their recombination in the bulk. ROS producing ability of different TiO₂ nanostructures (spheres or rods) coated with various dopamine stabilizing linkers is explored to investigate the influence of the coatings onto the ROS production. To simultaneously quantify the ROS production and explore enzyme activation, assay based on horseradish peroxidase (HRP) and fluorescent Amplex Red (AR) substrate was developed.

To further enhance the photo-induced ROS production and extend the inducing wavelength range to the visible part of the spectrum, hybrid TiO₂ –metallic NP nanocomposites were prepared using novel bifunctional dopamine based linker. Au and Ag nanoparticles were synthesized using bifunctional linker, which acts both as stabilizing agent and TiO₂ binding agent.

Upon the UV light (365nm) irradiation, all the synthesized nanocomposites showed excellent photocatalytic activity in comparison to the TiO₂ standard. Furthermore, the nanocomposites were also photoactive when irradiated with visible light (470nm), which is not the case in unmodified TiO₂.

The nanocomposites, as well as the ligand-modified TiO₂ NPs, were further used in biological experiments exploring enzyme switchability and cell toxicity (animal and plant) upon light irradiation (UV and visible).

Kurzzusammenfassung

Im Mittelpunkt dieser Dissertation steht die Preparation der photoaktiven, Radikale produzierenden Titaniumdioxide (TiO_2) Nanomaterialien, die sowohl für Enzymaktivierung angewendet werden können, als auch programmierten Zelltod (Apoptose) auslösen können. TiO_2 ist bekannter, erforschter, erhältlicher und ungiftiger Halbleiter mit außergewöhnlichen photokatalytischen Eigenschaften im Nanobereich. Wenn nämlich die TiO_2 -Nanopartikeln mit passendem UV-Licht bestrahlt werden, entstehen Elektron-Loch-Paare, die in den wässrigen Lösungen zur Produktion von reaktiven Sauerstoffspezies (ROS) führen. Die ROS-Produktionsfähigkeit der verschiedenen TiO_2 -Nanostrukturen (Nanoteilchen oder Nanostäbchen), funktionalisierten mit catecholbasierten Linkern, wurde erforscht, um den Einfluss der Funktionalisierung an die photokatalytische Eigenschaften der Nanostrukturen zu untersuchen. Um gleichzeitig ROS-Produktion zu quantifizieren und enzymatische Aktivität zu untersuchen, wurde ein auf Meerrettichperoxidase (HRP) und fluoreszente Amplex Red (AR) Substrat basierendes Assay entwickelt und verwendet.

Um die photoinduzierte ROS-Produktion weiter zu verbessern und die induzierende Wellenlänge auf das sichtbare Bereich des elektromagnetischen Spektrums zu erweitern, wurden die Nanohybride aus TiO_2 und Metalnanopartikeln mit Hilfe von neuem bifunktionellen dopaminbasierten Linker hergestellt. Der neue bifunktionelle Linker dient bei der Herstellung von Au- und Ag-Nanopartikeln sowohl als Stabilisierungsmittel als auch als TiO_2 -Bindemittel.

Alle hergestellte Nanohybride haben unter Bestrahlung mit UV-Licht (365 nm) hervorragende photokatalytische Eigenschaften im Vergleich mit dem TiO_2 -Standard gezeigt. Die Nanohybride wurden außerdem unter Bestrahlung mit sichtbarem Licht photoaktiv, was bei dem unmodifizierten TiO_2 -Standard nicht der Fall war.

Sowohl die Nanohybride als auch die ligandmodifizierten TiO_2 -Nanopartikeln wurden weiterhin in biologischen Experimenten, die Enzymschaltbarkeit und Zelltoxizität (bei Tieren- und Pflanzenzellen) unter sichtbarer und UV-Lichtbestrahlung untersuchen, verwendet.

2. Introduction

2.1. Nanoparticles (NPs)

The scientific interest in NPs has been steadily growing in the past few decades as they are considered a bridge between the atomic or molecular structures and bulk material, thus presenting a new form of matter. By IUPAC definition, the particle has to have all its dimensions in the 1-100 nm range to be classified as nanoparticle (NP). The reason for such definition lies in the fact that many material properties change when the dimensions of the bulk material are reduced to above range. Quantum confinement and increased surface to volume ratio are two mechanisms that are responsible for most of the novel properties of the NPs. As the wavefunctions of electrons and holes become confined by the physical dimensions of the nanocrystals, the electronic level structure and the resulting optical and electrical properties significantly change. For example, reducing the size of direct-gap semiconductors to nanometer range leads to a characteristic blue shift of the band gap energy. A discrete level structure develops as a result of the quantum confinement effect, which can be readily observed in the absorption and luminescence spectra of colloidal quantum dots (QDs). Metal NPs are another good example of size-dependent properties. In such NPs, conduction electron cloud is oscillated by an electromagnetic field thus producing a resonant surface-plasmon response. For metals with free electrons, the surface plasmon resonance appears in the visible range, leading to rich color changes of colloidal solutions of NPs of different sizes. Another interesting effect of the size reduction is the changed surface to volume ratio in comparison to the macroscopic materials. As a consequence, surface atoms of the nanoscale objects start to play a more important role. Such architecture makes NPs ideal material for catalysis where large surfaces are necessary to enhance the rate and yield of the reactions. ^[1]

In classification of NPs there is still no unanimous agreement. One of the accepted classifications of engineered NPs includes carbon-based materials (nanotubes, fullerenes and buckyballs), metal-based materials (including metal oxides and quantum dots), dendrimers (nano-sized polymers built from branched units of unspecified chemistry), composites (including nanoclays and polymers), liposomes as well as different metallic NPs. This list is by no means complete, as there are many other forms of materials being investigated and especially as the combinations of all of the above materials are also possible in form of hybrid NPs.

Regarding the NPs synthesis, one can generally take three different routes, physical, chemical or biological. The physical is further divided into mechanical (milling and melt mixing) and vaporous

(deposition and ablation) approach. As it often requires high vacuum as well as complex instrumentation, the physical route is regarded both as the most complicated and the most expensive one. The most widely used route is the chemical one, offering relatively straightforward methodologies (colloidal and sol-gel) that can be performed with inexpensive instrumentation. The syntheses are done at relatively low temperatures (<350°C), resulting in large quantities of the material of desired shape and/or size. In addition, doping with different atoms is possible during the synthesis,^[2] as well as during surface modification,^[3] patterning or self-assembly.^[4] Both chemical methods mentioned here were used in this dissertation for the synthesis of metal NPs (colloidal method) and semiconductor NPs (sol-gel method) and they will be elaborated in the following sections.

Biological route exploits various microorganisms (fungi, yeast, bacteria, *etc.*), plant extracts, enzymes or bio-based templates (DNA, viruses, diatoms, *etc.*) to induce conversion of NP precursor into NPs.^[5] Even though the most environmentally friendly one, its use is mostly reserved for the proof of concept studies in preparation of metallic NP as the quantity of the resulting nanomaterial is still relatively small.

As the properties of the nanomaterials strongly depend on their size and shape, it is desirable to produce them in a controlled and reproducible way to afford monodisperse suspensions and high yields. Amongst the stated routes, the chemical one best fulfills these requirements, which alongside other benefits that it possess, makes it preferable choice when synthesizing NPs.

In the last few decades the NPs found numerous applications both in science, technology, medicine and everyday life. Due to their extraordinary properties, and especially due to their size, which can be several orders of magnitude smaller than the cell, nanomaterials emerged as powerful tools to fight the diseases on the cellular level. The first generation of the NPs-based drugs has already claimed recognition in the clinical cancer research community as an effective tool against certain forms of cancer.^[6] To this date there are a dozen of NP-based anti-cancer drugs on the market and two dozen in clinical trials exploiting not only the carrier ability of the NPs but their physical and chemical properties as well (imaging, radical production, photothermal therapy, *etc.*).^[7] Chen *et al.* recently showed that PEG coated Au nanocages can be used as photothermal transducers for cancer treatment as they exhibit strong light absorption in the near-infrared region in which light can penetrate deeply into soft tissue.^[8] In another example, El-Sayed *et al.* functionalized the PEG coated Au NPs with membrane and nucleus penetrating peptides, thus delivering them to the cancer cell nucleus where they were shown to induce DNA Damage and cause cytokinesis arrest as well as apoptosis.^[9] Although the initial use of NP-based medicine was entirely focused on the cancer

treatment and imaging, the new applications are focusing on other health problems such as cardiovascular diseases (CVD).^[10]

Another interesting biomedical application of engineered NPs is in the development of biosensors.^[11] In such applications, particularly interesting are antibody- NP conjugates. For example, Hall *et al.* developed a method to amplify the wavelength shift observed from localized surface plasmon resonance (LSPR) bioassays by using Au NPs labeled with antibody .^[11a] The demonstrated 400% amplification of the shift upon NP-labeled antibody binding to analyte provides a way to improve the sensitivity of plasmon-based bioassays, paving the way for single molecule-based detection and clinically relevant diagnostics.

Besides nanomedical applications both in design of novel diagnostic and therapeutic platforms,^[12] NPs have found application in preparation of functional materials for energy production through solar energy.^[13] The NPs have higher surface area and higher optical absorption (requiring less material), shorter charge migration length (avoiding charge trapping and recombination), higher solubility (reducing the light scattering), tunable electronic structure (adjusting the band gap position and width) and possible plasmonic resonance with assisted charge injection (transferring electrons from noble metal NPs to the semiconductor NPs via SPR excitation in metal-semiconductor hybrids) and have therefore been used to produce systems where solar energy can be used for generation of hydrogen *via* water splitting^[14] or direct conversion to electricity as in solar cells.^[13b, 15] For example Murdoch *et al.* recently designed highly efficient water splitting system utilizing the synergy of Au and TiO₂ NPs.^[16] The obtained hydrogen is considered to be an alternative to the current fossil fuels as it is high in energy and the combustion product is nonpolluting water. Numerous reviews are dedicated to the solar cell design using various types of nanomaterials.^[17] One of the most promising designs is the solid state dye-sensitized solar cell (SS-DSSC) and recently, excellent efficiency was obtained using TiO₂ NPs and hybrid perovskite pigment.^[13b] The as synthesized SS-DSSCs are expected to rival the current solar cell technologies on the market.

Another promising application is concerning the growing problem of water pollution and industrial waste production. It is clear that this is one of the emerging problems to which nanotechnology could offer a solution. A range of materials have been employed for water remediation to remove antibiotics, heavy metals, pesticides and other polluting agents including hybrid nanomaterials mostly based on TiO₂.^[18] Just recently, graphene embedded TiO₂ NPs is an example of a NP-based system that shows great promise in waste water treatment, more specifically in removal of the toxic chromium (VI) ions.^[19] Another study has shown that the nanocomposite Ag/TiO₂ material is an effective way of virus inactivation in drinking water.^[20]

Above example clearly demonstrate the significance of nanoparticle materials and their use in a number of applications.

The following paragraphs will address each group of NPs employed within this thesis in a more detailed way, namely concerning their preparation, properties and applications.

2.1.1. Metallic Nanoparticles

Metallic NPs were historically first class of NPs to be used and made, although its composition was not thoroughly characterized and explored until the development of advanced microscopic and analysis methods in the 20th century. With the rise of nanotechnology, they have found application in nanomedicine and biosensing as well as design of functional materials.^[11b, 21] Three classes of metallic NPs were used in this thesis in preparation of hybrid materials with enhanced photocatalytical activity. These spherical NPs, namely gold (Au), silver (Ag) and copper (Cu), will be presented here, with particular emphasis on their properties, preparation methods and biomedical applications.

2.1.1.1. Gold Nanoparticles (Au NPs)

2.1.1.1. A) Properties of Au NPs

The first man-made artefact containing colloidal solutions dates back to the Roman times (4th century AD) when stained glasses have been made using mixture of Au and Ag NPs to achieve dichroic character (appearance of different colors depending on the path of the light) as in the case of famous Lycurgus cup (Figure 1). Although the nature of the used NPs must have eluded the craftsman that made the cup, the practical knowledge of making colloidal gold and silver obviously existed as early as Roman Empire. Another famous example of the colloidal gold use for ornamental purposes are the stained glass windows that were decorating the European churches. Recent studies have shown that, in addition of being beautiful, these decorative windows also served as air-purifiers when irradiated with sunlight (Figure 1).^[22]



Figure 1. Lycurgus cup dating from 4th century, an example of the early use of the Au NPs – left in transmitted light, right in reflected light.

The modern research of colloidal Au did not start until the mid of 19th century when Michael Faraday published his famous work on interaction of light with matter and for this purpose prepared Au colloid by using phosphorus to reduce a solution of gold chloride.^[23] He observed that colloidal gold solutions have drastically different properties from those of the bulk Au in particular concerning the color (colloid was intensely red). Today we know that the new optical properties, such as difference in color, are the result of the unique interaction between the light and the NPs.^[24] Namely, in metals the electrons can be divided into those localized around the nuclei and those moving freely, which are responsible for the high electrical and thermal conductivities. These free electrons of the metal NPs oscillate within the metal lattice in the presence of the oscillating electromagnetic field of the light.^[25] If the wavelength of the incident light is much larger than the particle size, the electron motion forms a dipole that oscillates at the frequency of the light. The resonance occurs at a particular frequency and such an effect is termed the localized surface plasmon resonance (LSPR) or the Mie resonance (after Gustav Mie who theoretically explained the effect). To calculate the frequency at which the resonance occurs one has to know the dielectric permittivity of the material (ϵ).

In general, for isotropic material, the ϵ is a complex quantity that depends on the frequency of the variable electric field ω .

$$\epsilon(\omega) = \epsilon_1(\omega) + i\epsilon_2(\omega)$$

The imaginary part is associated with the electrical resistance of the medium and indicates the phase shift between the dipole and electrical field oscillations. The $\epsilon(\omega)$ can be determined experimentally or calculated based on various models. According to the Mie theory, the total cross-section (C_{ext}) of absorption and scattering by a particle of radius R is

$$C_{ext} = \frac{24\pi^2 R \epsilon_M^{3/2}}{\lambda} \frac{\epsilon_2}{(\epsilon_1 + 2\epsilon_M)^2 + \epsilon_2^2}$$

, where ϵ_M is the real part of the dielectric permittivity of the surrounding medium. Taking into account that for Au, ϵ_2 depends weakly on the wavelength, and with the condition $\epsilon_1 = -2\epsilon_M$ fulfilled, the resonance is observed. According to the formula (2), the cross-section increases with the increasing size of the particle. In addition to this, there is a shift of the absorption maxima towards the longer wavelengths due to the electromagnetic retardation in larger particles.^[26] Owing to the above described LSPR absorption the Au NPs with sizes of 10 nm show strong absorption centered on 520 nm (in aqueous solutions). Together with the radiative dissipation of the incident light energy through scattering, indicated by the above described SPR effect, NPs have a tendency to heat up upon irradiation (non-radiative dissipation), which is a basis for hyperthermia used in some medical applications, in particular for destruction of cancer cells.^[27]

Furthermore, properties of Au NPs are not only size but also shape dependent. This dependence becomes obvious when gold rod-like NPs referred to as Au nanorods (Au NR) are compared to the spherical ones. As it is shown in Figure 2, the rods have two different plasmon resonances while the nanospheres possess only one. The two resonances are due to the plasmon oscillation along the short and the long axis of the rods, and the peak positions depend strongly on the ratio between these two axes (aspect ratio).^[28] With the increasing aspect ratio, the long-axis peak is shifted towards the longer wavelengths in the near infra-red (NIR) part of the spectrum. It is also worth noticing that the size dependent red-shift is more dramatic for rods than for spheres, allowing for LSPR peak adjustments in Au NRs.^[28b] In the meanwhile different shapes of Au NP have been successfully made among other cubes,^[29] stars,^[30] flowers.^[31]

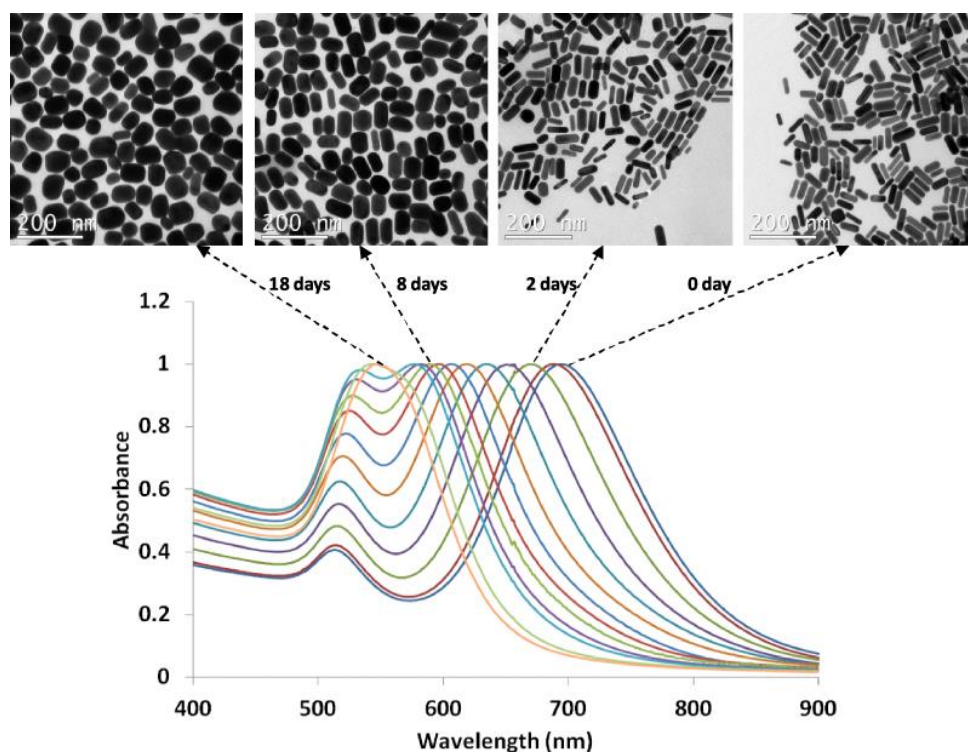
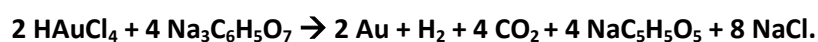


Figure 2. UV-Vis spectra of Au NPs and NR showing changing plasmon peak shifts depending on the shape and size of NPs. Figure adapted from Ref. 32 with permission. ^[32]

2.1.1.1. B) Different methods of Au NP preparation

To address the needs of the specific applications, many reliable and high-yielding methods for the synthesis of different shapes of Au NPs have been developed in the past decades. ^[33]

One of the most commonly used methods to synthesize the spherical Au NPs with small size deviation was established by Turkevich *et al.* in 1951 (*Turkevich method*). ^[34] This method uses the reduction of the Au salt precursor (hydrogen tetrachloroaurate, HAuCl_4) with citrate yielding monodisperse spherical NPs with diameters in the range between 10 and 20 nm as shown below:



The exact mechanism of the reaction is still not fully understood and is a subject of the ongoing scientific debate. The theory behind the NP growth, which is most widely accepted, is the *LaMer Nucleation-Growth* mechanism (Figure 3). ^[35] This theory states that there are several stages

of NP formation. Prior to the addition of the citrate (reducing agent), the gold in the solution is in its ionic form (Au^{3+}). With the addition of the reducing agent, gold atoms start to form ($\text{Au}^{3+} \rightarrow \text{Au}^0$) and their concentration increases rapidly until the solution becomes supersaturated, and the aggregation occurs in a process called *nucleation*. When the concentration of the atoms again falls below the supersaturation level, the formation of the new nuclei stops and the process of *growth* begins, where the freshly reduced ions attach on the surfaces of already formed nuclei.

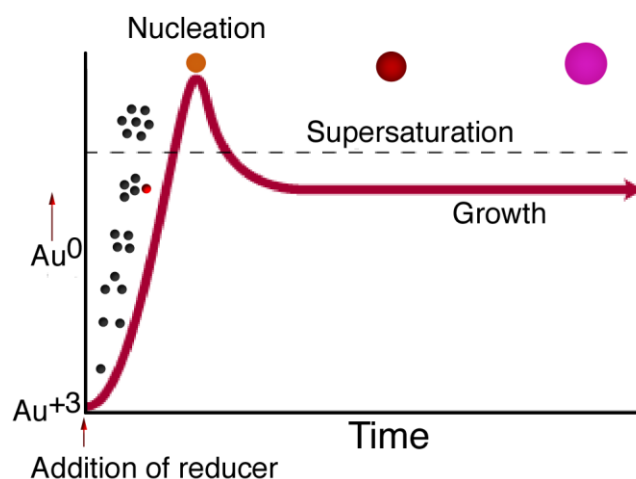


Figure 3. Nucleation-Growth mechanism for NPs according to *Volmer, Becker and Farkas* theory.

Both colloidal crystal nucleation and growth mechanism have been studied theoretically^[36] and experimentally with methods ranging from confocal microscopy^[37] and optical microscopy,^[38] over laser light scattering^[39] and electron microscopy.^[40] The results of these studies gave approximations of the critical nucleation size, crystal structure, and nucleation rates in NPs synthesis. Nevertheless, many aspects of the mechanism remain unknown as the studies failed to address the early stages of homogeneous crystallization, namely the structure and morphology of the intermediates. There is very little known about the start of the crystal facet formation as well as of the role that the impurities have in the process of the nucleation. With nucleation completed, the remaining dissolved Au atoms attach to the nucleation sites under an energy-reducing gradient until all atoms are removed from the solution. The final number of the particles in the solution is governed by the number of initially formed nuclei. With fixed concentration of the precursor, increase in the concentration of the reducing agent results in larger number of the nuclei and consequently, the resulting NPs will be smaller and more numerous. Finding the optimal ratio between the precursor and the reducing agent is therefore an important task. With optimized synthesis conditions, all nucleation sites are formed simultaneously, resulting in formation of monodispersed solutions of Au

NPs. Interestingly, in the first methods of NP preparation, citrate is used as both reducing and surface stabilizing agent.

Recently, there has been new development in the elucidation of the mechanism of the Turkevich reaction. In stark contrast to the *LaMer* model, it has been shown that the initially formed 5nm Au NPs self-assemble into transient structures in form of extensive networks of nanowires.^[41] The diameter of the nanowires progressively increases in size while simultaneously being fragmented into small segments until final NPs are formed. Such mechanism accounts for the color changes that arouse during the synthesis (pale yellow – AuCl_4^- , colorless Au^0 , dark purple –nanowires, ruby red – nanoparticles). One of the advantages of the *Turkevich* method is the use of relatively loosely bound citrate (through the –COOH groups) which allows subsequent surface ligand exchange with e.g. amine (–NH₂) or thiol (–SH) groups, therefore facilitating further surface modification.

Au NPs synthesized with this method are composed of an internal core of pure gold surrounded by a surface layer of adsorbed AuCl_2^- ions. Negatively charged ions are attached to the positive side of the citrate molecule, while the negative side is facing the solution. The negatively charged citrate groups on the surface of NPs increase their stability through electrostatic repulsion effect. After first publication, the *Turkevich* method was later revisited by many authors giving further improvements especially in widening the size range in which the particles can be obtained.^[42]

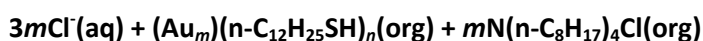
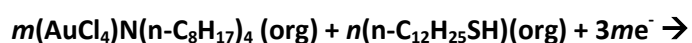
Many other methods for the synthesis of colloidal gold follow the steps of the *Turkevich* method to a great extent. The chosen precursor is predominantly hydrogen tetrachloroaurate (HAuCl_4) while the solvents and reducing agents are varied.

One method, a modification of which was used in this work, was devised by Oh *et al.*^[43] They reported a simple and efficient synthetic method to prepare Au NPs in aqueous phase using HAuCl_4 and thioctic acid-based surfactants. In their setup the precursor HAuCl_4 was reduced by NaBH_4 in the presence of thiolated poly(ethylene glycol) (PEG) ligands (Figure 4). The reduction follows the equation



The ligands were appended with bidentate thiol anchoring groups, known to have high affinity towards Au surfaces.^[44] The obtained NP's average diameters span over the size range between 1.5 and 18 nm, being much wider than a range achieved with other small molecules and polymer ligands. Each of the synthesized batches had a very narrow size distribution of about 10% of the average diameter. Furthermore, the NP size was controlled by varying the molar ratio of gold to PEG-ligand precursors, from 1:10 for small (1.5 nm) NPs, to 4000:1 for the big ones (18 nm). Further passivation of the as-prepared Au NPs allowed for *in situ* functionalization of the NP's surface with the desired functional groups (carboxylic and amine). The Au NPs prepared using this method exhibit remarkable stability in the presence of high salt concentrations, over a wide range of pHs (2–13), and a strong resistance to competition from dithiothreitol (DTT).

An entirely novel approach of Au NP synthesis was pioneered by *Brust* and *Schiffirin* in 1994 when they developed two-phase water-organic solvent synthesis of the Au NPs known now days as *Brust-Schiffirin* method.^[44] The idea behind this synthesis is to prepare NPs from reactants, which are spatially separated into two immiscible phases. In such way, the reaction rate between a metal precursor and a reducing agent NaBH₄ is limited by the interface area between the two liquid systems as well as by the rate of the reactant transfer aided by quaternary alkylammonium salt (tetra-*n*-octylammonium bromide - TOAB) from the aqueous to the organic phase. It is important to note that TOAB does not bind to the Au NPs particularly strongly and the solution aggregates gradually over the course of approximately two weeks.



To prevent the aggregation, *Brust* and *Schiffirin* added a stronger binding agent alkanethiol, which forms a protective monolayer, thus resulting in a stable NP solution. In such way hydrophobic, thiol stabilized NP are formed in organic layer. As some of the phase transfer agent may remain bound to the NPs, their physical properties, such as solubility, may be affected. In order to remove as much of the transfer agent as possible the NPs must be further purified by Soxhlet extraction.^[45] *Brust-Schiffirin* methodology was significant as it results in Au NPs, which are easily handled and can

be isolated and re-dispersed in common organic solvents without aggregation or decomposition. The initial method was later refined and simplified into single-phase synthesis that made the use of phase-transfer agent redundant.^[46] Many researches adopted the *Brust-Schiffrin* method and a huge variety of thiolated-derived capping agents were used in Au NPs synthesis. The method is further used in synthesis of metallic NPs of other metals (*e.g.* Ag and Cu).^[47]

Another widely used method today which allows the synthesis of larger Au NPs with small standard deviation in size is the seeding growth.^[48] The seeding growth methods are performed in several steps depending on the desired NP size. Small metal NPs are prepared first (*e.g.* using *Brust-Schiffrin* method) and later used as seeds (nucleation centers) for the preparation of larger NPs. The seeding growth methods were developed for size control of Au, Ag, Ir, Pd, and Pt NPs.^[49] With controlled number of pre-synthesized seeds and a growth conditions that inhibit any secondary nucleation, the synthesis of NPs can be simply controlled by varying the seed to precursor ratio. In general, these conditions include using a reducing agent (*e.g.* ascorbic acid) that is too weak to reduce the metal salt (in the growth stage) without the presence of seeds. It has been observed that the presence of the seeds, in the environment with small seed-to-precursor ratio, often induced further nucleation (rather than growth) thus resulting in poly-dispersed batches.^[50] To prevent the secondary nucleation, it is important that the NPs enlargement is performed gradually in a step by step manner, allowing a constant large seed-to-precursor ratio throughout successive growth steps.^[50] Jana *et al.* used 3.5 nm Au NPs as seeds to prepare Au NPs in the size range 5–40 nm having standard deviation of 10–15%.^[50] The Au seeds were prepared by commonly used NaBH₄ reduction in presence of the citrate as a capping agent. Secondary nucleation during the growth stage was inhibited by careful control of the growth conditions using a weak reducing agent (ascorbic acid), aqueous surfactant (cetyltrimethylammonium bromide - CTAB), and performing step by step seeding. The synthesized Au NPs were stable in the period of over 1 month. Recently, Ziegler and Eychmüller reported seeded growth synthesis of Au NPs in even wider range with diameters spanning over the 15-300 nm range, using ascorbic acid as reductant and tri-sodium citrate as stabilizer.^[51]

In addition to spherical NPs, a range of Au NPs of different shapes such as rod-like, triangular, and polygonal can be prepared mostly using seed mediated methods with spherical seeds.^[28a, 52] To synthesize desired anisotropic shape, one needs to use ligands with high affinities towards certain crystal facets in order to stop the growth in the direction of these facets. In this way, only the free facets are able to receive additional material and hence the particle grows anisotropically. An example for this is the Au NR synthesis, where citrate capped NPs, used as seeds, are mixed with CTAB (detergent with affinity towards 110 facet)^[52-53] and added to the growth solution (HAuCl₄ solution).

There are several factors that affect the quality and stability of Au NPs regardless of the method used for its synthesis. An important consideration leading to the preparation of stable Au NP solutions is the use of thoroughly cleaned glass apparatus (*aqua regia* cleaning), 0.2- μm -filtered solutions (syringe filters) and triple-glass-distilled water to remove all contaminants as even the trace amounts could have adverse effects on the quality of NP solution. Although the use of silanized glassware is often recommended, good results have consistently been obtained without any special glassware.

In addition to the most common chemical methods mentioned above, Au NPs can be synthesized using many physical (*e.g.* Laser Ablation Synthesis in Solution – LASIS) and biological routes. In one such example, Au NPs were prepared in metallthionein (MTs) rich cells. MT is a family of cysteine-rich (30% of their amino acid residues are cysteins), low molecular weight (typical MW < 7000 Da) proteins localized in the membrane of the Golgi apparatus. MTs have the capacity to bind both physiological (Zn, Cu, Se, *etc.*) and xenobiotic (Cd, Hg, Ag, As, *etc.*) heavy metals through the thiol group of its cysteine residues.^[63] The MTs were used in our group to synthesize various metal NPs (including gold ones). In order to have the reaction conditions under control, the MTs were *in-vitro* conjugated with protein of interest (POI). The maltose-binding protein (MBT) was chosen for that purpose, and was *in-vivo* connected to one, two or three copies of MTs. All the MT-MBT conjugates (1, 2 or 3 MTs) showed the ability to promote the Au NPs synthesis, although the experimental results obtained were not sufficiently clear to draw any strong conclusion on influence of number of MTs on the NPs growth.^[64]

2.1.1.1. C) Biomedical Applications of Au NPs

The Au NPs have made a tremendous impact in many areas of science and technology, although it is in nanomedicine and biological applications that they have made the deepest mark.

Due to their facile synthesis and surface modification, strongly enhanced and tunable optical properties as well as excellent biocompatibility, Au NPs have been extensively used in cancer research. High quality, high yield and size controllable colloidal Au NPs can be easily prepared by the known reduction methods (*Turkevich, Burst-Schiffrin*). The improvement of the of the synthetic methods in the last decade resulted in Au NPs of different shapes and structure including Au NRs,^[53] silica/gold nanoshells^[65] and hollow Au NPs,^[66] which all show largely red-shifted absorptions, an important property in photothermal cancer therapy due to the increased tissue penetration of the infra-red light.

Au NRs and nanoshells have been demonstrated for selective photo-thermal therapy using continuous wave (CW) near-infra-red (NIR) lasers mainly by the El-Sayed^[67] and Halas groups,^[65a, 68] respectively.

By using dark-field light scattering imaging, El Sayed and coworkers^[67b] found that Au NRs conjugated to anti-EGFR antibodies were well organized on the surface of cancer cells with relatively higher binding affinity, while they were randomly distributed nonspecifically on and around the normal cells, similar to the case of the Au nanospheres.^[67a] A CW laser with a wavelength at 800 nm, overlapping with the SPR absorption wavelength maximum of Au NRs at 800 nm, was used for the irradiation of the cells labeled with the NRs. It was found that the cancer cells required half the laser energy (10 W/cm^2) to be photo-thermally damaged as compared to the normal cells (20 W/cm^2), as attributed to the selective targeting of the overexpressed epidermal growth factor receptor (EGFR) on the cancer cell surface by the anti-EGFR conjugated Au NRs.

The work by Halas *et al.* has shown that Au nanoshells can be used for photo-thermal therapy in the NIR region by both passive cancer targeting (through enhanced permeability and retention effect) using PEG-conjugated Au nanoshells^[68-69] and active targeting using antibody-conjugated Au nanoshells.^[70] For *in vivo* therapy, the researchers achieved successful targeting using the PEGylated Au nanoshells injected directly into the tumor region^[69] or delivered intravenously.^[68] It was shown that NIR light of 820 nm at 4 W/cm^2 caused irreversible tumor tissue damage. Most notably, these studies show that laser dosages required to induce tissue damage using the plasmonic Au nanostructures are 10 to 25-fold lower than those used in studies employing photo-absorbing dyes (*e.g.* indocyanine green dye). Currently, the Au nanoshells assisted photo-thermal therapy developed in Halas group is undergoing Phase III clinical trials.^[65b]

There are many known compounds exhibiting high toxicity towards cancerous cells with unfortunate non-specific free-form toxicity when present in the body. Thus, there is strong interest in modifying such drugs, thereby reducing non-specific side effects and enabling higher dose delivery to target (cancerous) tissues. The strategies involve either encapsulation of drugs in various nano-engineered objects or binding of the drug molecules to the nanoparticle carriers. Multifunctional Au NPs have shown great potential for drug delivery as shown by Patra *et al.* who used 5 nm Au NPs as delivery vehicles for covalently bound cetuximab (active targeting agent) and gemcitabine (therapeutic payload in pancreatic cancer).^[71] The combination of cetuximab and gemcitabine alone has been investigated in Phase II trials of this disease with a clinical benefit response noted in 24 of the evaluable 61 patients (39%). Precise cancer targeting was achieved by employing antibodies specific for epidermal growth factor receptor (EGFR), which is overexpressed in up to 60% of pancreatic cancers. The AuNP-anti-EGFR-cetuximab-gemcitabine nanocomposite was superior to any of the agents alone or in combination *in vitro* and *in vivo*. Low doses of complex gemcitabine (2

mg kg⁻¹) led to >80% tumor growth inhibition in a pancreatic cancer model compared with 39% inhibition using the non-conjugated agents in combination.

The color changes of Au NPs colloids governed by the plasmon coupling between the adjacent particles have been widely used in the biosensor design and applications. The red color of well-dispersed Au NPs in solution, turns blue (or purple) when the NPs aggregate. With this intrinsic property of Au NPs, a series of biosensors based on predictable color changes have been designed to detect DNA (or RNA), proteins, and metal ions.^[72]

In 1997, Mirkin *et al.* pioneered a highly selective, colorimetric polynucleotide detection method based on mercaptoalkyloligonucleotide-modified Au NPs probes. As the single-stranded target oligonucleotides (30 bases) were introduced into a solution containing functionalized NPs, they triggered formation of polymeric networks of NPs with a simultaneous red to purple color change (agglomeration). The result is a color change from red to purple (or blue) which can be easily monitored by the naked eye, avoiding complicated instrumentation in the detection process. Hybridization was facilitated by freezing and thawing of the solutions, and the denaturation of these hybrid materials showed transition temperatures over a narrow range thus making the method highly specific. Transfer of the hybridization mixture to a reverse-phase silica plate resulted in a blue color upon drying that could be detected visually. It was reported that the un-optimized system could detect 10 femtomoles of an oligonucleotide. This creative method is quite generalizable to any other DNA or RNA sequence. It was subsequently used to detect various organisms including *Staphylococcus aureus* (MRSA),^[73] *Mycobacterium tuberculosis* (MTB) and MTB complex (MTBC)^[74] and much more as reviewed in several articles.^[75] In addition, this methodology can be integrated with some other emerging technologies. Chan *et al.* combined DNAzyme amplification with colorimetric coupling of surface plasmons of Au NPs for detection of infectious diseases.^[76] This method is based on a catalytic DNAzyme, which is much cheaper and more stable than its protein counterparts. They detected multiple DNA targets for various infectious diseases (gonorrhea and syphilis bacteria, malaria parasite, and hepatitis B virus). This method inherently requires no complex equipment, expensive reagents nor complicated operations, making it suitable for point-of-care diagnosis.

The strongly enhanced radiative properties such as absorption, scattering and plasmonic field for surface enhanced Raman of adjacent molecules make them extremely useful for molecular cancer imaging. In 2008, Qian *et al.* demonstrated *in vivo* tumor targeting and detection using the biocompatible and nontoxic PEGylated Au NPs and the surface-enhanced Raman scattering (SERS).^[77] Prior to this study, Krug *et al.* reported that Au NPs amplify the efficiency of Raman scattering by 14–15 orders of magnitude.^[78]

The PEGylated SERS Au NPs were found considerably brighter in comparison to semiconductor quantum dots with light emission in the near-infrared window. Further conjugation of tumor-targeting ligands such as single-chain variable fragment (ScFv) antibodies, enabled the researches to target the conjugated NPs to tumor biomarkers such as epidermal growth factor receptors (EGFR) on human cancer cells and in xenograft tumor models. The Raman enhancement from these tailored particles was then observed with electronic transitions at 633 or 785 nm via SERS.^[77]

El Sayed *et al.* used Au NPs for cancer imaging by transporting them into the cancer cell nucleus.^[9] In order to do so, they conjugated arginine–glycine–aspartic acid peptide (RGD) and a nuclear localization signal peptide (NLS) to a 30-nm AuNPs via PEG. RGD is known to target receptors on the surface of the cell, whereas NLS sequence is known to associate with karyopherins (importins) in the cytoplasm, enabling the translocation to the nucleus.^[79] The authors further demonstrated that RGD-AuNPs specifically target the cytoplasm and that the RGD/NLS-AuNPs specifically target the nuclei of cancer cells over those of normal cells.

Due to the remarkable properties and judging from the number of synthetic methods and applications reported, it is clear that Au NPs are one of the nanomaterials of utmost importance in bio-nanotechnology.

2.1.1.2. Silver Nanoparticles (Ag NPs)

2.1.1.2. A) Properties of Ag NPs

Ag NPs are one of the most investigated nanomaterials today^[80] and its properties and effects are broadly studied.^[81] It is estimated that nowadays about 320 tons/year of nanosilver are produced and used worldwide.^[82] Even though the changes in nomenclature have created confusion among scientists and policy makers, it is indisputable that products containing or entirely consisting of nanoparticulate silver have commercially been available for over 120 years and were used in preparation of pigments, photographic and wound treatment agents, conductive/antistatic composites, catalysts, and biocides. With such long and diverse history of Ag NPs application, it is clear that an extraordinary amount of research has been conducted concerning the chemistry of nanoscale silver, although it should be noted that until very recently, most of the researches did not use “nano” nomenclature.

Historically, the first known wide-spread practical use of Ag NPs was for staining the glass yellow in European cathedrals in the medieval age. Although the mechanism of interaction of light with colloidal metals was not clear, the methods of reproducible synthesis clearly existed. Already in 1889, M.C. Lea reported the controlled synthesis of citrate-stabilized silver colloid^[83] which must have measured between 7 and 10 nm in diameter as determined in the later studies by Frens and Overbeek in 1969.^[84] The use of proteins as stabilizers of Ag NPs has been described as early as 1902.^[85] Such protein-stabilized NPs, named *Collargol*, have been manufactured and used in medical applications commercially since 1897.^[86] *Collargol* has a mean particle size of 10 nm^[87] and as early as 1907 its diameter was determined to be in the nanorange.^[88] Further investigations into bactericidal properties of silver led to findings that silver ions and silver-based compounds are highly efficient in killing many major types of bacteria.^[89] It has been proposed that silver ions react with thiol groups of the vital enzymes thus inactivating them and causing bacterial death.^[90] Experiments have also shown that DNA loses its replication ability and detrimental structural changes in the membranes occur when the bacteria are treated with silver ions.^[91] In addition to this, antibacterial agents based on nanoparticulate silver have been shown to possess all the previously stated properties of the silver ions with an advantage of functionalization, targeting and many other physical properties specific to NPs.^[92] In the past few decades, many new properties of the colloidal silver have been observed and explained to a great extent resembling those of Au NPs including such phenomena as surface plasmon resonance (SPR),^[24, 93] high surface to volume ratios,^[24] catalytic activity,^[94] and high electrical double layer capacitance.^[95]

Among three noble metals (Au, Ag and Cu) that exhibit the SPR effect, the silver offers highest efficiency of plasmon excitation.^[96] As a matter of fact, the plasmon resonance in Ag NPs is one of the most efficient light – matter interactions. In other words, an Ag NP interacts with light stronger than most of other particles having the same size.^[97] The quantum efficiency of Rayleigh scattering on Ag NPs is orders of magnitude higher than that of the standard fluorophore (*e.g.* R6G),^[24, 98] allowing them to be imaged and characterized using dark-field optical microscopy and spectroscopy (DFOMS).^[98b, 99] When the size of the particles is further reduced and approaches the Fermi wavelength of the electrons (*i.e.* the electron de Broglie wavelength at the Fermi level; 0.5 nm for Ag and Au), the continuous density of the states gets broken up into discrete energy levels. As a consequence, the optical, electrical and chemical properties of these ultra-small NPs (sometimes called nanoclusters) changes dramatically.^[100] One of the interesting properties that arises in this size regime and offers many possibilities for practical application, is the strong fluorescent emission observed upon photo-excitation in the UV-Vis range.^[100b, 101]

Ag NPs shows exceptional photostability (non-blinking and non-photodecomposition) and is the only material whose plasmon resonance can be achieved at any wavelength of the visible spectrum (Figure 7).^[93] The drawback of Ag NPs in comparison with Au NPs lies in the ease of surface oxidation, which makes it less appropriate for some applications *e.g.* sensor and sensor and catalysts development. To circumvent such difficulties, methods for effective synthesis and stabilization of silver colloids have been developed, many of them relying on already described methodologies used for preparation of Au NPs. Two of the most used chemical methods that allow for synthesis of aqueous Ag NPs solutions are shortly discussed in the following chapter.

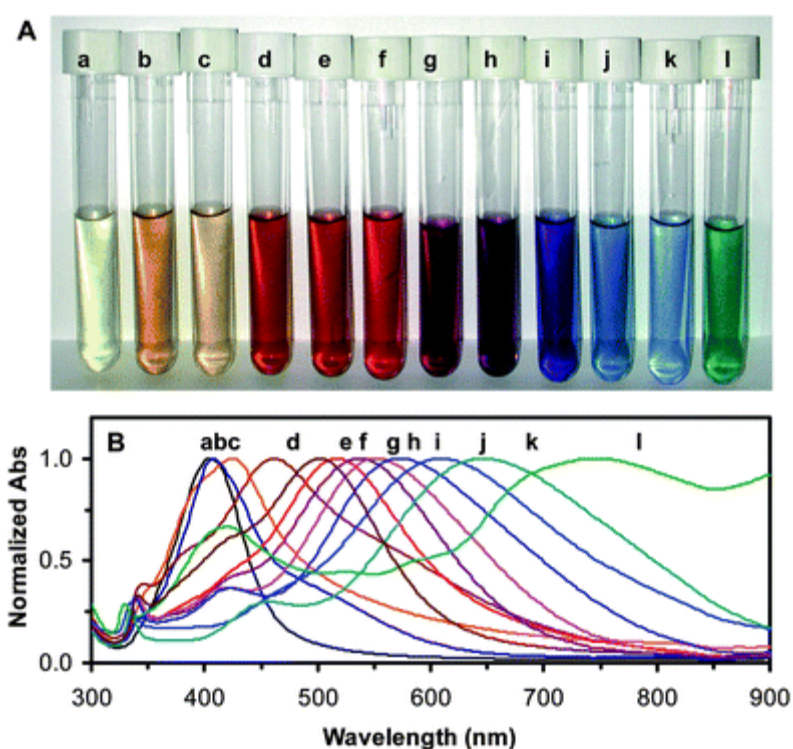


Figure 7. Absorption and scattering optical properties of colloidal Ag NPs (size range 2-85 nm) studies by UV-Vis absorption spectroscopy. (A) Different Ag NP showing the color distribution. (B) Normalized absorbance of UV-Vis absorption spectra of the Ag NPs shown in colloids of Ag NPs in (A). Figure adapted from Ref. 93 with permission.^[93]

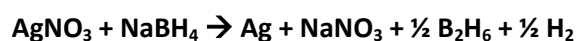
2.1.1.2. B) Methods for Ag NP preparation

The method used frequently in synthesis of Ag NPs is *Lee-Meisel* method based on already discussed *Turkevich* method.^[102] Employed precursor is the silver nitrate (AgNO₃) while citrate serves as the reducing and stabilizing agent. The mixture of silver nitrate and citrate is heated to the boiling point and the Ag NPs are subsequently formed as shown in the following reaction:



Unfortunately, the resulting colloids lack the precision and monodispersity observed with Au NPs, the particles are of different shapes and have relatively wide size distribution (60-200nm).

Referred to as *Creighton* method,^[103] the reduction of silver salts with NaBH₄ is the most common way of obtaining monodisperse Ag NPs. It is a 3-4 component system consisting of precursor, reducing agent, solvent and optionally, stabilizing agent. One of the first reports on the preparation of Ag NPs employed AgNO₃ precursor and NaBH₄ as a reducing agent:



and resulting in NPs in 1-10 nm size range, exhibiting the SPR peak at around 400 nm.

The NPs used as seeds can undergo further shape and size transformations under the kinetic control. The two main processes involved are the crystallization of initially amorphous NPs and their subsequent layer growth. Strong reducing agents such as NaBH₄ are conventionally used only in the formation of seed particle. The further controlled growth of anisotropic NPs is usually conducted in a medium containing organic reducing agents with hydroxyl or aldehyde functions. One compound often acts as both the reducing agent and the reaction medium (solvent) and one of the most frequently used is ethylene glycol. In the literature, use of ethylene glycol is referred to as the polyol methodology and it was first reported by Fiévet *et al.* as a simple route for obtaining colloidal particles of metals and alloys.^[104] In contrast to the fast reduction of Ag⁺ to obtain spherical NPs measuring up to 10 nm, the further crystallization and in particular, the layer growth, are slow

processes that takes considerable time. To accelerate them, elevated temperatures (100-200°C) are often used, meaning that the synthesis is often carried out in a boiling organic solvent.

The inner ordering and growth of NPs resemble the ageing of deposits known in inorganic and colloid chemistry. Ageing is accompanied by the inner structuring and growth of the coarse and the disappearance of the fine NPs. For NPs with the size above a certain value, the former process occurs while for smaller particles, the latter process takes place. This value is called the critical nucleus size. In the formation of Ag NP, such processes are intensified at 85°C. As the crystal structure of silver NP is formed, the selective dissolution of Ag⁺ ions from the individual facets becomes possible. To avoid that, a substance, which can selectively adsorb on a particular crystallographic facet (thus preventing their growth), is added to the system resulting in anisotropic growth of particles. One of the most often used growth stabilizing compound is poly(vinyl pyrrolidone) (PVP)^[105] but similar effects were also observed for polyacrylic^[106] and ascorbic acids,^[107] sodium citrate^[108] and other reagents.

Use of polyol method and various shape stabilizing additives allows for the synthesis of Ag NPs with various shapes including nanowires and NRs,^[107] nanocubes,^[108] nanoprisms,^[109] nanodisks,^[110] nanoplates^[111] and nanobelts.^[106] In addition, it has been shown previously that the polyol method is a convenient and versatile method for the preparation of many other metallic (Pd,^[112] Te^[113]) and bi-metallic (BiIn,^[114] FePt^[115]) NPs as well as metal-oxide^[116] NPs.

Ag NPs can also be prepared using biological macromolecules as templates. For example, amine functional groups of the peptides have been used to assemble silver and gold cations and then cap the growing NP surface following the cation reduction.^[117] Particularly interesting template is DNA molecule that can be used as a template for the formation of Ag nanowires due to its large length to diameter ratio. DNA molecules also have a high metal cation affinity, which when coordinated to the DNA can be reduced to form metallic NPs, which follow the helix contour of the template.^[118] DNA affinity towards Ag ions was also recently used to prepare write once- read many memory device based on light induced growth of conducting Ag NPs.^[119]

Due to the range of possible applications, the search for environmentally friendly synthetic methods for Ag NP preparation continues and methods based on the use of plant extracts (leaves, fruits, roots, seeds, and stems),^[120] enzymes,^[121] bacteria,^[122] biodegradable polymers^[123] or microwaves^[124] are constantly being utilized and refined.^[5b]

2.1.1.2. C) Biomedical Applications of Ag NPs

In the past few decades Ag NPs have been applied in various processes, including catalysis, optics, electronics and material engineering owing to their unique physical and chemical properties. Most of the applications of Ag NPs are as antibacterial/antifungal agents in biotechnology and bioengineering, textile engineering, water treatment, silver-based consumer products as well as in medicine.

It has long been known that Ag possesses strong antibacterial properties against both aerobic and anaerobic bacteria. The use of Ag in nanoparticulate form, as compared to its ionic form, increases its usefulness as the former keeps its antibacterial efficacy but offers reduced cellular toxicity. Although it was assumed that the toxicity stems from the Ag ions present on the surface of Ag NPs, Kim *et al.* clearly demonstrated that the superior antibacterial properties of Ag NPs stems from the free radicals formed on the surface of Ag NPs.^[125] It was also shown that Ag NPs can be useful for destruction of the emerging antibiotic-resistant species.^[126] Moreover, the combination of the antibiotics and Ag NPs has been recently employed showing efficient synergistic effects.^[127]

In addition to anti-bacterial properties, Ag NPs appears to have anti-inflammatory properties as well. Nadworny *et al.* investigated the effect of Ag NPs on a porcine model of contact dermatitis and established that Ag NPs had a direct anti-inflammatory effect, improving the healing process significantly in comparison with the controls.^[128]

Concerning the medicinal use in general, the use of nanoparticulate Ag is broadly divided into diagnostic and therapeutic applications. Early diagnosis is vital for treatment of many diseases, particularly different forms of cancer. Therefore there is a constant search for new methods that could detect low number or just a few cancer cells. In such an attempt, Lin *et al.* used Ag NPs based surface enhanced Raman scattering (SERS) method for non-invasive cancer detection and were able to perfectly differentiate the gastric cancer group from the normal group (100% sensitivity and 100% specificity).^[129]

In terms of therapeutics, the commonly used application of Ag NPs is in wound healing due to the Ag intrinsic anti-bacterial properties. In comparison to other Ag compounds, the use of Ag NPs has resulted in superior healing time and improved post-treatment cosmetics. Although the exact mechanism for these biological effects has not yet been elucidated, it was shown that wounds treated with Ag NPs, besides being bacteria resistant, also had improved collagen alignment resulting in better mechanical strength and shorter recovery times.^[130]

Ag NPs were also used in HIV-1 virus inhibition and it was demonstrated that NPs undergo a size-dependent interaction with the virus.^[131] It was suggested that Ag NPs interact with the HIV-1 virus via preferential binding to the gp120 glycoprotein knobs and as a consequence of this interaction, Ag NPs prevent viral binding to the host cells.

Concerning cancer treatment, interesting concept was described by Tse *et al.* based on Ag nanocomposite.^[132] Human epidermal cancer cells were targeted with folated Ag-dendrimer nanocomposite and the labeled cancer cells subsequently destroyed by the microbubbles generated through increased uptake of NIR laser light energy by the embedded Ag NPs.

Ag NPs can also be used as theranostic substrates offering both diagnostic and therapeutic properties. Theranostics is a new field of nanobiotechnology dealing with multifunctional nanocomposites combining therapeutic, diagnostic, and sensing modalities in a single nanostructure.^[12a, 133] Although the term “theranostics” has been coined quite recently,^[133d] it is now rapidly growing and promising field at the crossroads of plasmonics and nanomedicine.^[134] For example, Boca-Farcu *et al.* used folic acid conjugated, SERS-Labeled Ag nanotriangles (Ag NTs) for multimodal detection and targeted photothermal treatment on human ovarian cancer cells.^[135] By having wide range of optical activity (from visible to NIR region), these Ag NT-tags are capable of providing detailed spectroscopic information regarding their whereabouts by dark field microscopy and SERS, thus opening new opportunities for molecular diagnosis.

Currently, there is an effort to incorporate Ag NPs into a wide range of medicinal devices, including bone cement,^[136] surgical instruments,^[137] and surgical masks^[138]. Additionally, Samsung has created and marketed a material called *Silver Nano*, which includes Ag NPs on the surfaces of household appliances to prevent growth of bacteria.

The Ag NPs made a tremendous impact on today's era of medicinal science. The interesting properties of the Ag NPs are the guarantee that they would be continuously used as newer applications and protocols are being developed.

2.1.2. Metal Oxide Nanoparticles - Titanium dioxide - TiO₂ NPs

2.1.2. A) Properties of TiO₂ NPs

Metal oxides such as, among others, titanium-dioxide (TiO₂), iron oxide (Fe₂O₃ and Fe₃O₄) or zinc-oxide (ZnO), have an important role in numerous areas of chemistry, physics and material engineering. Due to their structural geometries, they can exhibit metallic, semiconductor or insulator characters. Furthermore, metal-oxide NPs possess many unique physical and chemical properties due to their size and high density of surface defects (corner or edge sites). In semiconductor metal oxide NPs, excitation involves separation of electron-hole pairs by a distance of several molecules or ions that build the lattice (Bohr radius – nanometer scale). The energy needed to make such charge separation is known as band-gap energy of the semiconductor. If the NP size is decreased below Bohr radius, the space in which the charges move also decreases, thus imposing an additional confinement. As a result, the band gap and the electron and hole kinetic energies increase, leading to an increase in the density of the charge carriers within and on the surface of the particles. Change of the structural and electronic properties change the physical and chemical ones, *e.g.* a change in the magnitude of the band-gap energy strongly affects the conductivity and chemical reactivity of the particles.^[139]

The optical conductivity is one of the fundamental properties of the metal oxides and can be determined experimentally through scattering and absorption. Due to quantum confinement, the absorption of light is both discrete and size dependent, although there is no unanimous theory that would explain this dependence completely.^[140] In some rough approximation, band gap energy would be governed by the inverse square of the nanoparticle size. For nano-crystalline semiconductors, both linear (one exciton per particle) and non-linear (multiple excitons) responses arise as a result of transitions between electron and hole discrete electronic levels. When considering transport properties, metal oxide nanomaterials may present ionic or mixed ionic/electronic conductivity. The number of the electronic charge carriers is a function of the band gap energy and the electronic conduction is referred as n- or p- type depending on the principal charge carrier (n-electrons, p-holes).

A special case of metal oxide nanomaterial is titanium dioxide (TiO₂) due to its stability, non-toxicity, excellent photocatalytic properties and abundance that is accompanied by its low-cost. In TiO₂ NPs, due to the rather low exciton radii, the quantum confinement effect is restricted to the particles with a diameter smaller than 10 nm. There are three main polymorphs of TiO₂: rutile, anatase and brookite (Figure 8).

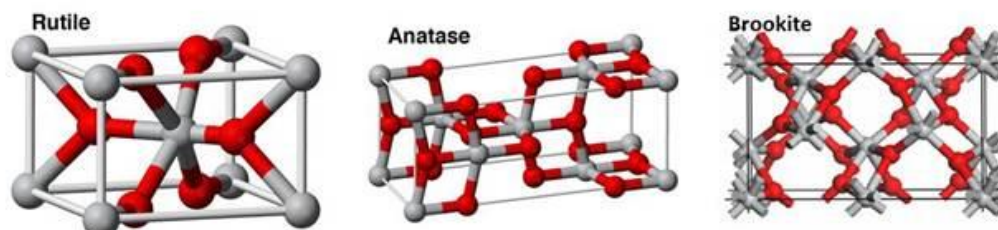


Figure 8. Ball-stick models of three TiO₂ polymorphs. Figure adapted from NANOMATERIALS: Inorganic and Bioinorganic Perspectives, Metal Oxide Nanoparticles, with permission.

The transformation sequence among these three polymorphs is size dependent. This is due to the energies of the three polymorphs being sufficiently close to one another that they can be reversed by small differences in the surface energy. If particle sizes of three nanocrystalline phases are equal, anatase is most thermodynamically stable at sizes less than 11 nm, brookite is the most stable for crystal sizes ranging from 11 to 35 nm, and rutile for NPs with diameters greater than 35 nm.^[141] In the TiO₂ nanomaterials, surface energy appears to be related to the under-coordinated Ti cations (six-fold coordination within the material and five-fold coordination on the surfaces) and there are few studies confirming that surface passivation has an important impact on nanocrystal morphology and phase stability.^[142]

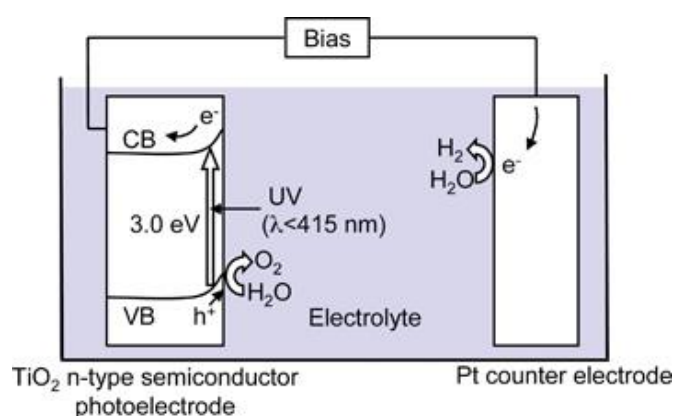


Figure 9. Fujishima-Honda experimental setup to investigate photochemical production of H₂ and O₂ from water under UV irradiation. Figure adapted from Ref. 143 with permission.^[143]

In 1972, Fujishima and Honda made an important discovery that promoted the field of photocatalysis and the use of TiO₂ as the leading material in that field (Figure 9).^[144] They found that photo-irradiation of an aqueous electrolyte-immersed TiO₂ (rutile) single-crystal electrode led to

evolution of oxygen (O_2) from the TiO_2 electrode and hydrogen (H_2) from the platinum counter-electrode when anodic bias was applied to the TiO_2 working electrode. This phenomenon is today known as *Fujishima-Honda* effect. Since then, TiO_2 has been in the focus of many investigations and applications including renewable energy (solar cells), self-cleaning surfaces (both in construction and textile industry), pollutant degradation, food preservation and many more.^[145]

When observed in more detail, photocatalysis of TiO_2 involves three processes: excitation, bulk diffusion and surface transfer of photoinduced charge carriers as presented in Figure 10.

In the first process, the NP absorbs a photon having energy larger than the band gap of the material of which the NP is built. This energy propels the electrons from the valence band to the conduction band of the NP, while the holes are left in the valence band.

During the second process, the excited electrons and holes separate and migrate to the surface of photocatalyst. This migration process is highly dependent on crystal structure, crystallinity, and the NP's size. If the separated electrons and holes meet during the migration, they disappear in a process known as recombination of electron-hole pairs, which results in a decrease in the photocatalytic activity.

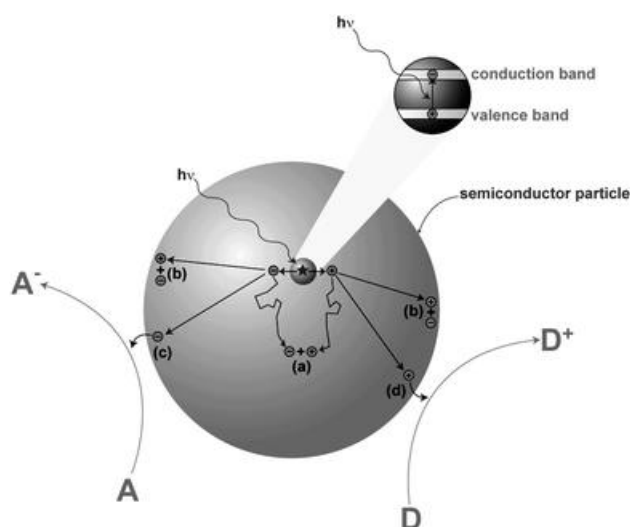
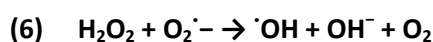
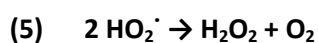
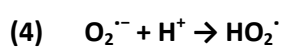
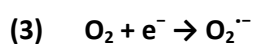
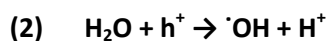
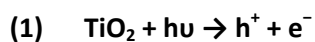


Figure 10. Photo-excitation processes in TiO_2 , excitation (recombination), bulk-diffusion and surface transfer with subsequent reduction and oxidation. (a) Electron and hole recombination in the bulk, (b) electron and hole recombination at the surface, (c) adsorbate reduction at the surface and (d) adsorbate oxidation at the surface. Figure adapted from Ref. 146 with permission.^[146]

Finally, separated electrons and holes can participate in the surface chemical reactions. For example, holes can react with surface adsorbed H_2O to produce hydroxyl radicals, while the electrons

are usually scavenged by O_2 to yield superoxide radical anions. These radical species formed in the solution can further react to give other cytotoxic reactive oxygen species (ROS) such as hydrogen peroxide (H_2O_2) and peroxy radicals, which are all harmful to cells and can be involved in a range of other chemical reactions. The major reactions that result in the formation of ROS are shown in equations (1)–(6).



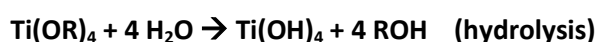
When talking about TiO_2 nanomaterials, it is important to mention a nanoparticulate powder commercially named TiO_2 P25 (also known as *Degussa* or *Aeroxide*). The TiO_2 P25 is a titania photocatalyst that is widely used due to its relatively high photocatalytic activity. As it is difficult to match P25 in its photocatalytic properties, it is often used as a standard. Since 1990, the photocatalytic reactions of P25 have been reported in more than thousand scientific reports.^[147] The P25 is composed of anatase and rutile crystallites, the reported ratio being typically 70:30 or 80:20, although it is not certain if the exact composition is known, presumably due to a lack of methodology for determination of crystalline contents in NPs.^[148] The wide-accepted, although not scientifically proven, hypothesis regarding P25 is that the synergetic effect of anatase and rutile crystallites induces its high photocatalytic activity, namely a transfer of photoexcited electrons and positive holes between interconnecting anatase and rutile crystals suppresses charge recombination and leads to the activity enhancement.^[149]

2.1.2. B) Preparation of TiO_2 NP

The synthesis of metal oxide NPs still poses a challenge due to the requirements for methods that yield monodisperse NPs of different sizes, with different dopants and surface functionalities. Liquid-solid transformations such as co-precipitation and sol gel processing are the mostly used ones

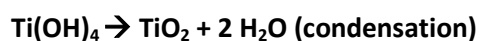
as they offer certain control over morphology as well as a possibility of *in-situ* functionalization of the particles.

The sol-gel method produces metal oxide NPs through the inorganic polymerization reactions and it consists of four steps: hydrolysis, poly-condensation, drying and thermal decomposition. Hydrolysis of the precursors, usually alkoxides (e.g. titanium isopropoxide), takes place upon addition of water or alcohols and results in the corresponding oxo-hydroxide as shown below:



, with R being an alkyl group.

The addition of an acid or a base further promotes the hydrolysis and the condensation of the molecules as they release water, forms networks of metal hydroxide:



In other words, hydroxyl species are polymerized by condensation and form porous and dense gel. Subsequently, drying and calcination leads to ultrafine porous oxides. The calcination at high temperatures is needed in order to clean the product of any remains of the organic precursor and to promote further crystallization. The size of the obtained NPs depends on the solution composition, pH and temperature and can be tuned by changing the reaction conditions.^[150] The sol-gel method has many advantages over other methods, namely ambient temperature of sol preparation and gel processing, product homogeneity, low temperature sintering, ease of making multi-component materials and most importantly, good control over NPs size and shape.^[151]

Another important advantage concerns the doping of the metal-oxide nanomaterials. The introduction of the metal ion to the sol during the gelation phase, allows for the uniform cation incorporation into the host lattice.^[152] For example, metal ions such as Ca^{2+} , Sr^{2+} , Ba^{2+} ,^[2a] Cu^{2+} ,^[152c] Fe^{3+} , V^{5+} , Cr^{3+} , Mn^{2+} ,^[2b] Pt^{4+} ,^[153] Co^{2+} ,^[154] Ni^{2+} ,^[2b] Pb^{2+} ,^[155] W^{6+} ,^[154] Zn^{2+} ,^[156] Au^{3+} ,^[157] Ag^+ ^[158] and many others were introduced into the lattice of sol-gel synthesized TiO_2 NPs, improving the

photocatalytic properties with varying extent. Most of the above stated examples and references are dealing with sol-gel synthesized TiO₂ NPs due to their wide-spread use. Nevertheless, other metal-oxide nanomaterials can be synthesized and modified in the same way (*e.g.* ZnO, Fe₂O₃, MnO, Al₂O₃ or MgO).^[159]

Precipitation methodology usually involves dissolving the salt precursor (sulfate, chloride, nitrate, *etc.*) in water (or some other solvent) to precipitate the oxo-hydroxide form with the help of certain physical transformation (change of temperature, pH, solvent evaporation, reactant concentration, *etc.*) or chemical processes (base or acid addition, use of complex forming agent).^[160] The formation of a new solid phase in liquid medium follows the *Nucleation-Growth* model. The controlled release of cations and anions can govern the kinetics of the nucleation and the particle growth thus affecting the size distribution of the obtained NPs. In TiO₂ NPs synthesis, co-precipitation involves precipitation of hydroxides by the addition of a solution of *e.g.* NaOH (NH₄OH, urea, *etc.*) to a precursor material and subsequent heating to promote the crystallization. It has been reported that lower processing temperatures result in better metal dispersion than the higher ones.^[161]

Regardless of the method used to obtain metal-oxide NPs, the studies of the preparation methods have shown that the crystallization does not entirely follow the traditional *Nucleation-Growth* mechanism. Although the basic idea of already discussed mechanism is regarded generally correct, in the growth mechanism some steps such as Ostwald ripening, a phenomenon which describes the change in an inhomogeneous structures over time and the growth of NPs in solution, may play the most significant role. .^[162]

Loryuenyong *et al.* used the sol-gel method to prepare TiO₂ NPs from titanium (IV) isopropoxide using either ethanol or isopropanol as the solvent and obtained mesoporous NPs were calcined at temperatures ranging from 300°C up to 700°C.^[163] It was found that the collapsing of the pores, crystal growth and anatase-rutile phase transformation were all depended on the increase in calcination temperature. Material's photocatalytic properties were also investigated and the NPs obtained in the isopropanol solvent showed an activity enhancement, which is explained by the ability of isopropanol to inhibit the anatase-rutile transformation through the control of the hydrolysis rate.

In another approach, Shchipunov *et al.* used ethylene glycol and polysaccharide xanthan to mimic mineralization in living organisms and TiO₂ nanomaterial formation on the polysaccharide template.^[164] The metal-oxide morphology was varied from fiber-like over nanoparticulate to plate-like by changing the xanthan-to-water ratio. TiO₂ obtained at ambient conditions did not show any crystallinity requiring additional calcination at temperatures ranging from 300°C to 900 °C, resulting in anatase and rutile, respectively.

The TiO₂ nanomaterial has been prepared in the form of powders, crystals, films, NPs, NRs and nanotubes (NTs) using the above mentioned as well as other methods including microemulsion technique,^[165] solvothermal methods,^[166] template/surface derivatization and ^[167] laser ablation in solution (LASIS)^[168] which will not be discussed in detail.

Following chapter will focus mainly on the biomedical application of TiO₂ nanomaterials which are mainly stemming from their photocatalytic properties although TiO₂ has also been used for design of solar cells,^[169] in electronics^[170] and electrochemistry.^[171]

2.1.2. C) Biomedical Applications of TiO₂ NPs

Biomedical applications of TiO₂ include the photodynamic therapy for cancer treatment, drug delivery systems, cell imaging, biosensors for biological assay and genetic engineering, and many others.^[172]

As described in details earlier (please see paragraph 2.1.2. A) upon light irradiation (wavelength < 385 nm), the photoinduced electrons and holes are formed in TiO₂ NPs and can further react with hydroxyl ions or water to form powerful oxidative radicals (*e.g.*, 'OH, HO₂'),^[173] which are capable of destroying the cell structure of bacteria, fungi and tumors. Due to this property many researchers have focused on the application of TiO₂ as a photosensitizer in cancer treatment.

The photo induced cell toxicity of TiO₂ was first reported on a TiO₂ film electrode by Fujishima *et al* who investigated the effect on *HeLa* cells.^[174]

Seo *et al.* successfully fabricated water-soluble TiO₂ NRs through a high-temperature non-hydrolytic method, which had higher toxicity towards human melanoma cells (A375) in the presence of UV irradiation than commercially available Degussa P25 NPs.^[175]

The important step in the study of TiO₂ was a demonstration of its anticancer activity *in vivo*.^[145a, 174b] Cai *et al.* injected *HeLa* cells under the skin of nude mice to induce tumor growth and when the size of tumors reached 0.5 cm, a solution containing TiO₂ NPs was injected directly to the tumor^[174b]. When the tumor was exposed to UVA light, the growth was significantly inhibited and after a repeating irradiation marked antineoplastic effect was observed.

TiO₂ NPs were also shown to significantly suppress the growth of bladder and glioma cancer cells implanted into mice, even prolonging the survival rate.^[176]

The aforementioned approaches to the cancer treatment are efficient, but they lack specificity. In order to increase the selective antitumor activity and reduce the non-selective cell damage and death, it is necessary to functionalize TiO₂ NPs with molecules that can specifically identify and bind to the cancer cells. Recently, monoclonal antibody proteins (CEA,^[177] pre-S1/S2,^[178]

IL13 α 2R^[179] and EGFR^[180]) with high affinity and specificity have been immobilized onto the surface of TiO₂ NPs. As these proteins are overexpressed on the surface of certain cancer cells, the antibody modified TiO₂ NPs are useful for directing the NPs towards the specific cell population.

Nanoparticulate TiO₂ has received considerable attention in efficient drug delivery system design. To facilitate further use in such systems, differently shaped TiO₂ NPs were prepared (whiskers,^[181] capsules,^[182] and porous shapes)^[183] so that drug can be combined on the surface or contained in the reservoir of TiO₂ NPs. In such way, nanoparticulate TiO₂ has been employed as a carrier material for various drugs, such as sodium phenytoin^[184] valproic acid,^[185] temozolomide,^[186] and doxorubicin.^[187]

Another application of TiO₂ NPs has been demonstrated in past few years and it concerns possible gene treatment strategies using DNA. Rajh and coworkers have conducted extensive research on the preparation of TiO₂-DNA hybrids.^[188] In 2003, they synthesized TiO₂-DNA conjugates containing DNA oligonucleotides covalently attached to 4.5 nm TiO₂ NPs.^[188] The new TiO₂-DNA hybrids retained both the intrinsic photocatalytic capacity of TiO₂ and the bioactivity of the oligonucleotide DNA. In addition, it was found that TiO₂-oligonucleotide nanocomposites have a novel biochemical function—controlled photoinduced endonuclease activity^[189] Important for these studies was the linking of biomolecules with TiO₂ through catechol containing linkers such as dopamine, which facilitates a hole transfer across the interface, establishing efficient crosstalk between the biomolecules and metal oxide NPs.^[190] Such TiO₂ NPs decorated with DNA oligonucleotides were capable of specific cleavage of mutated genomic DNA in a sequence-specific and inducible manner. Furthermore, the targeting activity was accomplished *via* oligonucleotide hybridization to an intracellular organelle containing complementary DNA sequence.^[188] When irradiated, a charge separation occurs within the TiO₂ NP effectively cleaving the defective gene. This opens new avenues not only to photo induced gene therapy but also “seek and destroy” strategy for elimination of defective cell.

It is obvious that the potential of TiO₂ nanomaterials is still far from exhausted and new developments in biomolecule attachment chemistry and photocatalytic activity might lead to the design of novel effective TiO₂ based treatment strategies.

2.1.3. Semiconductor Nanoparticles - Quantum Dots (QDs)

2.1.3. A) Properties of QDs

Colloidal semiconductor NPs or quantum dots (QD) are single crystals of semiconducting material having diameters in the nanometer scale. QDs were discovered in the early 1980s by Ekimov^[191] in a glass matrix and by Brus in colloidal solutions.^[192] The term "quantum dot" was later coined by Mark Reed.^[193] Morphology (size and shape) of QDs is precisely controlled by the duration of their synthesis as well as by the temperature and ligand molecules used^[194] and they have composition- and size-dependent absorption and emission (Figure 11 A and Figure 12). In addition, an electron-hole pair (or exciton) is formed when a photon with sufficient energy ($E_{\text{photon}} > E_{\text{band gap}}$) gets absorbed. This occurs with increased probability at higher energies (*i.e.* shorter wavelengths) and results in a broadband absorption spectrum as seen in Figure 11 A and B which is in sharp contrast to standard fluorophores, whose absorption energies have very narrow spectral range.^[195]

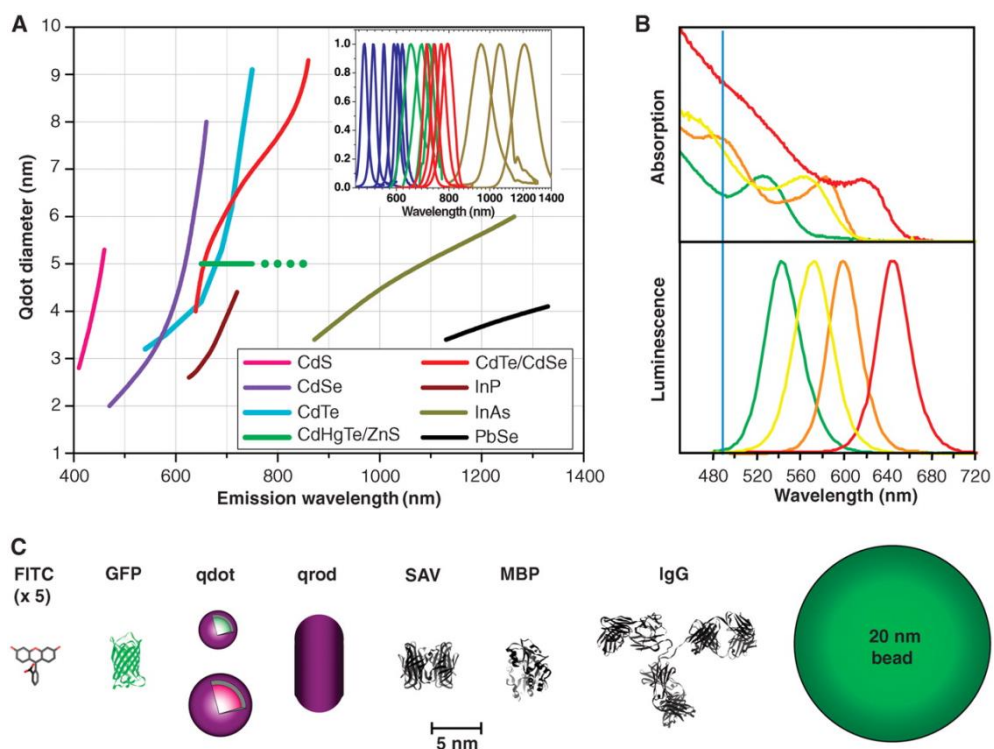


Figure 11. (A) Emission maxima and sizes of quantum dots of different composition. (B) Absorption (upper) and emission (lower) spectra of four CdSe/ZnS QDs samples. The blue vertical line indicates the 488-nm line of an argon-ion laser, which can be used to efficiently excite all four types of QDs simultaneously. (C) Size comparison of QDs and other nano objects.^[196] Adapted from Ref 196. with permission.

For nanocrystals smaller than the Bohr exciton radius (a few nanometers), energy levels are quantized, with values directly related to the QD size (quantum confinement).^[194] The radiative recombination of an exciton (characterized by a long lifetime, >10 ns)^[197] leads to the emission of a photon in a narrow, symmetric energy band (Fig. 11B) and makes another difference from the red-tailed emission spectra and short lifetimes of most fluorophores. The long fluorescence lifetime of QDs enables the use of time-gated detection to separate their signal from that of shorter lived species (*e.g.* background auto-fluorescence encountered in cells).^[198]

Surface defects prevent the exciton radiative recombination by acting as the temporary electron or hole “traps” in the crystal structure. The interchange between trapping and un-trapping events leads to irregular fluorescence (blinking), also visible at the single-molecule level.^[199] However, another consequence of this interchange is the reduced overall quantum yield (the ratio of emitted to absorbed photons). An efficient way of overcoming these problems, with a benefit of protecting surface atoms from oxidation and other chemical reactions, is to cap the QDs. Basically, the capping means growing a few atomic layers-thick shell of a material with a larger band gap on top of the bare nanocrystal core. This shell can be designed carefully to obtain quantum yields close to 90% and^[200] this step also enhances QD’s photostability by several orders of magnitude relative to conventional dyes.^[201]



Figure 12. Ten distinguishable emission colors of ZnS-capped CdSe QDs excited with a near-UV lamp. From left to right (blue to red), the emission maxima are located at 443, 473, 481, 500, 518, 543, 565, 587, 610, and 655 nm. (Figure adapted from Ref. 202 with permission.)^[202]

2.1.3. B) Methods of QD Preparation

There are several ways to confine excitons in semiconductors, resulting in different methods to produce QDs. Colloidal semiconductor nanocrystals are synthesized from precursor compounds dissolved in solutions in a manner very similar to already described chemical processes. Synthesis of

colloidal QDs usually involves three components including precursors, organic surfactants, and solvents.

The important milestone in synthesis of high-quality colloidal QDs came with the of high-temperature growth solvents/ligands (mixture of trioctyl phosphine/trioctyl phosphine oxide, TOP/TOPO), combined with pyrolysis of organometallic precursors, which yielded CdSe QDs with highly crystalline cores and size distributions of 8–11%.^[203] The same reaction combined with appropriate organometallic precursors was further used to overcoat the native CdSe core with a layer of wider-band gap semiconducting material (for example, ZnS and CdS).^[204] Fine-tuning this synthetic scheme highlighted the importance of the high-temperature solvent/ligand mixtures, along with using less pyrophoric salt precursors (CdO and Cd-acetate), for preparing reproducible high-quality nanocrystals.^[200, 205] QDs prepared using high-temperature routes are hydrophobic, thus phase-transfer to aqueous solution requires surface functionalization with hydrophilic ligands, either through 'cap exchange' or by encapsulating the original nanocrystals in a thick hetero-functional organic coating. These hydrophilic ligands mediate both the solubility of the QDs and serve as a point for further biofunctionalization (attachment of biomolecules).

There are many other colloidal methods to produce different semiconductors in nanoparticulate form. Typical QDs are made of binary alloys such as cadmium selenide (CdSe), cadmium sulfide (CdS), indium arsenide (InAs), and indium phosphide (InP) but may also be made from ternary alloys such as cadmium selenide sulfide (CdSeS). These QDs can contain as few as 100 to 100,000 atoms, with a diameter of 10 to 50 atoms. As QDs are mostly synthesized in nonpolar organic solvents, their hydrophobic surface ligands must be replaced by amphiphilic ones if the water solubility is required.^[3] Cadmium (Cd) and other heavy metals used in conventional QDs are a major concern for commercial applications of QD due to the possible leaking of the toxic material^[206] and efforts are made to stabilize QDs or prepare different types of more bio-friendly QD based on silica.^[206-207]

2.1.3. C) Biomedical Applications of QDs

QDs share the possible biomedical applications with other mentioned NP types including cell labeling and imaging as well as novel strategies to fight cancer on the molecular level.^[195] Many researches are focusing on imaging applications in single cell microscopy, tracking of individual cells, *e.g.*, metastasis, and whole animal imaging, as well as tackling the issue of targeting QDs to particular cellular structures, cells, and tissues.^[208]

Giraud *et al.* demonstrated the use of QDs labeling combined with fluorescence lifetime imaging microscopy (FLIM) for the detection of DNA hybridization events on DNA microarrays.^[209] The combination of the relatively long lifetime of QDs with a FLIM imager (combining evanescent wave excitation with wide field detection and a quadrant anode mounted on an inverted microscope) was used to increase the contrast ratio of DNA microarrays by a factor of two.

Ibáñez-Peral *et al.* investigate QDs as suitable multicolor optical labels of specific nucleotide probes for microbial identification using flow cytometry (FCM).^[210] Since individual QDs fluoresce and scatter below the resolution of the FCM, the authors conjugated QDs to paramagnetic beads (Dyna-beads). They found that the minimum fluorophore-concentration necessary for detection of QDs, (above the autofluorescent background) was 100-fold less than for the commonly used fluorophore (FITC), even under conditions of suboptimal excitation. Furthermore, their research also showed that QD-bead interaction noticeably influences their optical properties requiring further study of the system as well as QD for FCM applications in general.

Recently, Haro-González *et al.* investigated laser-induced thermal effects in optically trapped microspheres and single cells by QD-luminescence thermometry.^[211] Thermal spectroscopy has revealed a non-localized temperature distribution around the trap that extends over tens of micrometers, in agreement with previous theoretical models besides identifying water absorption as the most important heating source. The experimental results of thermal loading at a variety of wavelengths revealed an optimum trapping wavelength of around 820 nm for biological applications, producing minimum intracellular heating that is well below the cytotoxic level (43 °C), thus avoiding cell damage. Results included in this work reveal CdSe-QDs as versatile, efficient and accurate nano-thermometers for real time temperature monitoring of the local environment surrounding optically trapped micro-sized objects and single living cells.

In order to circumvent the limitations of tissue-penetrating properties of external light source, Hsu *et al.* coupled light-emitting protein Renilla luciferase to QDs (QD-RLuc8) for bioluminescence resonance energy transfer (BRET)-mediated PDT.^[212] When the conjugates are exposed to the luciferase's substrate coelenterazine, the energy released by substrate catabolism is transferred to the QDs through BRET, leading to QD light emission. This in turn activates the photosensitizer, meta-tetra-hydroxyphenyl-chlorin(m-THPC, Foscan®)-loaded micelles for PDT. The BRET-mediated PDT by QD-RLuc8 plus coelenterazine (20 µg/mL) successfully generated ROS (40.8%) and killed ~ 50% A549 cells at 2 µg/mL equivalent Foscan® *in vitro*. Significantly delayed tumor growth was shown *in vivo*, due to cell apoptosis under terminal deoxynucleotidyl transferase dUTP nick end-labeling assay (TUNEL) analysis without obvious weight loss.

Based on immune-histochemical observations, the proliferating cell nuclear antigen (PCNA)-negative area of tumor sections after BRET-mediated PDT was obviously increased compared to the PDT-untreated groups without an external light source. This QD-based PDT was shown to possess several clinical benefits, such as overcoming light penetration issues and treating deeper lesions that are intractable by PDT alone.

An interesting study was done by Nienhaus and coworkers in which they investigated the cellular uptake of small (diameter 4 nm) D-penicillamine coated QDs (DPA-QDs) by HeLa cells.^[213] They found that in contrast to larger NPs, small DPA-QDs accumulate at the plasma membrane prior to internalization with the uptake efficiency scaled nonlinearly with the NP concentration. They have also shown that a critical threshold density of QDs on the surface has to be exceeded for triggering their internalization. By using specific inhibitors (*e.g.* dynasore which acts as a specific inhibitor of endocytic pathways depended on the protein dynamin including clathrin- and caveolin-mediated endocytosis), they showed that DPA-QDs were predominantly internalized by clathrin-mediated endocytosis and to a smaller extent by macropinocytosis. Clusters of DPA-QDs were found in endosomes, which were actively transported along microtubules toward the perinuclear region. This work helped shedding more light on the interaction mechanism of QDs with living organisms, which is a prerequisite for the safe use of nanomaterials, enhancing potential benefits while limiting the associated health hazards.

2.2. Hybrid Nanomaterials

2.2. A) Properties of hybrid nanomaterials

In the past few decades, nanotechnology has gone from the basic research, where the challenge lied in devising the synthetic methods to control the morphology (size and shape) of the various nanomaterials, to the present, more practical stage of devising strategies where the well characterized building blocks are used to design more complex systems. Preparation of hybrid nanomaterials, containing two or more different nanostructures, creates further possibilities to enhance existing or tailored new properties. Actually, coating nanomaterials with stabilizing ligand, to prevent aggregation, make them water soluble or red-shift the excitation wavelength represents the simplest form of the hybrid structure. Such hybrids possess inherent characteristics of bare nanomaterial and ligand but synergistically introduce new properties such as changing the band gap

energy as in the case of ligand binding to TiO_2 .^[214] More complex systems are formed by addition of two or more nanostructured materials brought together through different synthetic methods.^[14b, 215]

Earliest examples of such systems are metal- semiconductor nanocomposites, obtained through growth of metal islands (*e.g.* Au, Ag, Cu or Pt NPs) on semiconductor NPs (*e.g.* ZnO or TiO_2).^[157, 216] In these early examples there was limited control over the architecture of the hybrid materials (semiconductor NPs shape and size and the metal NPs size and location) and mostly polydisperse suspensions were obtained. Further synthetic efforts aimed for a higher degree of control over the size and shape of the materials. For example, the selective growth of Au metal tips at the edges of CdSe semiconductor NRs was achieved *via* a simple solution reaction.^[217] Such Au tips provide anchor points that enable electrical connections and facilitate self-assembly of the semiconductor component. In addition the light induced charge separation at the nanoscale metal-semiconductor junction opened a possibility of various photocatalytic applications.^[14b, 218]

In general, attached metal NPs can be considered as a near-field source of electromagnetic (EM) radiation,^[219] whose resonant near-field penetrates into the semiconductor NP and rapidly decays near the metallic surface of NPs, providing a strong field gradient across the semiconductor NP.

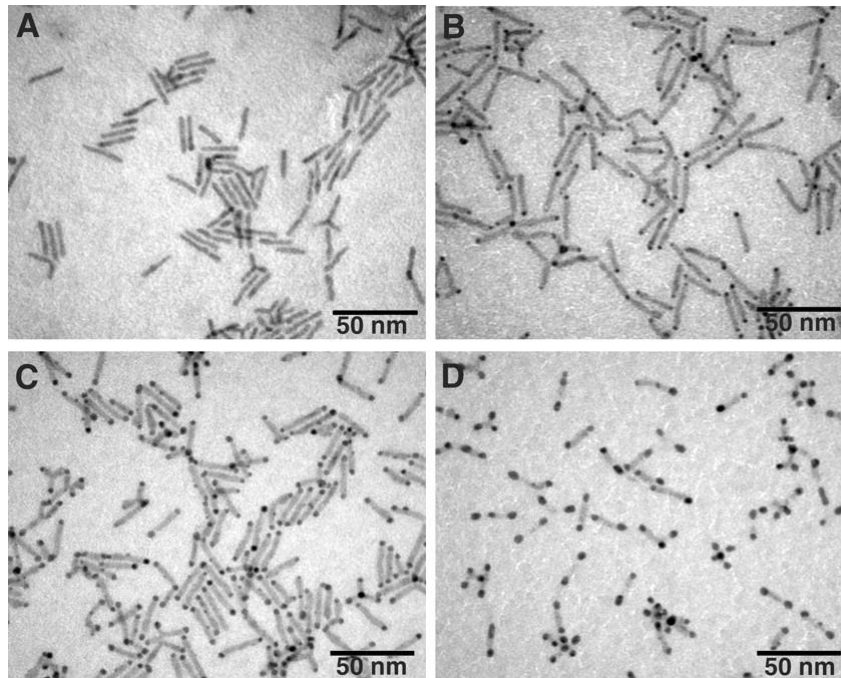


Figure 13. TEM images showing controlled growth of Au onto the tips of CdSe quantum rods. (A) Original rod sample, 29×4 nm. (B to D) Rod samples with Au NP head sizes of 2.2, 2.4 and 4 nm respectively. Adapted from Ref 217a with permission.^[217a]

Jain *et al.* presented atomistic simulations of oscillator strengths of individual transitions in matchstick-like CdSe–Au and CdS–Au NRs. A gradient resonant electric field propagates along the NR long-axis and allows quadrupole induced transitions and even higher multipolar order transitions, which are forbidden under far-field selection rules.^[220]

Another interesting example of the metal-semiconductor hybrid materials is a combination of noble metals and TiO₂, as in a case of widely studied Au/TiO₂ nanocomposites.^[16, 215a, 221] A number of studies have shown that Au NPs enable size dependent storage of electrons, with a possibility of their later release to the suitable acceptors.^[222] When coupled to nanoparticulate semiconducting TiO₂ materials, Au NPs can facilitate the shuttling of the photoexcited conduction band electrons to the species in the solution and so improve the photocatalytic performance as the charge carriers escape the recombination and can be involved in other processes at the nanomaterial interface.^[223] Recently, it has been reported that electron transfer from Au NPs to TiO₂ can also occur under visible light irradiation tuned to the surface plasmon resonance wavelength.^[222c, 224] In general, Au NPs have been particularly interesting for the photocatalytic nanocomposite preparation due to their stability, ease of preparation and remarkable electronic and optical properties.^[16] Valden *et al.* investigated the particle size effect on the catalytic activity of Au NPs supported on TiO₂ surface and found out that the maximum activity enhancement was achieved for Au NPs around 5 nm or smaller, which was later confirmed by other researchers.^[225] Kowalska *et al.* reported that particle sizes of both TiO₂ and Au are the key factors in controlling the level of photocatalytic activity.^[226] Many other noble metals were attached on the TiO₂ surfaces, including Ag,^[227] Pt,^[228] Cu^[229] and Pd.^[230]

Further on, various types of hybrid carbon-based nanostructures have been reported including metal-carbon nanotube (CNT),^[231] polymer-CNT^[232] and metal-graphene.^[233] For example, Zedan and coworkers reported the enhanced photothermal energy conversion by Au NPs of well-defined size and shape dispersed in graphene oxide (GO) solutions.^[233a] They demonstrated that the enhanced photothermal energy conversion by the Au–GO aqueous solutions can be tuned by controlling the shape of the Au nanostructures from spherical particles to short and long NRs. In addition, they also reported the synthesis of ultra-small Au NPs with diameters of 2–4 nm well-dispersed on the laser converted graphene nanosheets. They showed that the coupling of the laser-induced size reduction of the Au NPs with the laser conversion of graphene oxide into graphene (LCG) provides a novel method for the synthesis of ultra-small Au NPs from much larger particles with different sizes and shapes. These ultra-small Au–graphene nanocomposites could find application as novel photothermal energy convertor for a variety of thermochemical and thermo-mechanical

applications, in addition to photothermal therapy, such as heating and evaporation of liquids by solar energy, ignition of solid fuels, and welding of composite materials.

Finally, another important nanocomposite are the metal-polymer nanostructures made with two distinct synthetic approaches. The first consists of usage of polymers to stabilize NPs and results in nanoparticulate material,^[234] while the second one uses polymer matrices to embed them with NPs,^[235] resulting in membrane-like materials or 3-D structures. A polymer that is most often used for physiological stabilization of various NPs is poly(ethylene glycol) (PEG) as such nanocomposite circumvent some of the challenges encountered in nanomedical applications of nanomaterials. These include uptake by the reticulo-endothelial system (RES), in which NPs are rapidly shuttled out of circulation to the liver, spleen or bone marrow, and nonspecific binding of NPs to non-targeted or non-diseased areas.^[236] In both drug-delivery and imaging applications, the addition of PEG to NPs reduces RES uptake and increases circulation time versus uncoated counterparts^[237]. Aggregation decreases owing to passivized surfaces, and association with non-targeted serum and tissue proteins is diminished, resulting in so-called 'stealth' behavior. The PEG chains reduce the charge-based contact typical of proteins and small-molecule interactions. Solubility in buffer and serum increases due to the hydrophilic ethylene glycol repeats and the enhanced permeability and retention (EPR) effect is modulated due to NP size changes *via* addition of a PEG coat.^[238] Due to these attributes, PEGylated NPs generally accumulate in the liver a half to a third of the amount of non-PEGylated NPs and demonstrate higher tumor accumulation versus background.^[239] PEG is inexpensive, versatile and FDA approved for many applications.^[236]

As demonstrated, the number of hybrid nanomaterials is large and constantly growing. In this thesis we have worked typically with the metal-semiconductor nanocomposite materials and hence the following chapters on synthesis and biological applications are mostly dealing with such structures.

2.2. B) Preparation methods

Several main growth mechanisms have been used in synthesis of hybrid NPs, addressing the inherent challenge of combining often two intrinsically different materials within one nanocomposite platform in a controlled manner. The parameters that should be brought into consideration during the synthesis include the lattice constant mismatch and different crystal structures, the presence of polar facets, the interfacial energy among the materials, the materials miscibility, the presence of surface defects and the surface accessibility/reactivity.^[240]

One of the most widely used synthetic protocols for metal-semiconductor nanocomposites is the photoreduction of the metal salt precursors on the surface of the semiconductor NPs. This method is based on already discussed property of semiconductor NPs to produce electron-hole pairs upon appropriate light irradiation. The photo-excited electrons migrate to the surface of the semiconductor NP and reduce the metal ions present in the solution thus forming metallic island-seeds onto which further material can be deposited. Such procedure has successfully been used to prepare metallic-semiconductor hybrid nanomaterials including Ag/TiO₂,^[15, 241] Au/TiO₂,^[221b, 241] Pt/TiO₂,^[221a] Au/ZnO,^[242] and Ag/ ZnO.^[215b]

Another widely used approach is the self-assembly of NPs, in which the building blocks spontaneously organize into ordered structures taking advantage of the thermodynamic and spatial constraints.^[4] Nevertheless, in order to use the self-assembly of NPs in technological applications and to ensure efficient scale-up, it is necessary to impose a high level of directional control. Chemically, this means using external stimuli such as temperature, light, pH or solvent polarity, to control the molecular interactions at the colloidal interfaces.^[4] These stimuli induce a spatial distribution of the NPs, either through a direct intermolecular interaction between surface ligands or on the top of additional templates *such as* small molecules,^[243] linear polymers,^[244] biomolecules,^[245] and copolymers^[246].

Among other successful hybrid NPs synthesis routes, facet selective growth exploits the well-defined crystal structure of the semiconductor component to provide preferential nucleation and growth sites for the metal component.^[217a, 247] Furthermore, the absorption of the semiconductor component can be used for light induced growth of the metal component. A great example of light induced synthesis is the photodeposition of noble metal NPs on semiconductor surfaces (*e.g.* TiO₂ or ZnO), where the photoexcited electrons migrate to the surface of the semiconductor NPs and there reduce the noble metal ions.^[216, 248]

New hybrid NP morphologies resembling core/shell architectures were also obtained by allowing a diffusion of the metal components into the semiconductor^[249] or doping of semiconductor nanocrystals *via* a facile solution reaction.^[250]

The advanced strategies developed for growth of metal NPs is now allowing control of the morphology of the metal component in hybrid NPs.^[215a, 251] More complex hybrid NP architectures are being developed, with two different metallic components grown onto the semiconductor segment. For example, Tanaka and coworkers prepared such new type of photocatalyst by combining Pt and Au on WO₃, in which Pt NPs were loaded on Au NPs. To achieve the Pt-on-Au structure, Au particles were first loaded on WO₃ by using colloid photo-deposition method,^[252] and then Pt

particles were loaded on Au particles by using photo-deposition. The Pt/Au/WO₃ sample was used for formation of H₂ and O₂ under visible light irradiation in the presence of sacrificial reagents such as biomass under mediator-free conditions.^[253] Another development is the discovery of additional growth modes, specifically edge selective growth, which allowed for the synthesis of hybrid nanoscale inorganic cages. In the work by Oh *et al.* the manganese oxide (Mn₃O₄) nanocrystals were reacted with iron (II) perchlorate to produce hollow box-shaped nanocrystals of Mn₃O₄/γ-Fe₂O₃ (“nanoboxes”). These nanoboxes ultimately transformed into hollow cage-like nanocrystals of γ-Fe₂O₃ (“nanocages”). Because of their non-equilibrium compositions and hollow structures, these nanoboxes and nanocages exhibited good performance as anode materials for lithium ion batteries. The generality of this approach was demonstrated with other metal pairs, including Co₃O₄/SnO₂ and Mn₃O₄/SnO₂.^[254]

Many of the previously successful hybrid NP synthetic methods together with the resulting properties are discussed in several excellent review papers.^[14a, 215c, 240c]

2.2. C) Biomedical Applications

Due to the multifunctionality of nanocomposite materials, such structures are widely used in the field of theranostics (for definition see chapter 2.1.1.2. C). For example, Cheng *et al.* presented a new type of multifunctional NPs (MFNPs) based on up-conversion NPs (UCNPs) with combined optical and magnetic properties useful in multimodality imaging.^[255] The MFNPs were prepared by layer-by-layer (LBL) self-assembly. Ultrasmall superparamagnetic iron-oxide (Fe₃O₄) NPs (IONPs) are electrostatically adsorbed on the surface of a NaYF₄-based UCNP thus forming a UCNP–IONP nanocomplex, which is topped with a thin Au shell by seed-induced reduction growth. The layer of IONPs between UCNPs and the Au shell not only affords MFNPs magnetic properties but also strongly reduces the luminescence quenching effects of the Au shell to UCNPs. The UCNP–IONP–Au MFNPs are additionally coated with PEG to impart stability in physiological solutions used for *in vitro* targeted UCL, MR, and dark-field light scattering imaging. The SPR absorption contributed by the Au shell in MFNPs is used in dual-targeted photothermal ablation of cancer cells proving that such composite MFNPs are excellent candidate for applications in the multimodality biomedical imaging and therapy.

The use of multifunctional hybrid NPs as drug delivery systems for anticancer therapeutics has great potential for future targeted cancer therapy. A new drug delivery platform comprising of a magnetic core and biodegradable thermoresponsive shell of tri-block-copolymer was reported by

Andhariya *et al.*^[256] Oleic acid-coated Fe₃O₄ NPs and hydrophilic anticancer drug “doxorubicin” were encapsulated with PEO–PLGA–PEO (polyethylene oxide-poly D, L lactide-co-glycolide-polyethylene oxide) tri-block-copolymer. The hydrodynamic size of composite NPs was found to be 36.4 nm at 25 °C. The loading efficiency of drug was shown to be 89% with a rapid release for the initial 7 h, followed by the sustained release over a period of 36 h. The release of drug is envisaged to occur in response to the physiological temperature by de-swelling of thermoresponsive PEO–PLGA–PEO block-copolymer. This study demonstrated that temperature can be exploited successfully as an external parameter to control the release of drug, while the magnetic properties of the hybrid can be used for the targeted delivery.

A slightly different system was developed by Campardelli and coworkers.^[257] They produced stimuli-responsive drug delivery systems by encapsulating near-infrared (NIR) sensitive hollow Au nanoshells (Au NSs) together with the molecule to be released into biodegradable poly-lactic acid (PLA) sub-micron particles. The Au NSs (32 nm diameter, 4.5 nm shell thickness) were synthesized via galvanic replacement of cobalt NPs, using PVP as a stabilizer. The rapid heating of the PLA particles caused by NIR radiation enabled use of the PLA–Au NSs composites as a photo-triggered drug release system. Rhodamine was used as a test molecule to obtain release profiles under different irradiation conditions. They tuned the release by controlling the intensity of NIR exposition with complete release in less than 10 hours when applying intense NIR irradiation for a few minutes and 12 days of release when system is left undisturbed.

As a final example, Zhu *et al.* developed a multifunctional pH-sensitive superparamagnetic iron-oxide (SPIO) nanocomposite system for simultaneous tumor magnetic resonance imaging (MRI) and therapy.^[258] Small-size SPIO NPs were chemically bonded with antitumor drug doxorubicin (DOX) and biocompatible PEG through pH-sensitive acylhydrazone linkages, resulting in the formation of SPIO nanocomposites with magnetic targeting and pH-sensitive properties. The DOX-conjugated SPIO nanocomposites exhibited not only good stability in aqueous solution but also high saturation magnetizations. Under an acidic environment, the DOX was quickly released from the SPIO nanocomposites due to the cleavage of pH-sensitive acylhydrazone linkages. With the help of magnetic field, the DOX-conjugated SPIO nanocomposites showed high cellular uptake, indicating their magnetic targeting property.

An overview of further biomedical uses of nanocomposites is reviewed in many recent papers.^[12b, 133d, 259]

2.3. Nanoparticle Functionalization

Prerequisite for the application of the engineered NPs, in particular for biomedical uses, regardless of their type, is their proper surface functionalization, which controls the NP interaction with its environment. These interactions ultimately affect the colloidal stability and function of the NPs. The ligand molecules bound to the NP surface also control the growth and prevent the aggregation of the NPs. Depending on the NP material and a solvent in which it is dispersed, the choice of the appropriate ligand ultimately leads to its long-term stability and additional binding properties.

The surfactants are bound to NP surface by different mechanism including chemisorption, electrostatic attraction or hydrophobic interaction often provided by a head group of the ligand.^[3] Some chemical groups have been shown to possess strong affinity to inorganic surfaces (*e.g.* thiol to Au^[260] or hydroxyl to TiO₂)^[214], which is often exploited during synthesis and functionalization of NPs.

It should be noted that the interacting bonds between the inorganic NP surface and, *e.g.* an electron-donating end group of a surfactant, such as thiol,^[261] amine or phosphine,^[262] undergo dynamic and reversible binding,^[263] which might result in detachment of the surfactants (by excessive washing or mass action by another surfactant), which can further compromise the stability of the NPs leading to aggregation and precipitation. Therefore careful design strategies are needed to choose the proper binding ligand and this is largely depending on the subsequent application.

In aqueous solutions, which are required for biological/biomedical applications, hydrophilic NPs are stabilized by electrostatic repulsion between equally charged surfactants. However, in the presence of high salt concentrations, the electric field is shielded, which might cause the agglomeration (*via* van der Waals force or hydrogen bonds between the particles).^[264]

In general, in aqueous solutions, strongly charged surfactants (*e.g.* containing carboxylic or sulphonic acid groups), are found to be better NP stabilizers. Furthermore, surfactants offering steric stabilization, such as PEG, are more resistant to high salt concentrations than the ones that provide electrostatic repulsion, provided they are strongly bound to the NP surface.^[265] Finally, further stabilization can also be provided by surfactants having multiple anchoring heads such as polythiols or catechols.^[43, 266]

One of the most commonly used methods of introducing additional functional groups to the NP is a post-synthetic process referred to as ligand exchange. For example, citrate coated Au NP

prepared by Turkevich method are often additionally modified by exchange with the ligand possessing higher affinity to the NP surface, often containing thiol such as mercaptoacetic acid (MAA), mercaptopropionic acid (MPA) or mercaptoundecanoic acid (MUA) or any other thiol based surfactant.^[261b] Thiol functionality is considered to show the highest affinity to noble metal surfaces, particularly to Au.^[260] In spite this binding being often presented as chemisorption (sometimes also noted as covalent bond), the exact processes that occur and the microscopic nature of the bond are still not fully understood and are subject to research and discussion.^[267]

When high concentrations of Au particle solution are needed, NPs can first be modified with phosphines through salt-induced aggregation and redispersion in low-salt buffers^[268] following the ligand exchange with thiol-containing surfactants. This strategy is often used in the modification of Au NPs with DNA molecules leading to densely covered, highly concentrated solution of DNA-Au NP conjugates.^[269]

Ligand exchange can be used to introduce various functional groups but also biomolecules such as DNA, peptide or proteins to the surface of different NPs.^[270]

In a case of noble metal NPs such as Au NP, ligands contribute to the stabilization of the NPs and server to introduce additional functional groups for further attachment of *i.e.* biomolecules. But in the case of semiconducting materials such as TiO₂, ligands also affect the properties of the nanomaterial itself *i.e.* by shifting the band gap and therefore affecting the light activation energy needed to induce the photocatalytic activity.^[214] Due to their position, surface Ti atoms are only partially coordinated, thus presenting trapping sites for the photoexcited electrons, who in turn cannot take part in the reduction processes on the surface.^[271] Replacement of the solvent molecules (which poorly coordinate the surface Ti atoms) with strongly coordinating surfactants, shifts the energetic levels of such surface states above the conducting band energies. In this way, trap sites are removed and photoexcited electrons are free to participate in reduction processes, hence increasing the photocatalytic activity of TiO₂ NPs. Moreover, such surfactants build an inner sphere ligand-to-metal charge-transfer (LMCT) complex with the surface Ti atoms, which is capable of providing conduction band of the TiO₂ with injected electrons excited by low-energy photons (visible light). This strategy is used to overcome one of the major disadvantages of TiO₂ material, namely its wide band gap.

As already mentioned, the hydroxyl (-OH) functionality has strong affinity towards metal-oxide surfaces,^[272] which makes it attractive for the functionalization of TiO₂ nanoparticulate materials. Moreover, enediol functionalities (two OH groups) bind even stronger to TiO₂ surfaces by bridging the neighboring Ti atoms and thus leading to restoration of six-coordinated octahedral

geometry of surface Ti atoms as presented in Figure 13 (as well as single hydroxyl group). Functionalization of nanoparticulate TiO_2 of various sizes and the effect that it has on the optical and photocatalytic properties of TiO_2 NPs has been a topic of intense research in the past two decades.^[271, 273] It resulted in better understanding of the LMCT mechanism, in turn leading to more efficient and less energetically demanding TiO_2 photocatalysts (e.g. DSSC).

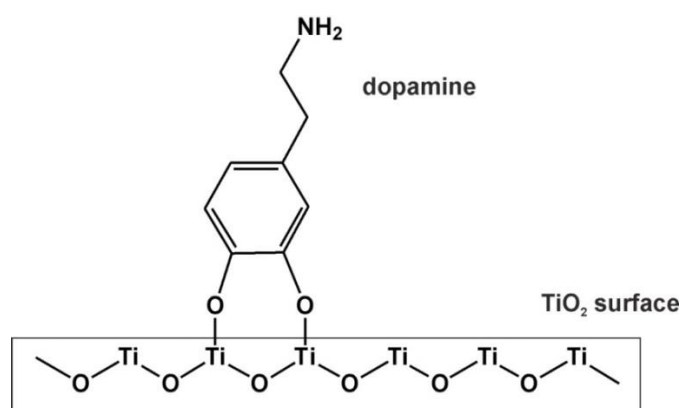


Figure 13. Bridging of the two surface Ti atoms with the enediol (dopamine) surfactant.

Enediols, such as different dopamine derivatives, were recently used also for stabilization and further functionalization of other oxide NP besides TiO_2 ,^[274] and it could be envisaged that increasing the library of catechol ligands will open a new avenue for the NP modification.

The use of engineered ligands for conjugating proteins to NPs has been much more successful in retaining protein structure and function (Figure 14). This type of attachment has traditionally been accomplished using standard amine-carboxylate coupling methods.^[279] More recently, the alkyne-azide Huisgen “click” reaction has been used to attach proteins to NPs, where in the presence of a catalyst, reactions can proceed with high yield and can also allow the site-specific conjugation of the azide or alkyne tagged proteins to the NP partners.^[280] This approach has been successful in binding a variety of proteins including lipase,^[281] horseradish peroxidase,^[282] and luciferase.^[283]

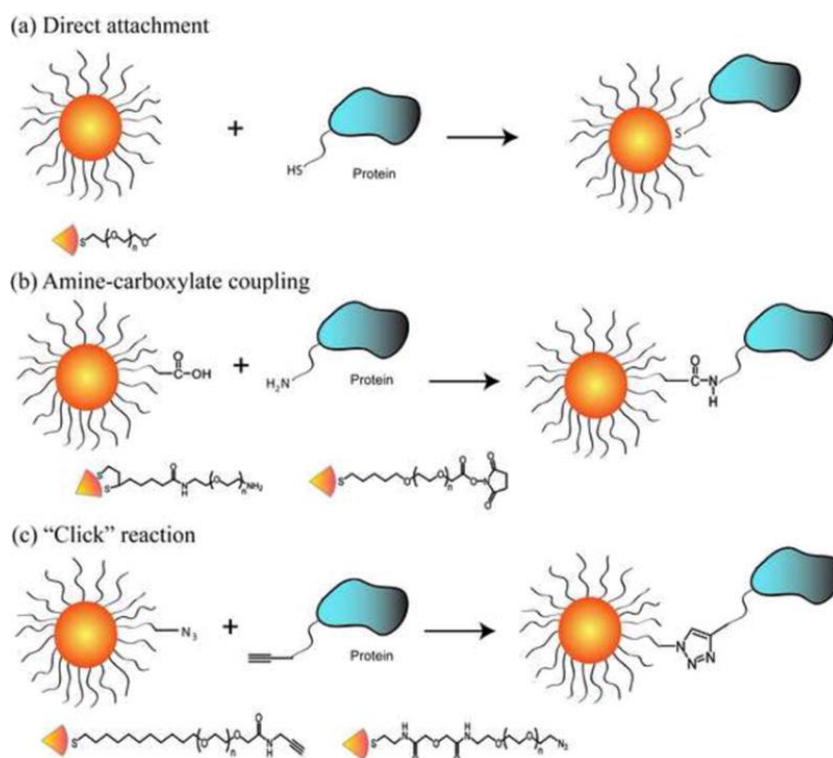


Figure 14. NP-protein complexation through covalent conjugation (a) The direct attachment of proteins to NPs using a thiol group on the protein surface. (b) Amine-carboxylate coupling using carboxylate-presenting NPs and amine groups on protein surface. (c) "Click" reaction using azide tagged NP and alkyne tagged protein. Representative ligands used to modify the NP surface are presented under each strategy. Adopted from Ref 278 with permission.^[278]

On the other hand, non-covalent conjugation of proteins to NPs provides an additional strategy to prepare NP-protein conjugates, in particular when proteins do not allow the use of chemical methods, which could cause the loss of activity.^[284] To overcome the short-comings of the non-covalent approach, the surface of NPs has been tailored (varying *e.g.* charge or hydrophobicity), to allow for region-specific interactions.^[285] Metal-mediated interactions provide a useful alternative that imparts selectivity to the NP-protein conjugation process. An often used strategy is through nickel-mediated interactions with His-tagged proteins,^[286] providing an effective control of NP-protein stoichiometry.^[287] An example of His-tag binding is given in the work by Medintz and coworkers,^[288] where they used the affinity of hexa-His peptides to directly conjugate fluorescent proteins to QD surfaces to create caspase sensors (Figure 15). In this system the His-tag and the peptide linker were long enough to minimize the denaturation observed above with cysteine-based immobilization.

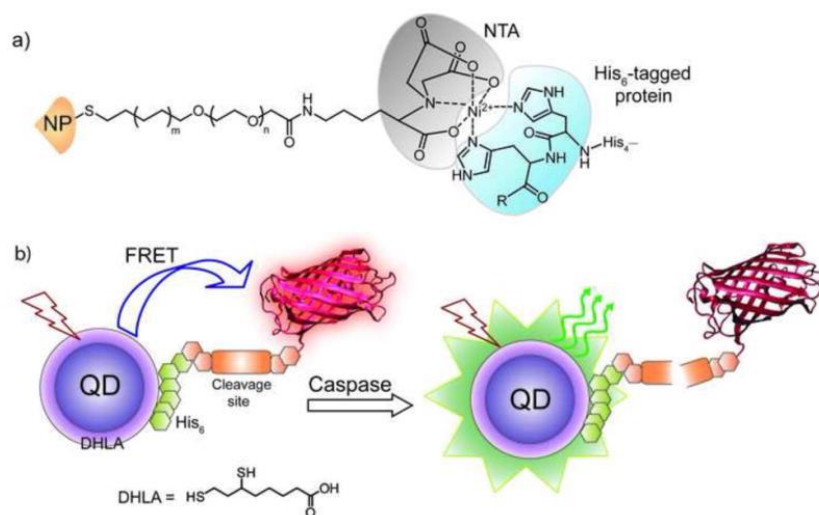


Figure 15. Metal-mediated non-covalent conjugation and its application (a) Depiction of metal-mediated high affinity conjugation of hexa-His tagged protein to nitrilotriacetic acid (NTA) functionalized NP. (b) Schematic of the QD-fluorescent protein sensor constructed through non-covalent conjugation between DHLA coated QD and mCherry protein with an N-terminal linker expressing the caspase 3 cleavage site and a His₆ sequence. The specific cleavage of the linker by caspase 3 removes FRET to enable protein sensing. Adopted from Ref 278 with permission.^[278]

This chapter is by no means comprehensive as many other methods for NP functionalization exist and many more are developed on a daily basis. Some excellent recent reviews on the subject are available.^[3, 278]

3. Goals/Aims

The main aim of presented thesis was to design hybrid TiO₂ materials with enhanced photocatalytic activity. To achieve that, a library of catechol containing bi-functional linkers was explored, to investigate the effect of the linker onto the photocatalytic activity of TiO₂. In such study, it is particularly important to investigate which (if any) ligands might have negative effects on TiO₂, such as induced agglomeration or ROS scavenging.

Bi-functional catechol containing linker was then prepared to allow binding of various noble metal (Au and Ag) and semiconductor NPs (CdS) to the surface of TiO₂ NPs in order to prepare hybrid nanocomposite with enhanced photocatalytic activity. Finally the photocatalytic activity of both TiO₂ and TiO₂ hybrid materials were investigated *in vivo* using different types of plant (tobacco, BY-2) and mammalian cells (HeLa, MCF7 and HEK293).

4. Results and Discussion

4.1. Lipoic Acid – Dopamine Bifunctional Linker (LA-DA)

In the following chapters, the synthesis of the N-[2-(3,4-Dihydroxyphenyl)ethyl]-5-[(3R)-1,2-dithiolan-3-yl]pentanamide (bi-functional Lipoic acid – Dopamine (LA-DA) linker) will be treated in more details. In addition, the account of characterization of the LA-DA linker will be given.

4.1.1. Synthesis of LA-DA Linker

Coupling of lipoic acid to dopamine hydrochloride was performed according to the literature procedure.^[289]

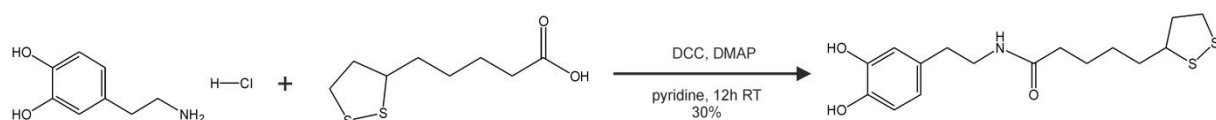


Figure 16. Synthetic Scheme for LA-DA linker.

In short, Dicyclohexylcarbodiimide was added to a solution of dopamine hydrochloride, DMAP, and (*R*)-lipoic acid in dry pyridine. The reaction mixture was stirred for 12 h at room temperature under anhydrous conditions. After evaporation under vacuum, the crude product was purified by column chromatography with CH₂Cl₂/CH₃OH solvent mixture in ratio 19:1. The yield of this procedure was 30%. The synthetic scheme is presented in Figure 16.

4.1.2. Characterization of LA-DA Linker

The final product was characterized by nuclear magnetic resonance (NMR) spectroscopy.

4.2. Nanoparticles Synthesis and Characterization

In the following chapters two different methods for synthesis of Au NPs will be treated in detail. The methods are based on the *Turkevich* method and its modifications. Furthermore, the results of the characterization of the as-synthesized NPs are presented and explained.

4.2.1. Citrate Au NPs

Citrate capped NPs were synthesized following the well-known *Turkevich* method.^[34] Prior to the synthesis, the glassware was thoroughly washed with 3:1 mixture of hydrochloric (HCl) and nitric acid (HNO₃) commonly known as *aqua regia* and rinsed with water until no trace of HCl could be smelled. Aqueous solution of HAuCl₄ was brought to boiling when sodium citrate was rapidly added. Shortly upon citrate addition, the solution rapidly changed color from pale yellow to black indicating the formation of dense network of Au nanowires as intermediates.

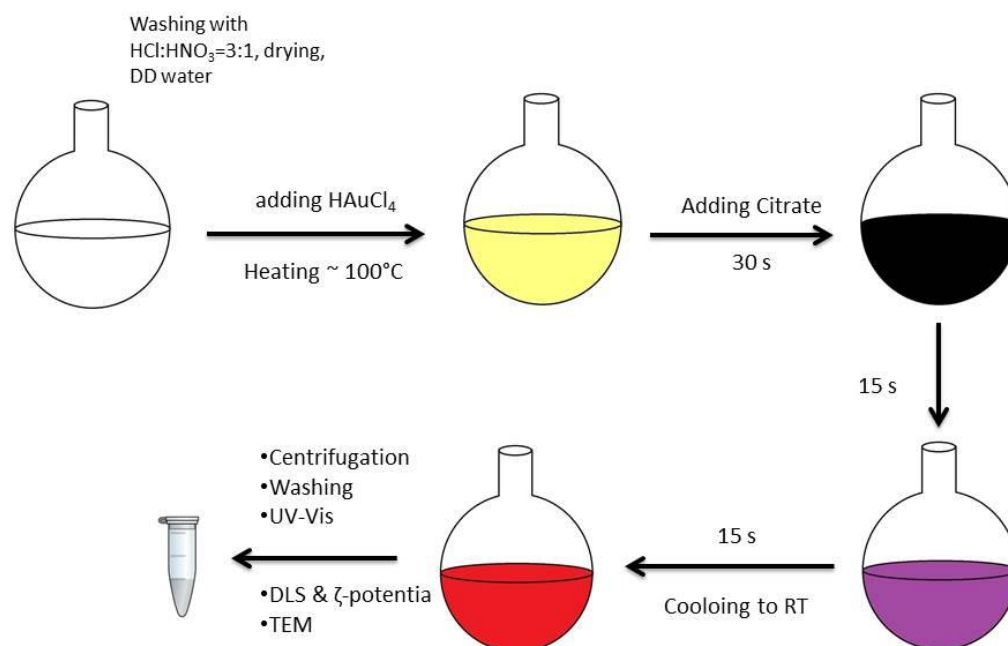


Figure 17. Scheme of Au NPs synthesis by *Turkevich* method (citrate capped).

The solution was boiled for the next 30 s, during which the color changed from black to wine-red indicating the formation of Au NPs. The synthesis steps are presented in Figure 17.

The Au NPs were characterized using various experimental method including transmission electron microscopy (TEM), ultra violet – visible (UV-Vis) absorption spectroscopy, dynamic light scattering (DLS) and zeta potential measurements. The average size was determined to be 12.5 nm with standard deviation of 2 nm as measured on 100 Au NPs using the *ImageJ* software. The SPR peak was found at 525 nm, in agreement with previous research. DLS measurements gave Z-average of 24.3 nm, confirming the presence of citrate molecules on the surface. The measured hydrodynamic radii of the Au NPs are larger than radii of bare cores measured from TEM micrographs as they refer to particles diffusion within a fluid. The NP diameter obtained by DLS measurements is the one of a sphere with same translational diffusion coefficient, which depends not only on core size of the NP, but also on any structure that abides on its surface. The summary of characterization citrate capped Au NPs is presented in Figure 18.

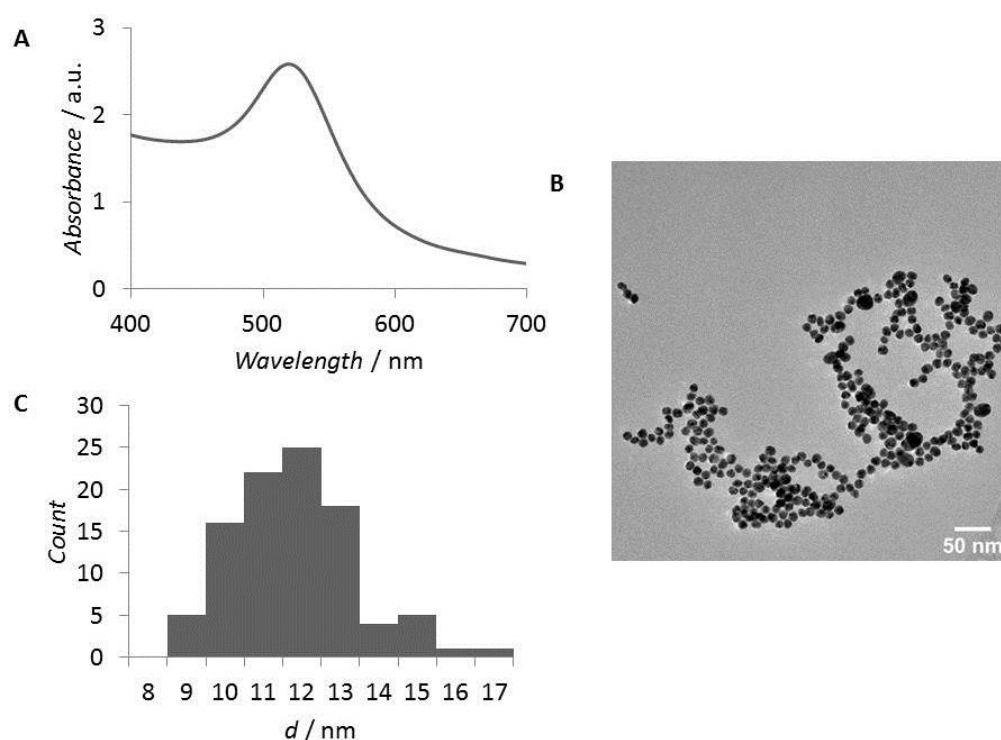


Figure 18. Characterization of Au NP capped with citrate. (A) UV-Vis spectra averages (N=3) (peak 525 nm), (B) TEM micrograph and (C) Size distribution (N=100).

Furthermore, the zeta potential measurements showed that the surface of NPs has negative charge of -41 mV indicating very stable colloid as the small particles with zeta potential higher than 30 mV (or lower than -30 mV) are considered stable.^[290] Somewhat smaller, citrate/tannic acid capped Au NPs, were synthesized by modifying the method reported by Slot and Geuze.^[291] All the glass ware was washed with *aqua regia* and gold salt solution was prepared by diluting HAuCl_4

solution in Milli-Q water. A second solution containing trisodium citrate, tannic acid and potassium carbonate dissolved in Milli-Q water was prepared. Both solutions were stirred while being heated to 60 °C. Once this temperature was reached, the tannic acid solution was added to the gold chloride solution. An immediate color change (from pale yellow to reddish-brown) was observed. The solution was then heated and left to boil for 2 min, and then removed from the heat source. The resulting colloid had a dark red color. The summary of the citric/tannic acid capped Au NPs synthesis is presented in Figure 19.

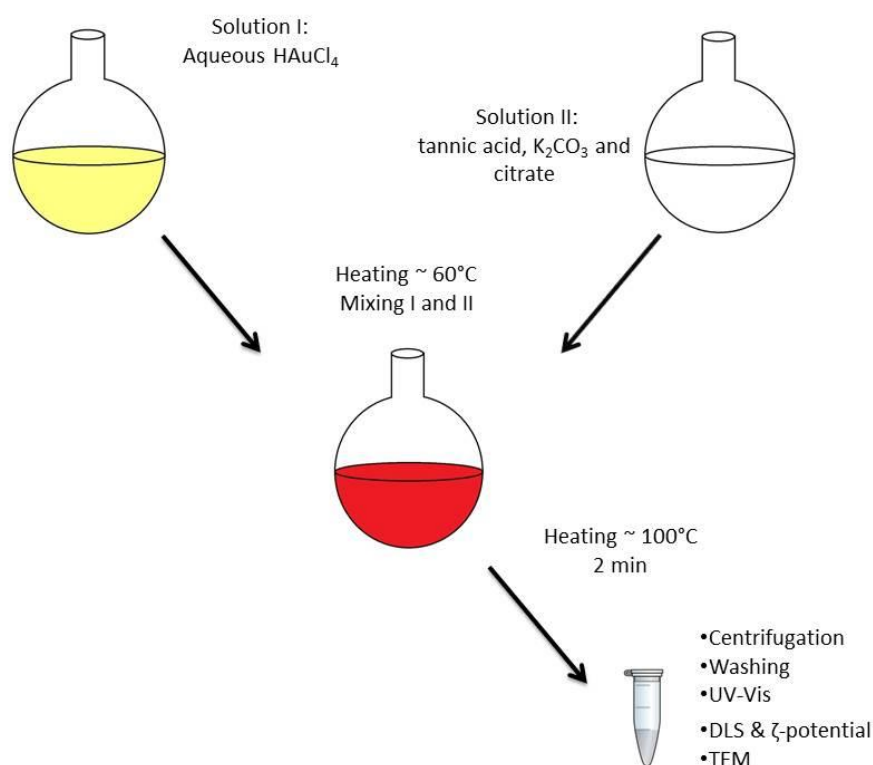


Figure 19. Scheme of Au NPs synthesis by modified *Slot* and *Geuze* method (citrate/tannic acid capped).

The resulting Au NPs were characterized using TEM, UV-Vis, DLS and Zeta potential. From TEM micrographs it was determined that the average diameter of the particles is 5.3 nm with standard deviation of 1.1 nm (N=100). The UV-Vis spectrum shows a SPR peak centered at 519 nm in agreement with previous research. The hydrodynamic radii obtained with DLS are slightly bigger than the bare core radii measured using TEM micrographs. Their values are centered on 15 nm, indicating the presence of surfactants, similar to the case of citrate capped NPs described earlier. The Zeta potential was measured at -36 mV, indicating stability of the colloid. The summary of characterization citrate/tannic acid capped Au NPs is presented in Figure 20.

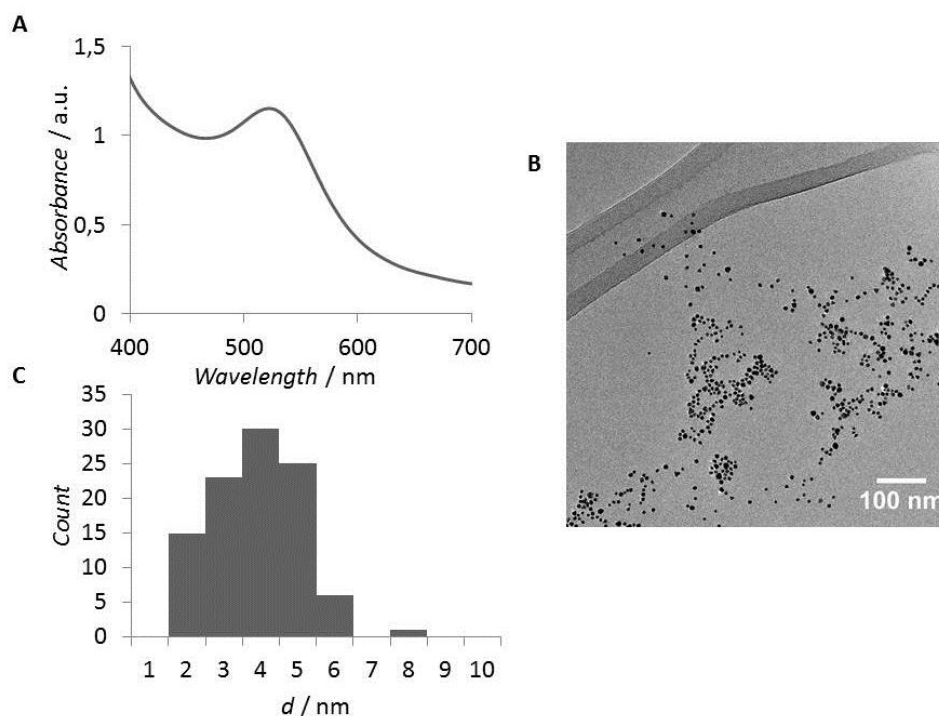


Figure 20. Characterization of Au NPs capped with citrate and tannic acid. (A) UV-Vis spectra averages (N=3) (peak 519 nm), (B) TEM micrograph and (C) Size distribution (N=100).

4.2.2. LA-DA coated NPs

In the following chapters, three different types of noble metal NPs (Au, Ag and Cu) and one type of semiconductor NPs (CdS) are synthesized with LA-DA linker as capping agent. As previously discussed, thiol functionality has a strong binding affinity towards metal surfaces, making it ideal choice for surface functionalization of metal NPs. In addition, the ratio of the linker to metal salt precursors determines the final size of the NPs indicating that a range of sizes can be obtained by changing it. Finally, as-synthesized metal NPs contain catechol moieties on their surface, which can further be used for modification of oxide NPs.

4.2.2.1. LA-DA capped Au NPs

Out of the three types of noble metal NPs synthesized, the thiol groups of the LA-DA linker have the highest affinity towards gold surfaces. This affinity has been discussed at length previously (Chapter 2.1.1.1.), and is responsible for stability to the functionalized Au NPs. There are two possible

routes to obtain functionalized Au NPs, either a ligand exchange or direct one-pot synthesis in the presence of the linker.

The LA-DA capped Au NPs were synthesized by slight modification of the method developed by Oh *et al.* The glassware used in synthesis was washed with *aqua regia*, thoroughly rinsed with water and dried on air. The LA-DA linker was dissolved in ethanol (EtOH) with heating, with following filtration in order to remove the undissolved linker. The HAuCl_4 was dissolved in Milli-Q water, added to LA-DA solution, and stirred for 1h. In this time the solution changed from pale yellow to transparent. Freshly dissolved aqueous solution of NaBH_4 was added drop-wise to the rapidly stirred colorless mixture. The color changed slowly to black and with continuing addition of NaBH_4 it turned wine-red, indicating NP formation. The mixture was stirred overnight on ambient temperature (RT). Multiple batches were synthesized with varying precursor-to-surfactant ratio (Au-to-LADA ratio from 1 to 25). The summary of the LA-DA capped Au NPs synthesis steps is presented in Figure 21.

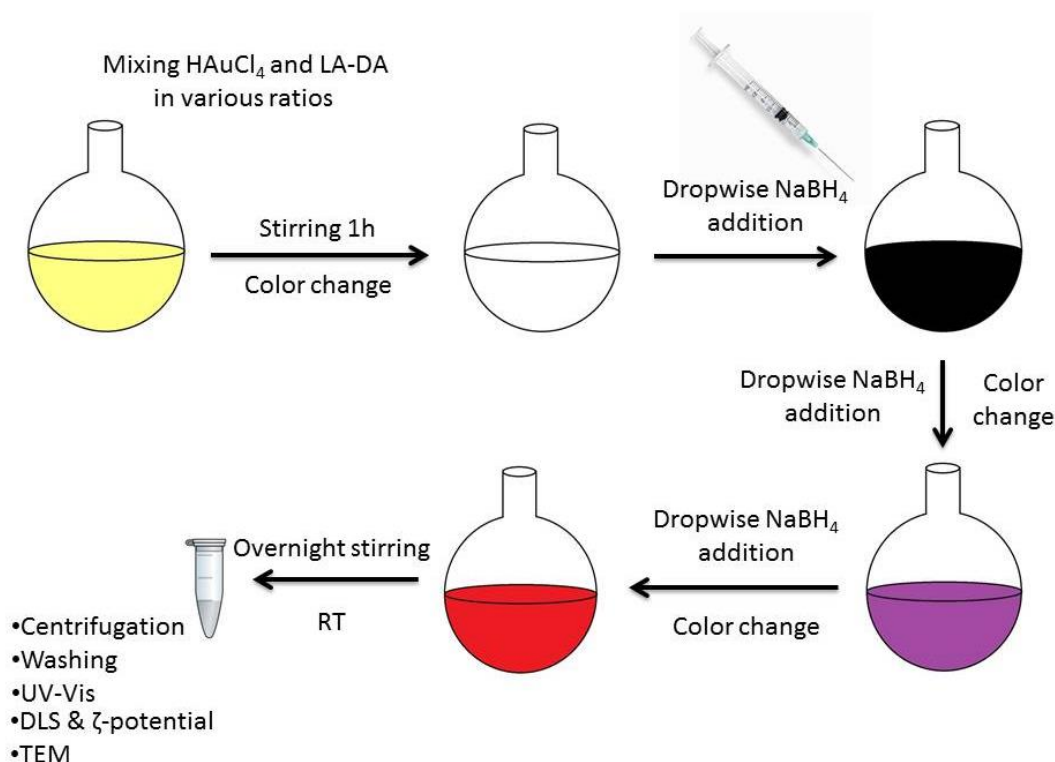


Figure 21. Scheme of Au NPs synthesis by modified Oh *et al.* method (LA-DA capped).

The TEM, UV-Vis, DLS and Zeta potential measurements of the obtained colloids were performed following the synthesis. As expected, the batches having higher Au-to-LADA ratio resulted in larger NPs, as the same amount of precursor is capped with least linker thus allowing growth of particles. The average diameter sizes in which the LA-DA capped Au NPs were synthesized ranged

from 1.5 nm to 20 nm (Fig. 22 A-C). The very small NP did not exhibit the SPR, while the peak of the larger ones red-shifted from 513nm to 531 nm with increasing diameter (Fig. 22 D).

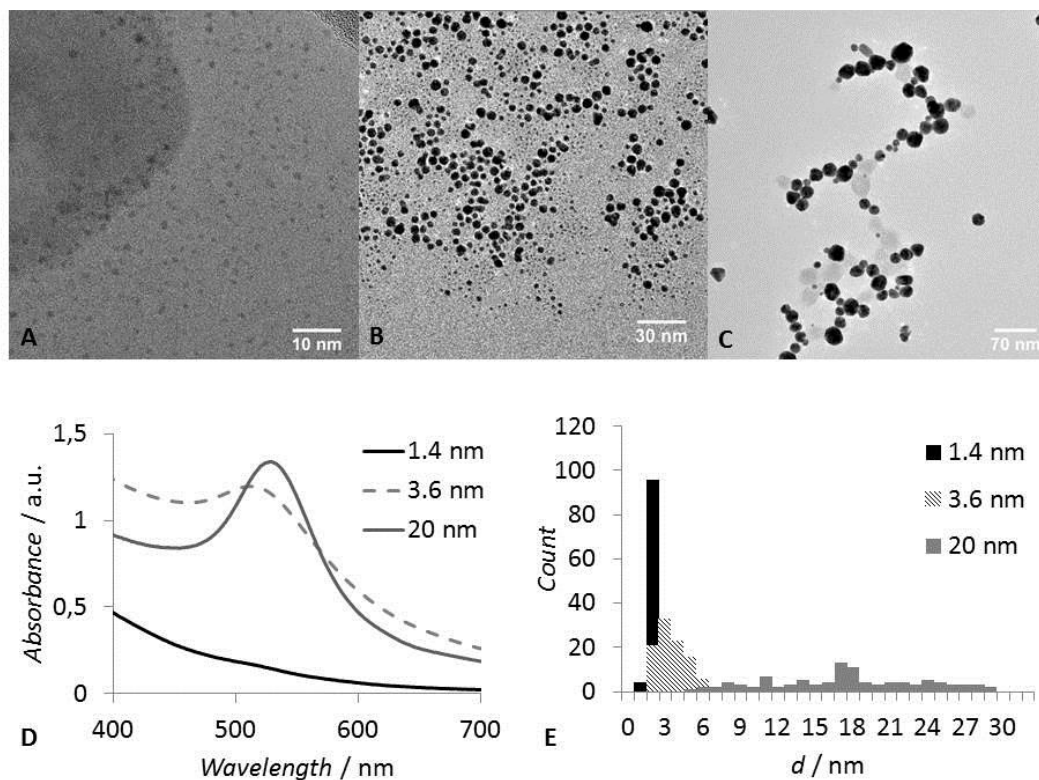


Figure 22. Characterization of Au NPs capped with LA-DA. TEM micrograph of particles having average diameter of (A) 1.4 nm NPs, (B) 3.6 nm NPs, (C) 20 nm NPs. UV-Vis spectra averages (N=3) (D) and size distributions (E) of the corresponding NPs (N=100).

The size distributions are presented in Figure 22 E. The standard deviation (SD) for small Au NPs was only 0.3 nm, for the medium ones it increased to 1.1 nm and for the largest it reached 6 nm. The growing SD was probably caused by the decreasing Au-to-LADA ratio, resulting in inhomogeneous nucleation and subsequent inhomogeneous growth.

The DLS measurements were only partially successful, the reason being that the Au NPs from the smallest batch (diameters < 2 nm) were below the limit of detection for the DLS instrumentation. For the medium sized Au NPs (diameters 2-6 nm) the resulting hydrodynamic radii were centered on 8.7 nm, in accordance with previous argumentation. The largest batch (diameter 10-30 nm), being the most polydispersed one, gave values centered on 78 nm. Zeta potential measurements gave the

same results for all the batches, as is to be expected due to the presence of the same surfactant molecule (LA-DA). The measured values were around -43 mV, indicating very stable colloid solutions of Au NPs in all cases. All the mentioned size dependent properties and some experimental details of the LA-DA capped Au NPs are summarized in Table 1.

Table 1. Size-dependent properties exhibited by Au NPs capped by LA-DA.

Sample	Au:LADA	d (TEM) / nm	SD / nm	d (DLS) / nm	SPR peak / nm	Zeta potential / mV
Au-LADA-1	1	1,4	0,3	-	-	-41
Au-LADA-2	10	3,6	1,1	8	513	-43
Au-LADA-3	25	20	6	78	531	-43

As shown in Table 2 Au-LADA-2 (size around 3.6 nm) were prepared several times with excellent reproducibility and have been used in the subsequent experiments.

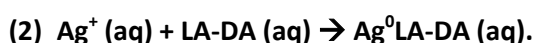
Table 2. Properties of different Au-LADA-2 samples prepared under same experimental conditions demonstrating high reproducibility of one-pot synthetic procedure.

Sample	Au:LADA	d (TEM) / nm	SD / nm	SPR peak / nm	Zeta potential / mV
Au NP - LADA – 2 (1)	10	3,3	0,8	516	-43
Au NP - LADA – 2 (2)	10	3,8	1,4	519	-43
Au NP - LADA – 2 (3)	10	3,5	1,2	513	-43

4.2.2.2. LA-DA capped Ag NPs

The synthesis of Ag NPs was performed using silver nitrate (AgNO_3) dissolved in Milli-Q water as a precursor. The aqueous solution of AgNO_3 was added to the EtOH solution of LA-DA in different Ag-to-LADA ratios and the mixture was stirred for 5 min prior to sodium hydroxide (NaOH) addition. Upon NaOH addition the colorless solution turned brown-yellow, indicating the formation of Ag NPs.

The high pH environment de-protonates thiol groups of the linker thus providing the conditions for Ag^+ reduction and NP formation. The synthesis of the LA-DA capped Ag NPs is presented in the following chemical equations (1-2):



The synthesized LA-DA capped Ag NPs were characterized using TEM, UV-Vis spectroscopy, DLS and zeta potential measurements. The Ag NPs obtained using 5, 10 and 20 Ag-to-LADA ratios, resulted in particles with average diameters of 4.7, 6 and 24.5 nm respectively, as measured by TEM. Similarly to Au NPs, they exhibit size-related red-shifting of the SPR peak. As expected, the SPR peaks of NPs with average diameters of 4.7 and 6 nm were both centered around 405 nm, due to their similar sizes. The larger particles with average diameter of 24.5 nm exhibited much broader SPR peak centered at 425 nm, confirming the broad size distribution of the batch as observed by TEM. The explanation for such broad size distribution in the batch synthesized with largest Ag-to-LADA ratio is the same as for the Au NPs, namely the “shortage” of surfactant results in less nucleation centers, which can then grow to larger sizes. The DLS measurements gave hydrodynamic radii of 10, 13 and 53 for Ag NPs of 4.7, 6 and 24.5 nm respectively. The Zeta potential of three different batches was measured around -60 mV, somewhat larger than the ones of Au NPs. The TEM micrographs, UV-Vis spectra and size distributions of LA-DA capped Ag NPs are graphically presented for comparison in Figure 24, while all the data are summarized in Table 3 below.

Table 3. Size-dependent properties exhibited by Ag NPs capped by LA-DA.

Sample	Au:LADA	d (TEM) / nm	SD / nm	d (DLS) / nm	SPR peak / nm	Zeta potential / mV
Ag-LADA-1	5	4,7	0,3	10	405	-62
Ag-LADA-2	10	6	1,1	13	405	-60
Ag-LADA-3	20	24,5	6	53	425	-61

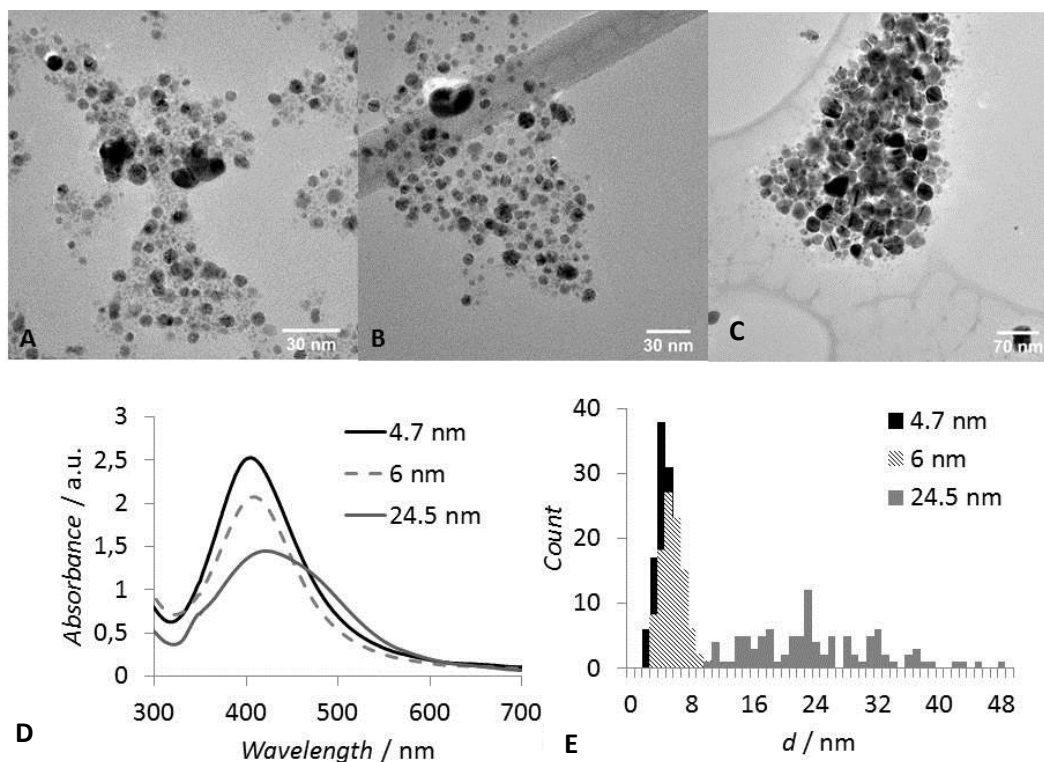


Figure 24. Characterization of Ag NPs capped with LA-DA. TEM micrograph of particles having average diameter of (A) 4.7 nm NPs, (B) 6 nm NPs, (C) 24.5 nm NPs. UV-Vis spectra averages (N=3) (D) and size distributions (E) of the corresponding NPs (N=100).

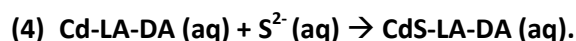
4.2.2.3. LA-DA capped Cu NPs

The experience gathered in the synthesis of Au and Ag NPs capped with LA-DA linker was put to use in the attempt to synthesize Cu NPs capped with the same linker. In spite of many attempts using different precursor to ligand ratios and reduction methods the synthesis of Cu-1 NPs was not successful. Due to the fast oxidation of the small copper metal clusters it is possible that both metal and metal oxide surfaces are available for the linkers, which would result in LA-DA possibly binding with both ends to the forming particles resulting in agglomeration. A suggested solution would be the use of the LA-DA linker with protected catechol during the synthesis, followed by de-protection and the activation of the hydroxyl groups in the post synthesis treatment. Another possibility is the use of organic solvents in an attempt to prevent the oxidation of the forming Cu NPs, which would in turn expose the metal facets to the bi-dentate thiol binding as in the Au and Ag NP case.

4.2.2.4. LA-DA capped CdS NPs (CdS-1)

4.2.2.4. A) Synthesis of CdS-1

The precursors cadmium acetate (Cd(Ac)) was dissolved in Milli-Q water and the pH was adjusted to 11 by NaOH addition, while the LA-DA was dissolved in EtOH and added subsequently to the Cd(Ac) solution. The mixture was bubbled with N₂ for 30 min, after which the Na₂S was added drop-wise into the solution. Stirring continued as well as the N₂ bubbling for the next 24h. The solution was centrifuged and the supernatant was discarded three times, while the pellet was dispersed in Milli-Q water. Finally, the CdS NPs were dispersed in Milli-Q water and stored on 4°C in the refrigerator. The synthesis is presented in the equations (1)-(4):



4.2.2.4. B) Characterization of CdS-1

The synthesized CdS-1 NPs were characterized through TEM, UV-Vis, DLS and Zeta potential measurements. The size, size distribution and UV-Vis absorption spectra are presented in Figure 26. From the graphs in Figure 26 it is obvious that the synthesized CdS NPs have an average diameter of 3.3 nm and very narrow size distribution. Zeta potential measurements were averaged on -30 mV, indicating a very stable colloid. The fluorescence of the CdS-1 QDs was measured upon 400 nm wavelength excitation. The resulting spectrum (Fig. 27) reveals that the emission of the CdS-1 strongly depends on the size of the particles. Even though the analysis of TEM micrographs shows relatively small size distribution, three emission peaks are seen in the fluorescence spectrum thus revealing the existence of different size populations of QDs with different physical properties. Barely detectable peak is noticed centered on 443 nm while the two prominent ones are centered on 488 and 533 nm. According to the literature, these peaks might be results of QDs having diameters of 1.6, 1.9 and 2.4 nm respectively, matching the TEM analysis and explaining relatively broad absorption peak in Fig. 26 (B).^[292]

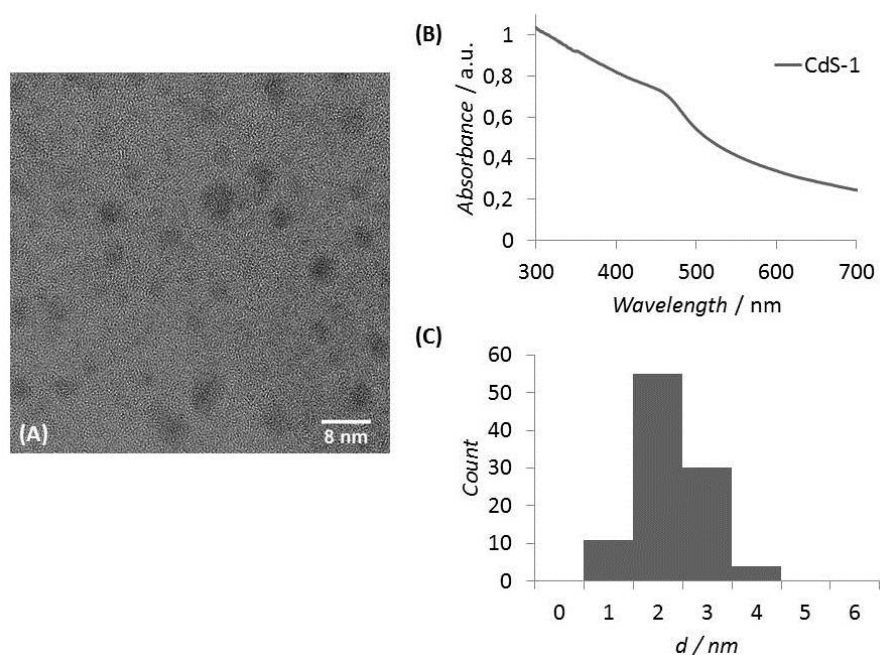


Figure 26. Characterization of CdS NPs capped with LA-DA. (A) TEM micrograph of particles having average diameter of 3.3 nm. UV-Vis spectra averages (N=3) (B) and size distributions (C) of the corresponding NPs (N=100).

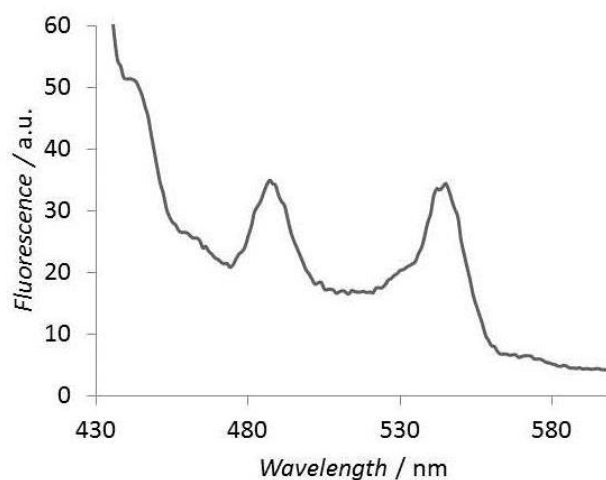


Figure 27. Fluorescence spectra of CdS-1 excited with 400 nm wavelength irradiation. The three peaks at 443, 488 and 533 nm are the consequence of the relatively broad size distribution (1-4 nm) of the particles and are assigned to the groups of particles having diameters 1.6, 1.9 and 2.4 nm respectively.

From the presented experimental results, it is clear that the CdS-1 QDs were successfully synthesized exhibiting the properties matching the ones already reported in the literature. Due to the size distribution, they exhibit numerous fluorescence peaks when irradiated by 400 nm light. The further suggested step (not done in this thesis) is the separation of the different sized QDs to obtain highly monodispersed batches with only one emission frequencies for the usage in *e.g.* cell labeling studies.

4.3. Functionalization of TiO₂ nanomaterials

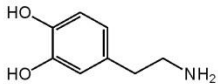
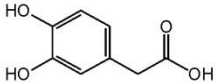
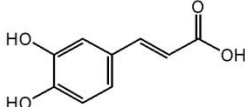
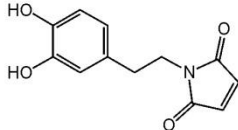
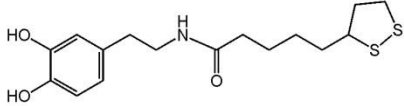
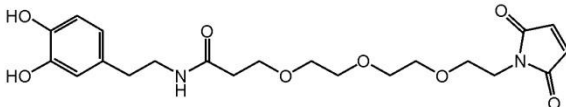
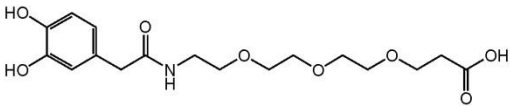
This chapter deals with functionalization of nanoparticulate TiO₂ materials with dopamine based linkers. The choice of the dopamine as the head group attaching to the TiO₂ surface is explained and the functionalization procedure is shortly described. The experimental results are presented and discussed with the emphasis on the photocatalytic activity of the functionalized TiO₂ and its difference from the unmodified material.

4.3.1. Functionalization of commercial TiO₂ NPs

TiO₂ are widely available nanomaterial, often used as a standard in the investigation of nanomaterial photocatalysis. Therefore there is a great interest in understanding how the presence of different groups on the surface affects its properties. The commercial TiO₂ NPs used in this work are the Degussa P25 TiO₂ NPs and Anatase NPs which were both modified and used as obtained by supplier. Both materials are composed of NP of approximate diameter of 21 nm and differ only in the type of the crystal phase. While Degussa P25 consists of mixture of rutile and anatase in 20:80 ratio, Anatase TiO₂ NPs are made of pure anatase.

4.3.1.1. *Library of Dopamine Based Linkers*

As already discussed in Chapter 2.3., the surface Ti atoms within unmodified NPs are under-coordinated in the case of unmodified NPs. The addition of linkers that covalently bind these under-coordinated atoms reduces the surface energy and restores the initial hexa-coordination present in the bulk material. Hydroxyl group (-OH) has a high affinity towards metal-oxide surfaces and if present within bidentate or higher-dentate compounds it results in stronger binding and increased stability of coated NP. Modified catechols containing two OH groups have been shown to bind strongly to the TiO₂ surface. In the study of the effect of different catechol ligands on TiO₂, 10 different catechol based linkers were used, 3 of which are commercially available (Dopamine-DA1, Caffeic acid-DA2 and DOPAC-DA3) and 7 synthesized within our group (DA4-DA10) (Figure 28).

DA 1		<p>4-(2-aminoethyl)benzene-1,2-diol Chemical Formula: $C_8H_{11}NO_2$ Molecular Weight: 153,18 Length: ~0.83nm</p>
DA 2		<p>2-(3,4-Dihydroxyphenyl)acetic acid Chemical Formula: $C_8H_8O_4$ Molecular Weight: 168,15 Length: ~0.8nm</p>
DA 3		<p>3-(3,4-Dihydroxyphenyl)-2-propenoic acid Chemical Formula: $C_9H_8O_4$ Molecular Weight: 180,16 Length: ~0.91nm</p>
DA 4		<p>1-(3,4-dihydroxyphenethyl)-1H-pyrrole-2,5-dione Chemical Formula: $C_{12}H_{11}NO_4$ Molecular Weight: 233,22 Length: ~1.07 nm</p>
DA 5		<p>1-(3,4-dihydroxyphenethyl)-1H-pyrrole-2,5-dione Chemical Formula: $C_{12}H_{11}NO_4$ Molecular Weight: 233,22 Length: ~1.07 nm</p>
DA 6		<p>N-(3,4-dihydroxyphenethyl)-3-(2-(2-(2,5-dioxo-2,5-dihydro-1H-pyrrol-1-yl)ethoxy)ethoxy)ethoxy)propanamide Chemical Formula: $C_{21}H_{28}N_2O_8$ Molecular Weight: 436,46 Length: 2.34 nm</p>
DA 7		<p>1-(3,4-dihydroxyphenyl)-2-oxo-6,9,12-trioxa-3-azapentadecan-15-oic acid Chemical Formula: $C_{17}H_{28}NO_8$ Molecular Weight: 371,38 Length: ~2.34 nm</p>

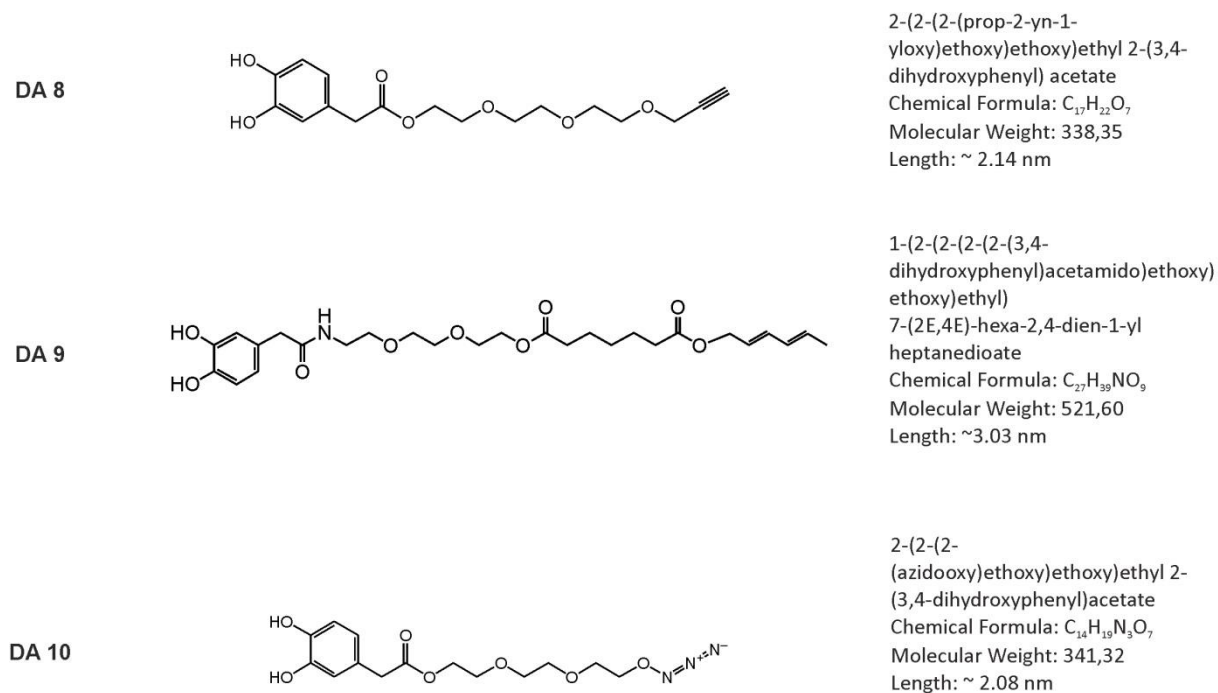


Figure 28. DA1-DA10: catechol based linkers used in modification of commercial TiO₂ NPs; structure, full chemical name and the lengths of the linkers.

4.3.1.2. Functionalization/Modification of TiO₂ NPs with Dopamine Based Linkers

Functionalization of both Degussa P25 and Anatase TiO₂ was performed using the same procedure. First, TiO₂ NPs were dispersed in water and the pH was set to 1.5 using HCl resulting better dispersions (due to the isoelectric point of the TiO₂ NPs that is near the pH of the water). The solutions were then pulse sonified in order to obtain the highest degree of dispersion of particles. The linkers were dissolved in EtOH and 2.5 μmol of linker was added per mg of TiO₂ NPs. Immediately upon addition of the linker to the solution, the color change from white to yellow-orange (Figure 29) depending on the linker was observed (for DA8-DA10 the color change was less obvious).

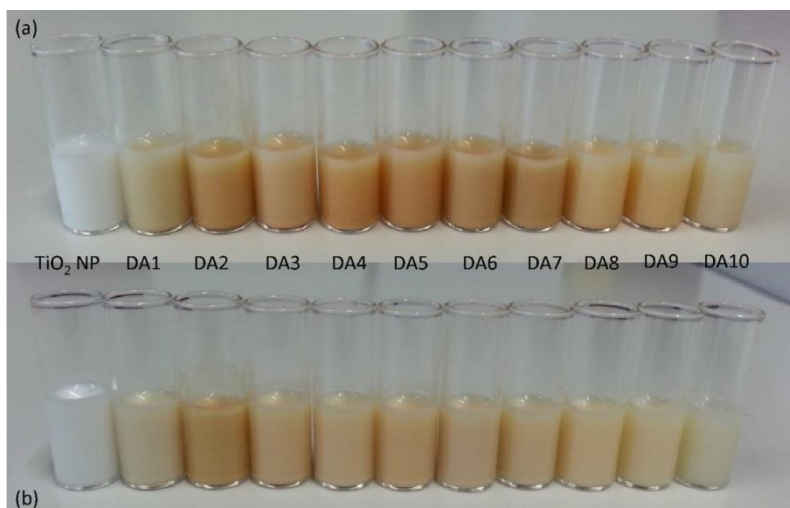


Figure 29. Charge transfer and color change upon addition of different linkers to (a) anatase and (b) Degussa P25 TiO₂ NPs.

4.3.1.3. Characterization of Functionalized TiO₂ NPs

The modified commercial TiO₂ NPs were further characterized with UV-Vis absorbance spectroscopy, DLS and zeta potential measurements. The results are presented in the following chapters.

4.3.1.3. A) UV-Vis

Representative UV-Vis spectra averages (N=3) of modified commercial (P25 and Anatase) TiO₂ NPs are shown in Figure 30 where it is for all cases observed that the addition of catechol linkers causes the change in absorbance and the appearance of the broad peak around 400 nm. This is a consequence of ligand to metal charge transfer complex (LMCT) formation. The electrons of the LMCT complex are excited with lower energy photons (hence the broad peak around 400 nm) than the intrinsic electrons of the unmodified TiO₂ NPs. In addition, the absorption is strongly enhanced for the UV-Vis transition region (300-400) due to the both LMCT and the intrinsic absorption of the pure ligands, which is mostly in the UV region. The modification of the hybrids did not affect the absorption in the visible and far visible range (above 500 nm) as the LMCT and ligand itself have no absorption in these regions. Almost identical features can be identified in the Anatase modified NPs).

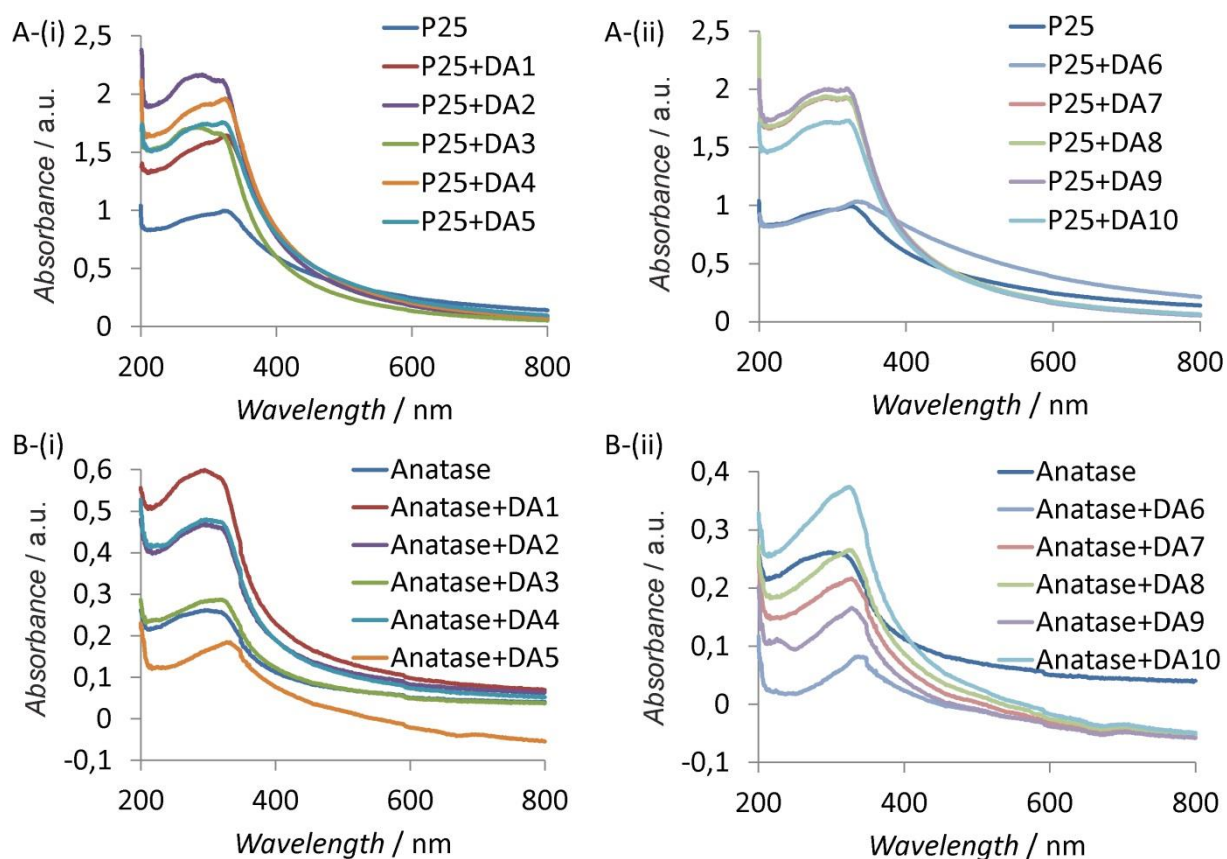


Figure 30. UV-Vis spectra averages (N=3) of modified TiO₂ (A) P25 and (B) Anatase.

4.3.1.3. B) DLS and Zeta potential

Zeta potential measurements of the modified TiO₂ NPs were one of the methods used to verify if the linkers were successfully attached to the surface of the NPs. Due to the different crystal phase composition resulting in differently shaped surface, the bare Degussa P25 and Anatase NPs exhibit different zeta potentials averages (N=10) (Shown in Figure 31). When modified with same catechol based linker, the zeta potentials of the different types of NPs show the same trend indicating the same principle of binding through catechol groups. More significant differences are observed for linkers containing longer ethylene glycol chains namely DA8, DA9 and DA10, indicating possible less successful modification and matching the absence of pronounced color change during and after the modification (Photo in Figure 29).

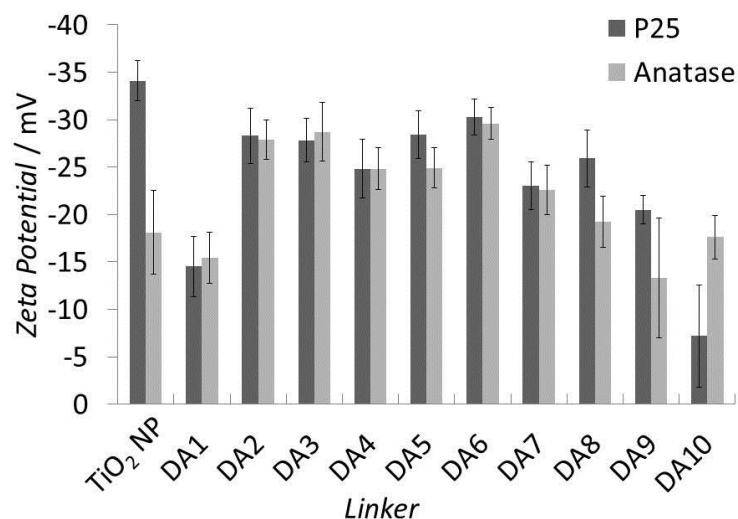


Figure 31. Zeta potentials averages (N=10) of the bare and catechol-based linker modified commercial TiO₂ NPs (P25 and Anatase)

In the Figure 31 one can observe that for *e.g.* dopamine (DA 1) linker modification (having positively charged amine functionality exposed) a decrease of zeta potential is observed compared to the unmodified NPs (from -32 mV to -15 mV for Degussa), while on the other had for the DOPAC (DA 2), Caffeic acid (DA 3) or linker DA 7 modification (negatively charged carboxylic acid functional group) the zeta values are similar in value and more negative in respect to the Dopamine linker (-28, -28 and -25 mV respectively). Further on, the DLS of the bare NPs as well as the modified ones was measured for both types of commercial TiO₂ NPs. The results are presented in Figure 32 (a) and (b).

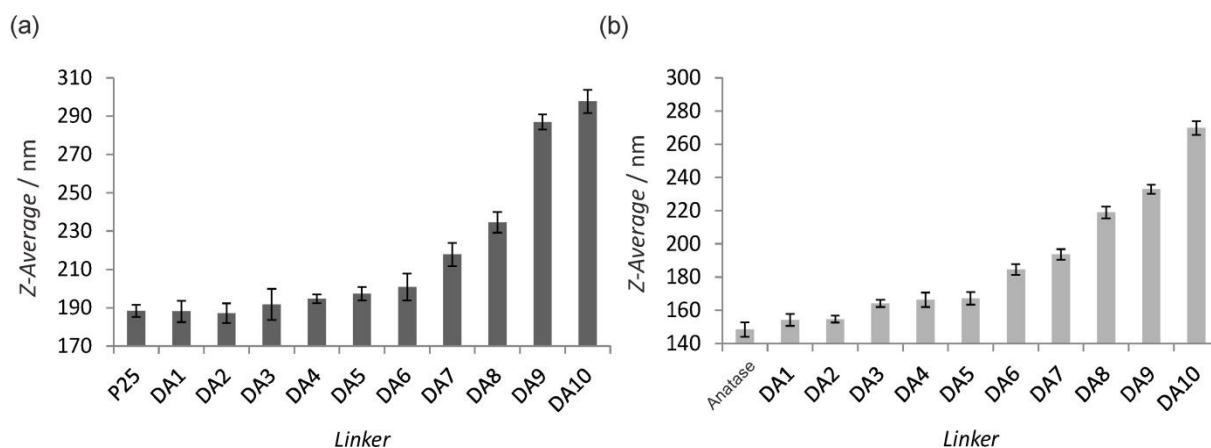


Figure 32. The average DLS measurements (N=12) of bare and linker modified (a) P25, (b) Anatase TiO₂ NPs.

The Figure 32 (a) and (b) present the averaged (N=12) measurements of the hydrodynamic radius of the bare and modified TiO₂ NPs. The presentation of the average value instead of the *e.g.* number value was chosen due to the clumped form in which the bare NPs are observed in the TEM micrographs. Due to the same reason, it is not to be expected to obtain the DLS results that match the exact sizes of the NPs (diameter ~21 nm). Quite on the contrary, much larger values for the hydrodynamic diameters were expected as the clumped NPs scatter much more light than the single ones do. Exactly such values were measured and presented in the Figure 32 (a) and (b), where the radii are almost 10 times larger than the ones stated by the supplier. Moreover, it is seen that the NPs modified with smaller linkers (DA 1 – DA 5) have similar hydrodynamic radii as the bare NPs, while the ones modified with larger linkers (DA 6 – DA 10) exhibit larger radii. This difference does not match the size of the linker, but it could be taken as an indication of the better surface arrangement of the smaller linkers resulting in the monolayer covering of the NP surface. When dealing with larger linkers on the other hand, one could encounter size related problems (*e.g.* linker bending or interaction between the free ends of the linkers) when trying to connect them to the NP surface, resulting in non-uniform coverage and larger hydrodynamic radius.

4.3.1.4. ROS Production of Functionalized TiO₂ NPs

The modified commercial TiO₂ NPs were investigated to determine whether there is a change in the photocatalytical properties upon modification. To investigate that enzyme based assay was employed in which a mixture of the horse radish peroxidase (HRP) enzyme and its substrate Amplex Red (AR) were added to the wells. In the presence of oxygen radicals (or its longer lived H₂O₂), HRP oxidizes non-fluorescent AR to highly fluorescent resorufin, which can be detected with standard fluorescence methods as presented in the Figure 33 (a) and (b). In general, 1 mg/mL stock solutions in PB (pH=6) of modified NPs were prepared and 10 µl added to the 96 well-plates. The plates were then irradiated with UV (365 nm) light for 10 min in the custom made reactor. The results of the ROS detection are presented in the Figures 34 (a)-(c).

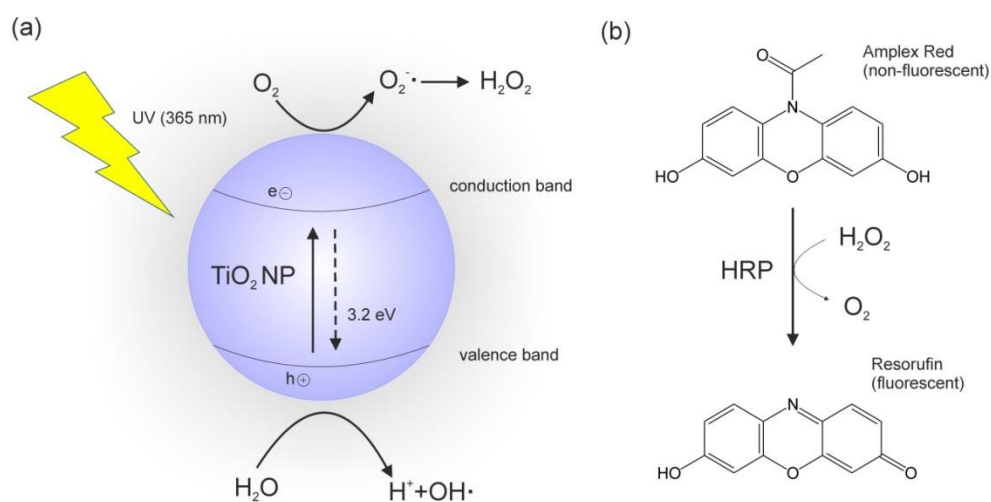


Figure 33. Generation of ROS under irradiation of semiconducting TiO_2 NP in aqueous solution (a) and the Ampliflu activity test for HRP peroxidase (b).

Figures 34 (a) and (c) show that all the linkers enhance the ROS production of the NPs although not all do it to the same extent. Linker attachment creates the charge transfer sphere on the surface of the NPs and the under-coordinated surface Ti atoms become coordinate and the bulk hexagonal lattice is restored.^[214] In this way the surface electron traps are eliminated allowing the previously trapped electrons to participate in the surface reactions. It could be expected that disappearance of the surface traps leads to the faster recombination of electrons with positive holes and therefore reduced recombination with water and O_2 present at the surface, but based on the obtained data this is not the case. However, there are differences between linkers, which indicated that the presence of different functional groups as well as the length of the ethylene glycol chain might play the role, although there is no clear pattern. For example, linker DA5 and DA7 show the smallest enhancement of the ROS production. Linker DA5 contains lipoic acid functional groups, which is known as strong antioxidant and could scavenge the newly produced radicals at the NP-solvent interface.^[293] However linker DA7 contains carboxylic acid group also present in linker DA2 and DA3, which show enhancement of the ROS production indicating that other factors such as the hydration of the TiO_2 surface (the amount of water present near the surface to allow for the ROS production) might play the role, but due to the time constrains this was not investigated further.

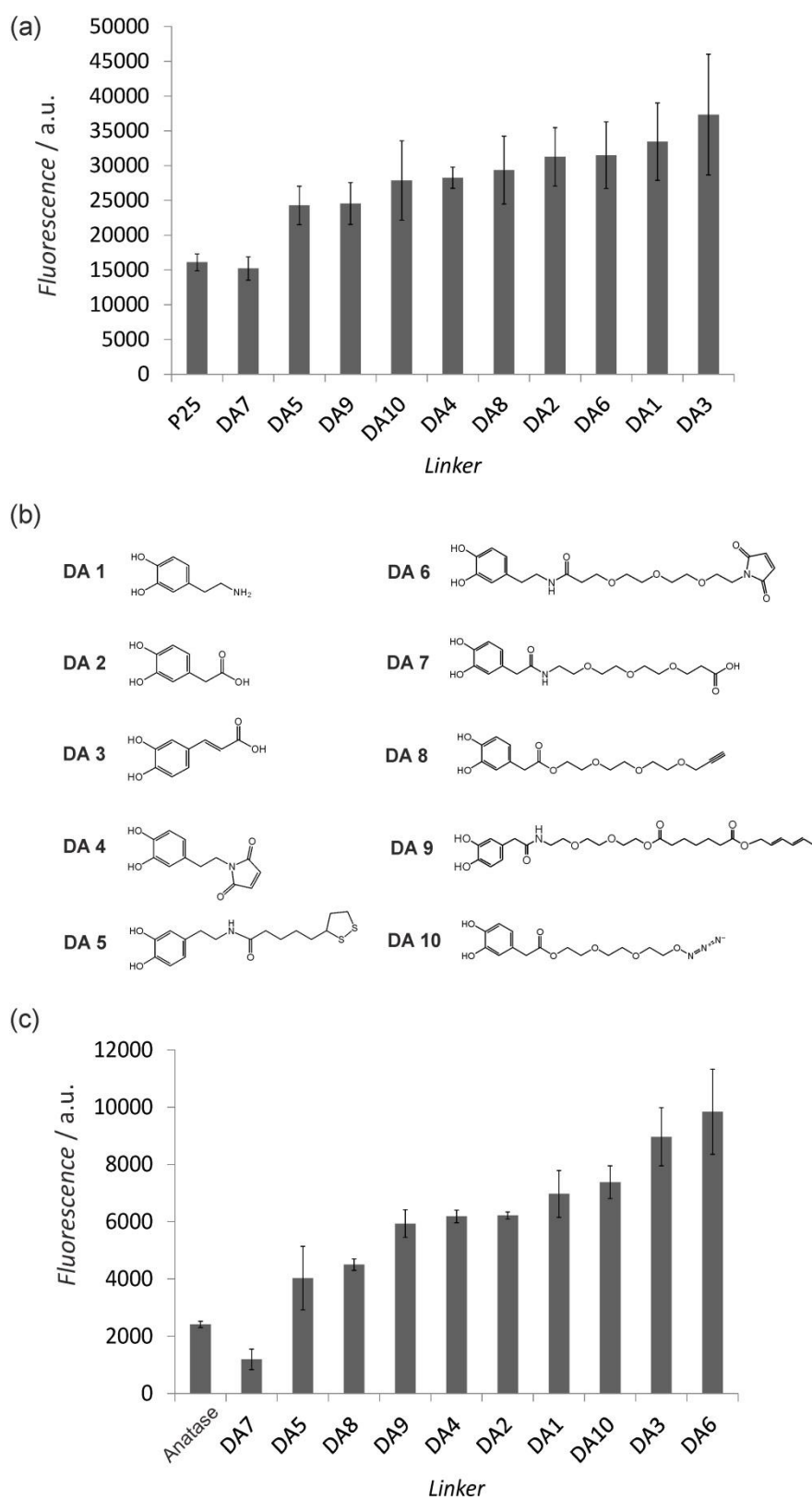


Figure 34. Averaged fluorescence measurements (N=3) indicating ROS production of the bare and modified (a) P25 and (c) Anatase TiO₂ NPs, after 365 nm irradiation, based on the HRP/AR assay; (b) Overview of the used linkers.

4.3.2. Functionalization of TiO₂ Nanorods (NR)

Once the role of the linkers was investigated showing that there is no significant decrease of the ROS production upon the surface modification, non-commercial, well defined TiO₂ structures were investigated. In attempt to prepare well defined structures with high ROS producing ability, TiO₂ nanorods (TiO₂ NRs) were prepared within the group and dopamine modification was performed in order to enable further biofunctionalization. The procedure and experimental results are presented in the following chapters.

4.3.2.1. TiO₂ NRs modification with Dopamine (DA)

TiO₂ NRs were prepared within the group (by Bianca Geiseler) using the optimized procedure first published by Seo *et al.* The rods with dimensions 17.6 by 3.6 nm were confirmed to be highly catalytic anatase phase nanomaterial. Although the TiO₂ NRs were synthesized in different batches with different times of synthesis, only the most catalytically active 8h ones were used for the DA1 modification.

The functionalization of the as-synthesized NRs proceeded through their re-suspension in toluene and direct addition of DA1 linker. Immediately upon DA1 addition, a color change from colorless to brown was observed indicating the formation of the LMCT complex. The reaction mixture was further stirred overnight at room temperature, after which it was purified by repeated centrifugation and supernatant finally dispersed in Mili-Q water (TiO₂NR+DA1). In addition to the color change, the modified NRs were characterized with IR spectroscopy, UV-Vis absorbance spectroscopy and zeta potential measurements. In Figure 37 presenting the UV-Vis absorbance spectra of the unmodified, DA1 modified TiO₂ NRs as well as the DA1 spectrum, it is visible that the absorbance of the DA1 modified TiO₂ NR (8h) is red-shifted towards the visible part of the electromagnetic spectrum due to the LMCT complex formation.

Successful surface modification was further confirmed by averaged (N=10) zeta potential measurements which changed from -39.4 mV to 38.7 mV upon addition of DA and due to the presence of positively charged amine group.

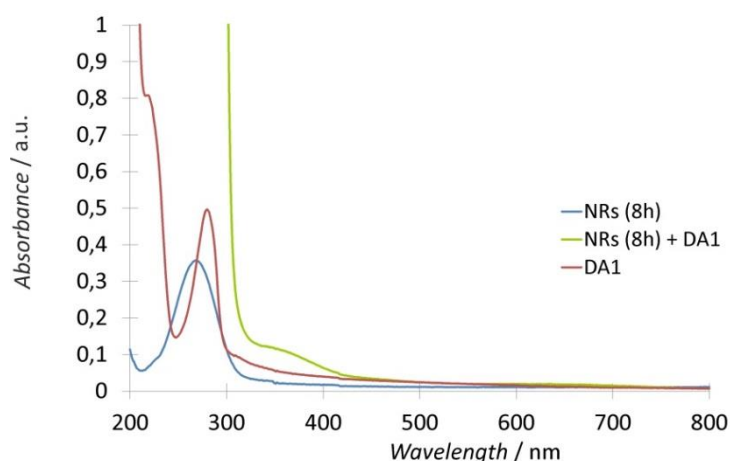


Figure 37. UV-Vis spectra average (N=3) of as-synthesized and DA 1 functionalized TiO₂ NRs (8h) together with DA 1 alone.

4.3.2.2. ROS production of modified TiO₂NR

As in the case of modified commercial NPs, it was interesting to see if the photocatalytic properties of TiO₂ NRs change with DA on their surface. HRP/AR assay was used to determine the ROS production upon 365 nm irradiation. The results are presented in Figure 38 and are significantly different from the ones obtained with the commercial NPs.

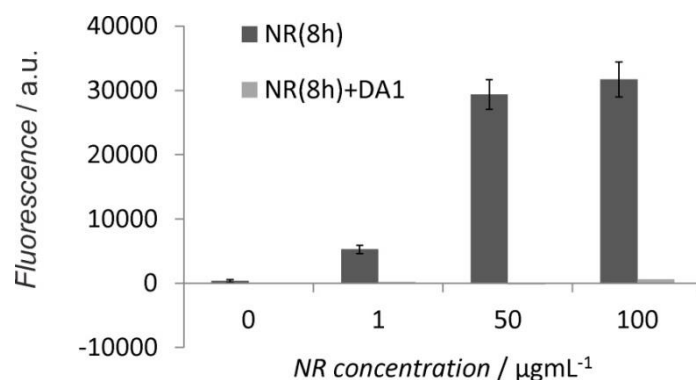


Figure 38. Averaged fluorescence measurements indicating ROS production of the bare and DA1 modified TiO₂ NRs, after 10 min 365 nm light irradiation, based on the enzymatic HRP/AR assay.

The ROS production of the TiO₂ NRs is inhibited upon the modification with DA1 linker. This strong inhibition effect of DA1 is at first in disagreement with the data obtained for commercial spherical NPs but could be clarified upon the close examination of the morphology of NR. Namely, NRs are merely 3.6 nm in width, which does not allow for the effective, diffusion controlled separation of the photoexcited electron-hole pairs thus opening the possibility for their relatively fast recombination. When the surface traps are additionally removed by DA1 modification, this improves the recombination process diminishing the possibility of electron-hole reaction with surface molecules and production of ROS. As the ROS production was suppressed, further attempts to biofunctionalize TiO₂ NRs through amide coupling were not done and future work needs to be focused on the preparation of bigger NR with high ROS producing ability.

In conclusion, the modification of TiO₂ nanomaterials with catechol based linkers turned out to be more complex than initially thought and an understanding the mechanism by which the surface linkers affect the ROS production will require additional experiments which were not performed due to the time constrains. Although it was assumed, prior to experimental study, that that catechol modification should decrease the photoactivity of TiO₂ nanomaterials through the trap removal action regardless of the morphology of the support, this was not the case. This assumption proved correct for the case of TiO₂ NRs, however the effect of the linkers on the spherical NPs was quite the contrary. Modification of spherical NPs (diameter ~ 21nm) with great majority of catechol-based linkers resulted in strong enhancement of the ROS production. It is argued that the relatively large NPs allow enough room for excitons to separate and that the trap removing in this case only further increases the ROS production by allowing the electrons to more efficiently reach surface and participate in the reactions.

4.4. Preparation and Study of Au/TiO₂ Nanocomposite

Au/TiO₂ nanocomposite synthesis method based on the building block approach is described below. The resulting material was studied through the information obtained with a wide range of available experimental methods.

4.4.1. Synthesis of Au/TiO₂ Nanocomposite Using Bifunctional LA-DA Linker

Two approaches were employed to obtain Au/TiO₂ hybrid with a goal to create a material with superior photocatalytic activity. The pivoting role in both approaches is given bifunctional LA-DA

linker that is used to prepare LA-DA capped Au NPs (Au-1). In addition, citrate coated Au NPs (Au-2) were utilized for preparation of control hybrid materials to investigate the role that LA-DA linker has in the formation of the nanocomposites. The main principle of nanocomposite design is given in Figure 39.

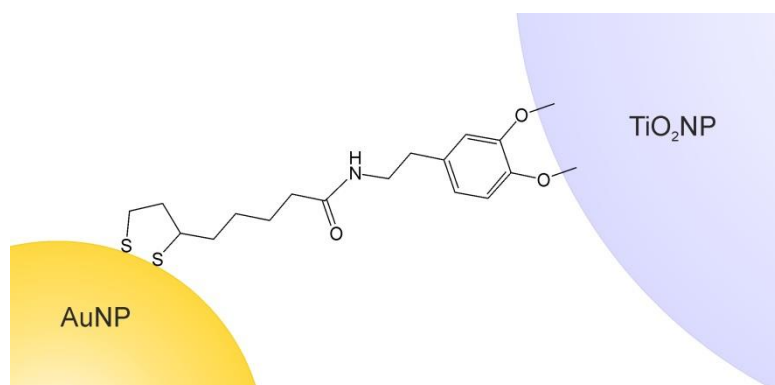


Figure 39. The scheme of the Au NP – TiO₂ NP interaction using lipoic acid – dopamine (LA-DA) linker.

4.4.1.1. Type A Nanocomposite – use of pre-prepared commercial TiO₂ NP (Degussa, P25)

The first approach involves binding of Au-1 and commercially available TiO₂ NPs (TiO₂A) to obtain hybrid named Au-1/TiO₂A. The synthesis of the Au-1 is described in Chapter 4.2.2.1., while the commercial TiO₂ powder is used as obtained by the supplier. As stated in chapter 2.1.1.1., the thiol groups on the lipoic acid end of the LA-DA linker attach to the Au NPs surface during the synthesis process. The involved LA-DA surfactant has two roles; it acts as a stabilizer of the Au NPs due to the bidentate attachment, and a linker for Au NP attachment on to the surfaces such as metal-oxides, *e.g.* TiO₂, which have an affinity for catechol groups. Figure 40 shows the principle of Au-1/TiO₂ A type hybrid preparation.

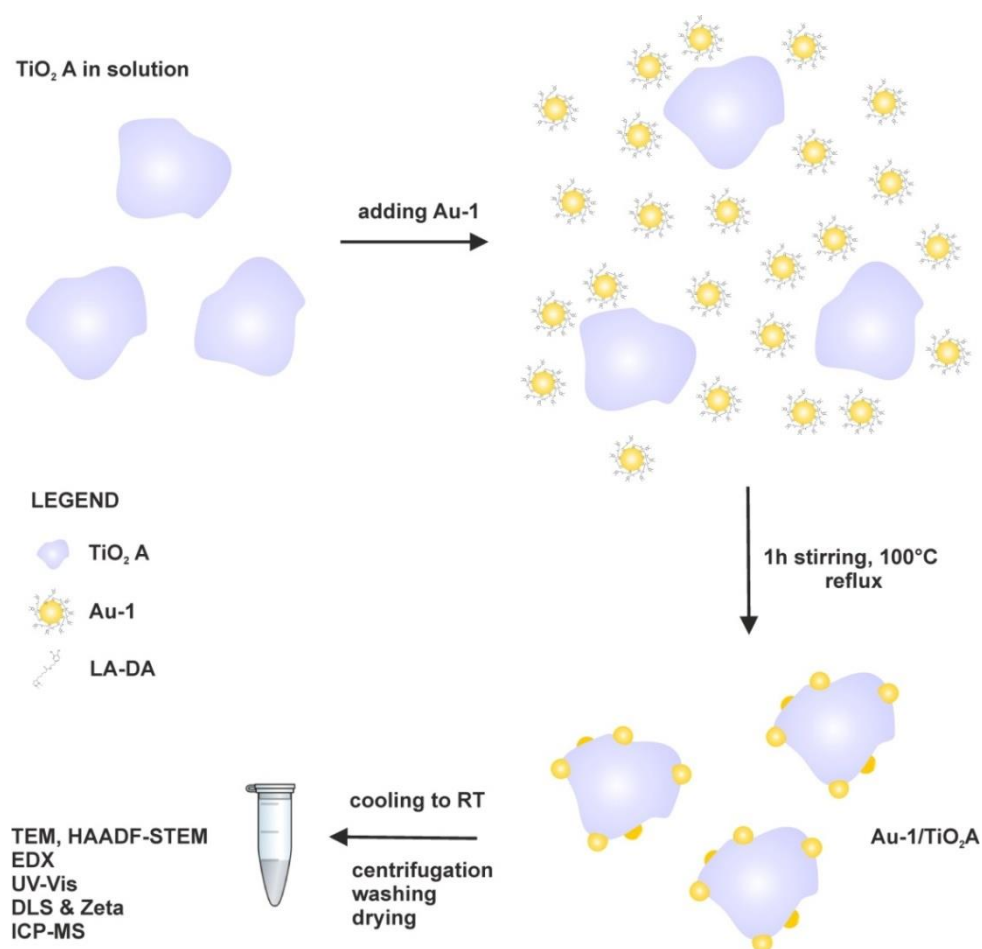


Figure 40. Scheme of Au-1/TiO₂A nanocomposite synthesis from commercial Degussa TiO₂ NPs and LA-DA modified Au NPs.

With the Au-1 in hand, the synthesis proceeds by simple mixing of the metal and semiconducting component in aqueous environment. More precisely, the TiO₂A are dispersed in Milli-Q water and stirred vigorously. The desired amount of Au-1 is added to the TiO₂A solution and the mixture is heated to boil. After 1h under reflux the synthesis is finished and the solution is left to cool to RT. Following the washing steps, the supernatant is discarded and the resulting material is vacuum-dried and stored in powder form. This procedure was repeated many times using different Au-1 to TiO₂A ratios in order to obtain nanocomposites with different Au loadings and to investigate how this affects the photocatalytic activity of the commercial TiO₂.

4.4.1.2. Type B Nanocomposite – growth of TiO₂ from titanium tetra-fluoride (TiF₄) precursor

The second approach utilized the Au-1 (average diameter 3.6 nm) as seeds for TiO₂ growth using TiF₄ as precursor resulting in Au-1/TiO₂ type B. As noted in the introduction, many different TiO₂ precursors have been used for preparation of crystalline nanostructures; among them TiCl₄,^[295] titanium tetraisopropoxide (TTIP),^[296] tetrabutyl titanate (TBOT)^[297] or titanium tetrabutoxide (TTB).^[298] Here, the TiF₄ was used due to its low hydrolysis rate thus enabling slower and gradual growth of TiO₂ shells as shown by Wang *et al.* in their work on TiO₂ nanocage synthesis.^[299] The growth of the TiO₂ shells is expected to be facilitated by the catechol moiety on the free (dopamine) end of the linkers.

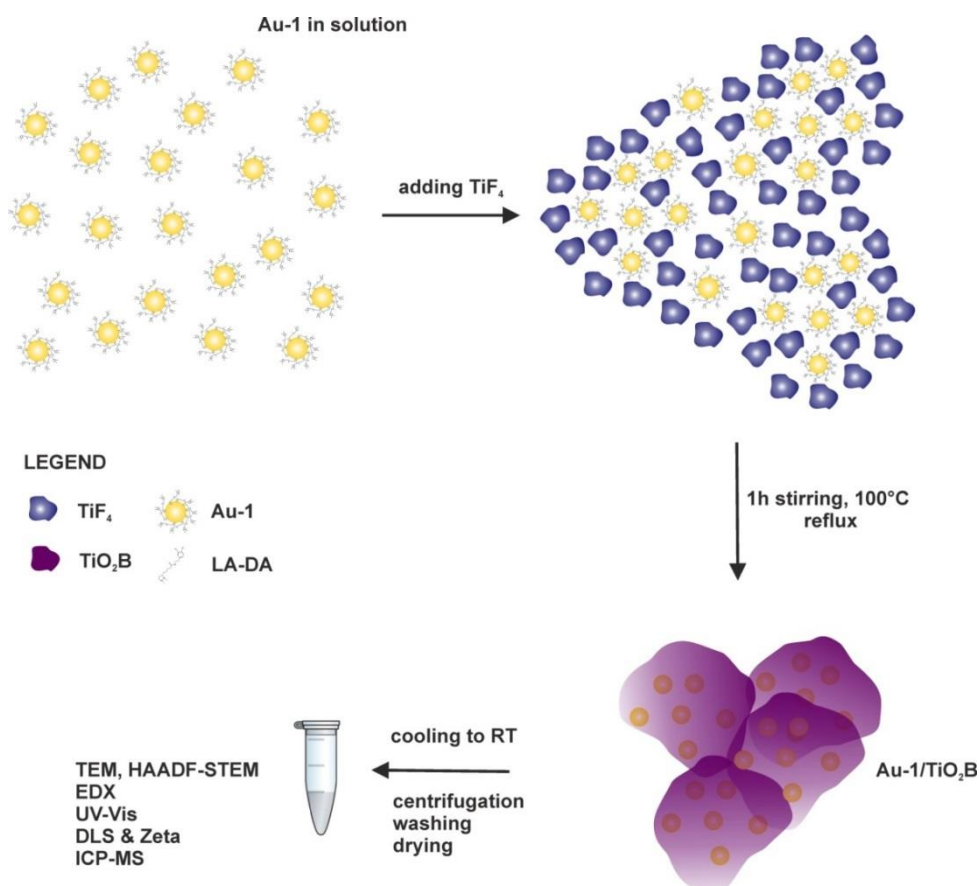


Figure 41. Scheme of Au-1/TiO₂B nanocomposite synthesis from Au-1 precursor using TiO₂ layer growth on Au seeds.

The principle of the Au-1/TiO₂ B synthesis is shown in Figure 41 and it begins with mixing the desired volumes of Au-1 and TiF₄. The mixture is then brought to boil and refluxed for 1h. During the procedure the red color of the Au NPs turns to violet due to the formation of TiO₂ shell and subsequent change of the dielectric constant in NP environment. The solutions is cooled to RT, washed, dried and stored in powder form. Again, the procedure was repeated with different Au-1 to TiF₄ ratios to obtain Au-1/TiO₂B nanocomposites with varying Au loadings and to investigate the effect that this might have on the catalytic properties.

4.4.2. Characterization of Synthesized Au/TiO₂ Nanocomposites (Type A and Type B)

In spite of the vast body of literature on the subject, it is still not really clear which Au loading should be used in Au/TiO₂ hybrid synthesis to obtain hybrid material with superior photocatalytic properties. Almost two decades ago, Bamwenda *et al.* have shown that the photo-catalytic properties of Au/TiO₂ hybrids vary significantly with Au-to-TiO₂ ratio, with highest activity reported for approximately 1 % wt of Au.^[300] Since then, and in contrast to the previously referred work, other groups have claimed that both higher^[16] or lower Au percentages result in higher photocatalytic activity of the hybrids.^[301] To explore the effect of Au % wt, we have prepared hybrids with an extensive range of Au loadings (from 0.1 up to 50% wt), which resulted in the significant difference in the color of the suspensions as presented in Figure 42 (a) and (b).

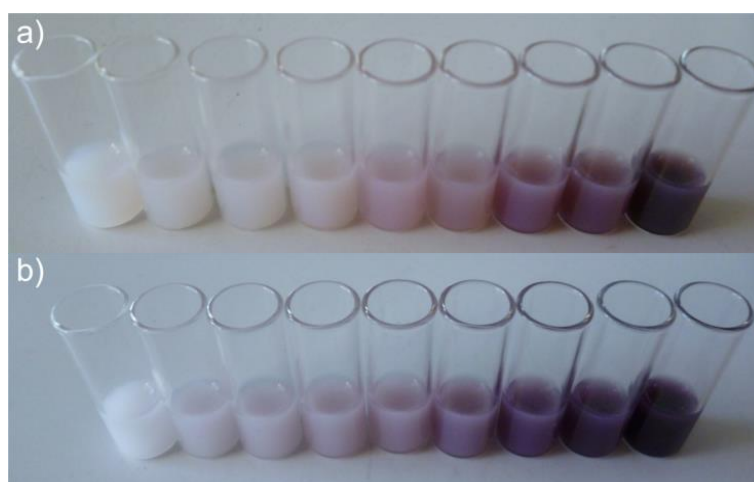


Figure 42. Colour changes observed in the suspension of a) Au-1/TiO₂A and b) Au-1/TiO₂B nanocomposite in pH 6 phosphate buffer (PB) with increasing % wt of Au (0.1, 0.25, 0.5, 1, 2, 5, 10, 20 and 50 from left to right hand side).

Subsequent TEM analysis indicated corresponding differences in the amount of Au present in the hybrid, while the confirmation of the exact Au loadings came from the inductively-coupled plasma mass spectrometry (ICP-MS) measurements.

4.4.2.1. Microscopic Analysis

4.4.2.1. A) TEM and HAADF-STEM Analysis

The synthesized hybrids were examined by TEM method to gain further information about their morphology. The resulting TEM micrographs of the selected hybrids of both types are presented in Figure 43.

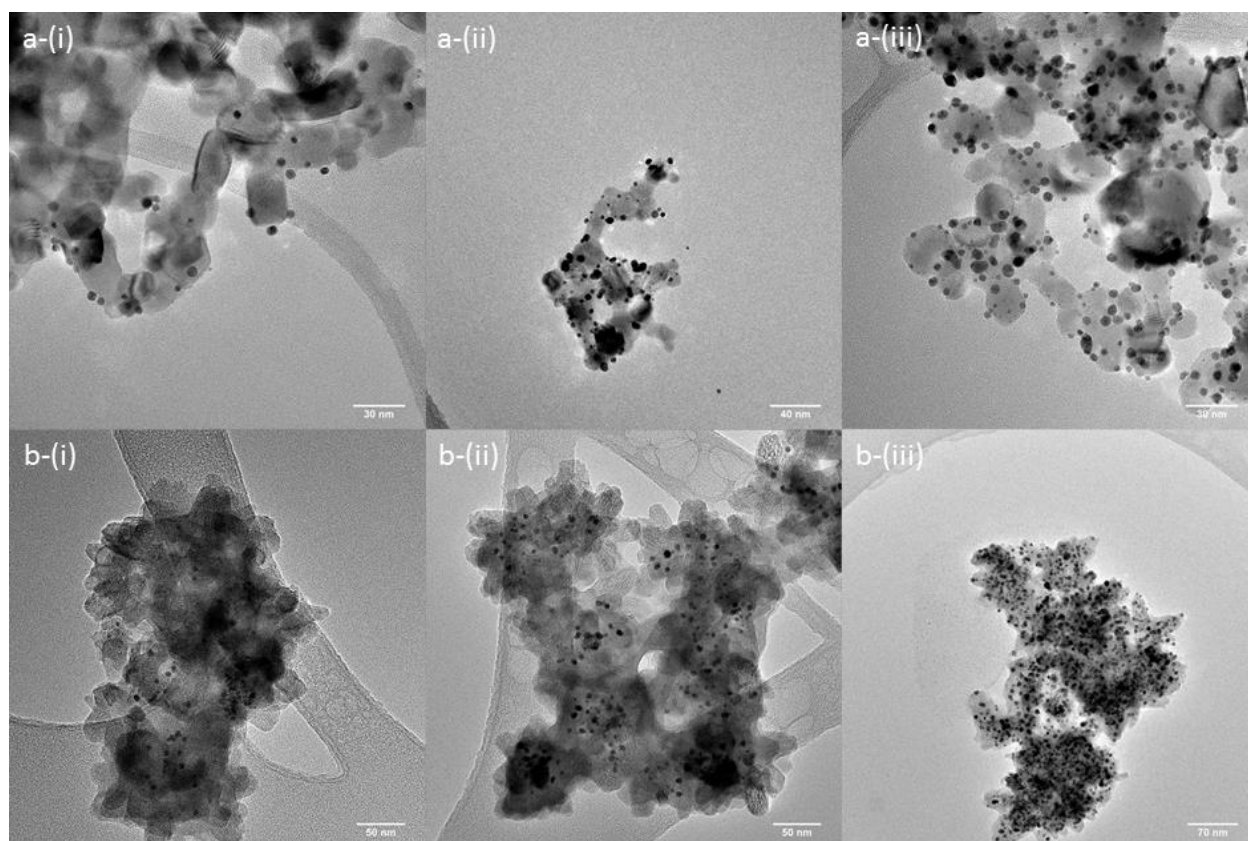


Figure 43. TEM images of a) Au-1/TiO₂A nanocomposite with i) 0.5% wt, ii) 5% wt, iii) 50% wt of Au-1 and b) Au-1/TiO₂B i) 0.5% wt, ii) 5% wt and iii) 50% wt Au-1.

Common feature observed in TEM images for all hybrids of Au-1/TiO₂A type is the placement of Au NPs, which, in spite of 2D nature of TEM micrographs, often seems to be on the lateral surface of TiO₂ NPs. This was confirmed by HAADF-STEM measurements in Figures 44 and 45. In contrast, such distribution of Au NPs is scarcely found in hybrids of the Au-1/TiO₂B type (only in the high 50% loading of the AuNP, but very rarely). This can be explained by employed synthetic routes (Figure 40 in 3.4.1.1. and Figure 41 in 3.4.1.2.).

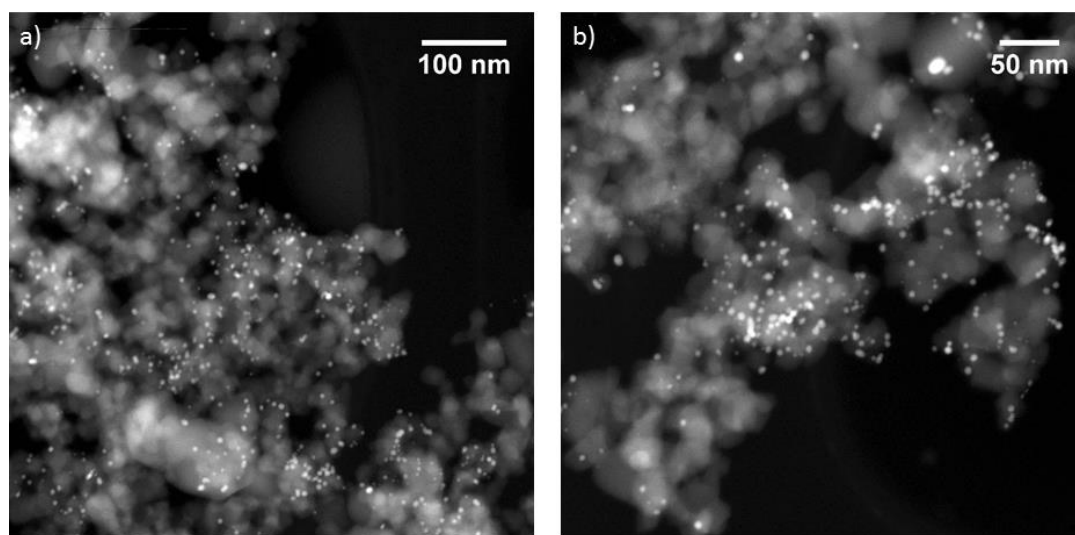


Figure 44. HAADF-STEM micrographs of 5% Au-1/TiO₂A hybrid: a) lower and b) higher magnification.

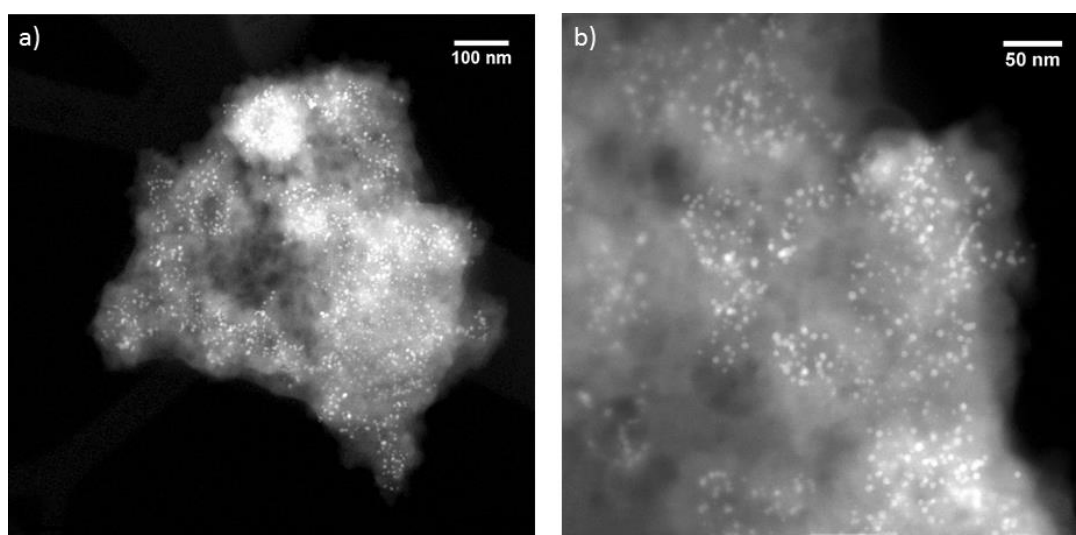


Figure 45. HAADF-STEM micrographs of 10% Au-1/TiO₂B hybrid: a) lower and b) higher magnification.

Namely, in Au-1/TiO₂A, prepared using linker coated Au NP, exposed catechol groups of the LA-DA linker, readily attach to the TiO₂ NPs, forming a nanocomposite in which Au NPs can be observed on the surface of the TiO₂ (Figure 40 in 3.4.1.1.). On the other hand, when the AuNP-1

seed-TiO₂ precursor methodology is used (type B composite), resulting Au-1/TiO₂B hybrid contains Au NPs embedded within the shell of TiO₂ crystalline material (Figure 41 in 3.4.1.2.).

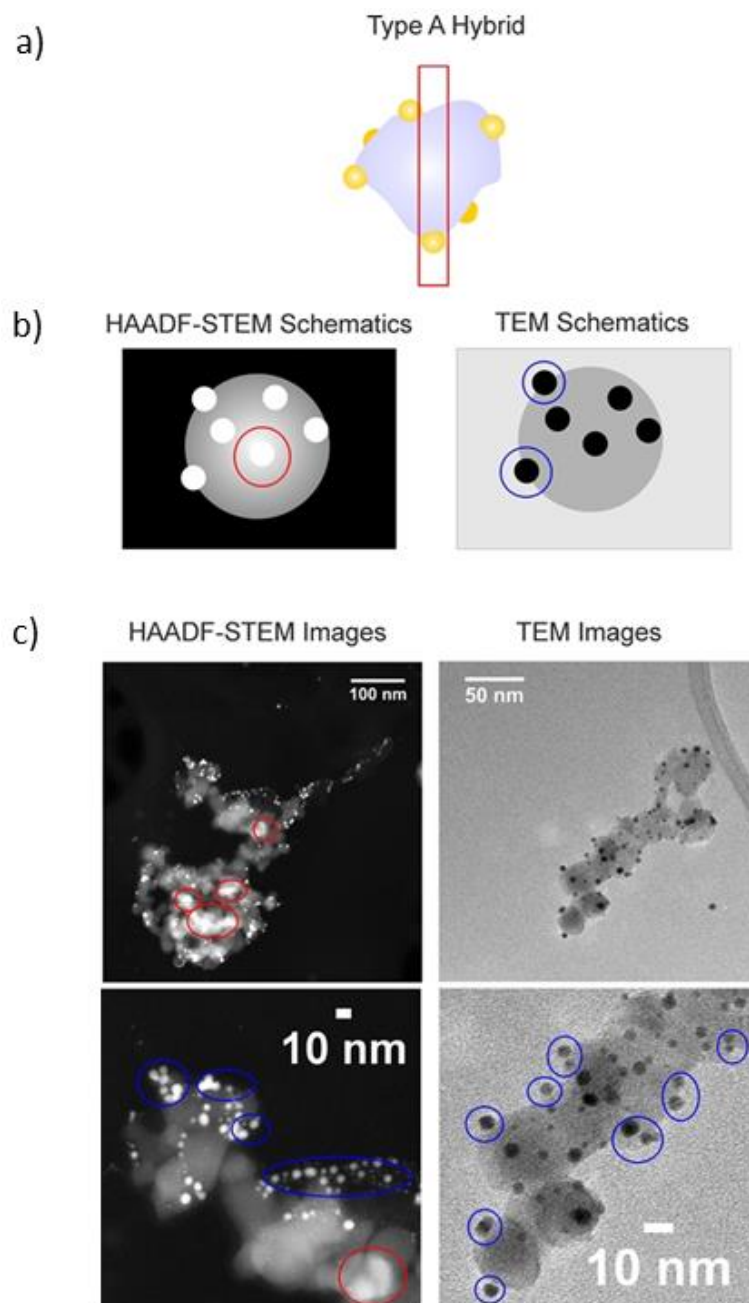


Figure 46. Schematics of the Au-1/TiO₂A hybrid with the cross-section marked with red rectangle (a). HAADF-STEM and TEM image schematics of the hybrid (b left and right). HAADF-STEM (c left) and TEM (c right) image of the Au-1/TiO₂B hybrid (together with higher magnifications). Red circles mark thick parts of the TiO₂A and blue ones laterally positioned Au-1.

Detailed TEM and HAADF-STEM analysis also indicated uniform distribution of Au NPs within the TiO₂ matrix. In both Figures 46 (a) and 47 (a), a red rectangle marks the cross-section through the thickest parts of the hybrids. Since the contrast in the HAADF-STEM images depends on the atomic number (Z) as well as on the sample thickness, the expected brightest parts of the HAADF-STEM images will be Au NPs (high atomic number) and thick parts of the TiO₂ (thickness). Furthermore, if the structure hypotheses are correct, the number of AuNP-1 in type B hybrid will correlate with the thickness of the hybrid (if the NPs are distributed in the volume, the thicker the hybrid the more of NPs present). On the other hand, such correlation is not expected in type A hybrid in which Au NPs are positioned on the surface of the nanocomposite.

The HAADF-STEM images confirm this assumptions and as expected the Au NPs in Figure 44 are not numerous in the area of high thickness, confirming the assumption of the type-A architecture where NP are mainly on the surface of the hybrid materials. In the Figure 46 (c) (right), one can see the TEM image of the type A hybrid, where many of the AuNPs (black spots) are to be seen attached on the lateral surface of the hybrid (blue circles), again confirming the assumptions of the type A architecture.

The HAADF-STEM image in the Figure 47 (c) (left) has a different appearance. The thickness (overall brightness) correlates well with the number of AuNPs observed. In other words, the thickest parts of the TiO₂ (red circles) are embedded with the most NPs, indicating that the Au NPs are volume distributed, which confirms the hypothesis about the type B architecture. The TEM image in the Figure 47 (c) (right) shows no AuNPs on the lateral surface of the hybrid but rather the NPs are embedded in the hybrid interior (green circles).

Further analysis of the lateral surfaces on TEM images of the hybrids only strengthens the two hypotheses. In Figure 48 the TEM images of the type A and B hybrids of the highest loading (20 and 50% Au) are presented and the AuNPs found on the lateral surface are marked with red circles. There is an obvious difference in a number of Au NP present on the lateral surface in type A as compared to type B. When the loading is further increased to 50% Au, few Au NPs can be observed also on the Type B composite surface most probably due to the large amount of starting Au NP, which cannot be embedded into TiO₂ material.

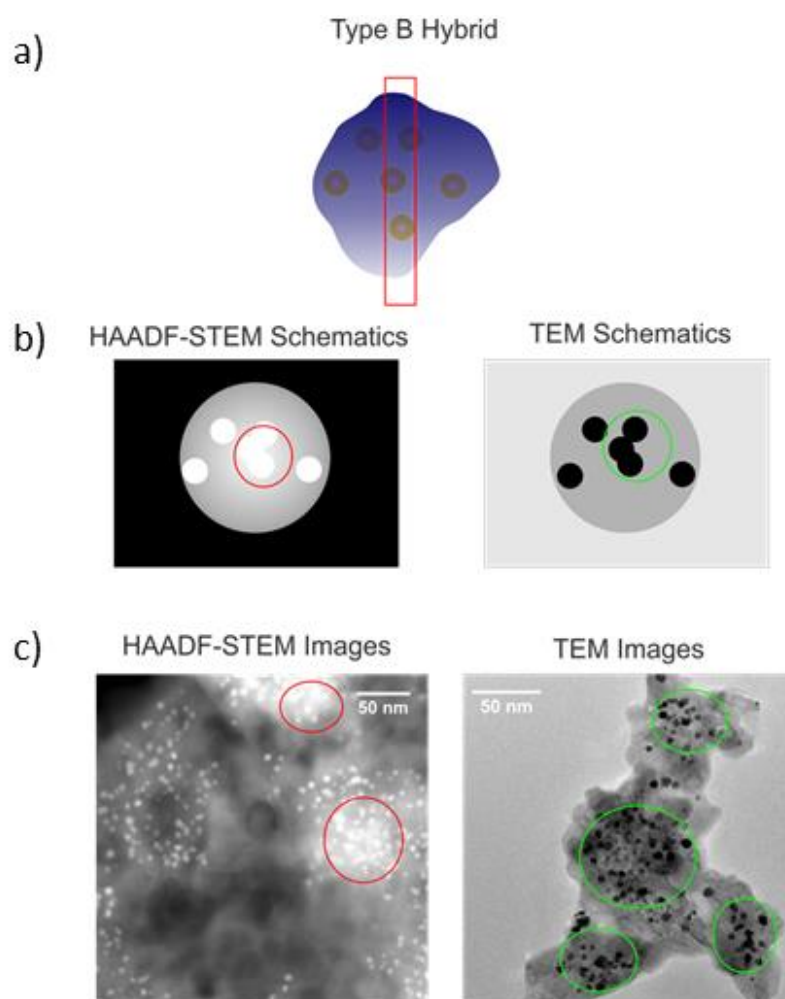


Figure 47. Schematics of the Au-1/TiO₂B hybrid with the cross-section marked with red rectangle (a). HAADF-STEM (b left) and TEM (b right) image schematics of the hybrid. HAADF-STEM (c left) and TEM (c right) image of the Au-1/TiO₂B hybrid. Red circles mark thick parts of the TiO₂B and green ones internally positioned Au-1.

In addition, the morphologies of the Au NPs (Au-1) was investigated after preparation of hybrid to see if there are any changes upon hybrid formation and the results show that Au NPs preserved their size and shape. This indicates that the both the amount and size of Au NPs in the hybrids can be controls enabling the study of their presence on the overall photocatalytic properties.

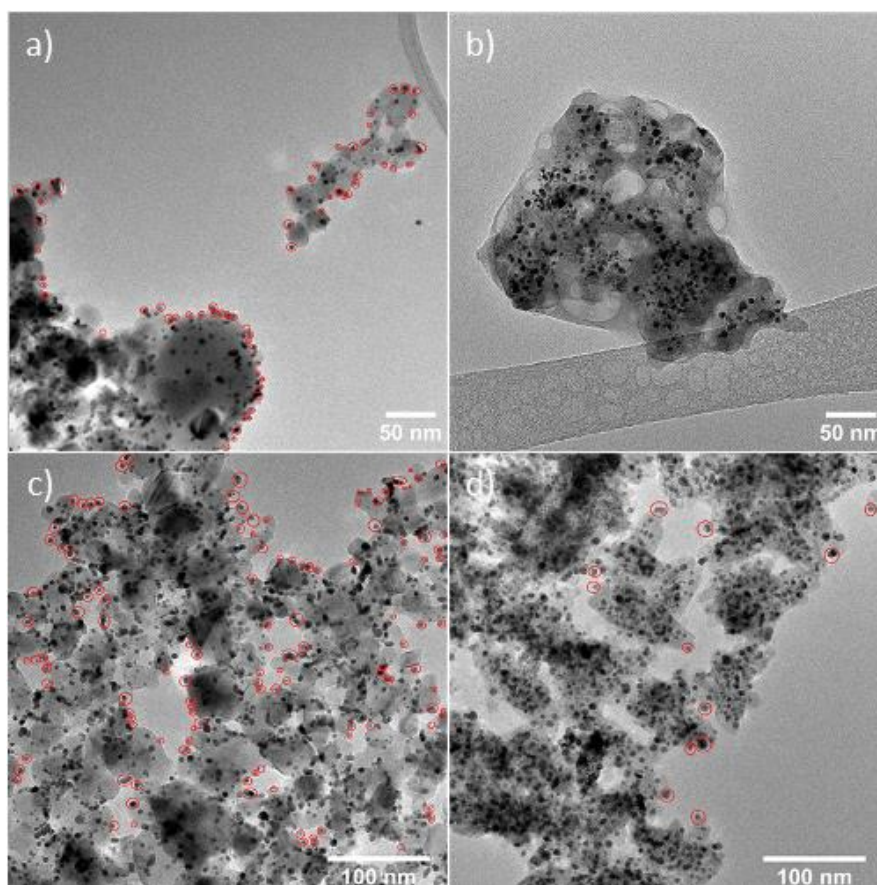


Figure 48. TEM images of: a) Au-1/TiO₂A 20% Au, b) Au-1/TiO₂B 20% Au, c) Au-1/TiO₂A 50% Au and d) Au-1/TiO₂A 50% Au. Red circles mark the laterally positioned Au NPs.

4.4.2.1. B) EDX Analysis

The EDX spectra were made on both hybrids (Au-1/TiO₂A and Au-1/TiO₂B) with same loading of 20% w/w. For each hybrid, the HAADF-STEM image was taken, and according to the image, two spots were chosen, one on the area where the contrast was high (Point 1, presumably Au) and one on the low contrast area (Point 2, presumably TiO₂) (Figure 49 a). The information obtained by EDX spectroscopy of Au-1/TiO₂A hybrid, confirmed that the hybrids consists of both Au and TiO₂ material. As expected from the HAADF-STEM micrographs, the measurement taken at Point 1 (bright area - presumably Au-1) contain many Au-related peaks (Figure 49 b), together with TiO₂ peaks from the surrounding TiO₂A and Cu peaks from the copper meshes on which the sample is held. Point 2 (darker area - presumably TiO₂A) on the other hand, shows only TiO₂ and Cu related peaks, confirming that the Au-1 is not present o that spot (Figure 49 c). The similar study was conducted with Au-1/TiO₂B hybrid, showing two distinct points at which EDX spectra was taken (Figure 50 a). As in the case of type-A hybrid, the results confirmed the presence of Au and TiO₂ at expected areas of type-B.

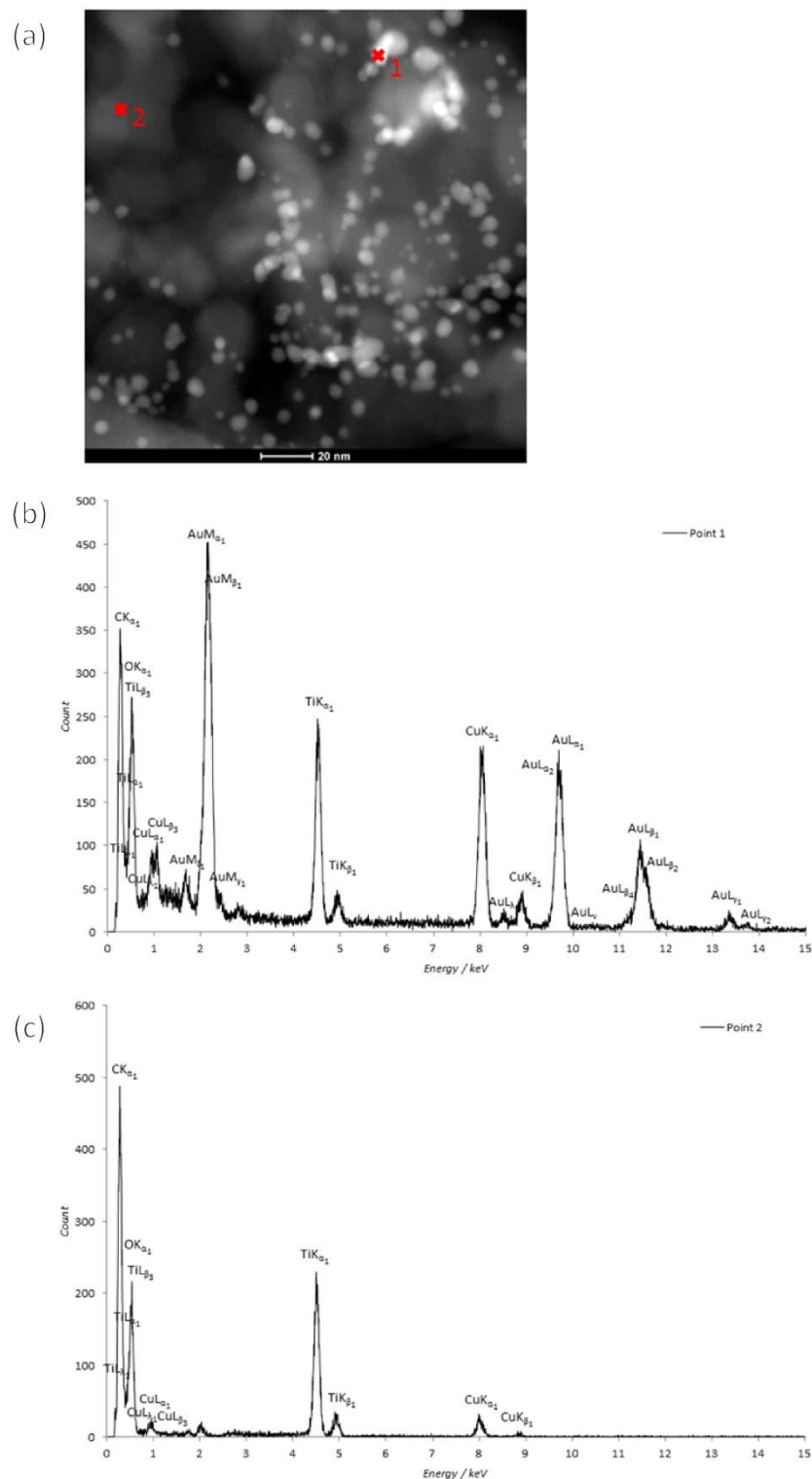


Figure 49. (a) HAADF-STEM micrograph of Au-1/TiO₂A (20% Au loading), with two red points designating the area where the measurements took place. Point 1, bright area - presumably Au-1. Point 2, darker area - presumably TiO₂A. (b) EDX spectrum of Au-1/TiO₂A 20% taken at Point 1. (c) EDX spectrum of Au-1/TiO₂A 20% taken at Point 2.

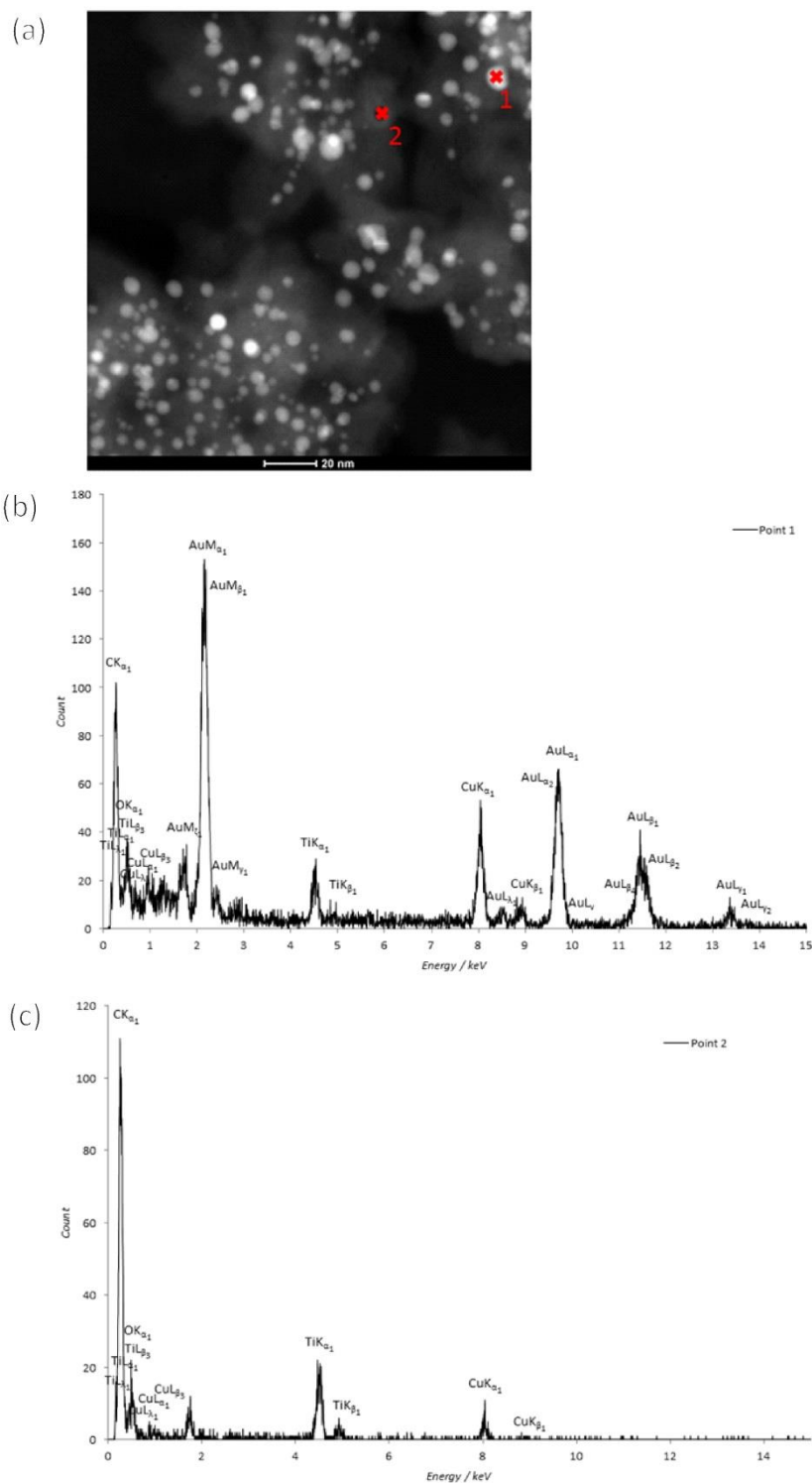


Figure 50. (a) HAADF-STEM micrograph of Au-1/TiO₂B (20% Au loading), with two red points designating the area where the measurements took place. Point 1, bright area - presumably Au-1. Point 2, darker area - presumably TiO₂B. (b) EDX spectrum of Au-1/TiO₂B 20% taken at Point 1. (c) EDX spectrum of Au-1/TiO₂B 20% taken at Point 2.

4.4.2.1. C) Selected Area Electron Diffraction (SAED)

SAED is an experimental technique used widely for obtaining information on the crystal structure of the investigated material. It was used here to determine the crystal structures of the two hybrid types and to detect possible differences.

The crystal structure of both type A and type B hybrids was determined to be mostly anatase TiO_2 . The diffraction rings are presented in Figure 51 (a) for Au-1/ TiO_2 A and 51 (b) for Au-1/ TiO_2 B. The difference between the two diffraction ring patterns was not observed (Figures 51 a and b). The measurements inferred that the systems are tetragonal, with space group $I41/amd$ and lattice parameters of $a=0.3784$ nm and $c=0.9514$ nm, matching the anatase data. The only difference between the patterns is the higher intensity of the rings obtained from Au-1/ TiO_2 A (Figure 51 a) due to the higher crystallinity of the TiO_2 A material used in its assembly. This results was confirm by additional Raman studies (see pg. 104)

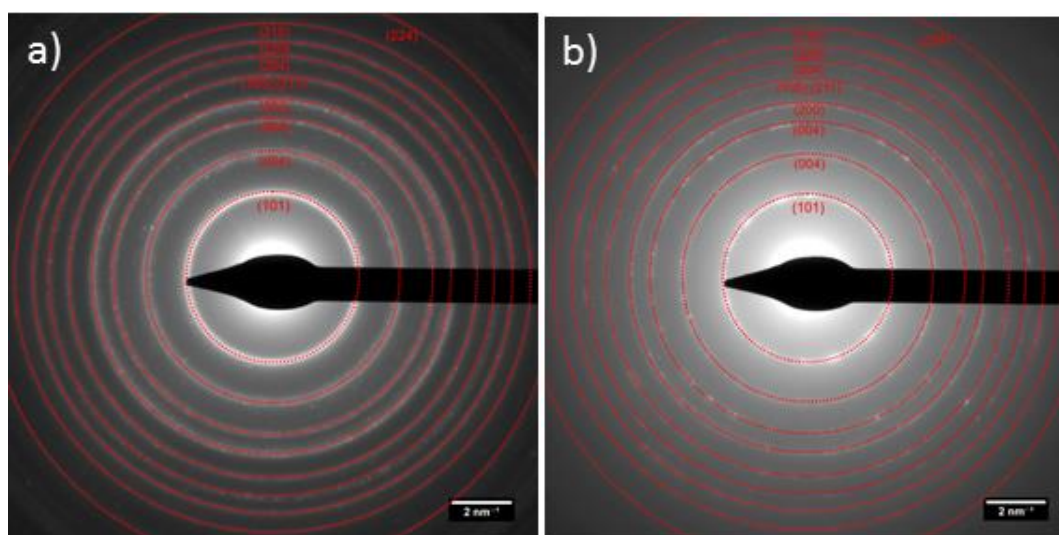


Figure 51. SAED of hybrids with 20% Au loading a) Au-1/ TiO_2 A and b) Au-1/ TiO_2 B.

4.4.2.2. *Spectroscopic analysis of Au/ TiO_2 Nanocomposites*

4.4.2.2. A) UV-Vis Absorption Spectroscopy

Further characterization of Au-1/ TiO_2 A and Au-1/ TiO_2 B hybrids was performed using UV-Vis absorption spectroscopy. Obtained spectra can be utilized for the study of the Au NPs plasmon band

shift due to the presence of TiO_2 in their vicinity. Nanosized semiconducting TiO_2 has been already shown to have high absorption in the UV part of the spectrum (3.0-3.2eV), which we confirmed from the measured absorption peaks around 340 nm in both hybrids.^[302] As shown in Figures 52 (a) and 52 (b), 550 and 580 nm Au NPs plasmon peaks are visible for Au-1/ TiO_2 A and Au-1/ TiO_2 B hybrid respectively (Au-1 plasmon peak being around 519 nm, see Table 2 in 3.2.2.1. on page 65).

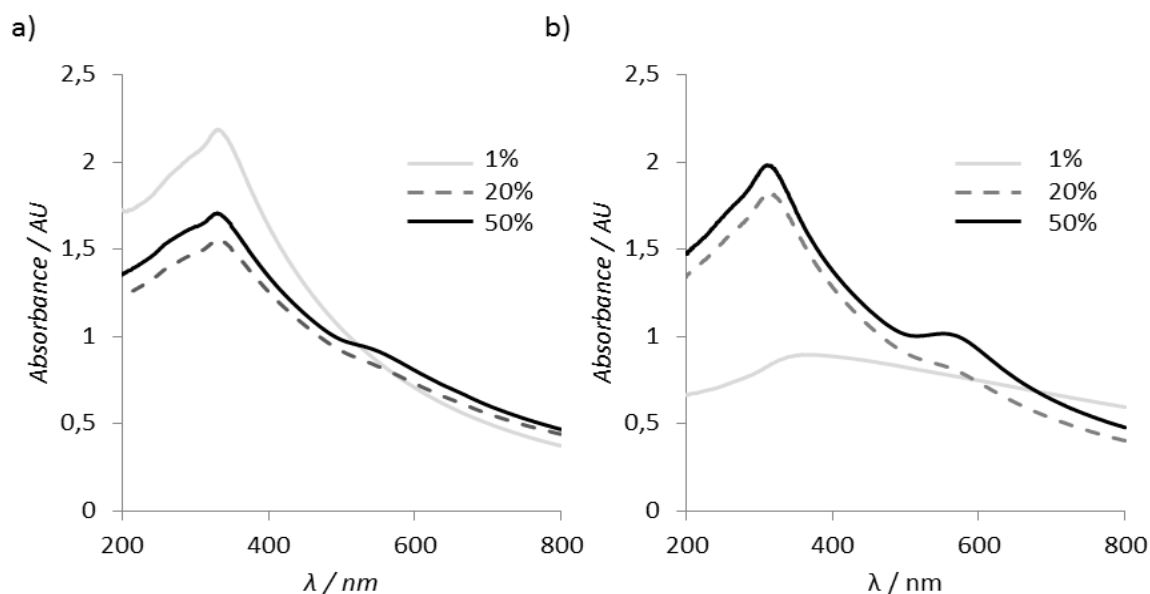


Figure 52. UV-Vis absorption spectra averages (N=3) of a) Au-1/ TiO_2 A and b) Au-1/ TiO_2 B hybrids with different Au loadings (1, 20 and 50% Au)

Stronger red shift in the Au-1/ TiO_2 B hybrid confirms the embedment of the Au NPs within TiO_2 matrix resulting in the change of surrounding dielectric constant and shift of the plasmon peak towards the longer wavelengths. In the Au-1/ TiO_2 A hybrid, where the Au NPs are attached to the surface of the TiO_2 NPs (only one part of their surroundings is changed), the red shift of the plasmon peak is less pronounced.

4.4.2.2. B) Raman Spectroscopy

Raman spectroscopy was used as a complementary method for the investigation of TiO₂ crystal structure in two types of hybrid. In Figure 53 Raman spectra of type A and type B hybrids, both with Au loadings of 0.25%, are presented for comparison. As expected, due to the lower temperatures (100 °C) used in preparation of TiO₂ phase in type B hybrid, the crystallinity is not as high as in the case of commercially available TiO₂A (annealing done on 500-600°C). Nevertheless, the peaks that are observed for type B hybrid still confirm the presence of the same crystal structure, namely the prevalence of anatase to rutile.

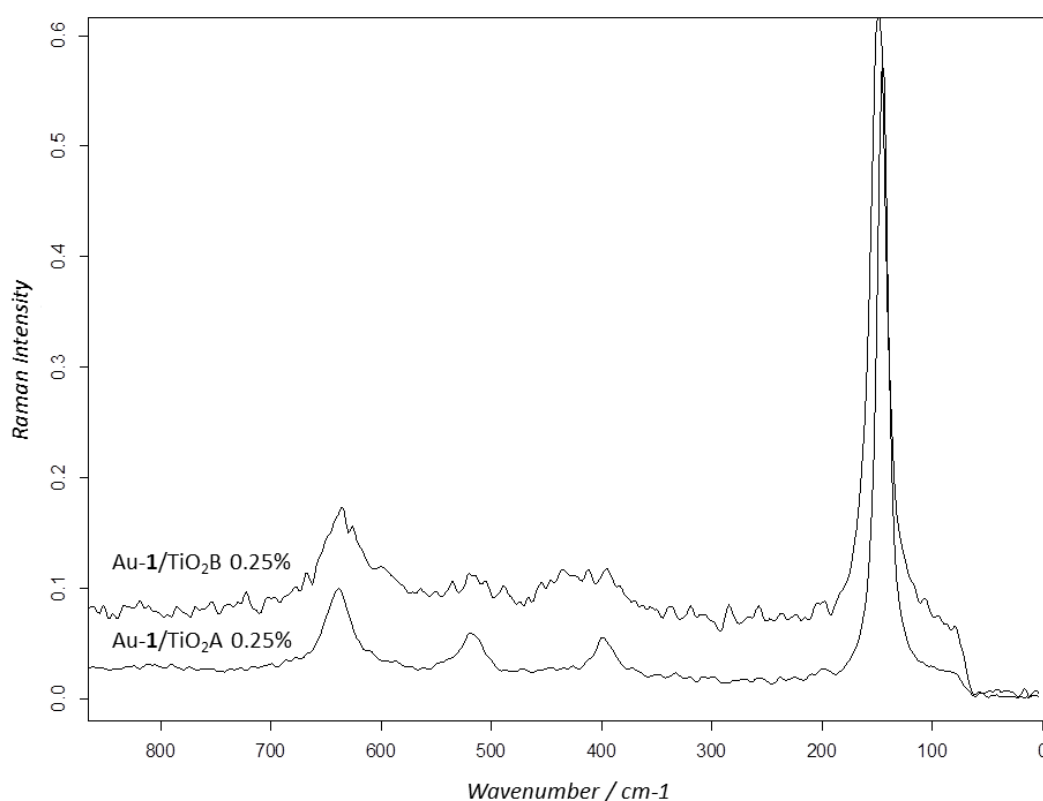


Figure 53. Raman spectra comparison between the 0.25% Au loaded type A and type B hybrids. The measurements were performed on the hybrids in powder form having 0.25% Au loading.

4.4.2.3. Inductively Coupled Plasma Mass Spectrometry (ICP-MS)

The ICP-MS measurements are done to determine the exact ratio between the amount of Au and Ti atoms in hybrids. In the synthesis of the hybrids, 9 different Au loadings (0.1, 0.25, 0.5, 1, 2, 5, 10, 20 and 50%) were planned in order to investigate the influence of Au loading on the photocatalytic properties of the hybrids. As the mass concentrations of both Au-1 and TiO₂A were known, simple calculations led to ratios of the materials that were supposed to result in wanted

ratios. With hybrids in hand the ICP-MS measurements were performed after chemical digestion of the hybrids in aqua regia. The theoretical and measured loadings of the two types of hybrids are presented and compared in Table 4.

Table 4. Comparison of calculated and ICP-MS measured Au/Ti ratios for Au-1/TiO₂A and Au-1/TiO₂B hybrids

Hybrid Type	Method	Au %									
Au-1/TiO ₂ A	Theory	0.1	0.25	0.5	1	2	5	10	20	50	
	Experiment (ICP-MS)	0.09	0.19	0.42	0.87	1.81	4.61	9.71	19.35	43.47	
Au-1/TiO ₂ B	Theory	0.1	0.25	0.5	1	2	5	10	20	50	
	Experiment (ICP-MS)	0.13	0.47	0.74	1.53	2.78	6.89	13.51	24.77	58.58	

As it can be seen from Table 4, the Au/TiO₂ hybrid synthesis using bifunctional LA-DA linker gives high control over the Au loading in the produced hybrids.

4.4.2.4. Zeta potential Measurement and Analysis

Further confirmation of lateral arrangement of Au-1 in type-A hybrids came from the averaged zeta potential measurements. As mentioned before, the zeta potential of Au-1 is -43mV, while the potentials of commercial and synthesized TiO₂ (TiO₂NP B) are around 20 mV (all measured in phosphate buffer, pH=6.0). When the zeta potentials of the type-A hybrids were measured, a steady decrease from -33 mV for 0.1% to -38 mV for 50% Au loading was observed due to the increasing amount of Au NPs on the surface of the hybrids (Figure 54).

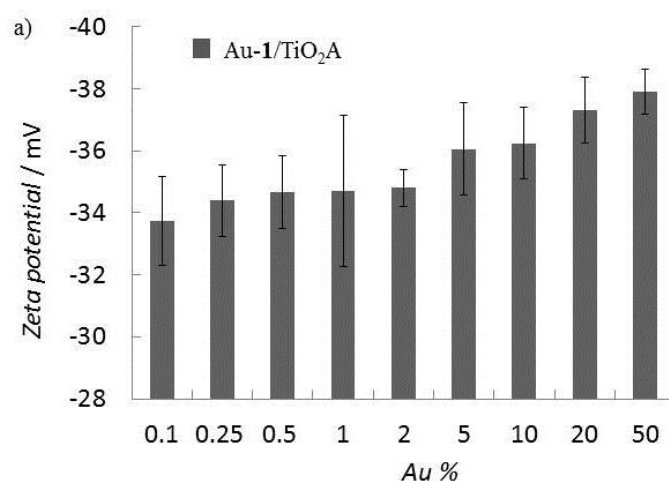
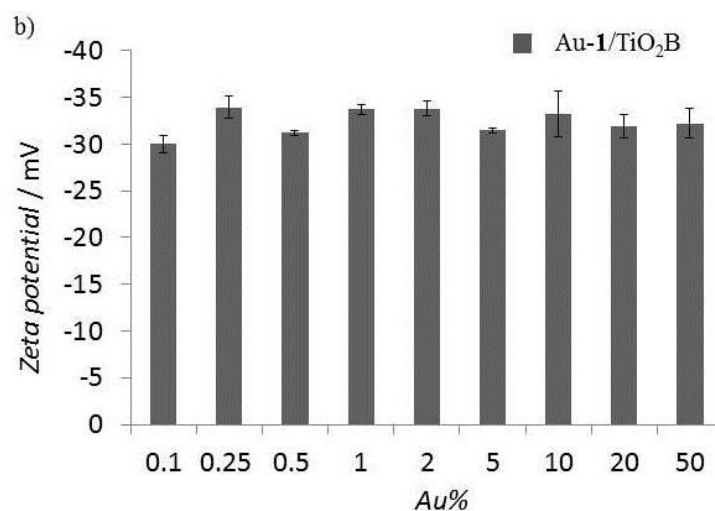


Figure 54. Zeta potential average (N=10) values of Au-1/TiO₂A hybrids.

On the other hand, the increase in Au loading in type B hybrid does not change the surface properties of the hybrid itself as the particles are embedded in TiO₂ matrix. This is confirmed by the value of measured zeta potentials which remain around -30 mV for all type B hybrids (with zeta potential of pure TiO₂B being around -30mV) (Figure 55).

**Figure 55.** Zeta potential average (N=10) values of Au-1/TiO₂B hybrids.

4.4.2.5. Controls

When the control samples were investigated containing citrate coated Au NPs (Au-2), resulting Au-2/TiO₂A hybrids lacked the coloration of the Au-1 counterpart (data not shown), indicating that the bifunctional LA-DA linker plays an important role in the preparation of the Au/TiO₂ nanocomposites.

TEM analysis of Au-2/TiO₂A hybrids showed that almost no Au NPs can be observed even for the higher Au loadings, confirming the assumption about the importance of LA-DA linker for attachment of Au NPs to the TiO₂ surface (Figures 56 a). In the case of type B hybrid, Au-2 were found to be uniformly embedded within the TiO₂ material, indicating that the choice of the linker does not play such an important role in the resulting distribution of Au NPs in type B hybrids (Figures 56 b).

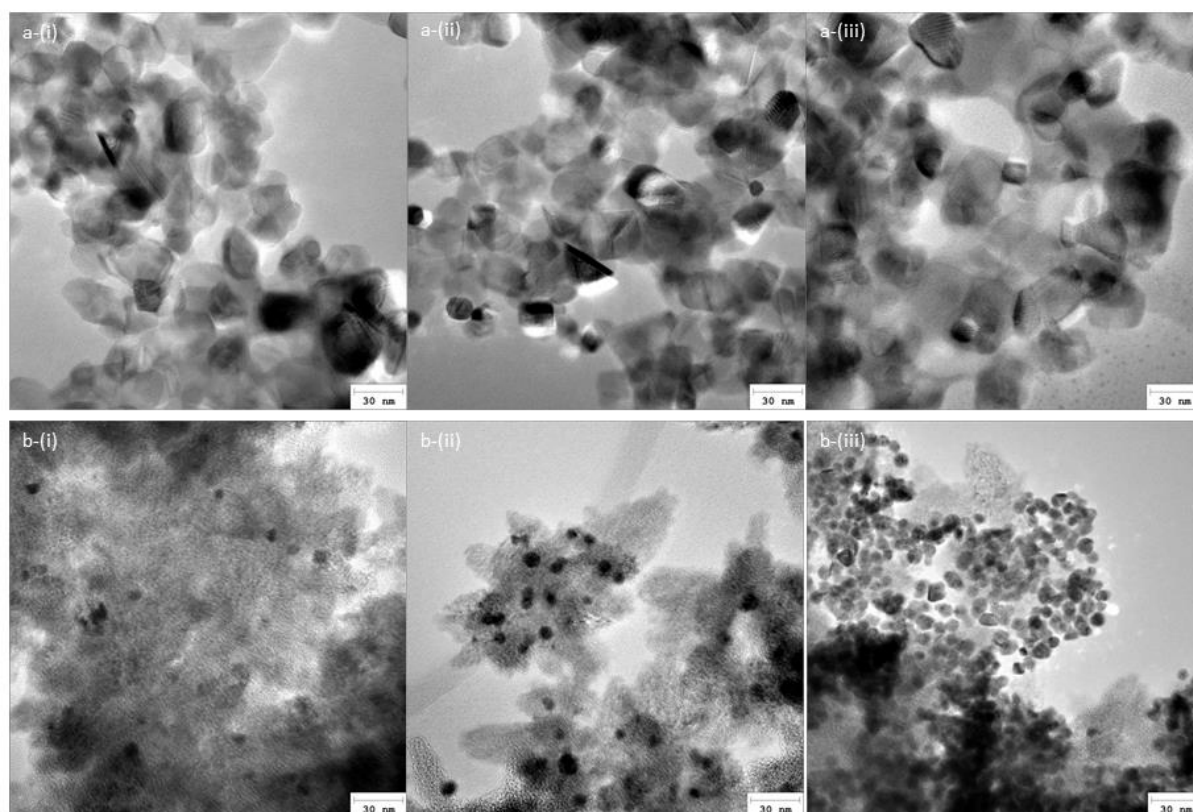


Figure 56. TEM images of a) Au-2/TiO₂A nanocomposite with i) 1% wt, ii) 5% wt, iii) 20% wt of Au-2, and b) Au-2/TiO₂B i) 1% wt, ii) 5% wt and iii) 20% wt Au-2.

4.4.3. ROS Production of Au/TiO₂ Nanocomposites

As described in the chapter 4.3.1.4., we have recently used activation of horseradish peroxidase (HRP) to study the activity of different TiO₂ nanostructures such as NRs and NPs and their applicability for enzymatic activation.^[303] Iron containing catalytic center of the peroxidase enzymes is activated by hydrogen peroxide to catalyze the oxidation of different organic species.^[304] We have therefore designed an assay to assess the photocatalytic activity of hybrid materials based on the HRP activation and the subsequent oxidation of its substrate, Ampliflu Red (Figure 57). Non fluorescent Ampliflu Red is oxidized into highly fluorescent product in the presence of HRP, which is activated by the ROS produced upon the irradiation of Au/TiO₂ hybrid material (controls were made to ensure that the Ampliflu Red does not oxidize only due to the presence of radicals, data not shown). Hence, on one hand, the photocatalytic activity is directly assessed by the fluorescence measurements and on the other hand, the efficiency of the hybrid system is studied on a biological platform paving a way for design of artificial catalytic systems based on enzymatic reactions.

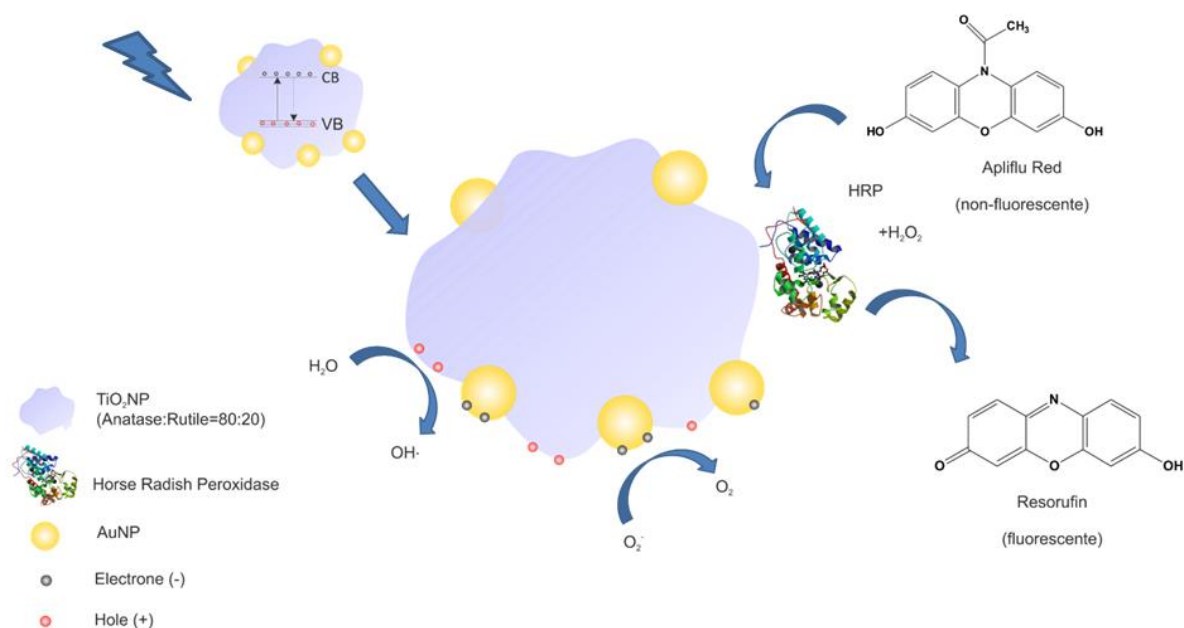
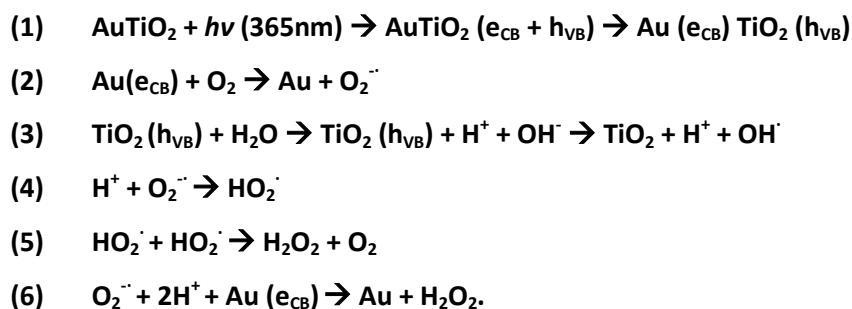


Figure 57. Photoexcitation of Au-1/TiO₂A hybrids and the principle of the enzyme activation and subsequent substrate oxidation, which can be assessed with fluorescence measurements.

4.4.3.1. ROS Production under UV Light Irradiation

As indicated in the introduction, TiO₂ nanostructured materials, in particular when doped with noble metals or QDs show high photocatalytic activity and have been shown to aid the generation of ROS species such as hydroxyl and superoxide radical and hydrogen peroxide (H₂O₂).^[252, 305] [145a, 297] The mechanism of the ROS production when the hybrid is irradiated by 365nm light is described by the following equations (1)-(6):



The role of the noble metal NPs or QDs is in prevention of recombination of the excited charges by serving as an electron sinks (Equation 1). During this time, the holes are free to reduce the

water molecules on the TiO_2 surface (Equation 3), having hydroxyl radical as in intermediate and hydrogen peroxide as an end result.

The photocatalytic activity of the hybrids excited by 365 nm UV-light was tested in the following way. The hybrids of all loadings were dispersed in PB in 1mg/mL concentration. The same amount of each hybrid PB solution was added to the wells of the multi-titer well-plate and irradiated by 365nm light for 10 min. After irradiation the mixture of HRP and AR was added to the wells and stirred in dark for 5 additional minutes.

The results of the fluorescence measurements with 540 nm excitations and 585 nm emissions are presented in Figure 58.

The benefit of the Au loadings is clearly visible as the production of the radicals in comparison to the bare TiO_2 NPs is increased by many folds. It is also evident that the peak performance is reached with relatively low Au loadings as reported previously. The reason for this lies in the fact that the overly charged Au NPs become recombination centers due to the electrostatical interaction with free holes. When the number of such centers increases, so does the recombination rate. This interaction is more obvious for type B hybrids, where the decline in radical production starts when loadings reach 5%. This is easily explained by the morphology of the hybrids. With type B having Au NPs distributed throughout the volume the holes do not need to diffuse long to find the electron residing in such a place.

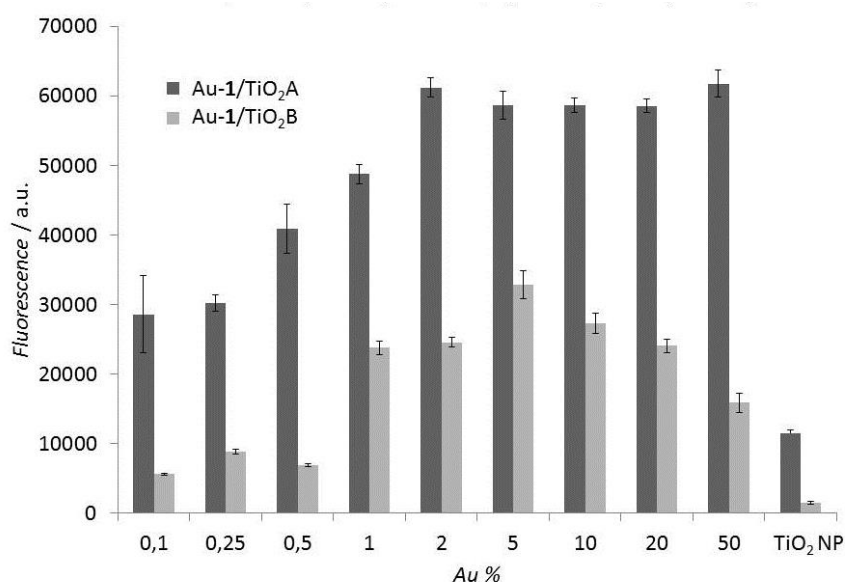


Figure 58. Photocatalytic activity/enzyme activation of Au-1/TiO₂A and Au-1/TiO₂B under 365 nm irradiation (N=3).

The photocatalytic supremacy of type-A hybrid towards type-B hybrid is explained in the following way. The crystallinity of TiO₂ NPs is higher in type A than in type-B, as observed in both Raman spectra and SAED diffraction rings (Chapter 4.4.2.1. and 4.4.2.2.), resulting in higher probabilities of electron-hole excitation upon 365 nm light irradiation. Furthermore, the Au NPs in type-A hybrid are placed on the surface of TiO₂ NPs thus allowing the stored electrons to play a part in redox reactions with the surrounding solution. On the contrary, Au NPs in type B are embedded in the TiO₂ matrix and thus cannot offer the stored electrons to the surface reactions. Nevertheless, both hybrids having 1 to 50 % Au loadings are superior to Degussa P25 (TiO₂A) NPs, which are used as standard and are considered an excellent photocatalytic material.

The presence of the hydrogen peroxide as the main ROS was confirmed by the experiment where the peroxide scavenging enzyme catalase was used. After the light irradiation, 2.5 μl (10 mg/mL) of catalase was added to the controls prior to HRP and Ampliflu Red addition after which the fluorescence was measured. As seen from the Figure 59, the catalase containing controls showed no fluorescence while the catalase free ones were highly fluorescent indicating the high production of peroxide by the hybrids (Equations 1-6). The controls were made where only the ROS production of the Au-1 particles was measured under UV light irradiation and it was confirmed that the tested particles were not good radical producers (data not shown).

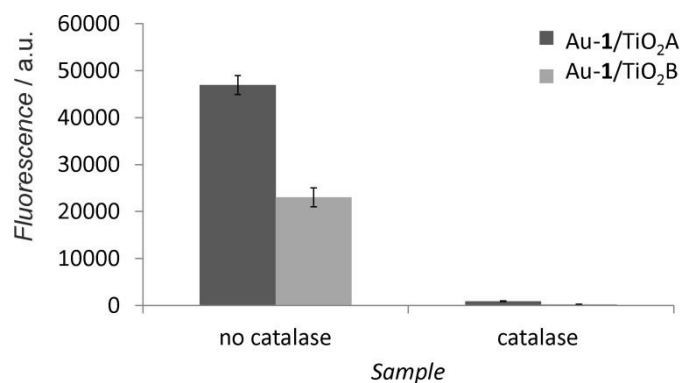
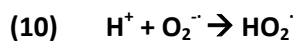
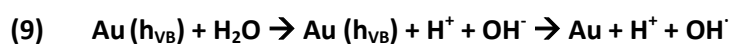
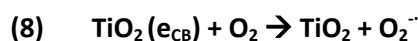


Figure 59. Photocatalytic activity of Au-1/TiO₂A and Au-1/TiO₂B hybrids both with 2% Au loadings, without and in the presence of peroxide scavenging enzyme, catalase (N=3).

4.4.3.2. ROS Production under Visible Light Irradiation

The mechanism of charge separation changes drastically when less energetic light of 470nm wavelength is used. Here, the Au NPs are photoexcited due to the SPR, and the electrons (hot electrons) are injected into the TiO₂ conductive band while the holes stay in the Au NPs.^[222c, 301, 306] The mechanism of the ROS production when the hybrid is irradiated by 470 nm light is described by the following equations (7)-(12):



The experimental setup is identical to the one described in the previous section differing only in the light source which is now taken to have wavelengths of 470 nm (visible blue light). The results of the fluorescence measurements with 540 nm excitations and 585 nm emissions are presented in Figure 60. As shown in Figure 60 the differences between the radical production of type-A and type-B are not as striking as in the case of 365 nm excitation. This is due to the already mentioned SPR-related mechanism of radical production. Here, the crystallinity of the TiO₂ material does not play such an important role as the hot electrons are injected from the Au NPs which are the same in both hybrids regardless of the loading. Similarly as in the 365nm irradiation case, all type-A hybrids have a slightly higher radical production than their type B counterparts. This is due to the morphology of the hybrids as discussed in the previous section, where Au NPs attached on the surface have advantage when compared to the embedded ones. Furthermore, the correlation between the Au loading and the radical production in both hybrid types, as presented in Figure 60, confirms the hypothesis of the SPR-related mechanism. The highest loaded hybrids (50%) show the highest fluorescence, indicating that the most radicals are produced for such loadings.

The comparison with the bare TiO₂ NPs shows that the produced hybrids have superior photocatalytic properties, especially for the Au loadings in the range of 1 to 50 %. In the case of 50% Au loading the hybrids exhibit ~6 fold increases in radical production in comparison to the standards.

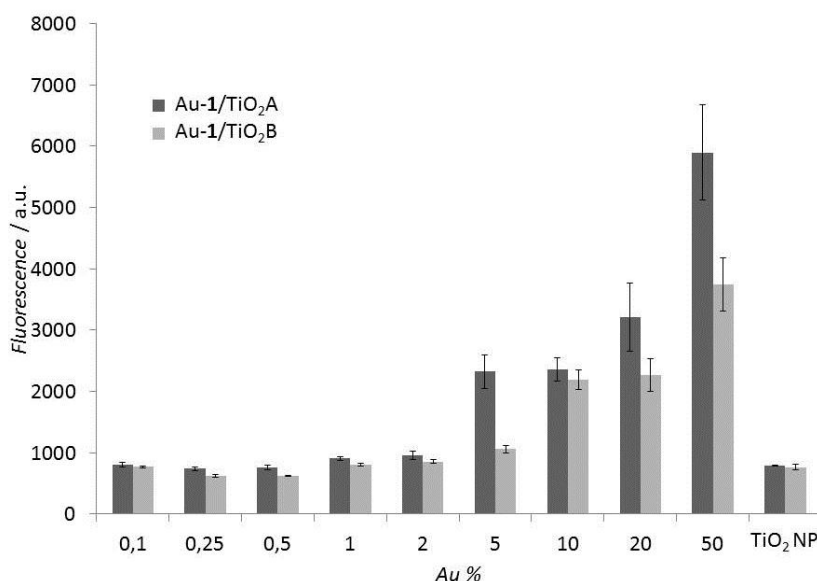


Figure 60. Photocatalytic activity/enzyme activation of Au-1/TiO₂A and Au-1/TiO₂B under 470 nm irradiation (N=3).

4.4.4. Switchability of the Enzymatic Activity in the Presence of Au/TiO₂ Nanocomposites

Finally, we were interested to see if we can achieve temporal control over the enzyme activation as demonstrated by Fruk *et al.* in case of ROS producing, photoactivatable CdS QDs.^[304b]

We have prepared the solution of HRP, Ampliflu Red and hybrid materials, and irradiated it with two different light sources (365 and 470 nm) in regular intervals (2 min).

4.4.4.1. Switchability of the Enzymatic Activity using UV Light Irradiation

From the graph presented in Figure 61 it can be clearly seen that the oxidation of the Ampliflu Red in presence of Au-1/TiO₂A of various loadings, increases only when irradiated with UV light (ON state) indicating that the enzyme is activated upon the irradiation of the hybrid material. The same is true for control TiO₂ NP although the photocatalytic activity is lower as seen from fluorescence intensities measured. When the light sources are switched off (OFF state) no activity increase can be observed. Results shown in Figure Z are in excellent agreement with the 365 nm photocatalytic enzyme activation of the Au-1/TiO₂A hybrid made in the previous section.

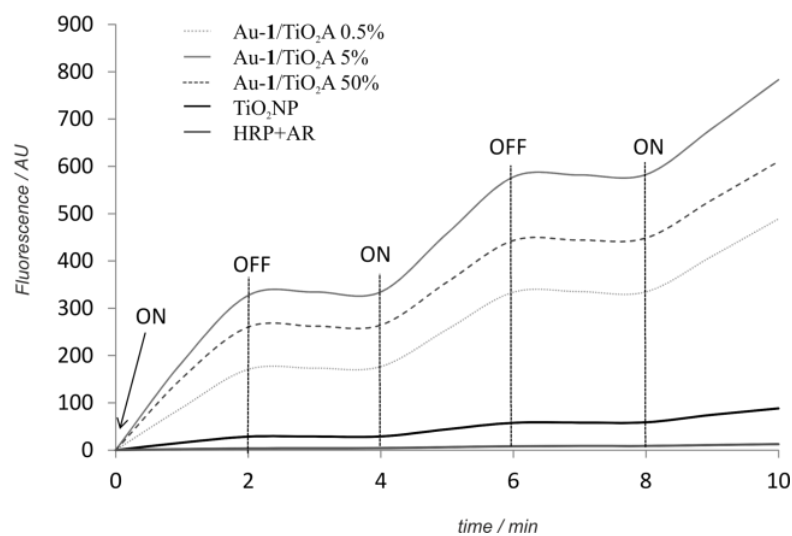


Figure 61. Photoswitchability of HRP by Au-1/TiO₂A hybrids using 365nm light irradiation (N=3).

The increase of Au loading in the hybrids up to the 5 %, leads to the increase of fluorescence, which is in direct correlation with the enzyme activity. The 365 nm HRP photoswitchability is also possible with the Au-1/TiO₂B hybrid, yet the resulting fluorescence is lower as it is in the ROS assay case (Figure 62).

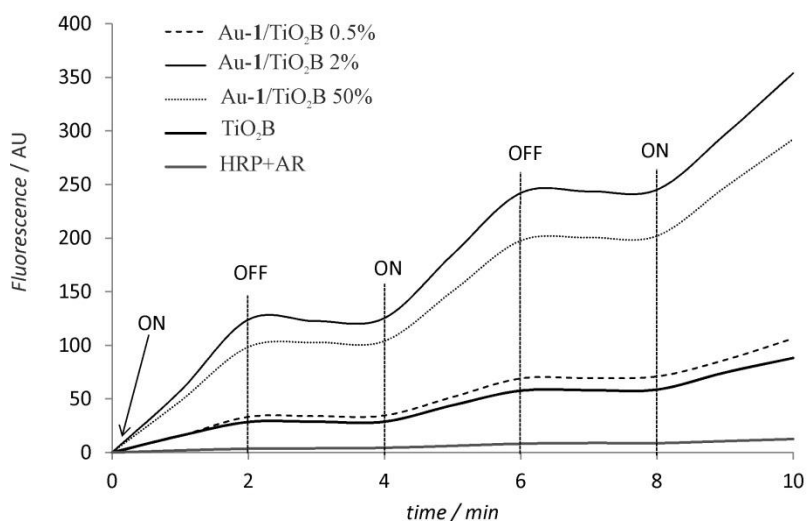


Figure 62. Photo-switchability of HRP by Au-1/TiO₂B hybrids using 365 nm light (N=3).

4.4.4.2. Switchability of the Enzymatic Activity using Visible Light Irradiation

In case of 470 nm irradiation (Figure 63), the best results were obtained for 50% Au-1/TiO₂A and 50% Au-1/TiO₂B confirming the results obtained previously using the standard enzymatic HRP/AR assay.

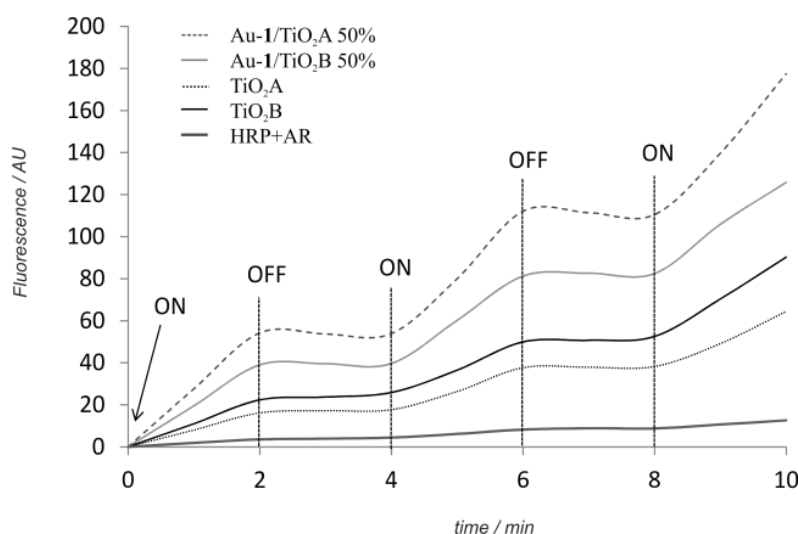


Figure 63. Photoswitchability of HRP by most active 50% Au-1/TiO₂A and 50% Au-1/TiO₂B hybrids using 470nm (N=3).

In conclusion, the Au/TiO₂ nanocomposites were successfully prepared using bifunctional, Au and TiO₂ binding linker, showing significant increase in photocatalytic activity and activation of peroxidase enzyme compared to commercial TiO₂ NPs. The synthetic method is simple and allows a good control of both Au NPs size distribution and Au loading range (0.1 to 50%). Although UV light is often used to activate TiO₂ based catalysts, the presence of Au NPs enables the use of visible light (lower energy) for activation, which is of particular interest for biological applications. Contrary to previous reports we have observed that in some hybrids the higher content of Au NPs leads to the increase of the catalytic activity of prepared material when 365nm light source is used. On the other hand, irradiation with visible light (470 nm) the photocatalytic activity of the hybrids increases with the Au loading. This type of material could find applications in catalysis, in particular light triggered enzyme activation or waste product removal.

4.4.5. Other TiO₂ Nanocomposite Materials

In addition to already discussed Au/TiO₂ hybrid, three other nanocomposite materials were synthesized, one semiconductor-semiconductor hybrid (CdS/TiO₂) and one additional metal-semiconductor hybrid (Ag/TiO₂). As they were not a centerpiece of this work, experimental data on these hybrids is not as extensive as in the previous section on Au/TiO₂ hybrid.

4.4.5.1. *Ag/TiO₂ Nanocomposite Prepared Using Bifunctional LA-DA Linker*

Firstly, Ag/TiO₂ nanocomposites synthesis will be presented together with the following characterization, as it is expected to possess very similar properties as Au/TiO₂ hybrid due to the similarity of the elements involved in their production.

4.4.5.1. A) Synthesis of Ag-1/TiO₂A hybrids

The 24.5 nm diameter LA-DA capped Ag NPs (Ag-1) and commercially available Degussa P25 powder (TiO₂A), were the chosen components for assembly of Ag-1/TiO₂A nanocomposites.

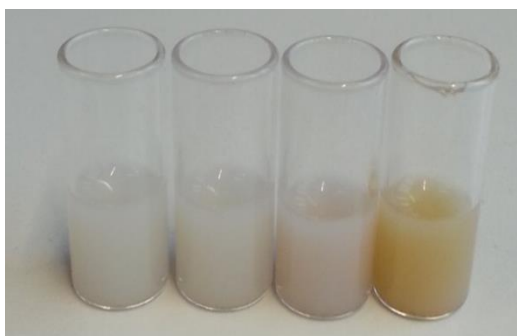


Figure 64. Colour changes observed in the suspension of Ag-1/TiO₂A nanocomposite in pH 6 phosphate buffer (PB) with increasing % wt of Ag (0.5, 1, 2 and 10 from left to right hand side).

Ag-1/TiO₂A synthesis was identical as the synthesis of Au-1/TiO₂A hybrid, only the chosen loadings were in a narrower range (0.5, 1, 2 and 10%). On visual inspection, the synthesized hybrids

had the coloration matching the loading percentages as seen on the photography of the hybrids in Figure 64.

4.4.5.1. B) Characterization of Ag-1/TiO₂A hybrids

On inspection of the TEM micrographs (Figure 65), the number of the observed Ag NPs matches the Ag loading percentages. As the Ag NPs have similar sizes to TiO₂, red arrows were used to discern them and to indicate the position of the Ag-1 on the micrographs.

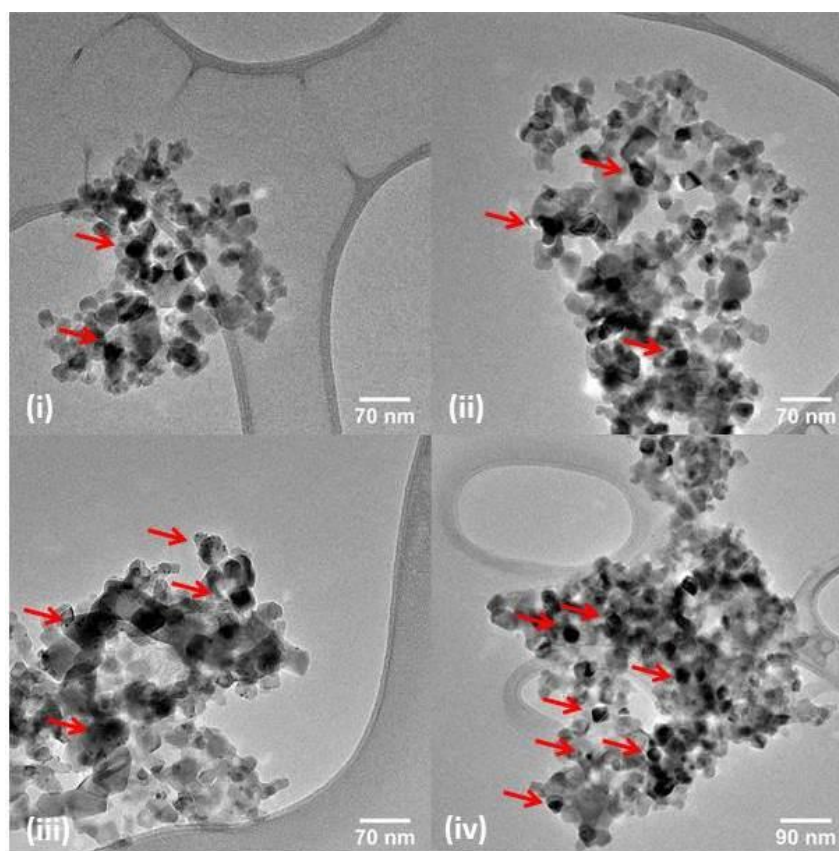


Figure 65. TEM images of Ag-1/TiO₂A nanocomposite with i) 0.5% wt, ii) 1% wt, iii) 2% wt and iv) 10% of Ag-1.

The UV-Vis absorption spectra of all the hybrids are presented in Figure 66. Contrary to the previous case of the Au/TiO₂ hybrids, here it cannot be claimed the SPR peaks of the Ag/TiO₂ hybrids red-shift in comparison to the Ag-1 due to their attachment to the surface of TiO₂ NPs (change of the surrounding dielectric constant), because the peaks are blended with the absorption peaks of the TiO₂ material, making it is difficult to separate the contribution of each material.

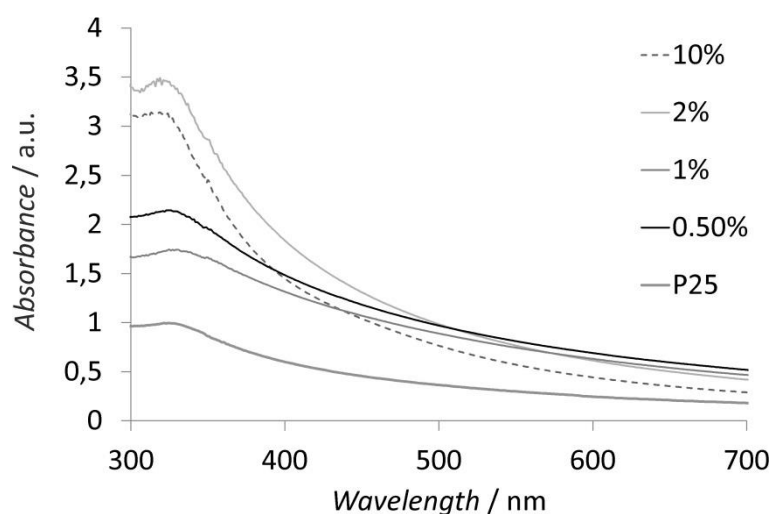


Figure 66. UV-Vis absorption spectra of Ag-1/TiO₂A hybrids with different Ag loadings (0.5, 1, 2 and 10% Ag)

Furthermore, the absorption spectra presented in Figure 66 does not match perfectly the naked eye observation presented in the Figure 64. A tail of absorption spectrum extending far into the visible region can be observed for all the synthesized hybrids, although the extent to which this happens does not correspond well with the loadings of the hybrids (*e.g.* one the basis of Figure Q, one would expect highest absorption for 10% loading).

The Zeta potential measurements gave value of -43, -42.5, -43.5 and -46 mV for hybrids with 0.5, 1, 2 and 10% respectively. This correlates relatively well with the idea that with the increasing of the Ag loading, the surface of hybrids becomes covered with negatively charged Ag NPs, thus shifting the zeta potential to more negative values.

4.4.5.1. C) Photocatalytic activity of Ag-1/TiO₂A hybrids

It was assumed that the Ag-1 NPs should act in a similar way when attached to TiO₂ NPs as do the Au-1 NPs in Au/TiO₂ hybrids. Hence, it is expected to observe the enhanced photocatalytic activity of the Ag-1/TiO₂A hybrids in comparison to the standard TiO₂A. The photocatalytic radical production of Ag-1/TiO₂A hybrids upon 365 nm light irradiation was measured with the standard enzymatic HRP-AR assay. The results are presented in Figure 67.

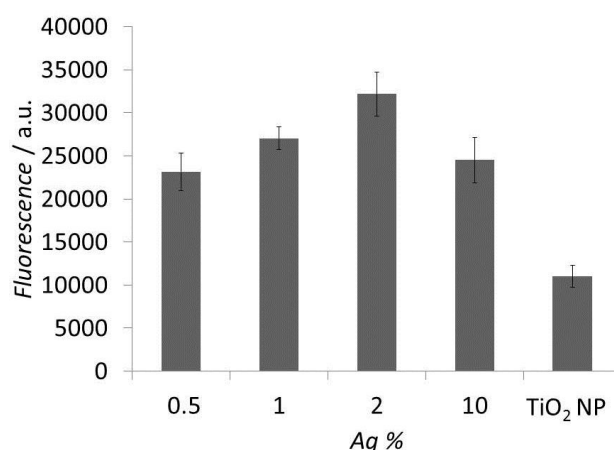


Figure 67. Photocatalytic activity/enzyme activation of Ag-1/TiO₂A under 365 nm irradiation.

The measurements presented in Figure W show that the photocatalytic activity of the Ag-1/TiO₂A hybrids indeed exceeds the one of the TiO₂ standard by 2-3 times depending on the Ag loading. Similarly to Au-1/TiO₂A, the radical production increases up to the 2% loading, when it starts to fall-off with increased addition of Ag NPs. While up to a certain loading (~2%) Ag NPs act as sinks for electrons and in that way prevent the charge recombination, increasing the loading to higher values brings an opposite effect (too many NPs at the surface, which electrostatically attract holes when filled with electrons and cause charge recombination). The controls were made to ensure that the radical production does not come from the Ag-1 alone (data not shown).

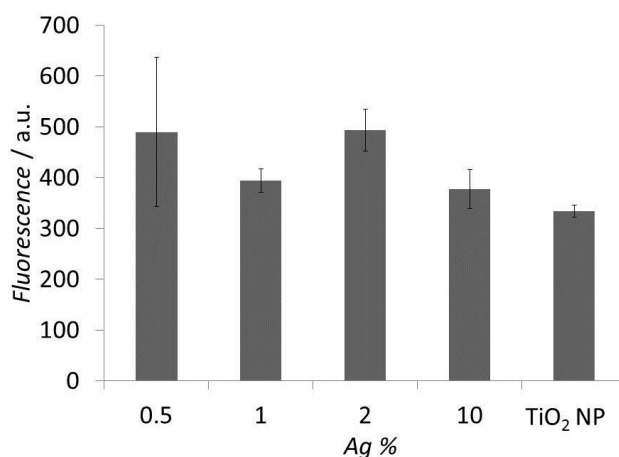


Figure 68. Photocatalytic activity/enzyme activation of Ag-1/TiO₂A under 470 nm irradiation.

Contrary to the Au/TiO₂ hybrids, the Ag-1/TiO₂A do not exhibit a high radical production upon visible light irradiation (Figure 68). Although, the small increase of activity compared to the TiO₂ standard is visible for all loadings, the enhancement is not comparable to the Au based hybrids. It

should be noted that the highest loading of the Ag/TiO₂ hybrids (10%) was lower than the case of the Au/TiO₂ (50%), and that the sizes of the loaded Ag-1 particles (25.5 nm), were few times larger than the ones in the Au/TiO₂ (3.6 nm) nanocomposites.

In conclusion, the use of bi-functional LA-DA linker for synthesis of the Ag/TiO₂ nanocomposites with different loadings was successful and the obtained material has shown excellent photocatalytic properties when irradiated with 365 nm light. The further optimization in synthesis would surely further improve these properties and possibly improve the catalysis upon visible light irradiation.

4.4.5.2. CdS/TiO₂ Nanocomposite Prepared Using Bifunctional LA-DA Linker

Secondly, the proof-of-concept CdS/TiO₂ nanocomposite synthesis will be presented, followed by the characterization of the obtained material.

4.4.5.2. A) Synthesis of CdS-1/TiO₂A hybrid

The 8 nm diameter LA-DA capped CdS NPs (CdS-1) and commercially available Degussa P25 powder (TiO₂A), were the chosen components for assembly of CdS-1/TiO₂A nanocomposite. The steps in the CdS-1/TiO₂A synthesis were identical to the steps in Au and Ag hybrid synthesis, although this time the procedure was only used for the proof-of-concept study with only one loading percentage of CdS-1 (approximately 20%). From the photography presented in Figure 69, one can see that the obtained hybrid (middle) is well dispersed and shares the features from both pure TiO₂ (left, white and turbid) and CdS-1 (right, yellow and clear).



Figure 69. Colours observed in the suspension of TiO₂A (left), CdS-1/TiO₂A (middle) and CdS-1 (right) in pH 6 phosphate buffer (PB).

4.4.5.2. B) Characterization of CdS-1/TiO₂A hybrid

Unfortunately, due to the very small size of the CdS-1 particles it was not possible to detect them in the TEM micrographs of the hybrids. Another reason for the inability to detect the attached particles is the relatively low atomic number of Cd and S in respect to *e.g.* Au, which results in weaker contrast of the CdS-1 in the TEM micrographs (Figures 70 a and b). UV-Vis absorbance of the CdS-1/TiO₂A hybrid is presented in Figure 70 b.

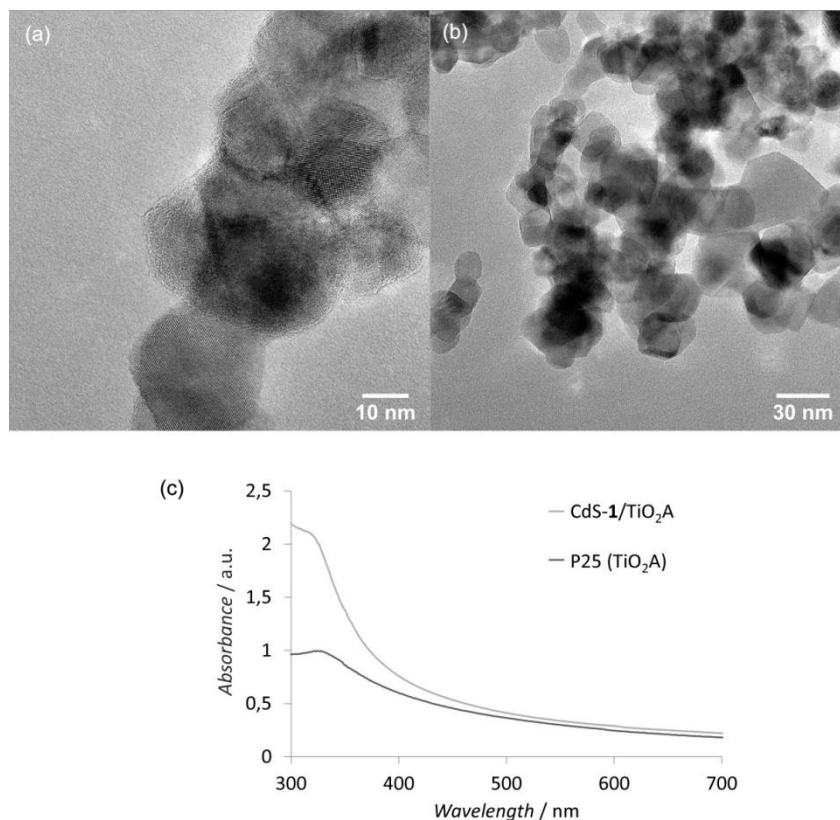


Figure 70. (a) and (b), TEM micrographs of the CdS-1/TiO₂A hybrid with different magnifications. (c) UV-Vis absorbance average (N=3) of the CdS-1/TiO₂A hybrid.

4.4.5.2. C) Photocatalytic activity of CdS-1/TiO₂A hybrid

To investigate whether the CdS NPs have the influence on the photocatalytic activity of the TiO₂A, the enzyme based assay was used to measure the radical production of the CdS-1/TiO₂A hybrid under UV light irradiation. The comparison between the standard TiO₂A and the CdS-1/TiO₂A hybrid is presented in the Figure 71.

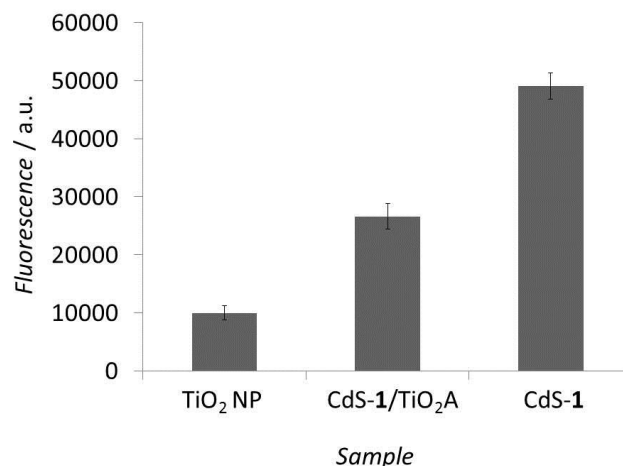


Figure 71. Photocatalytic activity/enzyme activation of TiO₂A, CdS-1/TiO₂A and CdS-1, under 365 nm irradiation (N=3).

At first, it seems that the CdS-1 particles have a similar effect on the photocatalysis of the TiO₂A. In the case of CdS-1/TiO₂A hybrid, the radical production is increased around 2 fold, while in the case of Ag-1/TiO₂A and Au-1/TiO₂A the increase was 3 and 5-6 fold, respectively. Nevertheless, when control experiments were made when only the CdS-1 particles were irradiated, it was discovered that they alone result in much higher radical production as presented in Figure 71. This is not surprising, as CdS-1 particles are semiconductor NPs, which undergo similar processes as TiO₂ NPs when irradiated with light of an appropriate wavelength. The difficulty in performing the control experiment is introduced as the exact loading of the CdS-1/TiO₂A is not known (it is assumed to be 20% based on the materials used in the synthesis). This unknown loading makes it difficult to determine the exact concentration of the CdS-1 that is to be used in control experiments and the full control of the experiment cannot be achieved without the exact determination of the amount of CdS-1 on the TiO₂ surface (ICP-MS measurements). The photocatalytic activity of the CdS-1/TiO₂A hybrid as well as CdS-1 particles was further investigated upon visible light irradiation (470 nm), where a different effect was observed (Figure 72). Here, both TiO₂A and CdS-1 alone showed relatively little activity when compared to the hybrid material, which indicates certain synergetic processes between the materials that enhance its activity upon the visible light irradiation.

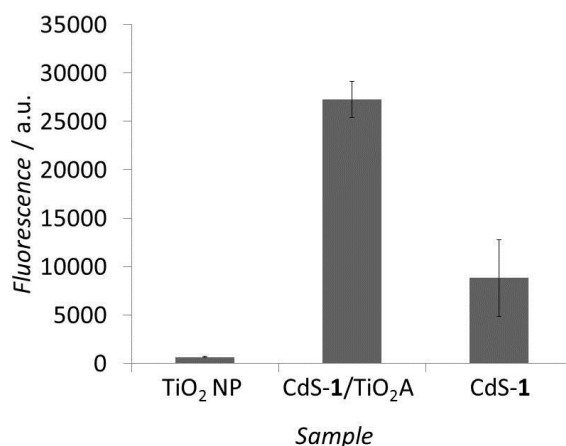


Figure 72. Photocatalytic activity/enzyme activation of TiO₂A, CdS-1/TiO₂A and CdS-1, under 470 nm irradiation (N=3).

The proof-of-concept CdS-1/TiO₂A study lacks a strong proof of successful assembly of its constituents, although some of the macroscopic properties and activation upon visible light irradiation are indicative of the hybrid formation.

4.5. Nanomaterial Light-induced (NALI) Cell Toxicity

In the following chapters the toxicity of the previously described nanomaterials in combination with light will be investigated using mammalian and plant cell lines. The study of toxicity mechanisms is one side, important to assess environmental impacts of nanomaterials and on the other, due to the recent developments on nanomedicine and importance of nanomaterials for programmed cell death.^[7] The results of such studies could have an effect on creating new strategies for biomedical applications or provide important information on hazards in the use of specific nanoparticulate structures.

4.5.1. *Nicotiana tabacum* cultivar Bright Yellow-2 (cv. BY-2) - Tobacco Cell Line

Established cell lines enable reproducible research and play an important role in the basic understanding of the molecular and cellular biology of mammalian and plant cells. The establishment of cell lines from plant tissues is relatively easy and numerous cell lines have been obtained from various tissues and species of higher plants. Among these, the tobacco BY-2 cell line, isolated by Kato

and coworkers in 1972,^[307] is rather unique and is well characterized.^[308] This cell line is highly homogeneous and shows an exceptionally high growth rate, multiplying 80- to 100-fold in 1 week and a high cell cycle synchrony can be obtained after treatment with aphidicholin. Due to their exceptionally high homogeneity and high growth rate, featuring still general behavior of plant cells, the BY-2 cells are used as model systems for higher plants. The diversity of cell types within any part of a naturally grown plant (*in vivo*) makes it very difficult to investigate and understand some general biochemical phenomena of living plant cells. The transport of a solute in or out of the cell, for example, is difficult to study because the specialized cells in a multicellular organism behave differently. Cell suspension cultures such as tobacco BY-2 provide good model systems for these studies at the level of a single cell and its compartments because tobacco BY-2 cells behave very similarly to one another. The influence of neighboring cells in the suspension is not as important as it would be in an intact plant. As a result, any changes observed as a consequence of an applied stimulus can be statistically correlated and it could be decided if these changes are reactions to the stimulus or just merely coincidental. BY-2 cells are relatively well understood, widely used and as a model plant system especially useful for studies of cell division, cytoskeleton, plant hormone signaling, intracellular trafficking, and organelle differentiation.

4.5.2. Nanoparticle Light Induced (NALI) Toxicity in plant cells

In the first NALI study, influence of the commercial P25 powder on the BY-2 cell line was studied. Both naked and modified TiO₂ NPs as described in the chapter 4.3.1.2. were used.

Standard NALI toxicity experiment proceeded as follows. The BY-2 cells were used when they were 3 days old, *e.i.* in their log phase. They were distributed in two 16-well plates and the desired TiO₂ NP (unmodified or functionalized) concentration was added to each well. One of the plates was then sealed with UV transparent foil and treated with UV light for 24h, while the other one was kept in the dark. The light source used was 4W UV hand lamp (365 nm) at distance of 3.5cm from the plate. After 24h, the cell death assay with Evans Blue was used for photometrical determination of cell death rate.

4.5.2.1. TiO₂ NP (P25) Light Induced Toxicity

Firstly, the NALI toxicity was measured for the unmodified P25 TiO₂ NPs. The results are presented in Figure 73.

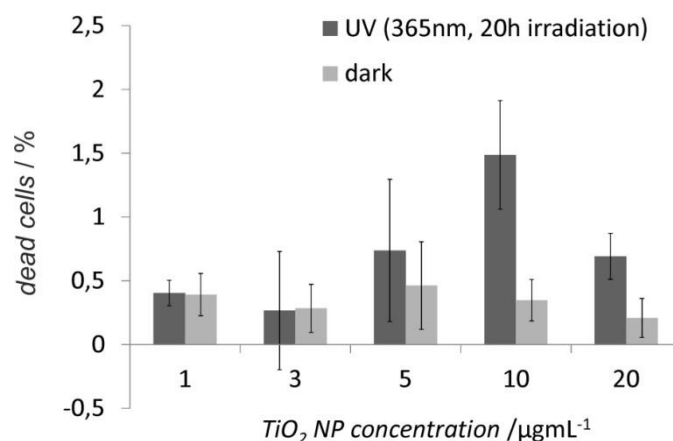


Figure 73. NALI toxicity average (N=3) in BY-2 cells for various concentrations of unmodified TiO₂ NP (P25).

As presented in Figure 73, the concentrations of TiO₂ NPs from 1 to 20 μg mL⁻¹ combined with 24h irradiation did not result in high BY-2 cell toxicity, with maximum reached for the 10 μg mL⁻¹ concentration, when approximately 1.5% of the cells were killed. The toxicity of the UV light alone accounted for 1% of the dead cells (subtracted background). Unfortunately, the expected increase in toxicity with the growing concentration was not observed due to the sudden drop of the number of counted dead cells with the highest NP concentration used (20 μg mL⁻¹). On the other hand, the expected lower toxicity in samples treated with the NPs alone, without the UV irradiation, was observed. The concentrations chosen were based on the data in literature,^[309] which resulted in significant cell toxicity in various other cell lines, although the data on TiO₂ NP plant cell toxicity was relatively scarce in comparison to bacteria or mammalian studies.

4.5.2.2. Dopamine Functionalized TiO₂ NP (P25) Light Induced Toxicity

The following NALI toxicity experiment was done with dopamine (DA) modified P25 TiO₂ NPs (TiO₂NP-DA) as it was shown (Chapter 4.3.1.2.) that catechol modified particles exhibit enhanced ROS production. The results are presented in Figure 74.

As shown in Figure 74, the concentrations of DA modified TiO₂ NPs from 1 to 20 μg mL⁻¹ combined with 24h irradiation resulted in somewhat higher BY-2 cell toxicity in comparison to the one demonstrated by the unmodified NPs, with maximum toxicity for 3 μg mL⁻¹ concentration, when approximately 2.5% of the cells were found dead.

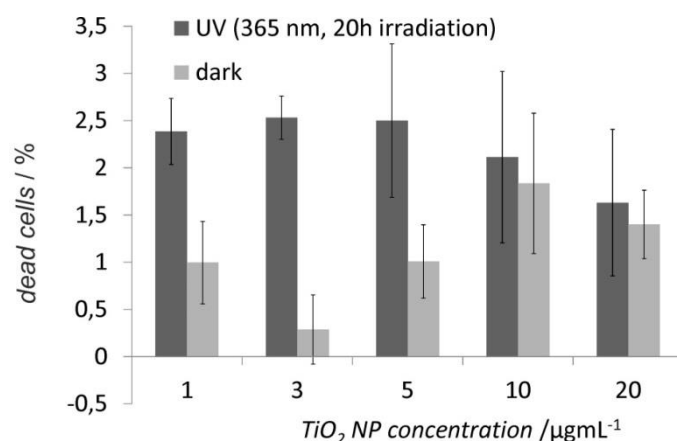


Figure 74. NALI toxicity average (N=3) in BY-2 cells for various concentrations of DA modified TiO₂ NP (P25).

The difference in BY-2 toxicities inflicted by untreated and treated P25 was expected to be bigger, as the DA modified P25 showed higher radical production based on the HRP/AR assay (Chapter 4.3.1.4.). Again, the expected dose response was not observed, as with higher concentrations, the number of observed dead cells does not seem to change much (Figure 74). Somewhat decreased toxicity was observed in samples treated only with NPs, without the UV irradiation, as it was to be expected.

The relatively low toxicity of irradiated unmodified and modified P25 particles toward BY-2 cells can be explained by the ability of plant cells to efficiently scavenge the radicals in their environment. In plants, ROS are continuously produced predominantly in chloroplasts, mitochondria, and peroxisomes^[310] and the production and removal of ROS must be strictly controlled. During the course of evolution, plant cells have developed several mechanisms (both enzymatic and non-enzymatic) that are able to transform highly reactive radical species into some less reactive compound (*e.g.* various peroxidases, super-oxide dismutase or cellular redox buffers ascorbate and glutathione) thus relieving the plant of oxidative damage.^[310] Furthermore, plant cells are known to use the radical production as a form of self-defense against pathogens invasion in a process known as oxidative burst (production of superoxide and hydrogen peroxide).^[310]

In the light of all the stated radical scavenging mechanisms, the reported low toxicity of various types of TiO₂ NPs is not an improbable result. It should be also mentioned that no systematic study of cell uptake was performed and that it is likely that the effects would be significantly higher when NP are internalized by the cell. Therefore, the future work should be focuses on biofunctionalization and study of TiO₂ internalization, where different, more prominent effects of the radical production might be expected.

4.5.3. Cancer Cell Lines

4.5.3.1. HeLa cell line

The HeLa cells are the oldest and most commonly used human cell line which was derived from cervical cancer cells taken from Henrietta Lacks, a patient who eventually died in 1951. The cell line was found to be remarkably durable and prolific as illustrated by its contamination of many other cell lines used in research.^[311] To a great extent it shares the similar attributes as already described BY-2 cell line, namely high homogeneity and an exceptionally high growth rate, as well as the negligible influence from the neighboring cells thus enabling good statistical analysis. HeLa cells have been used to explore the complex processes involved in the growth, differentiation, and death of cell that underlie a vast array of human diseases and have also served as the foundation for developing modern vaccines (polio vaccine), understanding viruses and other infectious agents and devising new medical techniques, such as *in vitro* fertilization. While other immortalized lines are now available, HeLa remains the most widely used cell line in biomedical research, referred to in more than 83,000 scientific publications (data taken from *ScienceDirect*).

4.5.3.2. MCF-7 cell line

MCF-7 is a breast cancer cell line isolated in 1970 from a 69-year-old Caucasian woman Frances Mallon who died the same year. The MCF-7 is an acronym of Michigan Cancer Foundation-7, referring to the institute in Detroit where the cell line was established in 1973 by Herbert Soule and co-workers. The study of this cell line enabled understanding the breast cancer as prior to MCF-7, it was not possible for cancer researchers to obtain a mammary cell line that was capable of living longer than a few months.^[312] MCF-7 and two other breast cancer cell lines, named T-47D and MDA-MB-231, account for more than two-thirds of all abstracts reporting studies on mentioned BCC lines, as concluded from a Medline-based survey.^[313] Similarly to HeLa cell line, MCF-7 cells are one of the more often used systems to explore nanomaterial based toxicity.^[314]

4.5.4. Non-cancer cell line

In this study also non cancer cell line were used, namely Human Embryonic Kidney 293 cells, also often referred to as HEK cell, which are a specific cell line originally derived from human embryonic kidney cells grown in tissue culture. They were generated in the early 70s by transformation of cultures of normal human embryonic kidney cells with sheared adenovirus 5 DNA in Alex van der Eb's laboratory in Leiden, The Netherlands.^[315] HEK 293 cells are very easy to grow and can be readily transfected and are often used biotechnology industry to produce therapeutic proteins and viruses for gene therapy. The HEK293 cell line is used extensively for the nanomaterial toxicity studies, and some of applications are described in the most recent publications including papers by Sadaf *et al.*,^[316] Takafuji *et al.*^[317] and Ribiero *et al.*^[318]

4.5.5. Nanocomposite Light Induced Toxicity on mammalian cells

In this section the results regarding the studies of nanocomposites light induced toxicity will be presented and discussed. This *in-vitro* research investigated the possibility of nanocomposite-light based anti-cancer therapy on various standardized cancer cell lines (HeLa, HEK293 and MCF-7).

The cell viability is assessed using the colorimetric 3-(4,5-dimethylthiazol-2-yl)-2,5-diphenyltetrazolium bromide based assay (MTT assay) which is an established method of determining viable cell number (CV-cell viability) in proliferation and cytotoxicity studies.^[319] This assay is based on the cleavage of the yellow tetrazolium salt, MTT, to form a soluble blue formazan product by mitochondrial enzymes, and the amount of formazan produced is directly proportional to the number of living cells, present during MTT exposure. Since the MTT assay is rapid, convenient, and economical, it has become a very popular *in vitro* technique for quantification of viable cells in many experiments. Tetrazolium dye assays can also be used to measure cytostatic activity (shift from proliferative to resting status) of potential medicinal agents and toxic materials.^[320] The scheme of the assay is presented in Figure 75.

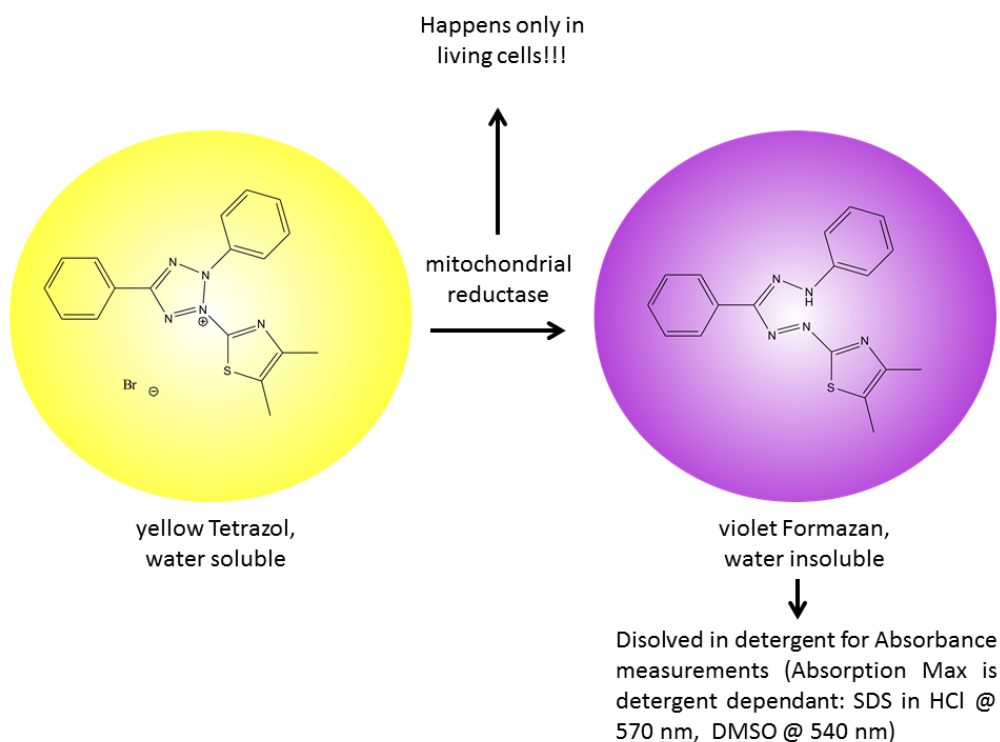


Figure 75. The Scheme of MTT assay. The cleavage of the yellow tetrazolium salt (MTT) by mitochondrial reductase enzyme leads to formation of a DMSO-soluble blue formazan product, amount of which is directly proportional to the number of living cells and can be detected using the standard absorption techniques.

In a standard experiment for the toxicity of one type of hybrid, three different types of cells (MCF-7, HeLa or HEK293) are used and for each cell type one of the plates is irradiated with UV light and the other, control sample, is kept in dark. Cells are counted and seeded on the 96-well plates with cell number depending on the line used (MCF-7 and HEK293 having 40 000 cells/ml, and HeLa with 20 000 cells/ml) and are transferred to the incubator where they are cultivated at 37°C for 24h. On the following day, the investigated nanocomposites are dispersed in cell-medium in various dilutions and then added to the cell-containing plates. One of the plates is immediately returned to the incubator, while the other one is treated with UV light (365 nm) for 15 min. On day 3 of the experiment, the MTT assay is performed in order to determine the viability of the treated cells. The MTT dye is added to the wells and the plates are then incubated for 2h on 37°C, following the addition of the DMSO to dissolve the possibly formed formazan. The amount of the purple formazan is determined through UV-Vis absorption spectroscopy.

4.5.5.1. Nanocomposite Light Induced Toxicity on HeLa cells

The Au/TiO₂ hybrid used in the NALI toxicity study HeLa cells was the Au-1/TiO₂A with 2% of Au loading. The 2% loading was chosen as the experiments were to be done with the UV light source (wavelength ~365 nm) and it was previously shown that such loadings exhibit high ROS production enhancement (not changing for increased Au loading %). The second hybrid used was the Ag-1/TiO₂A hybrid with 2% Ag loading as it has shown the highest ROS production among the Ag/TiO₂ hybrids when irradiated with 365 nm light. The third hybrid was the CdS-1/TiO₂A hybrid with approximate 20% loading of the CdS NPs.

Figure 76 shows the results of the MTT assay for irradiated and control HeLa cells. As expected, less viability is observed upon the light irradiation, with Au/TiO₂ hybrid exhibiting highest NALI toxicity due to the enhanced ROS production as shown in the previous sections (Chapter 4.4.3.1.). The concentration dependence has shown that the tolerance of the HeLa cells are quite high in the dark, with about 80% of CV for the 150 µg mL⁻¹ concentrations in Au and Ag based hybrids as well as for the bare TiO₂ NPs. For example, the median lethal dose (LC50) reported in the TiO₂ NPs (P25) cytotoxicity and inflammatory response study on human dermal fibroblasts and human lung epithelial cells was in ~250-350 µg mL⁻¹ range,^[321] with crystal phase depended toxicity (3.6 µg mL⁻¹ for anatase and 550 µg mL⁻¹ rutile). On the other hand, it was previously established that Au and Ag have relatively high intrinsic toxicity towards mammalian cells (25 µg mL⁻¹) when compared to the P25 TiO₂ material.^[322] As the Au and Ag based hybrids are mostly made out of the P25 TiO₂ material, the results presented in the Figure 76 confirm the mentioned findings, as the extrapolated LC50 for Au-1/TiO₂A and Ag-1/TiO₂A would be achieved for ~300 µg mL⁻¹ concentrations. On the other hand, the CdS/TiO₂ hybrid resulted with only about 25% of CV when administered in the 150 µg mL⁻¹ concentration, most probably due to the intrinsic toxicity exhibited by the present CdS-1 NPs. The previous findings suggest that the CdS cytotoxicity stems from the liberation of free Cd²⁺ ions due to deterioration of the CdS lattice.^[323] For example, cadmium (Cd²⁺) binding to sulfhydryl groups of critical mitochondrial proteins is suggested to be one of the mechanism of hepatocytes injury.^[323] As the rate of Cd²⁺ release depends strongly on the surface coatings, the low CV (25% for 150 µg mL⁻¹) in the case of the CdS/TiO₂ hybrid indicates that certain ruptures might occur when LA-DA is attaching to both CdS-1 and P25 TiO₂ NP, in which case the doors for the release of the Cd²⁺ would be wide open and high toxicity would be justified.

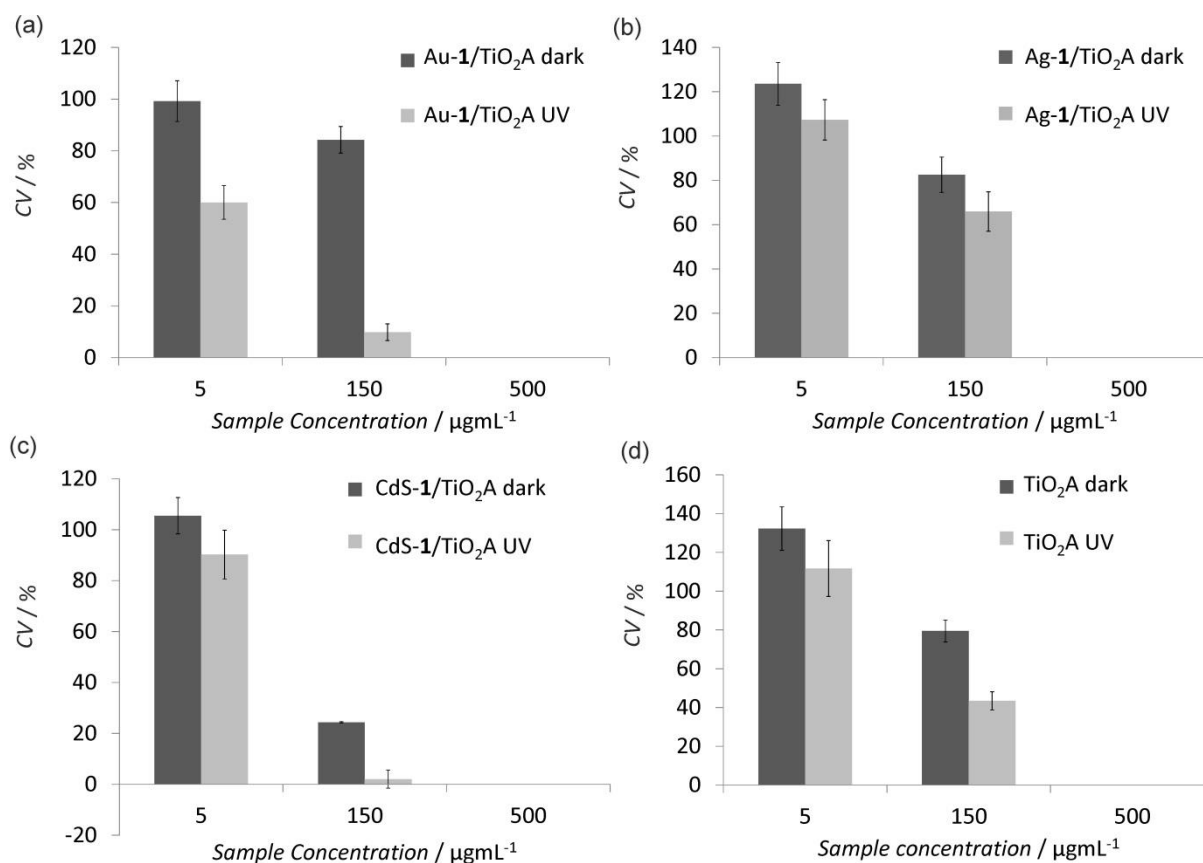


Figure 76. The cell viability (CV) of the hybrid/light treated and untreated HeLa cells determined with MTT assay. (a) Au-1/TiO₂A 2% Au-1 loading; (b) Ag-1/TiO₂A 2% Ag-1 loading; (c) CdS-1/TiO₂A ~20% CdS-1 loading; (d) bare P25 TiO₂NP (TiO₂A).

When the applied light is added into the equation, the most striking difference between the treated and untreated cells is seen for the Au/TiO₂ hybrid with ~60% decrease in CV of cells irradiated by 365 nm light. For all other hybrids and the bare P25 nanomaterial, in the case of the light irradiation, the decrease in CV is in the 25-30% range. These findings are similar to the ones reported by Sayes *et al.* who found 20% decrease in CV of the cells treated with P25 and 356 nm light for 20 min in comparison to the untreated ones.^[321] Given the fact that the Au/TiO₂ hybrids exhibited highest ROS production based on the HRP/AR assay, it was to be expected to detect highest NALI cell toxicity for the same hybrid. The relatively low inherent toxicity in the absence of light and high toxicity when the light is present for a short period of time (10 min), renders the Au-1/TiO₂A hybrid with 2% Au loading a good candidate for PDT against cancer.

4.5.5.2. Nanocomposite Light Induced Toxicity in MCF7 and HEK293 cells

Unfortunately the NALI toxicity studies were not successful in the case of the MCF7 cancer cell line and the HEK293 cell line. The reason for failure of these studies was the inability to obtain good correction values for the absorbance of the formazan.

In the previous experiment with HeLa cells, the maximum number of viable cells was determined from the wells containing only HeLa cells in the appropriate medium (100 % CV). As the hybrids/NPs that were added to the cells possess certain inherent absorption, a certain correction has to be made to obtain only the absorption of the formed formazan and to determine the number of viable cells correctly. These correction values (absorptions of the hybrids/NPs alone) were obtained from the wells containing only the hybrids/NPs in different concentrations (5, 150 and 500 $\mu\text{g mL}^{-1}$). In the case of the MCF7 and HEK293 studies, these correction wells were repeatedly emptied out in the process of replacement of the medium with DMSO, which is a final step of the MTT cell viability assay in which DMSO is needed to dissolve the otherwise cell-medium insoluble formazan. In this way the absorption of the finally formed formazan could not be corrected for the inherent absorption of the hybrids/NPs and the exact numbers for CV could not be determined. A possible reason could be traced to the different medium used in the case of the MCF7 and HEK293 cells (RPMI was used in the case of HeLa cells and DMEM in the case of the MCF7 and HEK 293 cells), but it has to be further investigated.

5. Conclusion

The work presented in this thesis can be coarsely divided into three major units, the modification of TiO₂ nanomaterials with catechol-based linkers, the synthesis of the various types of nanoparticulate metal-metal oxide nanocomposites and the application of the obtained nanomaterials in the light induced cell toxicity studies.

The TiO₂ modification was performed on the commercial NPs and on the in house synthesized NRs with quite a different effect on the photocatalytical properties of the materials. The NPs modification led to an enhanced ROS production as the surfactants formed a LMCT complex, removing surface electron traps and allowing the photoexcited electrons to participate in radical production. Dopamine (DA 1) modification resulted in one of the highest enhancement of ROS production, presumably due to its size that allows efficient trap removal through dense surface packing. DA 1 modified NRs exhibited low ROS production as the small width of the NRs (3.6 nm) does not allow spatial separations of the excitons, leading to their fast recombination. The DA 1 electron trap removal, in this case enhances the recombination process as the electrons are not protected by the traps. The modification of TiO₂ NRs with different aspect ratios could further test presented findings. The TiO₂ nanomaterials modified with catechol based linkers having different chemical functionalities at the free ends offers various possibilities for further modification (e.g. biofunctionalization). In addition to this, modified nanomaterials with superior photocatalytical properties may find application in various fields in which TiO₂ is readily used, ranging from renewable energy production (solar cells), self-cleaning materials to medicine.

In the second part of the work, the LA-DA linker was used in an efficient and simple synthesis of various metal-metal oxide nanomaterials. The LA-DA stabilized Au NPs (Au-1) were connected to the P25 by simple mixing on the elevated temperature (100°C, 1h). The loading of the Au-1 was controlled in a wide range allowing the investigation on its influence on photocatalytic properties of the hybrids. The observed trend that UV induced photocatalytic efficiency does not increase above the 2% Au loading confirmed the earlier findings. The attached Au-1 serve as sink for the electrons keeping them separated from holes thus enhancing the Au/TiO₂ catalytic properties. Upon 470 nm light irradiation, the ROS production correlates with Au loading (highest amount of ROS for the highest (50%) loading). This is explained by the SPR related ROS production mechanism which injects the hot-electrons in the conduction band of the adjacent TiO₂ NP, leaving a hole on the Au-1. The separated excitons then participate in the redox processes on the TiO₂ and Au-1 surfaces. Furthermore, the Ag-1/TiO₂A hybrids were made with similar ROS production-Ag loading trend as the

Au based hybrid. It is planned to produce the Ag/TiO₂ hybrids in the same loading range as for the Au case, and test the ROS production of such hybrids using the UV and visible light sources. To demonstrate versatility of the LA-DA based approach, LA-DA capped CdS QDs were made and used in semiconductor-metal oxide hybrid assembly. The ROS production of the CdS-1/TiO₂A hybrids (~20% CdS-1) indicated the existence of the synergetic effect between the materials as the 470 nm light irradiation resulted in higher ROS production compared to the TiO₂ NPs and CdS-1 alone. It is possible to imagine that the similar strategy would give good results even when the constituents are changed, *e.g.* Cu and ZnO, as long as they have affinity towards thiol (LA) and catechol (DA) functionalities.

Finally the synthesized nanomaterials were used in the NALI toxicity studies on plant (BY-2) and mammalian cell lines (HeLa, MCF7 and HEK293). In the BY-2 experiment it was shown that the cells have good tolerance to the P25 intrinsic and light-induced toxicity as the concentrations up to 20 µg mL⁻¹ resulted in less than 1% of cell death. The toxicity of the DA modified P25 was negligibly higher (~ 2% of dead cells). The small difference in number of dead cells between the light treated and untreated samples confirms the existence of efficient ROS scavenging mechanisms in the plant cell lines. The high ROS production of the hybrids motivated the investigation of their possible use in the PDT of cancer. The *in vitro* studies were made using two cancer cell lines (HeLa and MCF7) and one non-cancer cell line HEK293. Unfortunately, the imperfections of the MTT assay resulted in failure of studies on two cell lines (MCF7 and HEK293) due to the inability to obtain good corrections for the inherent absorbance of the used hybrids. The successful HeLa cell study showed that all the materials have intrinsic toxicity, resulting in no cell viability for 500 µg mL⁻¹ concentration regardless of the light treatment. On lower concentrations, the highest NALI toxicity is seen for the Au/TiO₂ hybrid with ~60% decrease in CV of irradiated cells while other hybrids and the bare P25 showed the 25-30% decrease. In addition to the NALI mechanism, it is suspected that the CdS/TiO₂ hybrid displays some inherent toxicity connected to the leaching of the toxic Cd²⁺ ions from the CdS lattice as the toxicity at 150 µg mL⁻¹ results in 20% CV in dark (for comparison, other hybrids at the same concentrations result in ~80% CV). Further optimization of the MTT assay for the MCF7 and HEK293 cells is planned allowing for the NALI toxicity experiments to be repeated, possibly confirming the findings on HeLa cells.

6. Experimental Part

6.5. Synthesis of nanomaterials

6.5.1. Synthesis of Au NPs

Prior to the synthesis all the glassware and stirrers were rinsed with *aqua regia*, a 3:1 mixture of the HCl and HNO₃ and were subsequently thoroughly washed with Mili-Q water until the HCl fumes could not be smelled. The glassware was dried and used in the synthesis.

6.5.1.1. Synthesis of 13 nm citrate Au NPs

In a typical procedure 30 mL (1mM) of aqueous solution of chloroauric acid (HAuCl₄·3H₂O) was brought to boil under reflux in a three neck round bottom flask. When the boiling point was reached 3 mL (38.8 mM) aqueous solution of trisodium citrate (Na₃C₆H₅O₇) was added abruptly and the mixture is boiled and stirred for additional 30 min when it was left to cool to RT. The obtained gold colloid was kept refrigerated at 4°C.

6.5.1.2. Synthesis of 5 nm citrate/tannic acid capped Au NPs

In a typical procedure 102 mL (0.465 mM) heated (60°C) aqueous solution of chloroauric acid was mixed with 26 mL heated (60°C) mixture of trisodium citrate (34 mM), C₇₆H₅₂O₄₆ (tannic acid) (5.9 mM) and potassium carbonate (K₂CO₃) (25 mM). The mixture was stirred overnight on RT, collected and kept refrigerated at 4°C.

6.5.2. LA-DA coated NPs

Synthesis of LA-DA coated Au NPs, Ag NPs and CdS NPs is described.

6.5.2.1. LA-DA coated Au NPs

In a typical procedure 36mL (1.4 mM) of aqueous solution of chloroauric acid was mixed with 180 μ l (30 mM) EtOH solution of LA-DA linker and the mixture was stirred for 1h on RT. The mixture was then reduced with 6 aliquots (1.6mL, 10mM) of sodium borohydride (NaBH_4) in a period of 5 min. The mixture was stirred overnight on RT, collected and kept refrigerated on 4°C. This procedure yielded Au NPs with diameters around 3-4 nm. To obtain different diameters ratio between the chloroauric acid and LA-DA linker should be changed accordingly (Table 5). The mass concentration of the NPs (mg/mL) was calculated by assuming the reduction of all the Au^{3+} ions in the precursor into Au^0 . To make sure that such assumption is correct a two-fold excess of the NaBH_4 was used than needed to reduce the used amount of precursor (3/8 mol of NaBH_4 is needed to reduce 1 mol of HAuCl_4).

Table 5. LA-DA capped Au NPs

Sample	Au:LADA	Average d / nm	SD / nm
Au-LADA-1	1	1,4	0,3
Au-LADA-2	10	3,6	1,1
Au-LADA-3	25	20	6

6.5.2.2. LA-DA coated Ag NPs

In a typical procedure 50mL (1.1 mM) of aqueous solution of silver nitrate (AgNO_3) was mixed with 10 mL (1 mM) water/EtOH (9:1) solution of LA-DA linker and the mixture was stirred for 5 min on RT. Sodium hydroxide (NaOH , 100 μ l, 2M) was added to the mixture causing the color change. The mixture was stirred overnight on RT, collected and kept refrigerated on 4°C. This procedure yielded Au NPs with diameters around 5 nm. In order to obtain larger diameters, ratio between the chloroauric acid and LA-DA linker should be changed accordingly (Table 6). The mass concentration was calculated in the same way as for the Au-1.

Table 6. LA-DA capped Ag NPs

Sample	Au:LADA	Average d / nm	SD / nm
Ag-LADA-1	5	4,7	0,3
Ag-LADA-2	10	6	1,1
Ag-LADA-3	20	24,5	6

6.5.2.3. LA-DA coated CdS NPs

First step in synthesis of CdS QDs was to dissolve the Cd precursor cadmium acetate dihydrate ($\text{Cd}(\text{CH}_3\text{COO})_2 \cdot 2\text{H}_2\text{O}$) in 100 mL Milli-Q water (1mM). The pH of the solution was then adjusted with addition of sodium hydroxide (1M) to equal 11. The solution was bubbled with nitrogen gas (N_2) for 30 min in order to remove the dissolved oxygen gas (O_2) and prevent Cd oxidation (with CdO as a result). 50 mL (1.35 mM) of aqueous sodium sulfide (Na_2S) was added drop-wise to the stirred solution. The stirring and bubbling continued for 24h when the CdS colloid was collected and refrigerated at 4°C.

6.5.3. Synthesis of hybrids

6.5.3.1. Synthesis of Au/TiO₂ Nanocomposite Using Bifunctional LA-DA Linker

The synthesis of the hybrid Au/TiO₂ material was performed in two steps. First, Au NPs capped with La-DA linker (linker-1) were prepared as described in the previous section on NPs preparation. Resulting batch of Au-1 NPs was then, in the second step, used as a starting material for preparation of two different types of hybrids. Type A hybrid, Au-1/TiO₂A, was prepared using commercially available TiO₂ NPs (P-25, Sigma) which was mixed with Au-1 NPs and refluxed for 1h. Hybrid type B, Au-1/TiO₂B, was prepared using TiF₄ as a precursor and Au-1 NP as seeds for the growth of TiO₂ shell. Appropriate amount of Au-1 NPs were mixed with suspension (in Milli-Q water) of TiO₂NPs (1mg/mL) to obtain Au loadings of 0.1, 0.25, 0.5, 1, 2, 5, 10, 20 and 50% wt (Table 7 –type A, Table 8-type B). The mixture was stirred vigorously and brought to boil for 1h, after which it was cooled down, centrifuged and washed 3 times with Milli-Q water prior to further use. The synthesis of control hybrids using Au NPs stabilized with citrate linker (linker-2) ^[324] as starting material, was prepared as described above. All samples were kept refrigerated in powder form and were

subsequently weighed and dispersed in phosphate buffer (PB, pH=6.0) in 1mg/mL concentration to obtain stock solutions of the hybrids.

Table 7. Au-1 and TiO₂ NPs weights used in synthesis of Au-1/TiO₂A hybrids with different loadings.

Au loading / %	m (Au NPs) / mg	m (TiO ₂ NPs) / mg
0.1	0.0109	18
0.25	0.02725	18
0.5	0.0545	18
1	0.109	18
2	0.218	18
5	0.545	18
10	1.09	18
20	2.18	18
50	5.45	18

Table 8. Au-1 and TiO₂ NPs weights used in synthesis of Au-1/TiO₂B hybrids with different loadings.

Au loading / %	m (Au NPs) / mg	m (TiF ₄) / mg
0.1	0.0115	29.4
0.25	0.02875	29.4
0.5	0.0575	29.4
1	0.115	29.4
2	0.23	29.4
5	0.575	29.4
10	1.15	29.4
20	2.3	29.4
50	5.75	29.4

6.5.3.2. Synthesis of Ag/TiO₂ Nanocomposite Using Bifunctional LA-DA Linker

The synthesis of the Ag-1/TiO₂A hybrid proceeded in two steps; firstly the LA-DA capped Ag NPs were synthesized as described in the previous section, and the resulting batch of Ag-1 NPs was then, in the second step, used as a starting material for preparation of Ag/TiO₂ hybrids with different loadings. Hybrid of type A, Au-1/TiO₂A, was prepared using commercially available TiO₂ NPs (P-25, Sigma) which was mixed with appropriate amount of Ag-1 NPs (Table 9) and refluxed for 1h, after

which it was cooled down, centrifuged and washed 3 times with *Mili-Q* water prior to further use. In the last centrifugation step, the supernatant was discarded and the hybrids were kept in the rotary evaporator until all the water was removed leaving hybrids in the powder form. All samples were kept refrigerated, protected from light and were subsequently weighed and dispersed in phosphate buffer (PB, pH=6.0) in 1mg/mL concentration to obtain stock solutions of the Ag/TiO₂ hybrids.

Table 9. Ag-1 and TiO₂ NPs weights used in synthesis of Ag-1/TiO₂A hybrids with different loadings.

Ag loading / % wt	m (Ag NPs) / mg	m (TiO ₂ NPs) / mg
0.1	0,009	15
0.5	0,045	15
1	0.09	15
2	0.18	15
10	0.9	15

6.6. Functionalization of TiO₂ nanomaterials

6.6.1. Functionalization of commercial TiO₂ NPs

The modification of both TiO₂ P25 and TiO₂ Anatase proceeded in the same way. The TiO₂ NPs were dispersed in water and the pH was set to 1.5 using HCl (1M). The stock solutions were then pulse sonified in order to obtain the highest degree of dispersion of particles. The used homogenizer was *200W Bandelin Sonoplus*, pulse 0.2/0.8, and the time of the sonification was 10 min. 2 mL of TiO₂ stock solution was added to the small glass beaker and the solution was magnetically stirred. The linkers were dissolved in EtOH and 2.5 μmol of linker was added per mg of TiO₂ NPs. Immediately upon addition of the linker in the solution, the color change was observed from white to yellow-orange nuances, depending on the linker used. The mixture was stirred for 5 min, when it was collected, centrifuged 3 times (13.2kRPM, 3 min) and washed by collecting the supernatant and re-dispersing in Milli-Q water using sonification (few pulses). Finally, the modified TiO₂ NPs were once more centrifuged, the supernatant discarded and the rest of the water was removed in rotary evaporator (*CONCENTRATOR Plus* from *Eppendorf*) until the dry powder form of the particles was obtained.

6.6.2. DA Functionalization of TiO₂ NRs

TiO₂ NRs (1.00 mg) were suspended in 2 mL toluene, followed by addition of 3.00 mg dopamine hydrochloride (DA) in 2 mL Milli-Q water. After few seconds, a color change from colorless to brown was observed indicating the formation of the ligand to metal charge transfer (LMCT) complex. The reaction mixture was further stirred overnight at 22°C. After purification by centrifugation (3x), the residue was dispersed in Milli-Q water.

6.7. Chemicals

Chemicals and solvents were purchased at *Sigma-Aldrich* or *Carl Roth* and were used without further purification.

6.8. Instrumentation used

The following chapters hold the details about the instrumentation used in this thesis as well as the details about sample preparation prior to measurements.

6.8.1. TEM and HAADF-STEM Microscopy / EDX Spectroscopy / Selected Area Electron Diffraction (SAED)

Transmission Electron Microscopy (TEM) images were obtained using a *CM200-FEG* microscope (*Philips*) operating at 200kV together with Selected Area Electron Diffraction (SAED). Further TEM imaging, High Angle Annular Dark-Field Scanning Transmission Electron Microscopy (HAADF-STEM) and Energy Dispersive X-Ray Spectroscopy (EDXS) were done on the *Titan³ 80-300* TEM microscope (*FEI*) operating at 300kV. TEM samples were prepared by putting droplets of sample suspension onto a 400 μm mesh copper TEM grid covered with a thin amorphous carbon film of less than 3 nm nominal thickness. Subsequently the prepared samples were dried in air at room temperature.

6.8.2. UV-Vis Absorbance Spectroscopy

UV-Vis absorbance spectra usually in the range from 200-800 nm were taken with Cary 300 Scan (*Varian*). The ~600 μ l of sample containing solvent having appropriate concentration (less than absorption maximum of 4 a.u.) was kept in the quartz cuvettes (*Hellma Analytics, Type 104.002B-QS*) during the measurements. All the measurements were baseline corrected.

6.8.3. Fluorescence Spectroscopy

Fluorescence spectra were taken with Cary Eclipse (*Varian*). The measurements were made on the sample volumes of ~200 μ l kept in the fluorescence quartz cuvette (*Starna GmbH, Type 26.160-F/Q/10/Z20*).

6.8.4. ICP-MS/ICP-OES

ICP-OES and ICP-MS measurements were performed using *OPTIMA 4300 DV* from *PerkinElmer* and *7500ce* from *Agilent* respectively. For the preparation, every sample was shaken for twenty seconds. With a single channel pipette 100 μ l up to 400 μ l has been taken out of the sample holder into a 50 ml auto sampler vial. This has been repeated for every sample twice or three times. To dissolve the hybrid nanoparticles a mixture of 6 ml HCl sub-boiled, 2 ml HNO₃ sub-boiled and 1 ml HF *Suprapur* reagent (*Merck Millipore*) has been added to the samples. The chemical digestion has been carried out by 80 °C in a drying oven over night. Afterwards the acid solution has been diluted to 40 ml. For the measurement, the presence of the elements was determined by optical emission spectrometry (*ICP-OES, OPTIMA 4300 DV* from *PerkinElmer*). The dilution factor for Ti was 10 to 25 and for Au 10. The matrix solution was 5% nitrohydrochloric acid. The analysis was accomplished with four different calibration solutions and an internal standard (Sc). The range of the calibration solutions did not exceed one power of ten. The three major wavelengths have been used for calculation. Because of the better detection limit for Au most of the samples were analyzed with *ICP-MS (Agilent 7500ce)* as well. The dilution factor of the samples for Au was 5 to 50 in a matrix solution of 5 % nitrohydrochloric acid. Indium (In) has been used as an internal standard. The range of the calibration solutions did not exceed one power of ten. The mass 197 for Au and 115 for In has been used for the calculation of the results. The analysis has been repeated three times in a row. These

implemented actions ensure an accurate determination of the titanium and gold content with less than 2% relative standard deviation and an error of measurement less than 3%.

6.8.5. DLS / Zeta potential measurements

Nano Zeta-Sizer (ZS Nano, Malvern) was used for DLS and zeta potential measurements. Prior to the DLS measurements the samples were filtered with 0.2 μ m syringe filters (*Spartan 30/0.2RC* from *Whatman*) in order to remove the dust and bigger particles or agglomerates. The sample was kept either in the Low-volume quartz batch cuvette (*Malvern, Type ZEN2112*) or in the disposable capillary cell (*Malvern, Type DTS1061*). The samples have been run multiple times. For the larger and more polydispersed samples the Z-Average was reported as the result of the measurements, while for the samples that have been known to be monodispersed the “% By Number” was used.

6.8.6. Other instrumentation

Fluorescence enzymatic assays were performed using *Synergy H1 Hybrid Multi-Mode Microplate Reader (Biotek)* using the 96-well plates (*Nunc*). Raman spectra were taken using *MultiRAM FT Raman Spectrometer (Bruker)*.

6.9. Techniques

6.9.1. The enzyme based HRP/AR fluorescence assay for determination of ROS production

The photocatalytic activity was assessed using Horseradish Peroxidase (HRP) – Ampliflu Red (AR) assay. In a black 96 well-plate, 10 μ l of sample (1mg/mL) was dispersed in 90 μ l of phosphate buffer (PB, pH=6.0) so that the total amount of liquid in the well prior to irradiation was 100 μ l. The plates were then placed into custom made irradiation device where a row of LED diodes of wanted wavelength (366 nm or 470nm) irradiated the plate wells for the wanted period of time. 40 μ l HRP (1.33 μ M) and 10 μ l AR (900 μ M) were then added to the irradiated wells, mixed 30 seconds and the fluorescence was subsequently measured using the multi-well plate reader. The sensitivity was set fixed to 65 and excitation and emission wavelengths were 540 and 585 nm respectively.

6.9.2. Light controlled activity of Horseradish Peroxidase (HRP)

10 μ l (1mg/mL) of hybrid was added to quartz cuvette containing 2 ml PB (pH=6.0) followed by addition of 500 μ l HRP (1.33 μ M) and 200 μ l AR (0.9mM) and the mixture was magnetically stirred. The cuvette was interchangeably kept in dark and irradiated by 366nm UV hand lamp (4W) (or 470nm LED array) in periods of 2 min with fluorescence measurement every minute (excitation and emission wavelengths were 540 and 585 nm respectively). The excitation and emission slits were set to size 5 and 2.5 respectively. The total duration of the experiment was 10min.

6.9.3. Evans Blue Cell Death Assays of Cells Treated with Nanoparticles

In the following tables is the description of the materials and processes used for the determination of the BY-2 cell viability treated with various nanomaterials and light via Evans Blue Cell Death Assays.

	Day 1	Approx. duration (for 8 samples) (min)
Treatment of Cells with NP / UV / Catalase		
<u>Designing the experiment</u>	<ul style="list-style-type: none"> • Treating the samples with various NPs (due to variation, duplicates to quadruplicates are recommended) • Controls: investigating the effect of any treatment that is combined with another treatment by itself. For example: <ul style="list-style-type: none"> ○ the effect of only UV light (testing this a few times is enough if there is no visible difference; it doesn't have to be repeated in each experiment) ○ the effect of NP in the dark (in each experiment because of the very large variation) ○ untreated cells ("negative control") ○ a positive control (e.g. a known substrate that in the dark causes 100% cell death, this is included as the positive control in each experiment to determine the % of dead cells) <p>It should be taken into account that depending on the UV lamp used, illumination might not be identical for each sample.</p>	20
<u>Materials:</u>	<ul style="list-style-type: none"> - two 24-well protein crystallization plates - NPs suspension (depending on the experiment) 	Pipet 1ml of cell suspension into each of

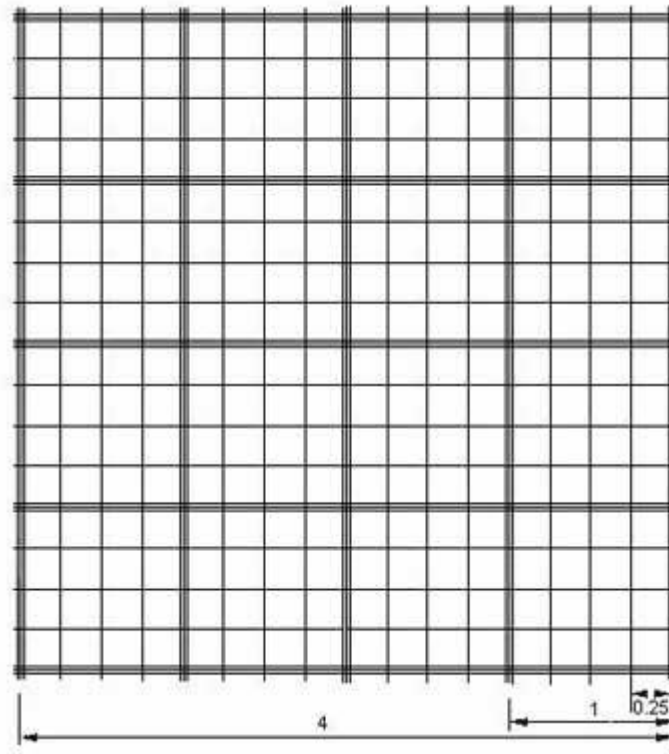
<ul style="list-style-type: none"> - ViewSeal UV transparent foil (<i>Greiner</i>) - Aluminium foil - tobacco BY-2 cells, appropriate dilution (typically 1x cells plus 2x MS medium, will result in approx. 2×10^5 cells / ml for 3 day old wild type cells) and of the desired age (typically 3 day old cells) 	8 labeled wells of a 24 well plate
If some of the samples will be treated with catalase, the appropriate volume of 50mM Tris-HCl (pH7) should be added to catalase-free samples.	5
If a large volume of a NP solution is added to a sample, the same volume of solvent (typically ddH ₂ O) should be added to the other samples (<i>e.g.</i> 10µl/ml of TiO ₂ NP added to a sample, 10µl of ddH ₂ O should be added to all other samples).	2
Adding catalase to appropriate samples.	5
Adding NP to appropriate samples.	2
If samples are to be kept in the dark they should be immediately (but carefully) wrapped in the aluminium foil. Samples that are to be treated with UV light should be sealed with <i>ViewSeal</i> (it can be re-used a few times).	2
Positioning on shaker in the desired setup.	2
Turning on light	5
Turning on shaker (100rpm)	2
Incubating for the desired duration	1
Counting the cells if necessary, using the Fuch-Rosenthal chamber	
Total duration of the experimental part	30

Determination of Cell Density with a Fuchs-Rosenthal Chamber

Materials:

counting chamber “Fuchs-Rosenthal” with its cover glass, light microscope, pipet

In the centre of the slide is the grid structure seen when looking at the Fuchs-Rosenthal chamber mounted on the microscope:



Total area of $4 \times 4 = 16 \text{ mm}^2$, is divided into 16 smaller squares of 1 mm^2 each which are further divided into 16 very small squares each measuring $0.25\text{mm} \times 0.25\text{mm} = 0.0625 \text{ mm}^2$. The height of the chamber is 0.2mm . Therefore, the total volume is $0.2\text{mm} \times 16 \text{ mm}^2 = 3.2 \text{ mm}^3$, which equals $3.2\mu\text{l}$.

	The outer “bumps” of the slide should be moistened and the cover glass should be pressed onto the slide in such way that an interference pattern is visible (the Newton’s rings, which means the two glass surfaces are close enough to each other), otherwise the volume will not be correct.	5
	Cell suspension should be pipetted to the edge of the cover glass at the central bump. The liquid will move to the grid structure <i>via</i> capillary forces. The chamber should be checked for air bubbles, and mounted on the microscope stage (objective 10x or 20x).	2
	The squares are counted in such a way that they are all counted without omitting any (such as by meandering). <i>All cells that lie on the right and top lines of a square should ne counted but not on the bottom and left lines (to avoid counting them twice)</i> . If the density is very high, only the 4 diagonal squares should be counted. If there are still too many cells they should be diluted again.	15
	Calculating the cell density: number of cells counted / volume (e.g. $3.2\mu\text{l}$)	

Day 2		
Cell Death Assay with Evans Blue		
Materials:		45min
<ul style="list-style-type: none"> - paper towels - Milli-Q water: plastic bottle (~ 250ml for 8 samples) and about 10ml in a small beaker - MS medium (~17ml) - Evans Blue Stock 2.5% - 8 staining chambers containing one of the little custom-made pots (2ml tube cut in half with dense grid glued in the place of the cut-off bottom; the sealing cap is removed as well) and a 10ml beaker each; the staining chambers are set into 10ml beakers, and 2mL of MS medium is added to each beaker (beakers should be aligned); pipetting 200µl of ddH₂O to each little pot - Forceps for holding the staining chambers - timer - 2x8 cut 1ml pipet tips - 8 cut 200µl pipet tips - uncut 1ml and 200µl tips - 1ml and 200µl pipets - labelled 1.5ml tubes (2x8) <p>For photometric measurement: 10% SDS solution, tube float, sonifier, photometer capable of measuring OD₆₀₀, vortex, 1% SDS solution</p>		
	Switching off the UV lamp / transferring samples to the staining room.	3
	Carefully removing the UV transparent foil (or aluminium foil).	2
	Transferring 800µl of each sample to a new 1.5ml tube.	3
	Opening caps of all sample containing tubes. Pipetting 88µl of 2.5% Evans Blue solution (<i>i.e.</i> final concentration is 0.25%) to each sample. Starting timer (set to 5min). Closing the lids. <i>Mixing by inverting tube a few times once every minute.</i>	6
	Immediately transferring 700µl of each sample to a staining chamber until all samples are sitting in the chambers.	3
	Lifting chamber, flushing with about 10ml of water from the bottle, making sure that cells do not splash out of the chamber. Liquid draining from the chamber should be almost clear after 10ml. <i>Removing flow-through from beaker, flushing the beaker a little, touching paper towel with staining chamber to remove some of the liquid (not drying completely), pouring some water (about 2ml) into beaker, setting staining chamber back into beaker. Repeating with remaining samples.</i>	5
	<i>Repeating this washing step once, setting the staining chamber into one of the</i>	5

	<i>little pots (that contain 200µl of water) after drying the membrane a little bit with a paper towel. Proceeding with remaining samples.</i>	
	<p>Re-suspending samples in equal volumes in 1.5 mL tubes and assuring that almost all cells are recovered from the membrane:</p> <p><i>With the 200µl pipet and cut tips, 100µl of the cells on the membrane are collected and transferred to a fresh 1.5 mL tube. With the 1ml pipet, adding 200µl of water to staining chamber in the little pot. Transferring 2x100µl of cell suspension to the same microfuge tube. In each suspension pipetting step making sure that a lot of cells are taken inside the pipet tip. Re-suspending them often helps. Repeating this step until the volume of 700µl has been transferred.</i></p>	15
	If multiple sets of staining are done (not recommend more than 2), such as 2x8, staining and washing of the others should be done now.	(0 or 45min)
	For the microscope examination, an adequate and equal volume of cells should be taken. For the photometric measurement, proceed with the following.	

Photometric determination of cell death rate		
	Adding 77µl of 10% SDS solution, vortex, putting tubes on a tube float	5
	Sonifying for 10min	12
	Vortexing	2
	Looking at blue colour intensity of suspensions. <i>With some experience it is possible to judge what dilutions are to be made in order to get reliable photometric data. Deciding what dilutions are to be used.</i>	2
	Centrifuging for 3min at 9000rpm (table top centrifuge)	4
	<p>While the centrifuge is running, preparing 1.5 mL tubes with appropriate volume of 1%SDS for dilutions.</p> <p><i>Use dilutions of 1 part sample plus 4 parts 1% SDS or 1 part sample plus 9 parts 1% SDS. i.e. prepare 400µl of 1%SDS or 450µl of 1%SDS, respectively.</i></p>	
	Using supernatant for photometric measurements. For diluted samples, adding 100µl or 50µl of sample to the prepared 400µl or 450µl 1%SDS containing 1.5 mL tubes, respectively.	5
	Switching on the photometer (Eppendorf). Choosing OD600 mode. Blanking with 1%SDS (button “blank”). Measuring blank again by pressing “sample” to	2

	verify that the blank results in an apparent absorbance of 0.	
	Measuring the samples. Absorbance should be below 3, values above exceed the range in which linearity exists between the reading and the real absorbance. Adjusting the dilution if necessary.	20
	Writing down absorbance and dilution, calculating undiluted absorbance.	2
	Cleaning the cuvette with water by rinsing a few times (no EtOH!).	2

Data Analysis		
	Entering the data into an Excel spreadsheet	5
	Calculating the cell death rate in % by dividing the OD600 by the (mean of the) 100 cell death positive control value	2
	Determining the averages for duplicates and standard errors.	2

6.9.4. MTT Assay

	Day 1	Approx. duration (for 2 plates) (min)
Planting the cells on the plates		
	<u>Designing the experiment</u> <ul style="list-style-type: none"> • Treating the samples with various NPs (due to variation repetitions are recommended) • Controls: investigating the effect of any treatment that is combined with another treatment by itself. For example: <ul style="list-style-type: none"> - the effect of only UV(365nm)/visible(470nm) light - the effect of NP in the dark (in each experiment because of the very large variation) - untreated cells (“negative control”) - a positive control (<i>e.g.</i> a known substrate that in the dark causes 100% cell death, this is included as the positive control in each experiment to determine the % of dead cells); in the MTT assay the formazan absorption determines the cell viability, the wells without 	20

	any cells should exhibit no absorption at all, nevertheless they should be treated with appropriate amount of NP/hybrids as to be able to correct for the intrinsic hybrid absorption in treated wells	
	<p><u>Materials:</u></p> <ul style="list-style-type: none"> - two 96-well plates - Tissue Culturing Flasks (TCF) with wanted cells - Glass pipettes (2mL, 5mL, 10 mL) - 50 mL tube - Clean bench - Suction pump - Incubator (37°C, 5% CO₂) - Trypsin/EDTA - PBS buffer - Pipettes 200µl with tips <p>Appropriate medium (depending on the experiment and cell type)</p> <ul style="list-style-type: none"> ○ MCF-7 and HEK293 DMEM ○ HeLa: RPMI 	10
	Removing the old medium from the TCF with the suction pump	1
	Wash the dead cells with 5 mL PBS. Removing the PBS with suction pump.	1
	Add 2mL of Trypsin/EDTA for the detachment of cells. Incubating 5 min on 37°C and 5% CO ₂ atmosphere.	7
	Adding 8 mL medium to the TCF.	1
	Possibly passage the cells to the new TCF when needed for further experiments (1mL of detached cells plus 9 mL of medium).	5
	Collecting the detached cells in a 50 mL tube. Centrifugation 1000 RPM, 4 min. Re-dispersing in ca. 20 mL medium.	7
	Counting the cells using <i>Fuch-Rosenthal</i> chamber	10
	<p>Making cell stock solution with appropriate concentration for each cell type:</p> <ul style="list-style-type: none"> ○ MCF-7: 40 000 cells/ml ○ HeLa: 20 000 cells/ml ○ HEK293: 40 000 cells/ml 	10
	This cell suspension should be pipetted in 2 plates (200µL/well, ~40mL of stock solution). The last row (H) should be left empty!	15
	Transferring the plates to the incubator. Incubating for wanted time (<i>e.g.</i> overnight)	2

	Day 2	Approx. duration (for 2 plates) (min)
Treatment of Cancer Cells with NP/hybrids + UV/visible light		
<p><u>Materials:</u></p> <ul style="list-style-type: none"> - two 96-well plates planted with desired cell line - Clean bench - Suction pump - Incubator (37°C, 5% CO₂) - NP/hybrid materials - UV or visible hand lamp - Pipettes 200µl - Tips <p>Appropriate medium without phenol red (depending on the experiment and cell type)</p> <ul style="list-style-type: none"> ○ MCF-7 and HEK293 DMEM ○ HeLa: RPMI 		10
	Prepare NP/hybrid solutions in an appropriate medium (without phenol red) having various concentrations (<i>e.g.</i> 5, 50, 150 and 500 µg/mL). Around 10 mL of solution of each concentration is needed.	20
	Removing the old medium from the plates with the suction pump	1
	Loading the wells of the plates with NP/hybrid solutions of appropriate concentrations. See scheme X.	20
	Transferring the dark kept plate to the incubator. Incubating for wanted time (<i>e.g.</i> overnight).	1
	Irradiating the other plate with UV or visible light in the wanted duration.	10-15
	Transferring the irradiated plate to the incubator. Incubating for wanted time (<i>e.g.</i> overnight).	1

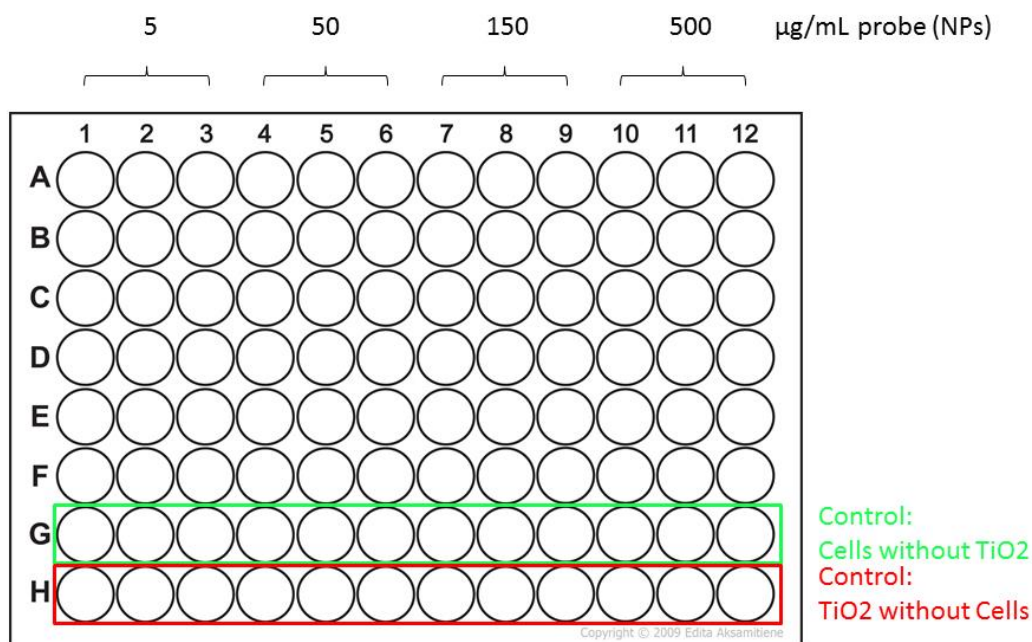


Figure 77. Scheme for loading one 96-well plate for the NALI toxicity experiment.

Day 3		Approx. duration (for 2 plates) (min)
Performing the MTT Assay		
<p><u>Materials:</u></p> <ul style="list-style-type: none"> - two 96-well plates planted with desired cell line, loaded with NP/hybrid material - one plate was irradiated with UV/visible light, while the other was kept in dark - Clean bench - Suction pump - Incubator (37°C, 5% CO₂) - DMSO - MTT - Pipettes 200µl - Tips <p>Appropriate medium without phenol red (depending on the experiment and cell type)</p> <ul style="list-style-type: none"> ○ MCF-7 and HEK293 DMEM ○ HeLa: RPMI 		20

	<p>Preparing the MTT-incubation solution:</p> <ul style="list-style-type: none"> - 1mL of 12mM MTT stock solution is needed per 96-well plate (2mL for 2 plates) - Dissolving 5mg MTT (kept in the fridge) in 1mL 1x PBS (10mg in 2mL for 2 plates) - As MTT is not easily soluble, sonicating for 15-30min is advised (vortexing in between) - Centrifuging (5min. 400 rpm) to separate the undissolved part of MTT - MTT-incubation solution is produced from the MTT-stock solution - In 10mL medium without phenol rot one adds 1mL MTT-stock solution - This is the volume needed for one 96-well plate (2mL (12mM) MTT in 20 mL medium for 2 plates) 	15
	Removing the old medium suspended with NP/hybrid material with suction pump.	2
	Add 100µL of MTT-incubation solution per well (in ALL wells!)	7
	Incubating the plates on 37°C for 2h	120
	Removing the incubation solution with suction pump.	2
	Adding 50µL DMSO per well.	10
	Incubate the plates on 37°C for 10min	12
	MTPR (Multi-titer Plate Reader) measurements	

	Day 3	Approx. duration (for 2 plates) (min)
MTPR (Multi-titer Plate Reader) measurements		
	<p><u>Materials:</u></p> <ul style="list-style-type: none"> - two 96-well plates planted with desired cell line, loaded with NP/hybrid material - one plate was irradiated with UV/visible light, while the other was kept in dark - the medium containing NP/hybrid was discarded and the plates were treated with MTT, washed and DMSO was added to dissolve the formed formazan - Multi-titer plate reader (<i>Biotek, H1</i>) - Clean bench - Suction pump - Incubator (37°C, 5% CO₂) - DMSO 	5

	<ul style="list-style-type: none"> - MTT - Pipettes 200μl - Tips 	
	Turn ON the computer and the instrument	2
	Run Gen 5 1.11 software	1
	Make the procedure with the following parameters: <ul style="list-style-type: none"> - Temp. 37°C - Orbital shake 1min - Absorption (A) at 540 nm 	5
	Inserting the plate correctly into the reader (A1 upper-right when facing the reader)	1
	Pressing Read to start the measurement	1
	When the measurement ends the results are exported in the Excel software by pressing the green Excel button in the software.	1
	Repeating for the other plates	5
	Turn OFF the computer and the instrument	1

7. Literature

- [1] aS. J. Guo, S. Zhang, S. H. Sun, *Angew Chem Int Edit* **2013**, *52*, 8526-8544; bM. Stratakis, H. Garcia, *Chem Rev* **2012**, *112*, 4469-4506.
- [2] aN. I. Al-Salim, S. A. Bagshaw, A. Bittar, T. Kemmitt, A. J. McQuillan, A. M. Mills, M. J. Ryan, *J Mater Chem* **2000**, *10*, 2358-2363; bJ. Wang, S. Uma, K. J. Klabunde, *Appl Catal B-Environ* **2004**, *48*, 151-154.
- [3] R. A. Sperling, W. J. Parak, *Ther Innov Regul Sci* **2013**, *47*, 1333-1383.
- [4] M. Grzelczak, J. Vermant, E. M. Furst, L. M. Liz-Marzan, *ACS nano* **2010**, *4*, 3591-3605.
- [5] aS. Gupta, S. Devi, K. Singh, *J Basic Microb* **2011**, *51*, 601-606; bD. Hebbalalu, J. Lalley, M. N. Nadagouda, R. S. Varma, *Acs Sustain Chem Eng* **2013**, *1*, 703-712.
- [6] Y. Barenholz, *Journal of controlled release : official journal of the Controlled Release Society* **2012**, *160*, 117-134.
- [7] R. B. Wang, P. S. Billone, W. M. Mullett, *J Nanomater* **2013**.
- [8] J. Y. Chen, C. Glaus, R. Laforest, Q. Zhang, M. X. Yang, M. Gidding, M. J. Welch, Y. N. Xia, *Small* **2010**, *6*, 811-817.
- [9] B. Kang, M. A. Mackey, M. A. El-Sayed, *Journal of the American Chemical Society* **2010**, *132*, 1517-+.
- [10] aC. Psarros, R. Lee, M. Margaritis, C. Antoniadis, *Maturitas* **2012**, *73*, 52-60; bV. Karagkiozaki, *J Nanopart Res* **2013**, *15*.
- [11] aW. P. Hall, S. N. Ngatia, R. P. Van Duyne, *J Phys Chem C* **2011**, *115*, 1410-1414; bL. Dykman, N. Khlebtsov, *Chemical Society reviews* **2012**, *41*, 2256-2282.
- [12] aJ. U. Menon, P. Jadeja, P. Tambe, K. Vu, B. H. Yuan, K. T. Nguyen, *Theranostics* **2013**, *3*, 152-166; bT. H. Kim, S. Lee, X. Y. Chen, *Expert Rev Mol Diagn* **2013**, *13*, 257-269.
- [13] aM. Gratzel, *Nature* **2001**, *414*, 338-344; bJ. Burschka, N. Pellet, S. J. Moon, R. Humphry-Baker, P. Gao, M. K. Nazeeruddin, M. Gratzel, *Nature* **2013**, *499*, 316-+.
- [14] aA. Vaneski, A. S. Sussha, J. Rodriguez-Fernandez, M. Berr, F. Jackel, J. Feldmann, A. L. Rogach, *Adv Funct Mater* **2011**, *21*, 1547-1556; bS. Rawalekar, T. Mokari, *Adv Energy Mater* **2013**, *3*, 12-27.
- [15] Q. P. Lu, Z. D. Lu, Y. Z. Lu, L. F. Lv, Y. Ning, H. X. Yu, Y. B. Hou, Y. D. Yin, *Nano Lett* **2013**, *13*, 5698-5702.
- [16] M. Murdoch, G. I. N. Waterhouse, M. A. Nadeem, J. B. Metson, M. A. Keane, R. F. Howe, J. Llorca, H. Idriss, *Nat Chem* **2011**, *3*, 489-492.
- [17] aM. Law, L. E. Greene, J. C. Johnson, R. Saykally, P. Yang, *Nature materials* **2005**, *4*, 455-459; bG. Li, R. Zhu, Y. Yang, *Nat Photonics* **2012**, *6*, 153-161.
- [18] X. L. Qu, P. J. J. Alvarez, Q. L. Li, *Water Res* **2013**, *47*, 3931-3946.
- [19] K. Zhang, K. C. Kemp, V. Chandra, *Mater Lett* **2012**, *81*, 127-130.
- [20] M. V. Liga, E. L. Bryant, V. L. Colvin, Q. L. Li, *Water Res* **2011**, *45*, 535-544.
- [21] H. W. Liao, C. L. Nehl, J. H. Hafner, *Nanomedicine : nanotechnology, biology, and medicine* **2006**, *1*, 201-208.
- [22] X. Chen, H. Y. Zhu, J. C. Zhao, Z. T. Zheng, X. P. Gao, *Angew Chem Int Edit* **2008**, *47*, 5353-5356.
- [23] M. Faraday, *Phil. Trans. R. Soc. Lond.* **1857**, *147*, 145-181.
- [24] P. K. Jain, X. H. Huang, I. H. El-Sayed, M. A. El-Sayed, *Accounts Chem Res* **2008**, *41*, 1578-1586.
- [25] P. K. Jain, K. S. Lee, I. H. El-Sayed, M. A. El-Sayed, *J Phys Chem B* **2006**, *110*, 7238-7248.
- [26] K. S. Lee, M. A. El-Sayed, *J Phys Chem B* **2006**, *110*, 19220-19225.
- [27] D. Pissuwan, S. M. Valenzuela, M. B. Cortie, *Trends Biotechnol* **2006**, *24*, 62-67.

- [28] aC. J. Murphy, T. K. San, A. M. Gole, C. J. Orendorff, J. X. Gao, L. Gou, S. E. Hunyadi, T. Li, *J Phys Chem B* **2005**, *109*, 13857-13870; bS. Link, M. A. El-Sayed, M. B. Mohamed, *J Phys Chem B* **2005**, *109*, 10531-10532.
- [29] C. J. Huang, Y. H. Wang, P. H. Chiu, M. C. Shih, T. H. Meen, *Mater Lett* **2006**, *60*, 1896-1900.
- [30] P. Senthil Kumar, I. Pastoriza-Santos, B. Rodriguez-Gonzalez, F. Javier Garcia de Abajo, L. M. Liz-Marzan, *Nanotechnology* **2008**, *19*, 015606.
- [31] J. Xie, Q. Zhang, J. Y. Lee, D. I. Wang, *ACS nano* **2008**, *2*, 2473-2480.
- [32] K. C. Ng, W. Cheng, *Nanotechnology* **2012**, *23*, 105602.
- [33] aV. Sharma, K. Park, M. Srinivasarao, *Mat Sci Eng R* **2009**, *65*, 1-38; bM. C. Daniel, D. Astruc, *Chem Rev* **2004**, *104*, 293-346.
- [34] J. Turkevich, P. C. Stevenson, J. Hillier, *Discuss Faraday Soc* **1951**, 55-&.
- [35] aN. R. Jana, L. Gearheart, C. J. Murphy, *Chem Mater* **2001**, *13*, 2313-2322; bB. Abecassis, F. Testard, O. Spalla, P. Barboux, *Nano Lett* **2007**, *7*, 1723-1727.
- [36] R. P. Sear, *J Phys Chem B* **2006**, *110*, 4985-4989.
- [37] U. Gasser, E. R. Weeks, A. Schofield, P. N. Pusey, D. A. Weitz, *Science* **2001**, *292*, 258-262.
- [38] aK. Q. Zhang, X. Y. Liu, *Nature* **2004**, *429*, 739-743; bL. E. Helseth, H. Z. Wen, R. W. Hansen, T. H. Johansen, P. Heinig, T. M. Fischer, *Langmuir : the ACS journal of surfaces and colloids* **2004**, *20*, 7323-7332.
- [39] aJ. L. Harland, W. vanMegen, *Phys Rev E* **1997**, *55*, 3054-3067; bX. M. Lin, G. M. Wang, C. M. Sorensen, K. J. Klabunde, *J Phys Chem B* **1999**, *103*, 5488-5492.
- [40] aM. B. Sigman, Jr., A. E. Saunders, B. A. Korgel, *Langmuir : the ACS journal of surfaces and colloids* **2004**, *20*, 978-983; bS. I. Stoeva, B. L. V. Prasad, S. Uma, P. K. Stoimenov, V. Zaikovski, C. M. Sorensen, K. J. Klabunde, *J Phys Chem B* **2003**, *107*, 7441-7448.
- [41] B. K. Pong, H. I. Elim, J. X. Chong, W. Ji, B. L. Trout, J. Y. Lee, *J Phys Chem C* **2007**, *111*, 6281-6287.
- [42] aG. Frens, *Nature-Phys Sci* **1973**, *241*, 20-22; bJ. Kimling, M. Maier, B. Okenve, V. Kotaidis, H. Ballot, A. Plech, *J Phys Chem B* **2006**, *110*, 15700-15707.
- [43] E. Oh, K. Susumu, R. Goswami, H. Mattoussi, *Langmuir : the ACS journal of surfaces and colloids* **2010**, *26*, 7604-7613.
- [44] M. Brust, M. Walker, D. Bethell, D. J. Schiffrin, R. Whyman, *J. Chem. Soc., Chem. Commun.* **1994**, 801-802.
- [45] C. A. Waters, A. J. Mills, K. A. Johnson, D. J. Schiffrin, *Chem Commun (Camb)* **2003**, 540-541.
- [46] O. Zaluzhna, Y. Li, C. Zangmeister, T. C. Allison, Y. J. Tong, *Chem Commun (Camb)* **2012**, *48*, 362-364.
- [47] aM. M. Oliveira, D. Ugarte, D. Zanchet, A. J. G. Zarbin, *J Colloid Interf Sci* **2005**, *292*, 429-435; bY. Z. Lu, W. T. Wei, W. Chen, *Chinese Sci Bull* **2012**, *57*, 41-47.
- [48] aK. R. Brown, M. J. Natan, *Langmuir : the ACS journal of surfaces and colloids* **1998**, *14*, 726-728; bK. R. Brown, D. G. Walter, M. J. Natan, *Chem Mater* **2000**, *12*, 306-313.
- [49] aA. Henglein, M. Giersig, *J Phys Chem B* **1999**, *103*, 9533-9539; bT. Teranishi, M. Hosoe, T. Tanaka, M. Miyake, *J Phys Chem B* **1999**, *103*, 3818-3827.
- [50] N. R. Jana, L. Gearheart, C. J. Murphy, *Langmuir : the ACS journal of surfaces and colloids* **2001**, *17*, 6782-6786.
- [51] C. Ziegler, A. Eychmuller, *J Phys Chem C* **2011**, *115*, 4502-4506.
- [52] B. Nikoobakht, M. A. El-Sayed, *Chem Mater* **2003**, *15*, 1957-1962.
- [53] L. Vigderman, B. P. Khanal, E. R. Zubarev, *Adv Mater* **2012**, *24*, 4811-4841.
- [54] B. G. Ershov, E. Janata, A. Henglein, A. Fojtik, *J Phys Chem-Us* **1993**, *97*, 4589-4594.
- [55] V. Amendola, M. Meneghetti, *Physical chemistry chemical physics : PCCP* **2009**, *11*, 3805-3821.
- [56] G. W. Yang, *Prog Mater Sci* **2007**, *52*, 648-698.
- [57] aT. Sakka, S. Iwanaga, Y. H. Ogata, A. Matsunawa, T. Takemoto, *Journal of Chemical Physics* **2000**, *112*, 8645-8653; bT. Tsuji, Y. Okazaki, Y. Tsuboi, M. Tsuji, *Jpn J Appl Phys 1* **2007**, *46*, 1533-1535.

- [58] W. T. Nichols, T. Sasaki, N. Koshizaki, *J Appl Phys* **2006**, *100*.
- [59] W. T. Nichols, T. Sasaki, N. Koshizaki, *J Appl Phys* **2006**, *100*.
- [60] R. Knochenmuss, *The Analyst* **2006**, *131*, 966-986.
- [61] F. Mafune, J. Kohno, Y. Takeda, T. Kondow, H. Sawabe, *J Phys Chem B* **2000**, *104*, 9111-9117.
- [62] F. Mafune, J. Kohno, Y. Takeda, T. Kondow, H. Sawabe, *J Phys Chem B* **2001**, *105*, 5114-5120.
- [63] P. Coyle, J. C. Philcox, L. C. Carey, A. M. Rofe, *Cell Mol Life Sci* **2002**, *59*, 627-647.
- [64] D. M. Kendziora, *PhD Thesis* **2013**.
- [65] aA. M. Gobin, M. H. Lee, N. J. Halas, W. D. James, R. A. Drezek, J. L. West, *Nano Lett* **2007**, *7*, 1929-1934; bJ. R. Cole, N. A. Mirin, M. W. Knight, G. P. Goodrich, N. J. Halas, *J Phys Chem C* **2009**, *113*, 12090-12094.
- [66] M. P. Melancon, W. Lu, Z. Yang, R. Zhang, Z. Cheng, A. M. Elliot, J. Stafford, T. Olson, J. Z. Zhang, C. Li, *Mol Cancer Ther* **2008**, *7*, 1730-1739.
- [67] aI. H. El-Sayed, X. H. Huang, M. A. El-Sayed, *Nano Lett* **2005**, *5*, 829-834; bX. H. Huang, I. H. El-Sayed, W. Qian, M. A. El-Sayed, *Journal of the American Chemical Society* **2006**, *128*, 2115-2120.
- [68] D. P. O'Neal, L. R. Hirsch, N. J. Halas, J. D. Payne, J. L. West, *Cancer letters* **2004**, *209*, 171-176.
- [69] L. R. Hirsch, R. J. Stafford, J. A. Bankson, S. R. Sershen, B. Rivera, R. E. Price, J. D. Hazle, N. J. Halas, J. L. West, *P Natl Acad Sci USA* **2003**, *100*, 13549-13554.
- [70] C. Loo, A. Lowery, N. J. Halas, J. West, R. Drezek, *Nano Lett* **2005**, *5*, 709-711.
- [71] C. R. Patra, R. Bhattacharya, E. F. Wang, A. Katarya, J. S. Lau, S. Dutta, M. Muders, S. F. Wang, S. A. Buhrow, S. L. Safgren, M. J. Yaszemski, J. M. Reid, M. M. Ames, P. Mukherjee, D. Mukhopadhyay, *Cancer research* **2008**, *68*, 1970-1978.
- [72] H. Pei, F. Li, Y. Wan, M. Wei, H. Liu, Y. Su, N. Chen, Q. Huang, C. Fan, *Journal of the American Chemical Society* **2012**, *134*, 11876-11879.
- [73] J. J. Storhoff, A. D. Lucas, V. Garimella, Y. P. Bao, U. R. Muller, *Nature biotechnology* **2004**, *22*, 883-887.
- [74] P. C. Soo, Y. T. Horng, K. C. Chang, J. Y. Wang, P. R. Hsueh, C. Y. Chuang, C. C. Lu, H. C. Lai, *Molecular and cellular probes* **2009**, *23*, 240-246.
- [75] E. Boisselier, D. Astruc, *Chemical Society reviews* **2009**, *38*, 1759-1782.
- [76] K. Zagorovsky, W. C. Chan, *Angew Chem Int Ed Engl* **2013**, *52*, 3168-3171.
- [77] X. M. Qian, S. M. Nie, *Chemical Society reviews* **2008**, *37*, 912-920.
- [78] J. T. Krug, G. D. Wang, E. Sr, S. M. Nie, *Journal of the American Chemical Society* **1999**, *121*, 9208-9214.
- [79] S. Nakielnny, G. Dreyfuss, *Cell* **1999**, *99*, 677-690.
- [80] B. Nowack, *Science* **2010**, *330*, 1054-1055.
- [81] A. Ivask, A. Elbadawy, C. Kaweeteerawat, D. Boren, H. Fischer, Z. Ji, C. H. Chang, R. Liu, T. Tolaymat, D. Telesca, J. I. Zink, Y. Cohen, P. A. Holden, H. A. Godwin, *ACS nano* **2013**.
- [82] B. Nowack, H. F. Krug, M. Height, *Environmental science & technology* **2011**, *45*, 1177-1183.
- [83] G. Frens, J. T. G. Overbeek, *Kolloid-Zeitschrift und Zeitschrift für Polymere* **1969**, *233*, 922-929.
- [84] G. Frens, J. T. Overbeek, *Kolloid Z Z Polym* **1969**, *233*, 922-&.
- [85] C. Paal, *Ber. Dtsch. Chem. Ges.* **1902**, *35*, 2224-2236.
- [86] K. Boese, *Dtsch. Z. Chir.* **1921**, *163*, 62-84.
- [87] N. E. Bogdanchikova, A. V. Kurbatov, V. V. Tret'yakov, P. P. Rodionov, *Pharm. Chem. J.* **1992**, *26*, 778-779.
- [88] H. Bechhold, *Z. Chem. Ind. Kolloide* **1907**, *2*, 33-41.
- [89] aR. M. Slawson, J. T. Trevors, H. Lee, *Arch Microbiol* **1992**, *158*, 398-404; bG. J. Zhao, S. E. Stevens, *Biomaterials* **1998**, *11*, 27-32.
- [90] aY. Matsumura, K. Yoshikata, S. Kunisaki, T. Tsuchido, *Applied and environmental microbiology* **2003**, *69*, 4278-4281; bA. Gupta, M. Maynes, S. Silver, *Applied and environmental microbiology* **1998**, *64*, 5042-5045.
- [91] Q. L. Feng, J. Wu, G. Q. Chen, F. Z. Cui, T. N. Kim, J. O. Kim, *Journal of biomedical materials research* **2000**, *52*, 662-668.

- [92] aI. Sondi, B. Salopek-Sondi, *J Colloid Interf Sci* **2004**, *275*, 177-182; bV. K. Sharma, R. A. Yngard, Y. Lin, *Adv Colloid Interfac* **2009**, *145*, 83-96; cJ. R. Morones, J. L. Elechiguerra, A. Camacho, K. Holt, J. B. Kouri, J. T. Ramirez, M. J. Yacaman, *Nanotechnology* **2005**, *16*, 2346-2353.
- [93] T. Huang, X. H. N. Xu, *J Mater Chem* **2010**, *20*, 9867-9876.
- [94] N. Pradhan, A. Pal, T. Pal, *Colloid Surface A* **2002**, *196*, 247-257.
- [95] A. Henglein, *Chem Rev* **1989**, *89*, 1861-1873.
- [96] U. Kreibig, M. Vollmer, *Springer Series in Materials Science* **1995**, *25*, 535p.
- [97] D. D. Evanoff, G. Chumanov, *J Phys Chem B* **2004**, *108*, 13957-13962.
- [98] aJ. Yguerabide, E. E. Yguerabide, *Analytical biochemistry* **1998**, *262*, 157-176; bT. Huang, P. D. Nallathamby, X. H. N. Xu, *Journal of the American Chemical Society* **2008**, *130*, 17095-17105.
- [99] aK. J. Lee, P. D. Nallathamby, L. M. Browning, C. J. Osgood, X. H. Xu, *ACS nano* **2007**, *1*, 133-143; bT. Huang, P. D. Nallathamby, D. Gillet, X. H. Xu, *Analytical chemistry* **2007**, *79*, 7708-7718; cS. Schultz, D. R. Smith, J. J. Mock, D. A. Schultz, *Proc Natl Acad Sci U S A* **2000**, *97*, 996-1001.
- [100] aJ. P. Wilcoxon, B. L. Abrams, *Chemical Society reviews* **2006**, *35*, 1162-1194; bJ. Zheng, P. R. Nicovich, R. M. Dickson, *Annu Rev Phys Chem* **2007**, *58*, 409-431.
- [101] H. Xu, K. S. Suslick, *Adv Mater* **2010**, *22*, 1078-1082.
- [102] P. C. Lee, D. Meisel, *J Phys Chem-U S* **1982**, *86*, 3391-3395.
- [103] J. A. Creighton, C. G. Blatchford, M. G. Albrecht, *J Chem Soc Farad T 2* **1979**, *75*, 790-798.
- [104] aF. Fievet, J. P. Lagier, B. Blin, B. Beaudoin, M. Figlarz, *Solid State Ionics* **1989**, *32-3*, 198-205; bB. Blin, F. Fievet, D. Beupere, M. Figlarz, *New J Chem* **1989**, *13*, 67-72.
- [105] T. Zhao, R. Sun, S. H. Yu, Z. J. Zhang, L. M. Zhou, H. T. Huang, R. X. Du, *Colloid Surface A* **2010**, *366*, 197-202.
- [106] J. W. Bai, Y. Qin, C. Y. Jiang, L. M. Qi, *Chem Mater* **2007**, *19*, 3367-+.
- [107] N. R. Jana, L. Gearheart, C. J. Murphy, *Chem Commun* **2001**, 617-618.
- [108] B. Wiley, Y. G. Sun, B. Mayers, Y. N. Xia, *Chem-Eur J* **2005**, *11*, 454-463.
- [109] D. M. Ledwith, A. M. Whelan, J. M. Kelly, *J Mater Chem* **2007**, *17*, 2459-2464.
- [110] S. H. Chen, Z. Y. Fan, D. L. Carroll, *J Phys Chem B* **2002**, *106*, 10777-10781.
- [111] S. H. Chen, D. L. Carroll, *Nano Lett* **2002**, *2*, 1003-1007.
- [112] Y. J. Xiong, J. Y. Chen, B. Wiley, Y. N. Xia, S. Aloni, Y. D. Yin, *Journal of the American Chemical Society* **2005**, *127*, 7332-7333.
- [113] Y. J. Zhu, X. L. Hu, *Chem Lett* **2004**, *33*, 760-761.
- [114] G. F. Xiao, Y. B. Zhao, X. L. Meng, Z. S. Wu, Z. J. Zhang, *J Alloy Compd* **2007**, *437*, 329-331.
- [115] C. Liu, X. W. Wu, T. Klemmer, N. Shukla, X. M. Yang, D. Weller, A. G. Roy, M. Tanase, D. Laughlin, *J Phys Chem B* **2004**, *108*, 6121-6123.
- [116] aP. L. Zhu, J. W. Zhang, Z. S. Wu, Z. J. Zhang, *Cryst Growth Des* **2008**, *8*, 3148-3153; bC. Feldmann, H. O. Jungk, *Angew Chem Int Edit* **2001**, *40*, 359-362.
- [117] aJ. M. Slocik, J. T. Moore, D. W. Wright, *Nano Lett* **2002**, *2*, 169-173; bE. Braun, Y. Eichen, U. Sivan, G. Ben-Yoseph, *Nature* **1998**, *391*, 775-778.
- [118] aJ. Richter, R. Seidel, R. Kirsch, M. Mertig, W. Pompe, J. Plaschke, H. K. Schackert, *Adv Mater* **2000**, *12*, 507-+; bJ. Richter, M. Mertig, W. Pompe, I. Monch, H. K. Schackert, *Appl Phys Lett* **2001**, *78*, 536-538; cM. Mertig, L. C. Ciacchi, R. Seidel, W. Pompe, A. De Vita, *Nano Lett* **2002**, *2*, 841-844.
- [119] Y. C. Hung, W. T. Hsu, T. Y. Lin, L. Fruk, *Appl Phys Lett* **2011**, *99*.
- [120] aS. M. Meshram, S. R. Bonde, I. R. Gupta, A. K. Gade, M. K. Rai, *Int Nanobiotechnol* **2013**, *7*, 28-32; bA. R. Vilchis-Nestor, V. Sanchez-Mendieta, M. A. Carnacho-Lopez, R. M. Gomez-Espinosa, M. A. Camacho-Lopez, J. A. Arenas-Alatorre, *Mater Lett* **2008**, *62*, 3103-3105; cS. Irvani, B. Zolfaghari, *BioMed research international* **2013**; dR. Agarwal, N. Agrawal, R. Singh, *Adv. Sci. Eng. Med.* **2014**, *6*, 203-207.
- [121] P. Mukherjee, A. Ahmad, D. Mandal, S. Senapati, S. R. Sainkar, M. I. Khan, R. Parishcha, P. V. Ajaykumar, M. Alam, R. Kumar, M. Sastry, *Nano Lett* **2001**, *1*, 515-519.

- [122] aR. Ramanathan, A. P. O'Mullane, R. Y. Parikh, P. M. Smooker, S. K. Bhargava, V. Bansal, *Langmuir : the ACS journal of surfaces and colloids* **2011**, *27*, 714-719; bN. Samadi, D. Golkaran, A. Eslamifar, H. Jamalifar, M. R. Fazeli, F. A. Mohseni, *J Biomed Nanotechnol* **2009**, *5*, 247-253.
- [123] aN. Vigneshwaran, R. P. Nachane, R. H. Balasubramanya, P. V. Varadarajan, *Carbohydr Res* **2006**, *341*, 2012-2018; bD. Maity, M. K. Bain, B. Bhowmick, J. Sarkar, S. Saha, K. Acharya, M. Chakraborty, D. Chattopadhyay, *J Appl Polym Sci* **2011**, *122*, 2189-2196.
- [124] M. N. Nadagouda, T. F. Speth, R. S. Varma, *Accounts Chem Res* **2011**, *44*, 469-478.
- [125] J. S. Kim, E. Kuk, K. N. Yu, J. H. Kim, S. J. Park, H. J. Lee, S. H. Kim, Y. K. Park, Y. H. Park, C. Y. Hwang, Y. K. Kim, Y. S. Lee, D. H. Jeong, M. H. Cho, *Nanomedicine : nanotechnology, biology, and medicine* **2007**, *3*, 95-101.
- [126] aS. Mohanty, S. Mishra, P. Jena, B. Jacob, B. Sarkar, A. Sonawane, *Nanomed-Nanotechnol* **2012**, *8*, 916-924; bM. Rai, A. Yadav, A. Gade, *Biotechnol Adv* **2009**, *27*, 76-83.
- [127] A. R. Shahverdi, A. Fakhimi, H. R. Shahverdi, S. Minaian, *Nanomedicine : nanotechnology, biology, and medicine* **2007**, *3*, 168-171.
- [128] P. L. Nadworny, J. Wang, E. E. Tredget, R. E. Burrell, *Nanomedicine : nanotechnology, biology, and medicine* **2008**, *4*, 241-251.
- [129] J. Lin, R. Chen, S. Feng, J. Pan, Y. Li, G. Chen, M. Cheng, Z. Huang, Y. Yu, H. Zeng, *Nanomedicine : nanotechnology, biology, and medicine* **2011**, *7*, 655-663.
- [130] K. H. Kwan, X. Liu, M. K. To, K. W. Yeung, C. M. Ho, K. K. Wong, *Nanomedicine : nanotechnology, biology, and medicine* **2011**, *7*, 497-504.
- [131] J. L. Elechiguerra, J. L. Burt, J. R. Morones, A. Camacho-Bragado, X. Gao, H. H. Lara, M. J. Yacaman, *Journal of nanobiotechnology* **2005**, *3*, 6.
- [132] C. Tse, M. J. Zohdy, J. Y. Ye, M. O'Donnell, W. Lesniak, L. Balogh, *Nanomedicine : nanotechnology, biology, and medicine* **2011**, *7*, 97-106.
- [133] aX. Y. Chen, *Theranostics* **2011**, *1*, 1-2; bE. Y. Lukianova-Hleb, A. O. Oginsky, A. P. Samaniego, D. L. Shenefelt, D. S. Wagner, J. H. Hafner, M. C. Farach-Carson, D. O. Lapotko, *Theranostics* **2011**, *1*, 3-17; cD. O. Lapotko, *Theranostics* **2013**, *3*, 138-140; dL. S. Wang, M. C. Chuang, J. A. Ho, *International journal of nanomedicine* **2012**, *7*, 4679-4695.
- [134] aW. Chen, N. Xu, L. Xu, L. Wang, Z. Li, W. Ma, Y. Zhu, C. Xu, N. A. Kotov, *Macromolecular rapid communications* **2010**, *31*, 228-236; bS. S. Kelkar, T. M. Reineke, *Bioconjugate chemistry* **2011**, *22*, 1879-1903.
- [135] S. Boca-Farcu, M. Potara, T. Simon, A. Juhem, P. Baldeck, S. Astilean, *Molecular pharmaceutics* **2013**.
- [136] P. Prokopovich, R. Leech, C. J. Carmalt, I. P. Parkin, S. Perni, *International journal of nanomedicine* **2013**, *8*, 2227-2237.
- [137] aC. H. Ho, E. K. Odermatt, I. Berndt, J. C. Tiller, *Journal of biomaterials science. Polymer edition* **2013**, *24*, 1589-1600; bM. S. Cohen, J. M. Stern, A. J. Vanni, R. S. Kelley, E. Baumgart, D. Field, J. A. Libertino, I. C. Summerhayes, *Surgical infections* **2007**, *8*, 397-403.
- [138] Y. Li, P. Leung, L. Yao, Q. W. Song, E. Newton, *The Journal of hospital infection* **2006**, *62*, 58-63.
- [139] J. C. Fan, K. M. Srekanth, Z. Xie, S. L. Chang, K. V. Rao, *Prog Mater Sci* **2013**, *58*, 874-985.
- [140] E. A. Meulenkamp, *J Phys Chem B* **1998**, *102*, 5566-5572.
- [141] H. Z. Zhang, J. F. Banfield, *J Phys Chem B* **2000**, *104*, 3481-3487.
- [142] aM. Lazzeri, A. Vittadini, A. Selloni, *Phys Rev B* **2001**, *63*; bA. S. Barnard, P. Zapol, *Phys Rev B* **2004**, *70*.
- [143] A. Kudo, Y. Miseki, *Chemical Society reviews* **2009**, *38*, 253-278.
- [144] A. Fujishima, K. Honda, *Nature* **1972**, *238*, 37-+.
- [145] aA. Fujishima, X. T. Zhang, *Cr Chim* **2006**, *9*, 750-760; bX. Chen, S. S. Mao, *Chem Rev* **2007**, *107*, 2891-2959.
- [146] K. Page, M. Wilson, I. P. Parkin, *J Mater Chem* **2009**, *19*, 3819-3831.
- [147] B. Ohtani, O. O. Prieto-Mahaney, D. Li, R. Abe, *J Photoch Photobio A* **2010**, *216*, 179-182.

- [148] B. Ohtani, *Chem Lett* **2008**, *37*, 217-229.
- [149] D. C. Hurum, A. G. Agrios, K. A. Gray, T. Rajh, M. C. Thurnauer, *J Phys Chem B* **2003**, *107*, 4545-4549.
- [150] C. Burda, X. B. Chen, R. Narayanan, M. A. El-Sayed, *Chem Rev* **2005**, *105*, 1025-1102.
- [151] D. Ganguli, *B Mater Sci* **1992**, *15*, 421-430.
- [152] aJ. C. S. Wu, C. H. Chen, *J Photoch Photobio A* **2004**, *163*, 509-515; bU. G. Akpan, B. H. Hameed, *Appl Catal a-Gen* **2010**, *375*, 1-11; cU. G. Akpan, B. H. Hameed, *J Colloid Interf Sci* **2011**, *357*, 168-178.
- [153] T. Lopez, R. Gomez, G. Pecci, P. Reyes, X. Bokhimi, O. Novaro, *Mater Lett* **1999**, *40*, 59-65.
- [154] A. Di Paola, E. Garcia-Lopez, S. Ikeda, G. Marci, B. Ohtani, L. Palmisano, *Catal Today* **2002**, *75*, 87-93.
- [155] aJ. G. Yu, J. C. Yu, B. Cheng, X. J. Zhao, Z. Zheng, A. S. K. Li, *J Sol-Gel Sci Techn* **2002**, *24*, 229-240; bJ. G. Yu, J. C. Yu, B. Cheng, X. J. Zhao, *J Sol-Gel Sci Techn* **2002**, *24*, 39-48.
- [156] Z. H. Yuan, J. H. Jia, L. D. Zhang, *Mater Chem Phys* **2002**, *73*, 323-326.
- [157] F. B. Li, X. Z. Li, *Appl Catal a-Gen* **2002**, *228*, 15-27.
- [158] H. E. Chao, Y. U. Yun, H. U. Xingfang, A. Larbot, *J Eur Ceram Soc* **2003**, *23*, 1457-1464.
- [159] aL. Spanhel, M. A. Anderson, *Journal of the American Chemical Society* **1991**, *113*, 2826-2833; bH. J. Lee, S. Y. Jeong, C. R. Cho, C. H. Park, *Appl Phys Lett* **2002**, *81*, 4020-4022; cJ. H. Lee, B. O. Park, *Thin Solid Films* **2003**, *426*, 94-99.
- [160] J. Tang, F. Redl, Y. M. Zhu, T. Siegrist, L. E. Brus, M. L. Steigerwald, *Nano Lett* **2005**, *5*, 543-548.
- [161] O. Carp, C. L. Huisman, A. Reller, *Prog Solid State Ch* **2004**, *32*, 33-177.
- [162] H. G. Yang, H. C. Zeng, *J Phys Chem B* **2004**, *108*, 3492-3495.
- [163] V. Loryuenyong, K. Angamnuaaysiri, J. Sukcharoenpong, A. Suwannasri, *Ceram Int* **2012**, *38*, 2233-2237.
- [164] Y. Shchipunov, I. Postnova, *Colloid Surface B* **2009**, *74*, 172-177.
- [165] M. Sanchez-Dominguez, L. F. Liotta, G. Di Carlo, G. Pantaleo, A. M. Venezia, C. Solans, M. Boutonnet, *Catal Today* **2010**, *158*, 35-43.
- [166] F. Lu, W. P. Cai, Y. G. Zhang, *Adv Funct Mater* **2008**, *18*, 1047-1056.
- [167] aM. Nidhin, R. Indumathy, K. J. Sreeram, B. U. Nair, *B Mater Sci* **2008**, *31*, 93-96; bE. Kharlampieva, T. Tsukruk, J. M. Slocik, H. Ko, N. Poulsen, R. R. Naik, N. Kroger, V. V. Tsukruk, *Adv Mater* **2008**, *20*, 3274-+.
- [168] C. L. Sajti, R. Sattari, B. N. Chichkov, S. Barcikowski, *J Phys Chem C* **2010**, *114*, 2421-2427.
- [169] B. Oregan, M. Gratzel, *Nature* **1991**, *353*, 737-740.
- [170] J. Kim, S. H. Lim, Y. S. Kim, *Journal of the American Chemical Society* **2010**, *132*, 14721-14723.
- [171] M. N. Hyder, B. M. Gallant, N. J. Shah, Y. Shao-Horn, P. T. Hammond, *Nano Lett* **2013**, *13*, 4610-4619.
- [172] Z. F. Yin, L. Wu, H. G. Yang, Y. H. Su, *Physical Chemistry Chemical Physics* **2013**, *15*, 4844-4858.
- [173] N. Serpone, A. E. Salinaro, S. Horikoshi, H. Hidaka, *J Photoch Photobio A* **2006**, *179*, 200-212.
- [174] aA. Fujishima, J. Ohtsuki, T. Yamashita, *Photomed. Photobiol.* **1986**, *8*, 45-46; bR. Cai, K. Hashimoto, Y. Kubota, A. Fujishima, *Chem Lett* **1992**, 427-430.
- [175] J. W. Seo, H. Chung, M. Y. Kim, J. Lee, I. H. Choi, J. Cheon, *Small* **2007**, *3*, 850-853.
- [176] aY. Kubota, T. Shuin, C. Kawasaki, M. Hosaka, H. Kitamura, R. Cai, H. Sakai, K. Hashimoto, A. Fujishima, *British journal of cancer* **1994**, *70*, 1107-1111; bC. Wang, S. Q. Cao, X. X. Tie, B. Qiu, A. H. Wu, Z. H. Zheng, *Mol Biol Rep* **2011**, *38*, 523-530.
- [177] J. Xu, Y. Sun, J. J. Huang, C. M. Chen, G. Y. Liu, Y. Jiang, Y. M. Zhao, Z. Y. Jiang, *Bioelectrochemistry* **2007**, *71*, 217-222.
- [178] C. Ogino, N. Shibata, R. Sasai, K. Takaki, Y. Miyachi, S. Kuroda, K. Ninomiya, N. Shimizu, *Bioorg Med Chem Lett* **2010**, *20*, 5320-5325.
- [179] E. A. Rozhkova, I. Ulasov, B. Lai, N. M. Dimitrijevic, M. S. Lesniak, T. Rajh, *Nano Lett* **2009**, *9*, 3337-3342.

- [180] K. Matsui, M. Segawa, T. Tanaka, A. Kondo, C. Ogino, *J Biosci Bioeng* **2009**, *108*, S36-S37.
- [181] Y. C. Zhu, H. L. Li, Y. Kolytyn, Y. R. Hacohen, A. Gedanken, *Chem Commun* **2001**, 2616-2617.
- [182] H. Strohm, M. Sgraja, J. Bertling, P. Lobmann, *J Mater Sci* **2003**, *38*, 1605-1609.
- [183] T. Y. Peng, D. Zhao, K. Dai, W. Shi, K. Hirao, *J Phys Chem B* **2005**, *109*, 4947-4952.
- [184] B. E. Heredia-Cervera, S. A. Gonzalez-Azcorra, G. Rodriguez-Gattorno, T. Lopez, E. Ortiz-Islas, G. Oskam, *Sci Adv Mater* **2009**, *1*, 63-68.
- [185] M. J. Uddin, D. Mondal, C. A. Morris, T. Lopez, U. Diebold, R. D. Gonzalez, *Appl Surf Sci* **2011**, *257*, 7920-7927.
- [186] T. Lopez, J. Sotelo, J. Navarrete, J. A. Ascencio, *Opt Mater* **2006**, *29*, 88-94.
- [187] aY. Qin, L. Sun, X. X. Li, Q. Q. Cao, H. Wang, X. F. Tang, L. Ye, *J Mater Chem* **2011**, *21*, 18003-18010; bK. C. W. Wu, Y. Yamauchi, C. Y. Hong, Y. H. Yang, Y. H. Liang, T. Funatsu, M. Tsunoda, *Chem Commun* **2011**, *47*, 5232-5234.
- [188] T. Paunesku, T. Rajh, G. Wiederrecht, J. Maser, S. Vogt, N. Stojicevic, M. Protic, B. Lai, J. Oryhon, M. Thurnauer, G. Woloschak, *Nature materials* **2003**, *2*, 343-346.
- [189] T. Paunesku, S. Vogt, B. Lai, J. Maser, N. Stojicevic, K. T. Thurn, C. Osipo, H. Liu, D. Legnini, Z. Wang, C. Lee, G. E. Woloschak, *Nano Lett* **2007**, *7*, 596-601.
- [190] aT. Tachikawa, Y. Asanoi, K. Kawai, S. Tojo, A. Sugimoto, M. Fujitsuka, T. Majima, *Chem-Eur J* **2008**, *14*, 1492-1498; bJ. Q. Liu, L. de la Garza, L. G. Zhang, N. M. Dimitrijevic, X. B. Zuo, D. M. Tiede, T. Rajh, *Chem Phys* **2007**, *339*, 154-163; cT. Rajh, Z. Saponjic, J. Q. Liu, N. M. Dimitrijevic, N. F. Scherer, M. Vega-Arroyo, P. Zapol, L. A. Curtiss, M. C. Thurnauer, *Nano Lett* **2004**, *4*, 1017-1023.
- [191] A. I. Ekimov, A. L. Efros, A. A. Onushchenko, *Solid State Commun* **1985**, *56*, 921-924.
- [192] R. Rossetti, S. Nakahara, L. E. Brus, *Journal of Chemical Physics* **1983**, *79*, 1086-1088.
- [193] M. Reed, *Scientific American* **1993**, *268*, 118-123.
- [194] A. P. Alivisatos, *Science* **1996**, *271*, 933-937.
- [195] G. P. C. Drummen, *Int J Mol Sci* **2010**, *11*, 154-163.
- [196] X. Michalet, F. F. Pinaud, L. A. Bentolila, J. M. Tsay, S. Doose, J. J. Li, G. Sundaresan, A. M. Wu, S. S. Gambhir, S. Weiss, *Science* **2005**, *307*, 538-544.
- [197] A. L. Efros, M. Rosen, *Annu Rev Mater Sci* **2000**, *30*, 475-521.
- [198] M. Dahan, T. Laurence, F. Pinaud, D. S. Chemla, A. P. Alivisatos, M. Sauer, S. Weiss, *Optics letters* **2001**, *26*, 825-827.
- [199] M. Nirmal, B. O. Dabbousi, M. G. Bawendi, J. J. Macklin, J. K. Trautman, T. D. Harris, L. E. Brus, *Nature* **1996**, *383*, 802-804.
- [200] P. Reiss, J. Bleuse, A. Pron, *Nano Lett* **2002**, *2*, 781-784.
- [201] A. Sukhanova, M. Devy, L. Venteo, H. Kaplan, M. Artemyev, V. Oleinikov, D. Klinov, M. Pluot, J. H. M. Cohen, I. Nabiev, *Analytical biochemistry* **2004**, *324*, 60-67.
- [202] M. Y. Han, X. H. Gao, J. Z. Su, S. Nie, *Nature biotechnology* **2001**, *19*, 631-635.
- [203] C. B. Murray, D. J. Norris, M. G. Bawendi, *Journal of the American Chemical Society* **1993**, *115*, 8706-8715.
- [204] aX. G. Peng, M. C. Schlamp, A. V. Kadavanich, A. P. Alivisatos, *Journal of the American Chemical Society* **1997**, *119*, 7019-7029; bM. A. Hines, P. Guyot-Sionnest, *J Phys Chem-US* **1996**, *100*, 468-471; cB. O. Dabbousi, J. RodriguezViejo, F. V. Mikulec, J. R. Heine, H. Mattoussi, R. Ober, K. F. Jensen, M. G. Bawendi, *J Phys Chem B* **1997**, *101*, 9463-9475.
- [205] Z. A. Peng, X. G. Peng, *Journal of the American Chemical Society* **2001**, *123*, 183-184.
- [206] D. Gerion, F. Pinaud, S. C. Williams, W. J. Parak, D. Zanchet, S. Weiss, A. P. Alivisatos, *J Phys Chem B* **2001**, *105*, 8861-8871.
- [207] aL. Li, T. J. Daou, I. Texier, T. K. C. Tran, Q. L. Nguyen, P. Reiss, *Chem Mater* **2009**, *21*, 2422-2429; bT. Pons, E. Pic, N. Lequeux, E. Cassette, L. Bezdetnaya, F. Guillemin, F. Marchal, B. Dubertret, *ACS nano* **2010**, *4*, 2531-2538.
- [208] M. A. Walling, J. A. Novak, J. R. E. Shephard, *Int J Mol Sci* **2009**, *10*, 441-491.

- [209] G. Giraud, H. Schulze, T. T. Bachmann, C. J. Campbell, A. R. Mount, P. Ghazal, M. R. Khondoker, A. J. Ross, S. W. J. Ember, I. Ciani, C. Tlili, A. J. Walton, J. G. Terry, J. Crain, *Int J Mol Sci* **2009**, *10*, 1930-1941.
- [210] R. Ibanez-Peral, P. L. Bergquist, M. R. Walter, M. Gibbs, E. M. Goldys, B. Ferrari, *Int J Mol Sci* **2008**, *9*, 2622-2638.
- [211] P. Haro-Gonzalez, W. T. Ramsay, L. M. Maestro, B. del Rosal, K. Santacruz-Gomez, M. D. Iglesias-de la Cruz, F. Sanz-Rodriguez, J. Y. Chooi, P. R. Sevilla, M. Bettinelli, D. Choudhury, A. K. Kar, J. G. Sole, D. Jaque, L. Paterson, *Small* **2013**, *9*, 2162-2170.
- [212] C. Y. Hsu, C. W. Chen, H. P. Yu, Y. F. Lin, P. S. Lai, *Biomaterials* **2013**, *34*, 1204-1212.
- [213] X. Jiang, C. Rucker, M. Hafner, S. Brandholt, R. M. Dorlich, G. U. Nienhaus, *ACS nano* **2010**, *4*, 6787-6797.
- [214] T. Rajh, L. X. Chen, K. Lukas, T. Liu, M. C. Thurnauer, D. M. Tiede, *J Phys Chem B* **2002**, *106*, 10543-10552.
- [215] aT. C. Damato, C. C. S. de Oliveira, R. A. Ando, P. H. C. Camargo, *Langmuir : the ACS journal of surfaces and colloids* **2013**, *29*, 1642-1649; bW. L. Ong, S. Natarajan, B. Kloostera, G. W. Ho, *Nanoscale* **2013**, *5*, 5568-5575; cU. Banin, Y. Ben-Shahar, K. Vinokurov, *Chem. Mater.* **2014**, *26*, 97-110.
- [216] C. Pacholski, A. Kornowski, H. Weller, *Angew Chem Int Edit* **2004**, *43*, 4774-4777.
- [217] aT. Mokari, E. Rothenberg, I. Popov, R. Costi, U. Banin, *Science* **2004**, *304*, 1787-1790; bT. Mokari, C. G. Sztrum, A. Salant, E. Rabani, U. Banin, *Nature materials* **2005**, *4*, 855-863.
- [218] R. Costi, A. E. Saunders, E. Elmalem, A. Salant, U. Banin, *Nano Lett* **2008**, *8*, 637-641.
- [219] K. L. Kelly, E. Coronado, L. L. Zhao, G. C. Schatz, *J Phys Chem B* **2003**, *107*, 668-677.
- [220] P. K. Jain, D. Ghosh, R. Baer, E. Rabani, A. P. Alivisatos, *P Natl Acad Sci USA* **2012**, *109*, 8016-8019.
- [221] aZ. K. Zheng, B. B. Huang, X. Y. Qin, X. Y. Zhang, Y. Dai, M. H. Whangbo, *J Mater Chem* **2011**, *21*, 9079-9087; bA. Tanaka, K. Fuku, T. Nishi, K. Hashimoto, H. Kominami, *J Phys Chem C* **2013**, *117*, 16983-16989.
- [222] aS. D. Jhaveri, D. A. Lowy, E. E. Foos, A. W. Snow, M. G. Ancona, L. M. Tender, *Chem. Commun.* **2002**, 1544-1545; bB. I. Ipe, K. G. Thomas, S. Barazzouk, S. Hotchandani, P. V. Kamat, *J. Phys. Chem. B* **2002**, *106*, 18-21; cS. Mubeen, G. Hernandez-Sosa, D. Moses, J. Lee, M. Moskovits, *Nano Lett* **2011**, *11*, 5548-5552.
- [223] aM. Jakob, H. Levanon, P. V. Kamat, *Nano. Lett.* **2003**, *3*, 353-358; bA. Takai, P. V. Kamat, *Acs Nano* **2011**, *5*, 7369-7376; cV. Subramanian, E. E. Wolf, P. V. Kamat, *J. Am. Chem. Soc.* **2004**, *126*, 4943-4950; dP. D. Cozzoli, M. L. Curri, A. Agostiano, *Chem. Commun.* **2005**, 3186-3188.
- [224] aY. Tian, T. Tatsuma, *J. Am. Chem. Soc.* **2005**, *127*, 7632-7637; bA. Furube, L. Du, K. Hara, R. Katoh, M. Tachiya, *J. Am. Chem. Soc.* **2007**, *129*, 14852-14853.
- [225] aM. Valden, X. Lai, D. W. Goodman, *Science* **1998**, *281*, 1647-1650; bX. F. Lai, D. W. Goodman, *J Mol Catal a-Chem* **2000**, *162*, 33-50.
- [226] E. Kowalska, R. Abe, B. Ohtani, *Chem. Commun.* **2009**, 241-243.
- [227] K. Awazu, M. Fujimaki, C. Rockstuhl, J. Tominaga, H. Murakami, Y. Ohki, N. Yoshida, T. Watanabe, *Journal of the American Chemical Society* **2008**, *130*, 1676-1680.
- [228] Y. Shiraishi, D. Tsukamoto, Y. Sugano, A. Shiro, S. Ichikawa, S. Tanaka, T. Hirai, *Acs Catal* **2012**, *2*, 1984-1992.
- [229] M. A. Behnajady, H. Eskandarloo, *Chem Eng J* **2013**, *228*, 1207-1213.
- [230] A. Mehri, H. Kochkar, S. Daniele, V. Mendez, A. Ghorbel, G. Berhault, *J Colloid Interf Sci* **2012**, *369*, 309-316.
- [231] aS. Sahoo, S. Husale, S. Karna, S. K. Nayak, P. M. Ajayan, *Journal of the American Chemical Society* **2011**, *133*, 4005-4009; bB. Xue, P. Chen, Q. Hong, J. Y. Lin, K. L. Tan, *J Mater Chem* **2001**, *11*, 2378-2381.
- [232] M. Moniruzzaman, K. I. Winey, *Macromolecules* **2006**, *39*, 5194-5205.
- [233] aA. F. Zedan, S. Moussa, J. Terner, G. Atkinson, M. S. El-Shall, *ACS nano* **2013**, *7*, 627-636; bR. Muszynski, B. Seger, P. V. Kamat, *J Phys Chem C* **2008**, *112*, 5263-5266.

- [234] aC. Boyer, M. R. Whittaker, V. Bulmus, J. Q. Liu, T. P. Davis, *Npg Asia Mater* **2010**, *2*, 23-30; bY. W. Cheng, L. Y. Yin, S. H. Lin, M. Wiesner, E. Bernhardt, J. Liu, *J Phys Chem C* **2011**, *115*, 4425-4432.
- [235] B. Domenech, M. Munoz, D. N. Muraviev, J. Macanas, *Nanoscale Res Lett* **2011**, *6*.
- [236] K. Knop, R. Hoogenboom, D. Fischer, U. S. Schubert, *Angew Chem Int Edit* **2010**, *49*, 6288-6308.
- [237] L. E. van Vlerken, T. K. Vyas, M. M. Amiji, *Pharmaceutical research* **2007**, *24*, 1405-1414.
- [238] aA. G. Kanaras, F. S. Kamounah, K. Schaumburg, C. J. Kiely, M. Brust, *Chem Commun (Camb)* **2002**, 2294-2295; bG. S. Kwon, *Critical reviews in therapeutic drug carrier systems* **2003**, *20*, 357-403.
- [239] R. Gref, Y. Minamitake, M. T. Peracchia, V. Trubetsky, V. Torchilin, R. Langer, *Science* **1994**, *263*, 1600-1603.
- [240] aA. M. Smith, A. M. Mohs, S. Nie, *Nature nanotechnology* **2009**, *4*, 56-63; bP. D. Cozzoli, T. Pellegrino, L. Manna, *Chemical Society reviews* **2006**, *35*, 1195-1208; cL. Carbone, P. D. Cozzoli, *Nano Today* **2010**, *5*, 449-493.
- [241] S. C. Chan, M. A. Barteau, *Langmuir : the ACS journal of surfaces and colloids* **2005**, *21*, 5588-5595.
- [242] P. Naknam, A. Luengnaruemitchai, S. Wongkasemjit, *Int J Hydrogen Energ* **2009**, *34*, 9838-9846.
- [243] W. H. Ni, R. A. Mosquera, J. Perez-Juste, L. M. Liz-Marzan, *J Phys Chem Lett* **2010**, *1*, 1181-1185.
- [244] R. Klajn, M. A. Olson, P. J. Wesson, L. Fang, A. Coskun, A. Trabolsi, S. Soh, J. F. Stoddart, B. A. Grzybowski, *Nat Chem* **2009**, *1*, 733-738.
- [245] A. J. Mastroianni, S. A. Claridge, A. P. Alivisatos, *Journal of the American Chemical Society* **2009**, *131*, 8455-8459.
- [246] A. Haryono, W. H. Binder, *Small* **2006**, *2*, 600-611.
- [247] C. O'Sullivan, S. Ahmed, K. M. Ryan, *J Mater Chem* **2008**, *18*, 5218-5222.
- [248] L. Carbone, A. Jakab, Y. Khalavka, C. Sonnichsen, *Nano Lett* **2009**, *9*, 3710-3714.
- [249] T. Mokari, A. Aharoni, I. Popov, U. Banin, *Angew Chem Int Edit* **2006**, *45*, 8001-8005.
- [250] D. Mocatta, G. Cohen, J. Schattner, O. Millo, E. Rabani, U. Banin, *Science* **2011**, *332*, 77-81.
- [251] aM. Berr, A. Vaneski, A. S. Susha, J. Rodriguez-Fernandez, M. Doblinger, F. Jackel, A. L. Rogach, J. Feldmann, *Appl Phys Lett* **2010**, *97*; bY. Shemesh, J. E. Macdonald, G. Menagen, U. Banin, *Angew Chem Int Edit* **2011**, *50*, 1185-1189.
- [252] A. Tanaka, A. Ogino, M. Iwaki, K. Hashimoto, A. Ohnuma, F. Amano, B. Ohtani, H. Kominami, *Langmuir : the ACS journal of surfaces and colloids* **2012**, *28*, 13105-13111.
- [253] A. Tanaka, K. Hashimoto, H. Kominami, *J. Am. Chem. Soc.* **2014**, *136*, 586-589.
- [254] aM. H. Oh, T. Yu, S. H. Yu, B. Lim, K. T. Ko, M. G. Willinger, D. H. Seo, B. H. Kim, M. G. Cho, J. H. Park, K. Kang, Y. E. Sung, N. Pinna, T. Hyeon, *Science* **2013**, *340*, 964-968; bJ. Zeng, Q. Zhang, J. Chen, Y. Xia, *Nano Lett* **2010**, *10*, 30-35.
- [255] L. Cheng, K. Yang, Y. G. Li, J. H. Chen, C. Wang, M. W. Shao, S. T. Lee, Z. Liu, *Angew Chem Int Edit* **2011**, *50*, 7385-7390.
- [256] N. Andhariya, B. Chudasama, R. V. Mehta, R. V. Upadhyay, *J Nanopart Res* **2011**, *13*, 1677-1688.
- [257] R. Campardelli, G. Della Porta, L. Gomez, S. Irusta, E. Reverchon, J. Santamaria, *J. Mater. Chem. B* **2014**, *2*, 409-417.
- [258] L. Zhu, D. Wang, X. Wei, X. Zhu, J. Li, C. Tu, Y. Su, J. Wu, B. Zhu, D. Yan, *Journal of controlled release : official journal of the Controlled Release Society* **2013**, *169*, 228-238.
- [259] T. Lammers, F. Kiessling, W. E. Hennink, G. Storm, *Molecular pharmaceutics* **2010**, *7*, 1899-1912.

- [260] J. C. Love, L. A. Estroff, J. K. Kriebel, R. G. Nuzzo, G. M. Whitesides, *Chem Rev* **2005**, *105*, 1103-1169.
- [261] aC. S. Weisbecker, M. V. Merritt, G. M. Whitesides, *Langmuir : the ACS journal of surfaces and colloids* **1996**, *12*, 3763-3772; bS. Y. Lin, Y. T. Tsai, C. C. Chen, C. M. Lin, C. H. Chen, *J Phys Chem B* **2004**, *108*, 2134-2139.
- [262] D. V. Leff, L. Brandt, J. R. Heath, *Langmuir : the ACS journal of surfaces and colloids* **1996**, *12*, 4723-4730.
- [263] aH. Dollefeld, K. Hoppe, J. Kolny, K. Schilling, H. Weller, A. Eychmuller, *Physical Chemistry Chemical Physics* **2002**, *4*, 4747-4753; bX. H. Ji, D. Copenhaver, C. Sichmeller, X. G. Peng, *Journal of the American Chemical Society* **2008**, *130*, 5726-5735.
- [264] T. Laaksonen, P. Ahonen, C. Johans, K. Kontturi, *Chemphyschem* **2006**, *7*, 2143-2149.
- [265] T. Sakura, T. Takahashi, K. Kataoka, Y. Nagasaki, *Colloid Polym Sci* **2005**, *284*, 97-101.
- [266] E. Oh, K. Susumu, A. J. Mäkinen, J. R. Deschamps, A. L. Huston, I. L. Medintz, *J. Phys. Chem. C* **2013**, *117*, 18947-18956.
- [267] aC. J. Ackerson, P. D. Jadzinsky, R. D. Kornberg, *Journal of the American Chemical Society* **2005**, *127*, 6550-6551; bP. D. Jadzinsky, G. Calero, C. J. Ackerson, D. A. Bushnell, R. D. Kornberg, *Science* **2007**, *318*, 430-433.
- [268] A. Moores, F. Goettmann, C. Sanchez, P. Le Floch, *Chem Commun* **2004**, 2842-2843.
- [269] C. A. Mirkin, R. L. Letsinger, R. C. Mucic, J. J. Storhoff, *Nature* **1996**, *382*, 607-609.
- [270] A. G. Dong, X. C. Ye, J. Chen, Y. J. Kang, T. Gordon, J. M. Kikkawa, C. B. Murray, *Journal of the American Chemical Society* **2011**, *133*, 998-1006.
- [271] J. Moser, S. Punchihewa, P. P. Infelta, M. Gratzel, *Langmuir : the ACS journal of surfaces and colloids* **1991**, *7*, 3012-3018.
- [272] H. Lee, N. F. Scherer, P. B. Messersmith, *P Natl Acad Sci USA* **2006**, *103*, 12999-13003.
- [273] aA. E. Regazzoni, P. Mandelbaum, M. Matsuyoshi, S. Schiller, S. A. Bilmes, M. A. Blesa, *Langmuir : the ACS journal of surfaces and colloids* **1998**, *14*, 868-874; bM. Vega-Arroyo, P. R. LeBreton, T. Rajh, P. Zapol, L. A. Curtiss, *Chem Phys Lett* **2005**, *406*, 306-311; cC. Creutz, M. H. Chou, *Inorganic chemistry* **2008**, *47*, 3509-3514.
- [274] aH. B. Na, G. Palui, J. T. Rosenberg, X. Ji, S. C. Grant, H. Mattoussi, *ACS nano* **2012**, *6*, 389-399; bG. Ramakrishna, H. N. Ghosh, *Langmuir : the ACS journal of surfaces and colloids* **2003**, *19*, 3006-3012.
- [275] aJ. J. Storhoff, C. A. Mirkin, *Chem Rev* **1999**, *99*, 1849-1862; bY. F. Wei, J. H. Kong, L. P. Yang, L. Ke, H. R. Tan, H. Liu, Y. Z. Huang, X. W. Sun, X. H. Lu, H. J. Du, *J Mater Chem A* **2013**, *1*, 5045-5052.
- [276] B. Samanta, H. Yan, N. O. Fischer, J. Shi, D. J. Jerry, V. M. Rotello, *J Mater Chem* **2008**, *18*, 1204-1208.
- [277] M. E. Aubin-Tam, H. Zhou, K. Hamad-Schifferli, *Soft Matter* **2008**, *4*, 554-559.
- [278] S. Rana, Y. C. Yeh, V. M. Rotello, *Curr Opin Chem Biol* **2010**, *14*, 828-834.
- [279] U. Drechsler, N. O. Fischer, B. L. Frankamp, V. M. Rotello, *Adv Mater* **2004**, *16*, 271-+.
- [280] E. Boisselier, L. Salmon, J. Ruiz, D. Astruc, *Chem Commun* **2008**, 5788-5790.
- [281] J. L. Brennan, N. S. Hatzakis, T. R. Tshikhudo, N. Dirvianskyte, V. Razumas, S. Patkar, J. Vind, A. Svendsen, R. J. M. Nolte, A. E. Rowan, M. Brust, *Bioconjugate chemistry* **2006**, *17*, 1373-1375.
- [282] M. X. Zhang, B. H. Huang, X. Y. Sun, D. W. Pang, *Langmuir : the ACS journal of surfaces and colloids* **2010**, *26*, 10171-10176.
- [283] Y. P. Kim, W. L. Daniel, Z. Y. Xia, H. X. Xie, C. A. Mirkin, J. H. Rao, *Chem Commun* **2010**, *46*, 76-78.
- [284] R. Hong, N. O. Fischer, A. Verma, C. M. Goodman, T. Emrick, V. M. Rotello, *Journal of the American Chemical Society* **2004**, *126*, 739-743.
- [285] H. Bayraktar, C. C. You, V. M. Rotello, M. J. Knapp, *Journal of the American Chemical Society* **2007**, *129*, 2732-+.

- [286] aJ. M. Abad, S. F. L. Mertens, M. Pita, V. M. Fernandez, D. J. Schiffrin, *Journal of the American Chemical Society* **2005**, *127*, 5689-5694; bJ. S. Kim, C. A. Valencia, R. H. Liu, W. B. Lin, *Bioconjugate chemistry* **2007**, *18*, 333-341.
- [287] M. De, S. Rana, V. M. Rotello, *Macromol Biosci* **2009**, *9*, 174-178.
- [288] K. Boeneman, B. C. Mei, A. M. Dennis, G. Bao, J. R. Deschamps, H. Mattoussi, I. L. Medintz, *Journal of the American Chemical Society* **2009**, *131*, 3828-+.
- [289] A. Di Stefano, P. Sozio, A. Cocco, A. Iannitelli, E. Santucci, M. Costa, L. Pecci, C. Nasuti, F. Cantalamessa, F. Pinnen, *J. Med. Chem.* **2006**, *49*, 1486-1493.
- [290] R. Greenwood, K. Kendall, *J Eur Ceram Soc* **1999**, *19*, 479-488.
- [291] J. W. Slot, H. J. Geuze, *Eur J Cell Biol* **1985**, *38*, 87-93.
- [292] Y. M. Mo, Y. Tang, F. Gao, J. Yang, Y. M. Zhang, *Ind Eng Chem Res* **2012**, *51*, 5995-6000.
- [293] H. Moini, L. Packer, N. E. L. Saris, *Toxicology and applied pharmacology* **2002**, *182*, 84-90.
- [294] I. A. Jankovic, Z. V. Saponjic, E. S. Dzunuzovic, J. M. Nedeljkovic, *Nanoscale Res Lett* **2010**, *5*, 81-88.
- [295] aS. Swetha, S. M. Santhosh, R. G. Balakrishna, *Photochem. Photobiol.* **2010**, *86*, 628-632; bM. N. Tahir, P. Theato, P. Oberle, G. Melnyk, S. Faiss, U. Kolb, A. Janshoff, M. Stepputat, W. Tremel, *Langmuir : the ACS journal of surfaces and colloids* **2006**, *22*, 5209-5212.
- [296] aZ. W. Seh, S. Liu, M. Low, S. Y. Zhang, Z. Liu, A. Mlayah, M. Y. Han, *Adv. Mater.* **2012**, *24*, 2310-2314; bV. Subramanian, E. E. Wolf, P. V. Kamat, *Langmuir : the ACS journal of surfaces and colloids* **2003**, *19*, 469-474.
- [297] W. Li, J. P. Yang, Z. X. Wu, J. X. Wang, B. Li, S. S. Feng, Y. H. Deng, F. Zhang, D. Y. Zhao, *J. Am. Chem. Soc.* **2012**, *134*, 11864-11867.
- [298] P. Ramasamy, D. M. Seo, S. H. Kim, J. Kim, *J. Mater. Chem.* **2012**, *22*, 11651-11657.
- [299] Z. Wang, X. W. Lou, *Adv. Mater.* **2012**, *24*, 4124-4129.
- [300] G. R. Bamwenda, S. Tsubota, T. Nakamura, M. Haruta, *J. Photoch. Photobio. A* **1995**, *89*, 177-189.
- [301] C. Gomes Silva, R. Juarez, T. Marino, R. Molinari, H. Garcia, *J. Am. Chem. Soc.* **2010**.
- [302] aK. M. Reddy, S. V. Manorama, A. R. Reddy, *Mater. Chem. Phys.* **2003**, *78*, 239-245; bB. Geiseler, L. Fruk, *J. Mater. Chem.* **2012**, *22*, 735-741.
- [303] B. Geiseler, M. Miljevic, P. Müller, L. Fruk, *J. Nanomater.* **2012**.
- [304] aE. Derat, S. Cohen, S. Shaik, A. Altun, W. Thiel, *J. Am. Chem. Soc.* **2005**, *127*, 13611-13621; bL. Fruk, V. Rajendran, M. Spengler, C. M. Niemeyer, *Chembiochem* **2007**, *8*, 2195-2198.
- [305] G. S. Li, D. Q. Zhang, J. C. Yu, *Environ Sci Technol* **2009**, *43*, 7079-7085.
- [306] Z. Zhang, L. Zhang, M. N. Hedhili, H. Zhang, P. Wang, *Nano Lett* **2013**, *13*, 14-20.
- [307] K. Kato, Y. Shiozawa, A. Yamada, M. Noguchi, K. Nishida, *Agr Biol Chem Tokyo* **1972**, *36*, 899-&.
- [308] T. Nagata, Y. Nemoto, S. Hasezawa, *Int Rev Cytol* **1992**, *132*, 1-30.
- [309] L. K. Braydich-Stolle, N. M. Schaeublin, R. C. Murdock, J. Jiang, P. Biswas, J. J. Schlager, S. M. Hussain, *J Nanopart Res* **2009**, *11*, 1361-1374.
- [310] K. Apel, H. Hirt, *Annu Rev Plant Biol* **2004**, *55*, 373-399.
- [311] W. A. Nelsonrees, R. R. Flandermeyer, *Science* **1976**, *191*, 96-98.
- [312] C. Glodek, *PhD Thesis* **1990**.
- [313] M. Lacroix, G. Leclercq, *Breast Cancer Res Tr* **2004**, *83*, 249-289.
- [314] aJ. Pi, H. Jin, R. Y. Liu, B. Song, Q. Wu, L. Liu, J. Jiang, F. Yang, H. H. Cai, J. Y. Cai, *Appl Microbiol Biot* **2013**, *97*, 1051-1062; bM. Heidari Majd, J. Barar, D. Asgari, H. Valizadeh, M. R. Rashidi, V. Kafil, J. Shahbazi, Y. Omid, *Advanced pharmaceutical bulletin* **2013**, *3*, 189-195; cD. Baba, Y. Seiko, T. Nakanishi, H. Zhang, A. Arakaki, T. Matsunaga, T. Osaka, *Colloids and surfaces. B, Biointerfaces* **2012**, *95*, 254-257.
- [315] F. L. Graham, J. Smiley, W. C. Russell, R. Nairn, *J Gen Virol* **1977**, *36*, 59-72.
- [316] A. Sadaf, B. Zeshan, Z. Y. Wang, R. H. Zhang, S. H. Xu, C. L. Wang, J. Yang, Y. P. Cui, *J Nanosci Nanotechno* **2012**, *12*, 6900-6906.

- [317] M. Takafuji, K. Kitaura, T. Nishiyama, S. Govindarajan, V. Gopal, T. Imamura, H. Ihara, *J. Mater. Chem. B* **2014**, *2*, 644-650.
- [318] T. Ribeiro, S. Raja, A. S. Rodrigues, F. Fernandes, J. P. S. Farinha, C. Baleizao, *Rsc Adv* **2013**, *3*, 9171-9174.
- [319] P. W. Sylvester, *Methods Mol Biol* **2011**, *716*, 157-168.
- [320] K. A. Janes, M. P. Fresneau, A. Marazuela, A. Fabra, M. J. Alonso, *Journal of Controlled Release* **2001**, *73*, 255-267.
- [321] C. M. Sayes, R. Wahi, P. A. Kurian, Y. P. Liu, J. L. West, K. D. Ausman, D. B. Warheit, V. L. Colvin, *Toxicol Sci* **2006**, *92*, 174-185.
- [322] N. M. Schaeublin, L. K. Braydich-Stolle, A. M. Schrand, J. M. Miller, J. Hutchison, J. J. Schlager, S. M. Hussain, *Nanoscale* **2011**, *3*, 410-420.
- [323] A. M. Derfus, W. C. W. Chan, S. N. Bhatia, *Nano Lett* **2004**, *4*, 11-18.
- [324] W. Haiss, N. T. Thanh, J. Aveyard, D. G. Fernig, *Anal. Chem.* **2007**, *79*, 4215-4221

8. List of Publications

1. Geiseler, B., Miljevic, M., Müller, P. and Fruk, L., “Phototriggered Production of Reactive Oxygen Species by TiO₂ Nanospheres and Rods”, *J. Nanomat.*, Vol. 2012, 9 pages, **2012**.
2. Miljevic, M., Geiseler, B., Bergfeldt, T., Bockstaller, P. and Fruk, L., “Enhanced Photocatalytic Activity of Au/TiO₂ Nanocomposite Prepared Using Bifunctional Bridging Linker”, *Adv. Funct. Mat.*, 24, 7, 907–915 **2014**.

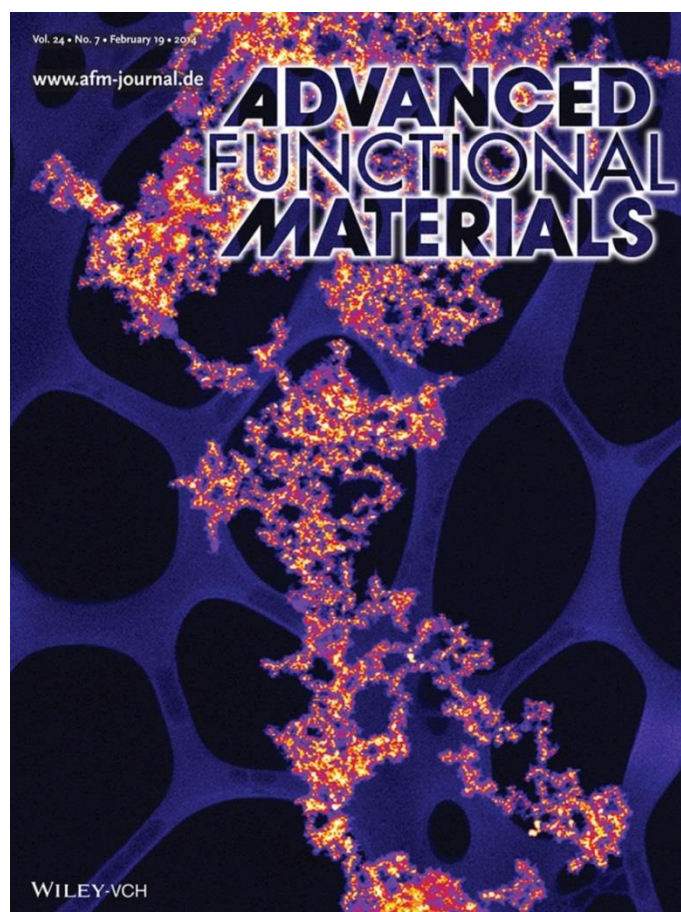


Figure 78. Inside cover image of Advanced Functional Materials journal (7/2014, page 907); a gold-titanium dioxide (Au/TiO₂) hybrid prepared using a bifunctional bridging linker. The bright yellow spots are Au NPs stabilized by a LA-DA linker, which are then bound to TiO₂ matrix (purple). This hybrid material shows remarkable catalytical activity towards activation of heme containing enzyme upon light irradiation.

9. List of Abbreviations

°C	centigrade/Celsius
μl	microliter
Ag NP	Silver Nanoparticles
AR	Amplex Red
Au NP	Gold Nanoparticles
a.u.	arbitrary units
BRET	Bioluminescence Resonance Energy Transfer
BY-2	tobacco cell line Bright Yellow - 2
CEA	Carcinoembryonic antigen
cm ²	squared centimeter
CV	Cell Viability
CTAB	Cetyltrimethylammonium Bromide
CW	Continuous Wave
DA	Dopamine
DCFH	Dichlorodihydrofluorescein
DFOMS	Dark-field Optical Microscopy and Spectroscopy
DLS	Dynamic Light Scattering
DMEM	Dulbecco's Modified Eagle Medium
DMSO	Dimethyl suloxide
DNA	Deoxyribonucleic Acid
DOX	Doxorubicin
DPA	D-penicillamine
DSSC	Dye-Sensitized Solar Cell
DTT	Dithiothreitol
EDXS	Energy Dispersive X-ray Spectroscopy
EGFR	Epidermal Growth Factor Receptor
EPR	Enhanced Permeability and Retention
FCM	Flow Cytometry
FITC	Fluorescein isothiocyanate
FLIM	Fluorescence Lifetime Imaging Microscopy
HAADF	High Angle Anular Dark Field
HEK293	Human Embryonic Kidney cells

List of Abbreviations

HeLa	Cervical cancer cell line
HIV-1	Human Immunodeficiency Virus Type 1
HRP	Horse Radish Proxidase
h	hour
IR	Infra-red
IUPAC	International Union of Pure and Applied Chemistry
L	liter
LA	Lipoic Acid
LASiS	Laser Ablation Synthesis in Solution
LC50	Median Lethal Dose
LBL	Layer-by-Layer
LCG	Laser Conversion of Graphene oxide into graphene
LMCT	Ligand-to-Metal Charge Transfer
LSPR	Localized Surface Plasmon Resonance
MAA	Mercaptoacetic Acid
MBT	Maltose-Binding protein
MCF7	Breast cancer cell line
MF NPs	Multifunctional Nanoparticles
min	minute
mL	mililiter
MPA	Mercaptopropionic acid
MRI	Magnetic Resonance Imaging
MRSA	Methicillin-resistant <i>Staphylococcus aureus</i>
MT	Metallthionein
MTB	<i>Mycobacterium tuberculosis</i>
MTBC	<i>Mycobacterium tuberculosis</i> Complex
MTT	Methylthiazol Tetrazolium
MUA	Mercaptoundecanoic Acid
MW	Molecular Weight
NALI	Nanoparticle Assisted Light Induced
NIR	Near-infrared
NLS	Nuclear Localization Signal
nm	nanometer
NP(s)	Nanoparticle(s)
NR(s)	Nanorod(s)

List of Abbreviations

NT(s)	Nanotriangle(s)
PAA	Poly(acrylic acid)
PCNA	Proliferating Cell Nuclear Antigen
PDT	Photo-dynamic Therapy
PEG	Poly(ethyleneglycol)
PEO	polyethylene oxide
PLA	Poly-lactic Acid
POI	Protein of Interest
PVP	Poly(vinyl pyrrolidone)
QD(s)	Quantum Dot(s)
R	radius
RES	Reticulo-Endothelial System
RGD	Arginylglycylaspartic Acid
RNA	Ribonucleic Acid
ROS	Reactive Oxygen Species
RPM	Revolutions Per Minute
RPMI	Cell medium
RT	Room Temperature
SAED	Selected Area Electron Diffraction
scFv	single-chain variable fragment
SDS	Sodium Dodecyl Sulfate
SERS	Surface-enhanced Raman Spectroscopy
SPIO	Superparamagnetic iron-oxide
SS	Solid State
STEM	Scanning Electron Microscopy
TA	Thioctic Acid
TEM	Transmission Electron Microscopy
TOAB	Tetra-n-octylammonium Bromide
	Terminal deoxynucleotidyl transferase dUTP Nick
TUNEL	End Labeling
UCNP	Up-converting Nanoparticles
UV	Ultra Violet (light)
Vis	Visible (light)
W	Watt

10. Acknowledgments

I would firstly like to thank my mentor, Dr. Ljiljana Fruk for all the inspiration and guidance that she provided during my stay in Karlsruhe, both in the course of my PhD studies and outside of the lab. I could not have imagined a better boss!

Secondly, I would like to thank the DAAD, without who's financial support this work would not be possible.

Further on, I am grateful for the help of Ishtiaq Ahmed, for his hard work, for his patients and readiness to assists at any time.

I would like to thank Dennis Bauer for the scientific discussions that resulted in many nice ideas and great results. I would also like to thank him for the great energy and *buena onda* that he brings into everything that he does!

I would like to thank Bianca Geiseler and Dania Kendziora for helping me to get in the lab!

Cheng Chen, Antonina Vigovskaya and Lukas Stolzer were the best co-workers!

Many of the experiments reported in this thesis were done in collaborations with other groups. Many thanks go to Prof. Dr. Nienhaus and his co-workers Shang Li and Stefan Brandholt for the help in DLS and Zeta measurements, Prof. Dr. Stefan Bräse and Dr. Nicole Jung for the help in Raman Spectroscopy measurements, Prof. Dr. Dagmar Gerthsen and her co-workers Andreas Lefarth, Philipp Müller and Pascal Bockstaller for the TEM imaging, Prof. Dr. Peter Nick and his co-workers Dr. Jan Maish and Johanna Kraher for the help in the BY-2 cell studies, Dr. Clemens Franz and his co-workers Ramona Ring, Tetyana Gudzenko and Carina Gonnermann for help in the mammalian cell studies and finally Dr. Thomas Bergfeldt for the ICP-MS measurements.

I would like to thank the administrative staff of the CFN, Andreas Elkeries the IT (and jack of all trades) manager, administrative assistants Frau Bender and Frau Mösle, the financial officer Andreas Martin and the administrative manager Dr. Christian Röthig, for providing excellent working environment.

It is always comforting to know that whatever you do and whatever the results are, your family stands behind you. I would like to thank my mother Olivera, my father Vladimir and my grandmother Nevenka for giving me this priceless feeling.

The same goes for my buddies Bruno and Luka, who were always there for me.

The last and the most important thank you goes to my love Maja Petrovic who was all the time by my side, sharing all the ups and downs. This would not be possible without her.

11. Curriculum Vitae

VOĆARSKA CESTA 59
10000 ZAGREB
CROATIA

CELL PHONE 0049 176 783 05658
E-MAIL miljevic.marko@gmail.com

Marko Miljević

Personal Information

- Nationality: Croatian
- Age: 30
- Place of Birth: Zagreb, Croatia

Objective

Gaining knowledge, working experience and PhD in the field of nanobiotechnology and /or nanomedicine.

Education

[Dates Attended] [Company/Institution Name]

2002 **Secondary School Diploma**

2002 – 2004 **University of Zagreb, Croatia**
Faculty of Electrotechnics and Computer Engineering

- undergraduate student

2004 – 2009 **University of Zagreb, Croatia**
Faculty of Sciences , Physical Department

- undergraduate student
- Diploma thesis: *“Magnetoencefalography and localization of visual cortical activity”*, mentor doc. dr. Sc. Selma Supek

2010 – 2014 **Karlsruher Institut für Technologie, Germany**
Center for Functional Nanostructures

- PhD student

Awards received

Scholarship of the Republic of Croatia , 2002-2004

Deutscher Akademischer Austausch Dienst (DAAD), 2010-2014

Interests and activities

Nanotechnology applied to medicine (Biophysics, Drug delivery, Cancer Treatment, Imaging).

Languages

Croatian (mother language), English (fluent), German (good), French (beginner)

Work experience

[Dates Attended] [Company/Institution Name]

2006 – 2007

**Ruđer Bošković Institute, Zagreb, Croatia
Division for Marine and Environmental Research**

- student project under supervision of prof. Vesna Svetličić
- study highlights the capacity of AFM for investigating surface properties of live cells
- project title:

***“MORPHOLOGICAL AND MECHANICAL CHARACTERIZATION OF MARINE
DIATOM *Cylindrotheca fusiformis*”***

Conferences

- *International Meeting on AFM in Life Science and Medicine*, Barcelona, Spain, 2007. (with poster “Morphological and mechanical characterization of Marine Diatom *Cylindrothecae fusiformis*”)
- *ISAC XXIV International Congress*, Budapest, Hungary, 2008.
- *Mind and Brain VI*, Dubrovnik, Croatia, 2009.
- *Biomag 2010*, Dubrovnik, Croatia, 2010.
- *CFN Summer School on Nano-Biology*, Bad Herrenalb, Germany, 2011.
- *Clinical Nanomedicine & Targeted Medicine*, Basel, Switzerland, 2013.

Marko Miljevic
Sedanstrasse 4
76185 Karlsruhe

Karlsruhe, 28.02.2014

To whom it may concern.

This thesis is the result of my work done in the Centre for Functional Nanostructures, Karlsruhe Institute of Technology in the period between 01.10.2010 and 05.03.2014 under the supervision of Dr. Ljiljana Fruk.

With this letter I would like to declare the originality of the thesis and state that in its writing only the results obtained in the above stated period were used. Furthermore, these results are documented in the four (4) laboratory journals that were kept throughout the work and are available for inspection. The introductory part was written with help of the already published work in peer reviewed journals available through the KIT network as well as with the use of internet resources. The experimental results obtained in collaborations are acknowledged on the last pages of the thesis.

Marko Miljevic

